AEDC-TR-99-4

Experimental and Theoretical Study of Cavity Acoustics

R. E. Dix and R. C. Bauer
Sverdrup Technology, Inc./AEDC Group

May 2000

Final Report for Period October 1997 through September 1998

Approved for public release; distribution is unlimited.

ARNOLD ENGINEERING DEVELOPMENT CENTER
ARNOLD AIR FORCE BASE, TENNESSEE
AIR FORCE MATERIEL COMMAND
UNITED STATES AIR FORCE

NOTICES
When U. S. Government drawings, specifications, or other data are used for any purpose other than a definitely related Government procurement operation, the Government thereby incurs no responsibility nor any obligation whatsoever, and the fact that the Government may have formulated, furnished, or in any way supplied the said drawings, specifications, or other data, is not to be regarded by implication or otherwise, or in any manner licensing the holder or any other person or corporation, or conveying any rights or permission to manufacture, use, or sell any patented invention that may in any way be related thereto.
Qualified users may obtain copies of this report from the Defense Technical Information Center.
References to named commercial products in this report are not to be considered in any sense as an endorsement of the product by the United States Air Force or the Government.

This report has been reviewed by the Office of Public Affairs (PA) and is releasable to the National Technical Information Service (NTIS). At NTIS, it will be available to the general public, including foreign nations.

APPROVAL STATEMENT

This report has been reviewed and approved.

PHI-ANH T. BUI, Capt, USAF
Technology Project Manager
Applied Technology Division
Test Operations Directorate

Approved for publication:

FOR THE COMMANDER

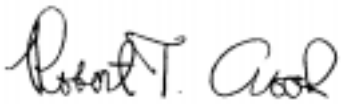

ROBERT T. CROOK
Assistant Chief, Applied Technology Division
Test Operation Directorate

REPORT DOCUMENTATION PAGE	Form Approved OMB No. 0704-0188

The public reporting burden for this collection of information is estimated to average 1 hour per response, including the time for reviewing instructions, searching existing data sources, gathering and maintaining the data needed, and completing and reviewing the collection of information. Send comments regarding this burden estimate or any other aspect of this collection of information, including suggestions for reducing the burden, to Department of Defense, Washington Headquarters Services, Directorate for Information Operations and Reports (0704-0188), 1215 Jefferson Davis Highway, Suite 1204, Arlington, VA 22202-4302. Respondents should be aware that notwithstanding any other provision of law, no person shall be subject to any penalty for failing to comply with a collection of information if it does not display a currently valid OMB control number
PLEASE DO NOT RETURN YOUR FORM TO THE ABOVE ADDRESS.

1. REPORT DATE *(DD-MM-YYYY)*	2. REPORT TYPE	3. DATES COVERED *(From - To)*
April 2000	Final Report	October 1997 - September 1998

4. TITLE AND SUBTITLE

Experimental and Theoretical Study of Cavity Acoustics

5a. CONTRACT NUMBER
F40600-95-C000017

5b. GRANT NUMBER

5c. PROGRAM ELEMENT NUMBER
64408D

6. AUTHOR(S)

R. E. Dix and R. C. Bauer, Sverdrup Technology, Inc., AEDC Group

5d. PROJECT NUMBER
4594

5e. TASK NUMBER

5f. WORK UNIT NUMBER

7. PERFORMING ORGANIZATION NAME(S) AND ADDRESS(ES)

Arnold Engineering Development Center/DOT
Air Force Materiel Command
Arnold Air Force Base, TN 37389-9011

8. PERFORMING ORGANIZATION REPORT NUMBER

AEDC-TR-99-4

9. SPONSORING/MONITORING AGENCY NAME(S) AND ADDRESS(ES)

Air Force Seek Eagle Office
Eglin AFB, FL 32542

10. SPONSOR/MONITOR'S ACRONYM(S)

11. SPONSOR/MONITOR'S REPORT NUMBER(S)
AFSEO

12. DISTRIBUTION/AVAILABILITY STATEMENT

Approved for public release, distribution is unlimited.

13. SUPPLEMENTARY NOTES

Available in Defense Technical Information Center (DTIC)

14. ABSTRACT

Between 1986 and 1990, a large database was compiled at AEDC from the results of wind tunnel experiments investigating the aerodynamics of flow over open cavities. The database, known as the Weapons Internal Carriage and Separation (WICS) database, covered four experiments that were completed in the AEDC wind tunnels. The initial database documentation focused on the test and data, but included very little analysis of the results. The purpose of the present work is to report analysis of the cavity acoustics and trajectory data. In addition, an updated engineering mathematical model for cavity aeroacoustics is presented.

15. SUBJECT TERMS

cavity, acoustics, aeroacoustics, weapons bay, store separation, experimental data, mathematical model, trajectory, database, wind tunnel

16. SECURITY CLASSIFICATION OF:			17. LIMITATION OF ABSTRACT	18. NUMBER OF PAGES	19a. NAMES OF RESPONSIBLE PERSON
a. REPORT	b. ABSTRACT	c. THIS PAGE			Capt. Phi-Anh Bui
Unclassified	Unclassified	Unclassified	U	216	19b. TELEPHONE NUMER *(Include area code)* (931) 454-5863

PREFACE

The work reported herein was done at the Arnold Engineering Development Center (AEDC), Air Force Materiel Command (AFMC), at the request of the Air Force Seek Eagle Office, (AFSEO), Eglin Air Force Base, FL. Analysis was done by Sverdrup Technology, Inc., AEDC Group, support contractor for testing at AEDC, AFMC, Arnold Air Force Base, TN, under Program Element 62602F. The effort was accomplished as Job Number 4594. The Air Force Project Manager was Capt. Brett Indermill, AEDC/DOT. Work was accomplished during the period October 1997 through September 1998, and the manuscript was submitted for publication on January 3, 2000.

CONTENTS

Page

1.0 INTRODUCTION 7
2.0 WIND TUNNEL TEST PROGRAM. 8
2.1 Wind Tunnels 8
2.2 Models 9
2.3 Instrumentation. 10
3.0 PROCEDURES 12
3.1 Flow Conditions 12
3.2 Model Attitude 12
3.3 Data Acquisition. 13
3.4 Data Corrections and Statistical Measurement Uncertainties 14
4.0 EXPERIMENTAL RESULTS AND COMPARISONS 14
4.1 Cavity Acoustics Databases 14
4.2 Boundary Layer at the Leading Edge of the Cavity. 15
4.3 Acoustic Response: Clean Cavity, Flow Direction 16
4.4 Acoustic Response in the Depth and Width Directions 17
4.5 Acoustic Response: Clean Cavity, Along Top Side Wall 21
4.6 Fluctuating Pressures on the Surface of a Store In and Near a Cavity. 21
4.7 Trajectories. 22
5.0 DEVELOPMENT OF A SPECTRAL PREDICTION METHOD 25
5.1 Fluctuating Pressure Spectra 25
5.2 Mathematical Model of Cavity Acoustics 26
5.3 Application of the CAP2 Code - Edgetone Frequencies 27
5.4 Application of the CAP2 Code - Scaling Acoustic Predictions. 28
5.5 Application of the CAP2 Code - Pressure Spectra. 29
5.6 Application of the CAP2 Code - Acoustic Attenuation (Spoilers). 30
6.0 CONCLUSIONS 30
REFERENCES. 33

ILLUSTRATIONS

Figure Page

1. Schematic of the Captive Trajectory Support System (CTS) in Tunnel 4T. 35
2. Sketch of the Tunnel 4T Test Section, Showing Model Location 36
3. Photograph of WICS Models Installed in Tunnel 4T 37
4. Sketches of Supersonic Tunnel A and the CTS System. 38
5. Photograph of WICS Models Installed in Tunnel A 40
6. Dimensions of the WICS Flat-Plate/Cavity Model 41
7. Spoiler Model Sketches 44
8. Store Model Sketches. 47
9. Dimensions of the Stings Used to Support Store Models 49

Figure Page

10. Static Pressure Orifice Locations . . . 51
11. Dynamic Pressure Transducer Locations . . . 55
12. Locations of Other Sensors . . . 58
13. Sketch of the Boundary-Layer Rake . . . 60
14. Points of Measurement of Static and Dynamic Pressures on the GMPM Model . . . 61
15. Measured Boundary-Layer Profiles at the Leading Edge of the Cavity . . . 62
16. Comparison of Measured and Predicted Boundary-Layer Velocity Profiles. . . . 64
17. Predicted Height of the Boundary Layer at the Leading Edge of the Cavity. . . . 65
18. Comparison of Measured and Natural Acoustic (Open Organ Pipe) Modal Frequencies for the WICS cavity, L/D = L/W = 4.5 . . . 66
19. Measured Spectra Along Vertical Planes on the Upstream Wall, L/D = 4.5. . . . 69
20. Measured Spectra in the Y Direction on the Upstream Wall, L/D = 4.5 . . . 76
21. OASPL on the Upstream Wall of an L/D = 4.5 Cavity . . . 83
22. Comparison of Spectra on the Upstream Wall of Two Independent Cavities . . . 84
23. Measured Spectra along Lateral Planes on the Floor of an L/D = 4.5 Cavity, X/L = 0.06 . . . 86
24. Measured Spectra Along Lateral Planes on the Floor of an L/D = 4.5 Cavity, X/L = 0.51 . . . 91
25. Measured Spectra Along Lateral Planes on the Floor of an L/D = 4.5 Cavity, X/L = 0.94 . . . 96
26. Measured Spectra Along Vertical Planes on the Downstream Wall, L/D = 4.5, Re = 3×10^6 . . . 101
27. Measured Spectra Along Lateral Planes on the Downstream Wall, L/D = 4.5, Re = 3×10^6 . . . 108
28. OASPL on the Downstream Wall of an L/D = 4.5 Cavity. . . . 115
29. Measured Spectra Along the Top of the Side Wall of an L/D = 4.5 Cavity . . . 116
30. Comparison of Spectra Sensed on the Floor of a Cavity with Spectra Sensed on the Body of a Generic Store Model, M_∞ = 0.60... . . . 121
31. Comparison of Spectra Sensed on the Floor of an L/D = 4.5, Cavity with Spectra Sensed on the Body of a Generic Store Model, M_∞ = 0.95 . . . 130
32. Comparison of Spectra Sensed on the Floor of an L/D = 4.5 Cavity with Spectra Sensed on the Body of a Generic Store Model, M_∞ = 1.20 . . . 139
33. Comparison of OASPL on the Bottom of an L/D = 45 Cavity and on the GMPM Store . . . 148
34. Separation Trajectories of a Store Jettisoned from an L/D = 4.5 Cavity at Transonic and Supersonic Freestream Mach Numbers . . . 150
35. Separation Trajectories of a Store Jettisoned from an L/D = 4.5 Cavity at Two Different Release Points, M_∞ = 0.95 . . . 155
36. Separation Trajectories of a Store Jettisoned from an L/D = 4.5 Cavity at Two Different Release Points, M_∞ = 1.20 . . . 160
37. Separation Trajectories of a Store Jettisoned from an L/D = 9.0 Cavity at Two Different Release Points, M_∞ = 0.95 . . . 165

Figure Page

38. Separation Trajectories of a Store Jettisoned from an L/D = 9.0 Cavity at Two Different Release Points, $M_\infty = 1.20$ 170
39. Repeatability of a Separation Trajectory of a Store Jettisoned from an L/D = 9.0 Cavity, $M_\infty = 0.95$. 175
40. Relationship between Rossiter's Vortex Phase Constant, γ_R, and Cavity L/D 180
41. Typical Spectra and Rossiter's Predicted Edgetones for the L/D = 4.5 Cavity 181
42. Experimental Values of γ_R and Theoretical and Experimental Values of ϕ_D for a Cavity of L/D = 4.5 with $M_\infty = 0.60$ and $Re = 3 \times 10^6$ 185
43. Variation of γ_R, and ϕ_D with Freestream Mach Number, from Data and CAP2. 186
44. Location of the Transducer Mounting Block in the Cavity Scale Experiments. 187
45. Comparison of Measured and Predicted Spectra for an L/D = 4.5 Cavity, Including Values of the OASPL and the Natural Acoustic Frequencies, $Re = 3 \times 10^6$ 188
46. Comparison of Predicted and Experimental Values of the Effectiveness of a Spoiler Installed near a Cavity as a Function of the Scaling Parameter, L/δ; Cavity L/D = 4.5 and M_∞ =0.60. 192
47. Comparison of Experimental and Predicted OASPL in the Presence of a 0.45-in. Sawtooth Spoiler, L/D = 4.5 193
48. Comparison of Experimental and Predicted Overall Acoustic Levels in a Cavity in the Presence of a Boundary-Layer In-Bleed Flow Upstream of the Cavity 194

TABLES

Page

1. Full-Scale Store Characteristics 195
2. Nominal Flow Conditions for the Tests 196
3. Statistical Confidence Intervals for the Test Data 197

APPENDIX

A. Development of the Cavity Acoustics Spectral Prediction Code, (CAP2 Code). 199

NOMENCLATURE. 206

1.0 INTRODUCTION

During the period 1986 – 1990, a large database was compiled at the AEDC from the results of a series of wind tunnel experiments investigating the aerodynamics of flow over open cavities. The database, known as the Weapons Internal Carriage and Separation (WICS) database, covered four experiments that were completed in the AEDC wind tunnels: three at subsonic to transonic conditions, and one at supersonic conditions. Four types of data were recorded: (1) aerodynamic loads acting on store models at a grid of spatial locations near a generic flat-plate and cavity model; (2) surface pressure distributions acting on the plate/cavity model and on one store model; (3) fluctuating (or acoustic) pressures acting on the plate/cavity and on one store model; and (4) separation trajectories for stores jettisoned from the cavity. The data were intended to be useful in both analytical and experimental development studies, including computational fluid dynamic (CFD) code development, airframe design, and weapons integration. Because of the size of the database – some 13 GB of raw data recorded using hundreds of model configurations and dozens of test conditions – very little analysis was performed, primarily because there were no practical analytical methods available for predictions against which to compare the experimental results. It must be noted that computational fluid dynamic (CFD) techniques were in development, but the many tens of hours of time required to obtain a solution prevented routine use. Examples of the state of computational capabilities include the work of Suhs (Ref. 1), and Rizetta (Ref. 2).

After completion of the database, development of the needed analytical techniques of predicting cavity acoustics began on two fronts. First, an engineering method of predicting some of the acoustic results recorded during the experiments was developed. (The term “engineering method” is used to describe the methodology because not only were fundamental analytical aerodynamic relations set forth as a model, but also there was a need to specify some arbitrary constants to establish a proper correlation between the predictions and the experimental data.) The prediction technique was in the form of a computer code designated the CAP Code (for Cavity Acoustic Prediction Code), that could be used on a variety of personal computers and modest workstations (Refs. 3 and 4). Second, in the eight years since the database was compiled, the purely analytical approach, i.e., CFD, has continued to mature, with continuous increases in the efficiency of large computing machines and the continuing development of mathematical and computational models of fluid flow.

It is, in fact, the increasing interest in predicting cavity acoustics using CFD technology that has led to a reopening of the WICS database for the further analysis that is described herein. Not only would additional discussion of the many configurations that were investigated be of significant use in validating CFD techniques, but also there is confidence to be gained in comparison of the WICS results with those of other similar investigations that have been completed at other test facilities.

2.0 WIND TUNNEL TEST PROGRAM

2.1 WIND TUNNELS

2.1.1 Transonic Tunnel

Tests in the subsonic, transonic, and low supersonic Mach number range were done in the AEDC Aerodynamic Wind Tunnel 4T, a closed-circuit tunnel in which continuous flow can be maintained at various values of freestream density. Using the two flexible opposite walls of the two-dimensional nozzle, Mach number in the freestream can be set at any value from 0.1 to 2.00. Stagnation pressure (P_t) can be maintained at any value from 300 to 3700 psfa. Stagnation temperature (T_t) ranges from approximately 550° to 580° R. The test section is 4 ft square and 12.5 ft long, with perforated walls. Wall porosity can be varied from 0.5 percent to 10 percent open. During testing, the effects of blockage and shock reflection can be reduced by suction of a portion of the airflow from the test section through the porous walls into a plenum chamber surrounding the test section.

Single models can be supported in the test section with a conventional sector-sting system with a pitch range of approximately −8 to 28 deg. A model can also be rolled from −180 to 180 deg about the centerline of the sting. In the captive trajectory testing mode, two separate and independent support systems are used. The aircraft model is attached to the primary sector-sting system, and the store model is mounted on a strain-gage balance. The balance is, in turn, attached to a sting that is connected to the Captive Trajectory Support (CTS) system, which moves the store model about in six degrees of freedom totally independent of the aircraft model via commands issued by a computer. Trajectory simulation begins with transmission of the outputs of the strain-gage balance in the store model to the CTS system computer. Equations of motion of the store are solved for acceleration, velocity, and displacement of the store model. On the basis of the predicted displacements, commands are issued by the computer to servo-controlled motors that move the store model in the linear and angular degrees of freedom, thereby simulating a separation trajectory. A sketch of a typical trajectory test installation and a block diagram of the routing of computer commands and data are shown in Fig. 1. A sketch of the test section, including model location during testing, is shown in Fig. 2, and a photograph of the models installed in the tunnel is shown in Fig. 3. A more complete description of the CTS technique is available in Ref. 5.

2.1.2 Supersonic Tunnel

Tests beyond Mach number 2 were done in the AEDC Aerodynamic Wind Tunnel A, a closed-circuit tunnel with a 40-in.-square test section in which continuous flow can be maintained at various values of freestream pressure. Continuous-curvature nozzle contours are set using the flexible top and bottom walls of the two-dimensional nozzle, providing a means of setting Mach number in the freestream at any value from 1.5 to 5.5. Stagnation pressure can be maintained at any value from 29 to 200 psia, with stagnation temperature to 750°R.

Single models can be supported by a sting attached to a support strut that provides a capability of rolling a model from 180 to −180 deg and pitching ±15 deg when the center of rotation is in the most downstream position. (At the forward-most center of rotation position, model pitch is limited to ±10 deg.) During captive trajectory testing, two separate and independent model support systems are used in the same manner as in Tunnel 4T. A sketch of Tunnel A and the CTS system is shown in Fig. 4, and a photograph of the models installed in the tunnel is shown in Fig. 5.

2.2 MODELS

2.2.1 Generic Cavity

A simple rectangular cavity with an opening 18 in. long (streamwise) and 4 in. wide (transverse to the flow) was built into a 47-in.-long by 16-in.-wide flat plate (Fig. 6). A 1/4-in.-wide strip of No. 60 size grit was applied across the width of the plate and 1 in. aft of the sharp leading edge to promote laminar-to-turbulent transition of the boundary layer. Along the longitudinal edges of the flat plate, tip plates were installed to add stiffness and reduce three-dimensional flow over the surface of the plate. Tip plates used during the tests in Tunnel 4T were 2 in. high (Fig. 6a), but 6-in.-high tip plates were used in Tunnel A (Fig. 6b). In the Tunnel A version of the cavity model, the additional height provided by the 6-in. tip plates allowed installation of two side-by-side 3-in.-diam portholes of Schlieren-quality optical glass for observations of unsteady flowfield characteristics inside the cavity. The view through the Schlieren windows was protected from distortion by the freestream flow by installing a fairing to bridge the gap between the inside of the tip plates and the outsides of cavity. Solid cavity side walls were used in Tunnel 4T, because there is no Schlieren capability there.

The cavity floor could be installed at any of several discrete locations between 0 and 4 in. (Fig. 6c). Only 1.25-in., 2-in., and 4-in. depths were used during the tests, providing cavities of length-to-depth ratios (L/D) of 14.4, 9.0, and 4.5, respectively.

2.2.2 Acoustic Suppression – Spoilers

Two types of boundary-layer spoilers were used, as illustrated in Fig. 7: vertical and flap, each spanning 0.8 of the width of the cavity (W). Several styles of vertical spoilers were used, including fine- and coarse-pitch sawtooth, solid, and porous, as shown in Figs. 7a – 7e. The fine-pitch sawtooth (Fig. 7a) was used during most of the tests, although a limited amount of fluctuating pressure data was recorded with a coarse-pitch sawtooth (Fig. 7b). Spoiler height was selected based on boundary-layer calculations made using Whitfield's Shear Work Integral Method (SWIM) Code (Ref. 6). Using the SWIM Code, a prediction was made of the turbulent boundary-layer height (δ) developing over the flat plate to the leading edge of the cavity opening. The predicted height, 0.15 in. at $M_\infty = 5.00$ and a unit Reynolds number (Re) of 3×10^6 per foot, was used as a design factor. Subsequently, sawtooth and flap spoilers were made in one, two, and three times that of the boundary-layer height, i.e., 0.15, 0.30, and 0.45 in. (also referred to as 1δ, 2δ, and 3δ spoilers). When either sawtooth or flap spoilers were installed, the primary streamwise location (X), expressed as a fraction of cavity length (L), was at the leading edge of the

cavity opening (X/L = 0). Some data, however, were recorded with the spoilers at a location forward of the cavity (X/L = –0.2).

2.2.5 Store Models

A scale factor of one-tenth of full scale was selected for store model fabrication. Although several store configurations were included in the experiments, only two will be discussed – a contemporary missile configuration with canards and tail surfaces, and a generic slender missile shape (Fig. 8). The following designations are used herein:

Store Configuration	Model Designation
Contemporary Missile	AIM-9L
Generic Missile Pressure Model	GMPM

2.2.6 Stings

Using the CTS system to move a store model about to either record a table of store loads data over a grid of spatial locations or to simulate a separation trajectory requires a (preferably) rear-entry "sting" to support the store model. Because preservation of the acoustic response of the cavity and the flow field over the afterbody and fins of a store model is clearly important, penetration of the downstream wall of the cavity with a store-model support could not be allowed. Therefore, offset or crank-shaped stings were used to support the store models from the CTS system. The leading edge of the 90-deg bend in the sting was only from 2.2 to 3.2 in. downstream of the base of the store model (depending on the store model), which was only from three to six base diameters. Conventional practice avoids support interference by delaying any increase in sting cross section until greater than five base diameters downstream of the model base. Therefore, the potential for support interference from the crank-shaped stings was large, and the data recorded using the stings should be used with appropriate discretion. The stings are illustrated in Fig. 9.

2.3 INSTRUMENTATION

2.3.1 Generic Cavity

Static pressure on the plate and cavity model surfaces could be measured at 95 locations: 26 on the flat plate, and 69 on the walls and ceiling of the cavity (Fig. 10). However, during the first phase of testing, WICS4T1, only pressure orifices 1 through 92 were available. Pressures were sensed using electronically scanned pressure (ESP) modules, rated at 5-psi maximum differential (psid), mounted on the backside of the flat plate. A near-vacuum was used as the reference. For verification purposes, one channel on each transducer module was connected to a known pressure source of 2 psia. The temperature of each pressure transducer module was monitored to provide a means of correcting for any possible temperature-induced zero shift. Module temperatures were controlled by water cooling within ±1°F during the Tunnel A tests.

Fluctuating pressures were measured with Kulite® differential transducers at up to 45 locations: 7 on the flat plate, and 38 on the walls and ceiling of the cavity (Fig. 11). Not all transducers were available during the tests. During WICS4T1, only 33 transducers were installed, and for WICS4T2, only 39 were connected, so that 6 could be installed in the GMPM pressure store. Each transducer was rated at ±5 psi, with a maximum allowable differential pressure three times the nominal rating, i.e., 15 psi. Each reference pressure port was vented to the static pressure in the instrument housing on the backside of the flat plate, which was approximately equal to freestream static pressure (P_∞). Up to 64 channels of transducer signals could be simultaneously sampled, converted from analog to digital form, filtered, and recorded on a magnetic hard disk using a MASSCOMP® minicomputer as a process controller and data analyzer. Transducer signals were scanned at a rate of 10,000 samples/sec, producing a data flow of approximately 1 MB/sec. Consequently, about 30 data points could be stored on the disk. When the disk was full, data were transferred to a magnetic tape. Coincident with testing, the MASSCOMP system performed a fast Fourier transform (FFT) analysis on about half the data recorded for a given data point to provide on-line power-spectral-density (PSD) spectra for some selected transducers. The FFT analysis was performed on ensembles of 1024 points, and a typical PSD spectrum represented an average of 25 ensembles.

Angle of attack of the generic cavity model was measured with a gravity-sensing angular position indicator (Schaevitz®). An optical proximity sensor (Fig. 12) was mounted in the flat-plate surface downstream of the cavity to provide a means of locating store models accurately in a reference position prior to beginning a move-pause data recording sequence.

Two single-axis accelerometers were used to provide a measurement of model vibrations. One was mounted on the backside of the flat plate just upstream of the cavity to sense vertical acceleration in the Z direction. The other was mounted on the backside of the downstream bulkhead of the cavity to sense axial acceleration in the X direction (Fig. 12).

Five hot-film constant-temperature anemometers were installed along the flat plate upstream of the cavity (Fig. 12). The output from all five gages verified that turbulent flow was established well upstream of the cavity.

In the supersonic tests in Tunnel A, four Chromel®-Alumel® thermocouples were mounted on the backside of the model to monitor plate and cavity surface temperatures. One thermocouple was located just forward of the cavity on the surface of the plate, one each on the upstream and downstream cavity bulkheads, and one approximately in the middle of the ceiling of the cavity (Fig. 12).

During blockage evaluation tests for the Tunnel A test, the thickness of the boundary layer approaching the cavity was determined using a “rake” consisting of ten tubes aligned vertically, one above the other, extending from the surface to 0.3 in. above the surface of the plate (Fig. 13). The rake was not used at any other time.

2.3.2 Store Model Instrumentation

Aerodynamic loads acting on the contemporary missile model were measured using a small six-component internal strain-gage balance of 0.3-in. diam, designed for a maximum 7.2-lb normal force.

Surface pressures acting on the body of the Generic Missile Pressure Model (GMPM and GMPM-F) were sensed through 38 orifices connected to an ESP unit, as was done for the plate and cavity model. Fluctuating pressures were sensed through six Kulite® transducers (Fig. 14) that were identical to the transducers installed in the plate and cavity model. Forces and moments acting on the GMPM store were not measured, since the interior volume of the model was completely filled by static pressure tubing and transducer wiring.

2.3.3 Flow Visualization

During the WICS Tunnel A test, Schlieren photographs of the store-cavity flow field were recorded for all configurations and test conditions at selected model attitudes. A double-pass optical flow visualization system was used. Both black-and-white and color Schlieren high-speed movies (4000 frames/sec) were also recorded for selected test conditions. Schlieren visualization was not possible in Tunnel 4T.

3.0 PROCEDURES

3.1 FLOW CONDITIONS

Data were recorded at Mach numbers in the range from 0.60 to 2.00 in Tunnel 4T, and from 2.00 to 5.04 in Tunnel A. A nominal unit Reynolds number of 3×10^6 per foot was selected, but since Tunnel 4T is usually run at a constant P_t of 1200 psfa, unit actually varied from 1.9 to 3.0×10^6. The selected value of 3×10^6 was maintained during the tests in Tunnel A. In addition, some data were recorded in both Tunnel 4T and Tunnel A at constant Reynolds numbers of 1×10^6, 2×10^6, and 3×10^6 per foot. Nominal values of the flow conditions are listed in Table 1.

3.2 MODEL ATTITUDE

Because of the large frontal area of the plate/cavity model, angle of attack of the plate was restricted to a maximum of 5 deg to limit tunnel blockage. The plate and cavity model was always set at zero sideslip. During a test in Tunnel 4T, the angle of attack of the plate/cavity model was set using the on-board inclinometer. During the tests in Tunnel A, initial model alignment was accomplished by injecting the cavity model and adjusting angle of attack using the on-board inclinometer.

3.3 DATA ACQUISITION

3.3.1 Surface Static Pressures

Static pressures acting on the surfaces of the plate and cavity model were measured during cavity-alone runs and, in general, at the same spatial grid points as force and moment data for the store models. Static pressures acting on the GMPM models were measured at the specified spatial grid points in and near the cavity and in the freestream. During the tests in Tunnel 4T, all static pressure orifices were scanned at a rate of 20,000 samples/sec at intervals of 0.01 sec. During the tests in Tunnel A, static pressures and rake pressures were averages of ten samples taken over a time span of 1.0 sec. Because of the fluctuating nature of flow over cavities, the pressures recorded using these conventional pressure sampling techniques can hardly be called “static,” and indeed, the resulting measurements were characterized by large variability. Surface static pressures sensed in this manner have been documented previously, and will not be discussed further herein.

3.3.2 Fluctuating Pressures

In Tunnel 4T, a signal was transmitted from the Digital Data Acquisition System (DDAS) to the MASSCOMP system to initiate the fluctuating pressure recording and analysis cycle. Similarly, in Tunnel A, a programmable controller was used to provide the appropriate sequencing commands between the MASSCOMP system and the tunnel data system. In both tunnels, a signal from the controller commanded the MASSCOMP to initiate data acquisition. The recording process continued for 25 sec (15 sec for file management and 10 sec of actual data acquisition), during which time the tunnel data system was prevented from taking any action. After data were recorded, a signal was transmitted by the MASSCOMP system via the controller to release the tunnel data system.

All transducer outputs were sampled simultaneously 10,000 times each second for at least 5 sec during a typical data point, producing approximately 50,000 pressure measurements for each transducer. These time-ordered data were transformed into power spectral density (PSD) graphs in the frequency domain using conventional fast Fourier transform (FFT) techniques. The set of pressure-time samples for each data channel was partitioned into subsets, or ensembles, of 1024 samples each. Consequently, the bandwidth of the transformed data was 10,000/1024, or approximately 9.76 Hz. Spectra from 25 ensembles were averaged to obtain the final PSD spectrum in the frequency domain. Spectra extended over the range 0 - 5000 Hz to be consistent with the sampling rate. All spectral data presented herein have been calculated with the Hanning data-tapering “window.”

3.3.4 Forces and Moments Acting on the Contemporary Missile Model

Data were recorded at discrete values of store position and attitude following a specified move-pause sequence. Each force and moment data point recorded during the experiments in Tunnel 4T represented a moving average of the most recent 100 samples from a set of samples collected each 0.01 sec as a continuous background task. During the experiments in Tunnel A,

each force and moment data point represented the average of ten data samples recorded at intervals of 0.006 sec. The averaged force and moment data were corrected for first- and second-order balance-interaction effects, model tare weight, and balance-sting deflections. Conventional six-degree-of-freedom force and moment coefficients were calculated for each store using the maximum diameter and corresponding cross section area of the store body as the reference length and area, respectively, and the center-of-gravity location as the moment reference point. Specific dimensions, in full-scale units, for the contemporary store configuration discussed here are listed in Table 2. Forces and moments acting on the GMPM store could not be measured, because the interior volume of the model was completely filled by static pressure tubing and transducer wiring.

3.4 DATA CORRECTIONS AND MEASUREMENT UNCERTAINTIES

In Tunnel 4T, Mach number in the freestream was maintained within ±0.010 of the specified value, with a calculated uncertainty of ±0.003. Mach number in the freestream of Tunnel A was maintained within ±0.016 of the selected value.

Quality of the experimental data was estimated by considering the effects of both systematic and random errors. Statistical confidence intervals of ± two standard deviations, i.e., assured to include 95 percent of the measured values, were estimated from: (1) the calibrations of the instruments used to sense the pressure and temperature of the airflow; and (2) the repeatability and uniformity of the freestream flow during calibration of the wind tunnel. Confidence intervals for the model force and pressure instrumentation systems were estimated from calibrations of the systems made using secondary standards with accuracies traceable to the National Institute of Standards and Technology. By using a Taylor series method of error propagation (Ref. 7), the values of the above intervals were combined to determine the 95-percent confidence intervals of the force and moment coefficients. The values of the various uncertainties are listed in Table 3a for force and moment measurements, and in Table 3b for static surface pressure measurements.

A Schaevitz absolute angle indicator attached to the underside of the flat plate was used to set angle of attack of the generic cavity model. Consequently, corrections for the angular displacement of the generic cavity model attributable to the primary sting support deflections were unnecessary. Confidence intervals for position and attitude of the generic cavity model are listed in Table 3c.

4.0 EXPERIMENTAL RESULTS AND COMPARISONS

4.1 CAVITY ACOUSTICS DATABASES

In the following sections, a general discussion of each of the four types of data collected during the WICS tests is first presented, then sample data from the database for some typical configurations are discussed. Much of the data recorded for many of the configurations included in the database was described in a previous document; hence, the discussion presented here is concentrated on those items not previously documented.

Although many investigations of tangential flow over cavities have been made, the number has increased rapidly during the last 20 or so years, and one would expect that many databases exist against which to compare a selected database to establish credibility and validity. Indeed, a literature survey revealed over 400 journal articles, papers from various symposia, and reports from the National Aeronautics and Space Administration (NASA) and NASA-sponsored investigations - all published since 1962 and dealing with cavity acoustics. It is beyond the scope of the current report to furnish a bibliography of these works. Instead, the reader in search of such a list is directed to the work of Komerath (Ref. 8), who has compiled a list of 94 documents, most of which may be considered to be key contributions to the subject. Very little data could be compared with the WICS data, however, because adequate descriptions of the flow conditions were not published with the results. In particular, it will be clear from the work described in Section 5 that knowledge of the character of the approaching boundary layer is crucial to understanding and predicting the acoustic response of a cavity.

One set of data published by Tracy and Plentovich (Ref. 9) was useful in at least partially validating the WICS database. These investigators conducted experiments in a slotted wall transonic wind tunnel, the Langley 8-Foot Transonic Pressure Tunnel, using a flat-plate and cavity model similar to the WICS model. The NASA cavity model was equipped with a floor that could be set at discrete depths, side-wall inserts for width adjustments, and a motor-driven downstream wall that could provide a wide range of cavity lengths. Just as in the AEDC/WICS experiments, a strip of grit was applied near the leading edge of the flat plate to ensure the existence of a turbulent boundary layer at the upstream wall of the cavity. Although fluid dynamic and geometric similarity to the WICS experiments was not exact and the normalized locations of transducers on the two different models were not identical, some portions of the two databases can be compared for validation of trends, as will be illustrated in subsequent sections.

4.2 BOUNDARY LAYER AT THE LEADING EDGE OF THE CAVITY

Using the “rake” of multiple tubes described in Section 2.3.1, the boundary-layer profile at the leading edge of the generic cavity was defined. Total pressures in the boundary layer were recorded at the following conditions:

Mach Number	Unit Reynolds Number, per foot
2.50	2.2, 2.9, and 3.1
3.51	2.0
5.04	3.2

Corresponding total pressure profiles are illustrated in Fig. 15.

An experimental boundary-layer velocity profile was determined from the measured total pressures with two assumptions: (1) that the total temperature was constant throughout the boundary layer; and (2) that the static pressure was constant and equal to the known freestream static pressure. The velocity profile was then integrated to obtain the absolute value of the momentum thickness (θ). Then, knowing θ, the Reynolds number based on θ ($Re_{N\theta}$) was determined. Next, it was assumed that the velocity profile could be represented by a power law profile with an exponent of 1/N. The value of N was determined using the following empirical equation from Ref. 10:

$$N = 0.89 \times \ln(Re_{N\theta}) - 1.65 \tag{1}$$

Finally, knowing N, the ratio θ/δ was determined, and hence, the experimental δ. The analytical value of δ, as obtained from Whitfield's SWIM Code (Ref. 6), was essentially identical to the experimental value of δ. The value of N based on the theoretical value of δ was used to determine θ, which was found to be equal to the experimental value. Analytical and experimental velocity profiles are compared in Fig. 16. The variation of δ over the Mach number range of the experiments is illustrated in Fig. 17.

4.3 ACOUSTIC RESPONSE: CLEAN CAVITY, FLOW DIRECTION

Acoustic data in the frequency domain are presented in one of two formats, either sound pressure level (SPL), or the nondimensional parameter, p_{rms}/q_∞. In relating the two parameters, following equations were used:

$$SPL = 20 \times \log\left(\frac{P_{rms}}{P_{ref}}\right) \tag{2}$$

where the reference pressure, P_{ref}, was assumed to be the international threshold of audibility (2 Pascals, or approximately 2.9×10^{-9} psi), so that

$$SPL \approx 20 \times \log\left(\frac{P_{rms}}{2.9 \times 10^{-9}}\right) \tag{3}$$

and

$$\frac{P_{rms}}{q_\infty} = \frac{P_{ref} \times 10^{\frac{SPL}{20}}}{q_\infty} \approx \frac{2.9 \times 10^{\frac{SPL - 180}{20}}}{q_\infty} \tag{4}$$

Because the wind tunnel results were recorded at various values of q_∞, comparison of data recorded at various Mach numbers and total pressures is more meaningful using p_{rms}/q_∞ than SPL as the dependent variable. However, in the frequency domain, SPL is often more intuitive and convenient. Furthermore, when data from cavities of different size are compared, the Strouhal Number is used:

$$S = \frac{fL}{V_\infty} \tag{5}$$

4.4 ACOUSTIC RESPONSE IN THE DEPTH AND WIDTH DIRECTIONS

4.4.1 Spectra Along the Streamwise Axis of Symmetry

Many transducers were installed along the streamwise axis of symmetry of the cavity opening, and the corresponding acoustic spectra and levels have been documented previously. It has been established experimentally that the highest amplitudes occur in a rectangular cavity at the upper region of the downstream wall, where the oncoming flow stagnates. Illustrations of the centerline spectra sensed in the high-pressure region of the downstream wall by transducer K18 (Fig. 11) are included here for reference (Fig. 18). The natural frequencies of the cavity in the streamwise (length), lateral (width), and depth directions were calculated using equations for an open organ pipe:

$$f_L = \frac{a_t}{2L} \tag{6}$$

$$f_L = \frac{a_t}{2W} \tag{7}$$

$$f_L = \frac{a_t}{4D} \tag{8}$$

and are represented by vertical lines at the corresponding frequencies in Fig. 18. The natural frequencies of the deep, open-flow cavity (L/D = 4.5), calculated for a range of flow conditions typical of the WICS experiments, are listed in the following table:

M_∞	T_t, °R	a_t, ft/sec	f_L, Hz	f_D, Hz	f_W, Hz
0.60	554	1153	384	865	1730
0.95	548	1147	382	860	1721
1.05	553	1152	384	864	1728
1.20	550	1149	383	862	1724
1.50	562	1162	387	871	1742
2.00	581	1182	394	886	1773
2.75	580	1181	394	886	1771
3.51	661	1260	420	945	1890
5.04	601	1201	400	901	1802

It is clear from Fig. 18 that the modal tones that are generated by the flow over the cavity are not the classical organ pipe tones. Another mechanism is the source of the tones, which will be discussed in a subsequent section.

4.4.2 Spectra Off the Streamwise Axis of Symmetry – Upstream Wall

Fluctuating pressures acting on the cavity walls at locations off the longitudinal axis of symmetry of the cavity have not been previously documented. Several transducers were, in fact, located off the centerline on both upstream and downstream walls and at three streamwise locations on the floor of the cavity, as illustrated in Fig. 11.

On the upstream wall, the spectra for transducers K3 and K4 on the centerline of the cavity and transducers K24 and K25 near the corner (Fig. 11.b) are of particular interest. An important observation can be made from the data illustrated in Fig. 19. At Mach numbers 0.60, 0.95, and 1.20 (Figs. 19a, 19b, and 19c, respectively), when the spectra are compared along parallel vertical planes, i.e., K3 and K4 as a pair aligned in the vertical, or Z direction, and K24 and K25 as a pair on a vertical line near the corner of the cavity, it is clear that the spectra of each pair are remarkably identical at frequencies less than about 860 Hz, i.e., the natural frequency of the cavity in the vertical, or depth direction (see the table in Section 4.4.1). At frequencies less than the natural depth frequency, the longitudinal modes dominate, and the spectra from all transducers are identical. However, at frequencies above the natural depth frequency (indicated by the solid vertical line labelled f_D), separate and essentially parallel spectra for each of the transducers are clear. These offset spectra are evidence of lateral pressure gradients in the cavity attributable to acoustic waves crossing the cavity in the vertical, or Z, direction. This observation is important for two reasons: (1) the existence of vertical modes has not been previously reported or demonstrated in the literature; and (2) vertical gradients can be important with regard to the structural and functional integrity of items placed in the cavity. Of course the differences in level that are noted at the higher frequencies are broadband in nature and contribute little to the overall strength of the pressure field (120 db represents only about 0.42 psf, whereas 170 db indicates a pressure of 132 psf). Nevertheless, the existence of vertical gradients should be considered in the design of cavities and contents.

The same remarks apply when the transducers are considered to be pairs aligned in the lateral direction. Specifically, in Fig. 20, when the spectra from transducers K3 and K24 are compared (transducers aligned in the lateral, or Y direction at a normalized depth of $Z/D = -0.2$), and the spectra from transducers K4 and K25 are compared (transducers aligned in the lateral direction at $Z/D = -0.49$), one notices that the spectra for each pair are identical at frequencies less than about 1730 Hz, i.e., the natural frequency of the cavity in the lateral (width) direction (see the table in Section 4.4.1). Again in Fig. 20, at frequencies above the natural width frequency, indicated by the dashed vertical line labelled f_W, once again separate and essentially parallel spectra for each of the transducers are observed. In this case, the offset spectra are evidence of lateral pressure gradients in the cavity attributable to acoustic waves crossing the cavity in the lateral, or Y, direction. Again, just as in the case of the Z direction, this observation is important for two reasons: (1) the existence of lateral modes has not been previously reported or demonstrated in the literature; and (2) lateral gradients can be important with regard to the

structural and functional integrity of items placed in the cavity. Once again, the differences in level that are noted at the higher frequencies are broadband in nature and contribute little to the overall strength of the pressure field, but the existence of lateral gradients should be considered in the design of structures and contents.

Experiments at Mach numbers 2.0, 3.5, and 5.0 were completed in the AEDC Supersonic Tunnel A several months before the experiments in AEDC Transonic Tunnel 4T, and it was noted at that time that transducers K3 and K24 were not functioning properly. The spectra corresponding to the output of those transducers are clearly of little value, and are illustrated here to assist in identifying bad data (Figs. 19g, 19i, 19k, 19m and 19n). The properly functioning transducers, however (K4 and K25), again display essentially identical spectra up to the natural frequency of the cavity in the lateral direction. In Fig. 21, it is clear, therefore, that the amplitude of the dominant edgetone modes – and hence the overall sound pressure level – vary little across or up and down the upstream wall of the open-flow, or "deep" cavity. However, at frequencies equal to or greater than the natural frequencies based on depth and width, vertical and lateral waves will cause gradients in broadband levels of approximately 2 to 5 db over half the cavity depth or width.

An indication of qualitative agreement between NASA (Ref. 9) and WICS experimental results can be gained from the spectra illustrated in Fig. 22. Exact agreement cannot be expected because of differences in model geometry, flow conditions, and the test facilities, but general agreement is apparent. Normalized pressure data (p_{rms}/q_{∞}) for the NASA experiments were not available; hence, results are presented as sound pressure level in the frequency domain. Because the edgetones generated by the flow separating at the leading edge of the cavity are a function of cavity length, a direct comparison of the NASA and WICS results in the absolute frequency domain appears to be weak. However, when the results are displayed in the normalized frequency domain using Strouhal number [Eq. (5)], the comparison is good. The comparison cannot be made throughout the entire WICS frequency range because the NASA data are reported for a frequency domain of 0 to 2000 Hz, as opposed to the WICS domain of 0 to 5000 Hz. The WICS frequency domain was selected without a specific application in mind.

4.4.3 Spectra Off the Streamwise Axis of Symmetry – Across the Cavity Floor

In addition to the transducers installed on the floor of the WICS cavity along the streamwise longitudinal axis of symmetry, transducers were installed to the side of the centerline at three longitudinal stations, i.e., at 6, 51, and 94 percent of the length of the cavity (Fig. 11). Spectra from the transducers on the floor are illustrated in Figs. 23 through 25. Just as in the case of the forward wall, the lateral spectra and levels were essentially identical for frequencies less than about 1750 Hz, the lateral natural frequency of the cavity (see the table in Section 4.4.1). At frequencies above 1750 Hz, separate, parallel spectra for each of the transducers were recorded. These offset spectra are further evidence of lateral pressure gradients in the cavity, and in particular, on the floor (Z/D = -1).

The evidence of lateral modes is particularly strong in the subsonic and transonic régime (Figs. 23a–e, 24a–e, and 25a–e). Note that in all cases, as the spectra separate above 1700 to 1800 Hz, the spectra from the centerline transducers are lowest in amplitude (K6, K12, and K15), with

the highest amplitude spectra associated with the transducers nearest the wall (K26, K27, and K28). Relative amplitudes of this sort can be attributed to the passage of pressure waves in the lateral direction, with a quicker phasing at the wall than on the centerline because of reflection from the wall. A general increase in broadband noise in the 3000- to 4000-Hz range was noted at all Mach numbers in Tunnel 4T i.e., between 0.6 and 2.0, but that increase has been identified by Credle (Ref. 11) as background noise in the porous wall Tunnel 4T. However, the first harmonic, or second mode, of the natural frequency in the width direction is also about 3500 to 3600 Hz. That the increase is at least partially attributable to the second lateral mode may be deduced by noting that at the second mode frequency of approximately 3600 Hz, the spectra from transducers on the centerline (K6, K12, and K15) become stronger in amplitude than the spectra from the transducers at 2Y/W = 0.45 (K21, K22, and K23), and in fact match the amplitudes of the spectra from the transducers near the wall (K26, K27, and K28). Phasing of the lateral acoustic waves can explain the shift in amplitude.

Clearly, the character of the spectra on the floor of the cavity is additional evidence of the existence of lateral modes in the cavity. Finally, just as for the upstream wall, the gradient of overall sound pressure level laterally across the cavity ranges from 1 to 10 db, depending on Mach number and location (Figs. 23j, 24j, and 25j).

4.4.4 Downstream Wall

At the downstream wall, just as on the upstream wall, there were pairs of transducers that may be compared vertically and horizontally. See Fig. 11 for detailed locations of the transducers. Spectra from the transducers are illustrated in Figs. 26–28.

In Fig. 26, spectra from the transducers aligned in the Z, or depth (vertical), direction are compared (transducers K17 and K18 on the longitudinal plane of symmetry of the cavity, and transducers K29 and K30 near the corner). The modal amplitudes on the centerline (transducers K17 and K18) and near the corner (transducers K29 and K30) at Mach numbers 0.6, 0.95, and 1.20 are strongest of any location in the cavity, and display the existence of the same tones at each location (Figs. 26a, b, and c). It is clear why most investigations of cavity acoustics have concentrated on the upper downstream wall. However, there is not nearly the strong evidence of depth or width modes as at the upstream wall or on the cavity floor. This observation, together with the strong motivation to document maximum loads for design purposes, may well explain why the existence of depth and lateral modes elsewhere in the cavty has been overlooked.

Comparisons of spectra in the Y, or width (lateral), direction can be made by referring to Fig. 27. Here, transducers K18 and K30 are paired near the opening of the cavity (Z/D = –0.18), and K17 is paired with K29 at a depth of Z/D = –0.49. Again, as expected, the longitudinal (flow-wise) modes dominate, with the transducers on the centerline sensing higher levels than those near the corner in the transonic régime up to Mach number 1.50 (Figs. 27a, b, and c). At Mach number 1.50 and above, and at a location approximately halfway down into the cavity (Z/D = –0.49), the transducer near the corner at (K29) senses higher levels than the transducer on the centerline (K17). No explanation is offered for the change in trend.

In Fig. 28, it is clear that differences in overall spectral amplitudes in the Z, or depth (vertical), direction are strong, approximately 8 to 10 db, representing a decrease of about 3 in pressure from near the cavity opening to halfway down in the cavity. A gradient of that magnitude should clearly be important in structural and functional design.

4.5 ACOUSTIC RESPONSE: CLEAN CAVITY, ALONG TOP SIDE WALL

Spectra from transdaucers mounted near the top of the cavity along the side wall (transducers K31, K32, and K33, at longitudinal stations X/L = 0.06, 0.51, and 0.94, respectively, Fig. 11) are illustrated in Fig. 29. It is clear that there is no frequency shift between axial stations for any of the dominant modes, regardless of Mach number. At frequencies less than about 3000 Hz, the lowest amplitudes occur in the quieter region of the cavity at the upstream transducer, as expected, ranging from 2 to 10 db lower than modal amplitudes at mid-cavity and at the downstream wall. Above 3000 Hz, all of the sidewall transducers tend to sense the same broadband level. In the supersonic regime, all three sidewall transducers sense the same fluctuations – broadband or modal – with only minor differences.

Overall sound pressure levels along the side wall are illustrated in Fig. 29j. In the subsonic and transonic regimes, overall levels in the middle of the side wall are accentuated by the approximately 10-db decrease in level at the forward, quieter region of the cavity.

4.6 FLUCTUATING PRESSURES ON THE SURFACE OF A STORE IN AND NEAR A CAVITY

The presence of fluctuating pressures acting on the surface of a store during separation-like motions near the cavity was studied by using the CTS System to support and move the GMPM, Section 2.3.2, and Fig. 8b. Because a force and moment balance could not be installed in the GMPM together with the tubes and wiring for the pressure measurements, actual separation trajectories could not be simulated. Instead, the GMPM store was positioned in a grid of locations in and near the 4-in.-deep cavity (L/D = 4.5), recording surface pressure data in the same manner that force and moment data were recorded using balance-equipped models. Both conventional static pressure instrumentation and dynamic pressure transducer outputs were recorded. The static pressure data will not be discussed here.

Fluctuating, or acoustic, pressures acting on the surface of the GMPM body were sensed at six locations along the vertical centerline of the model: three on the “upper” surface, i.e., the surface nearest the cavity, and three on the “lower” surface, i.e., the surface facing out of the cavity toward the freestream (Fig. 8b). With respect to the body axes of the cavity, the transducers were located at X/L values of approximately 0.25, 0.35, and 0.46. Spectra were generated in the same manner as for the cavity model (Section 3.4.2). In Figs. 30 – 32, the spectra are illustrated along with spectra from transducers mounted in the cavity at locations opposite the transducers in the GMPM. With the axial centerline of the GMPM model aligned on the longitudinal plane of symmetry of the cavity and parallel to the plane of the cavity opening, the model was moved along one vertical path, parallel to the Z direction, and located at each of three positions relative to the cavity opening along that path. The locations were at Z = –3.0, 0, and 1.2 in., corresponding to Z/D

values of –0.75, 0, and 0.30. The angles of attack of both cavity and GMPM models were maintained at 0 deg. Data are illustrated for three Mach numbers, viz., 0.60 (Fig. 30), 0.95 (Fig. 31), and 1.20 (Fig. 32). Consequently, there are nine graphs for each Mach number, or 27 total, grouped location along the translation path at each Mach number. Also illustrated are spectra for the empty cavity compared with spectra in the cavity with the GMPM in place. The overall sound pressure level along the bottom of the cavity at each Mach number and for each vertical location of the GMPM store model is illustrated in Fig. 33.

First, with respect to the cavity spectra, in every case, the presence of the GMPM model and supporting sting caused a decrease in amplitude of the primary modes (first, second, and third) of approximately 2 to 5 db (spectra at the bottom of each page of Figs. 30–32). This observation is true regardless of location of the GMPM model along the Z, or vertical (depth) translation path. Furthermore, there was an increase of approximately 50 to 100 Hz in the primary mode frequencies. A possible explanation can be found by applying a well-known modal prediction method developed by Rossiter (Ref. 12), and modified by Heller, Holmes, and Covert (Ref. 13):

$$f_m = \frac{V_\infty}{L} \times \frac{(m - \gamma_R)}{\frac{M_\infty}{\sqrt{1 + 0.2M_\infty^2}} + \frac{1}{0.57}} \tag{9}$$

When the shifted numbers in Rossiter's equation are substituted, an effective cavity length of approximately 17.5 in. can be calculated. Recalling that the sting supporting the GMPM model was approximately 0.5 in. in diameter, one can conclude that the presence of the sting causes an effective "acoustic shortening" of the cavity.

With respect to the fluctuating pressure spectra in the cavity, the modal frequencies sensed on the store and in the cavity always agreed at all locations along the body, at all locations of the GMPM along the Z traverse, and at all Mach numbers. As illustrated in Fig. 33, it was also true that the transducers on the cavity side of the GMPM at X/L = 0.25 sensed fluctuations of greater magnitude than the transducers on the freestream side at all Mach numbers tested. The differences ranged from 3 to 10 db higher on the cavity side. However, at the X/L station of approximately 0.35, fluctuations were of lower amplitude on the cavity side of the store than on the freestream side, but at X/L = 0.56, higher amplitudes existed on the cavity side once more. In other words, the pressure that acts over the surface of a store translating out of a cavity has an acoustic frequency content corresponding to that of the cavity response to flow separation at the leading edge, but with modal amplitudes that vary along the length of the store.

4.7 TRAJECTORIES

Trajectories of stores ejected from the three cavities were simulated using the 1/10-scale store models and the CTS system. Assumptions required for the simulations included a hypothetical ejection system that would impart to the store, in full-scale units, a downward (+Z axis) translational velocity of 30 ft/sec and a pitch velocity of –1 rad/sec (nose down) at the end of an 8-in. ejector stroke. A few trajectories were simulated starting at the end of an 18-in. stroke.

(Store motion parameters at the end of the ejector stroke are designated “EOS.”) The cavity was assumed to be flying level at 20,000 ft with a load factor of 1.0. (Discussion is limited here to one store configuration ejected from two cavities, the L/D = 4.5 or the L/D = 9.0.)

Trajectories representing ejection of a contemporary missile from a clean cavity in the transonic regime are illustrated in Figs. 34 – 39 for L/D = 4.5. (The designation “clean” is used to indicate that there were no attached features such as spoilers, ramps, or doors.) In Fig. 34, the accelerations, velocities, and displacements of the store during separation at Mach numbers 0.95 and 1.20 are compared. (Only five of the conventional degrees of freedom are shown, since rolling motion of the CTS system was intentionally disabled.) In addition, the translational and angular displacement data at one supersonic condition (Mach number 2.00) are included, even though the accelerations and velocities of the store are not available.

In all graphs illustrating the streamwise, or X displacement, the sign on the X displacement has been changed from the conventional CTS direction (which is positive X upstream) to a positive direction of downstream simply to make the displacement intuitive. In other words, an unpowered store ejected straight downward will usually translate downstream during the free portion of the trajectory. As a result, the slope of the displacement curve will be of opposite sign to the velocity in the X direction, a graph of which is displayed immediately above the displacement graph. Angular accelerations, velocities, and displacements are illustrated in the d and e panels of Figs. 34 – 38. At both Mach number 0.95 and 1.20, despite significant variations in acceleration and velocity, there is little movement of the store in the longitudinal (X) and lateral (Y), directions (Figs. 34a and 34b, respectively). In Figs. 34b–e, the periodic forces acting on the store during passage through the shear layer are evident in the acceleraions of the store in the lateral and vertical directions. (Fluctuations in acceleration in the flow, or X, direction attributable to the presence of the shear layer are apparently negligible.) However, because of the significant velocity imparted to the store at the end of the jector stroke (30 ft/sec), the time during which the store is exposed to the shear layer is short. At 30 ft/sec, the store can pass through a 4-ft-thick shear layer in approximately 150 msec, during which the large inertia of the store (Table 2) precludes significant response to the fluctuating flow field. Consequently, the corresponding linear and angular displacements in the later and vertical directions are not severe (again, Figs. 34b–e).

Two different release points (end-of-stroke, or EOS) were simulated in each cavity. In the 4-in.-deep cavity, the EOS points were with the centerline of the store model at 2 in. inside the cavity (Z/D = –1) and at 1.2 in. inside the cavity (Z/D = –0.3). In the 2-in.-deep cavity, the EOS points were at 0.2 in. inside the cavity (Z/D = –0.1) and at 0.8 in. outside the cavity in the shear layer (Z/D = 0.4).

Accelerations, velocities, and displacements of the store subsequent to release at the two different EOS points in the deep (L/D = 4.5) cavity are illustrated in Fig. 35 for Mach number 0.95, and in Fig. 36 for Mach number 1.20. At both Mach numbers, the trajectories from either EOS point are uneventful, with very little movement in the X, or longitudinal (flow-wise) and Y, or lateral (width) directions, despite fluctuating accelerations passing through the shear layer (approximately 0.15 sec). The one notable feature is the lack of pitch angle displacement at either Mach number when the trajectory began at the EOS position near the cavity opening (Z/D = – 0.167), despite the

initial pitch rate of 1 rad/sec nose down that was imposed as an initial condition. A possible explanation may be that when the store is near the cavity opening, the lower lifting surfaces extend into the freestream beyond the shear layer, and are therefore unaffected by the shear layer. The combination of stable forces acting on the surfaces in less disturbed flow, the short time of passage through the shear layer, and the inertia of the store tends to overcome the influence of the shear layer.

Trajectories from the two EOS positions in and near the transitional cavity (L/D = 9.0) are illustrated in Fig. 37. The tones produced by flow over the L/D = 9.0 cavity are weaker than the tones that develop in the deeper L/D = 4.5 cavity; hence, the effect of the shear layer on store motion would be expected to be less than for the deeper cavity. Indeed, for both Mach number 0.95 and 1.20, movement in the longitudinal and lateral degrees of freedom, X and Y, respectively, is insignificant, and in the Z direction movement is essentially linear and intuitive. In the yaw degree of freedom, just as for the 4-in. cavity, yawing displacement is almost unaffected by the fluctuating pressures in the shear layer. However, the positive excursion at M = 0.95 and the negative displacement at M = 1.20 (compare Fig. 37e with Fig. 38e) may indicate a bias imparted by the fluctuating shear layer at the moment of separation. Finally, in the pitch degree of freedom, a significant effect of the shear layer can be detected. When the store is released just inside the cavity (Z/D = −0.167), the pitching acceleration increases sharply, and the nose-down pitch displacement increases. But when the store is released outside the cavity (Z/D = 0.667), a larger portion of the lifting surfaces is exposed to the smoother freestream beyond the shear layer, and the effect of the shear layer is almost nonexistent (Fig. 38e).

Separation trajectories were repeated in a few cases, and an indication of repeatability can be obtained from Fig. 39. The trajectory at Mach number 0.95 from the L/D = 9.0 cavity was repeated, albeit only once, with generally good results. It is interesting to note that despite the fluctuating lateral and vertical accelerations experienced by the store model in passing through the shear layer (undoubtedly because of the random phasing of the time of release and the state of the shear layer), the translational and angular displacements were closely matched. This result is again evidence of the imperturbability of the store when launched with a significant outward velocity that minimizes exposure time to the shear layer.

It can be concluded that the threat to a successful jettison of an object out of a cavity represented by the presence of the shear layer can be reduced if either the ejection velocity and initial pitch rate are sufficiently high (e.g., on the order of 30 ft/sec and −1 rad/sec, respectively), or if the store is finally released at a position outside the shear layer. Another often-used approach is to employ some sort of spoiler forward of the cavity to interact with the shear layer and interfere with the coupling of the acoustic edgetones generated by flow separation at the leading edge of the cavity and the acoustic organ pipe-like cavity response. The effectiveness of a spoiler erected at the leading edge to thicken the boundary layer artifically, and thereby make less sharp the flow gradients between the quiescent cavity and the freestream, and hence, to suppress the effects of the shear layer, has been documented by several other investigators, and will not be discussed here.

5.0 DEVELOPMENT OF A SPECTRAL PREDICTION METHOD

5.1 FLUCTUATING PRESSURE SPECTRA

5.1.1 Frequency Predictions – Rossiter's Method

Predictions of the modal frequencies in the cavities are frequently made using the method of Rossiter (Ref. 12), as modified by Heller, Holmes, and Covert (Ref. 13):

$$f_m = \frac{V_\infty}{L} \times \frac{(m - \gamma_R)}{\frac{M_\infty}{\sqrt{1 + 0.2M_\infty^2}} + \frac{1}{0.57}} \tag{10}$$

The value 0.57 is asserted to represent V_v/V_∞, i.e., the ratio of the velocity of propagation of a vortex moving across the cavity opening to the velocity of the freestream. East (Ref. 14) identified a range of values for V_v/V_∞ from 0.35 to 0.65. Heller, Holmes, and Covert (op. cit.) suggested the value of 0.57, with which Smith and Shaw (Ref. 15) later concurred. Several values of the phase constant, γ_R, were listed by Rossiter, representing best choices for the cavities of various L/D ratio that were included in that investigation. The values are illustrated as discrete data points in Fig. 40, with a linear curve fit applied by forcing the equation to pass through (0, 0). Modal frequency predictions for the WICS deep cavity (L/D = 4.5) were made using the modified Rossiter equation with a value of g_R of 0.28 for the L/D = 4.5 cavity, consistent with the linear fit to the data illustrated in Fig. 40. Comparisons of the predicted and measured frequencies are illustrated in Fig. 41, along with the acoustic natural frequencies (organ pipe frequencies) of the cavity. Agreement between predicted and measured values was only fair for the first three modes over the range of Rossiter's experiments, viz., $0.40 < M_\infty < 1.20$. However, for modes 4 and 5, and at Mach numbers above 1.20, the modal frequencies were underpredicted.

The flow model proposed by Rossiter and the other investigators cited above relies on the shedding of a vortex at the leading edge of the cavity as the cause of the deflection of the shear layer into the cavity, with stagnation at the downstream bulkhead causing a second deflection of the shear layer out of the cavity to conserve mass. At the downstream bulkhead, the stagnating flow is assumed to reflect from the bulkhead at a frequency equal to the frequency of the vortex shedding, but not in phase. The modes of oscillation and the phase shift are treated in the analytical model with the term $(m-\gamma_R)$ in the numerator. Clearly, only longitudinal modes in the cavity are considered in the equation.

Since the Rossiter equation treats only longitudinal modes, it is a two-dimensional model, and is not totally adequate for three-dimensional cavities. A slightly different model is envisioned here, with the detectable resonant frequencies of pressure oscillation within the cavity considered to be only partially dependent on the vortex shedding frequency. Two separate processes must be considered, viz. the vortex shedding and the cavity response. First, vortices will separate at the leading edge of the cavity opening at a frequency determined by the freestream velocity and the characteristics of the approaching boundary layer. Second, the response of the fluid in the cavity to excitation by any flow phenomenon will be determined by the geometry of the cavity, the

condition of the surfaces of the cavity, the contents of the cavity, and the characteristics of the fluid in the cavity, particularly the sonic speed. The two-dimensional Rossiter model only approximates coupling of the two processes. However, the current cavities are decidedly three-dimensional, with a length-to-width ratio (L/W) of 4.5, which is on the same order as the L/D. Consequently, in addition to the dominant longitudinal modes, it is demonstrated unequivocally herein that lateral and vertical modes also exist (Section 4.4). Vertical modes were also observed by Plumblee, Gibson, and Lassiter to dominate the response of a very deep cavity of L/D = 0.8 (Ref. 16).

5.1.2 Frequency and Amplitude Predictions: CAP and CAP2 Codes

The experimental results described in Section 4 were used at the AEDC in a study that produced a new model for predicting both frequency and amplitude response of a cavity, called the Cavity Acoustic Prediction Code, or CAP Code. The results were documented in an AEDC Technical report in 1991 (Ref. 3) and a symposium paper in 1992 (Ref. 4). Since those results were published, additional development of the CAP Code produced an advanced version, called the Cavity Acoustic Code, or CAP2 Code. The full development of the CAP Code is described in the cited references; hence only a brief review of the mathematical development of the CAP2 Code is discussed here.

5.2 MATHEMATICAL MODEL OF CAVITY ACOUSTICS

The mathematical model presented in this report is the same as that used in the CAP Code (Ref. 3), with all the empirical equations related to the turbulent mixing process replaced by theoretical results obtained from an application of the Chapman-Korst mixing theory (Ref. 17). As a result, the theory involves only three empirical parameters. One is for the similarity parameter for turbulent mixing that is a function of Mach number, and assumed to be the same as for a free jet (Refs. 18 and 19). Another is for the constant of proportionality between Reynolds shear and turbulent kinetic energy that has been experimentally determined for both boundary layers and turbulent mixing zones (Ref. 20). The third is for the damping terms that are used in a frequency response function that determines the relative amplitudes of the peaks in the pressure spectrum.

To begin with, the theory assumes that the broadband acoustic waves generated by the turbulent mixing zone trigger much stronger pulses in the form of vortices that roll up in the mixing zone. These vortices produce pressure pulses at the so-called “edgetone” frequencies. As a result, the turbulence has discrete frequencies in its spectrum, yet no energy has been added or removed; hence, it is reasonable to assume the mean-flow turbulent kinetic energy is the same as for a free-jet mixing zone. The mean-flow turbulent kinetic energy is assumed to be linearly related to the Reynolds shear stress, which is determined by the Chapman-Korst mixing analysis (Ref. 17). Euler’s equation is then used to determine the overall rms pressure in the turbulent mixing zone. The overall rms pressure acting on the downstream wall of the cavity is then assumed to be the same as that at the downstream end of the mixing zone. The associated pressure spectrum is estimated using a unique response function that was formulated using the edgetone frequencies as the reference frequencies, an assumption considered appropriate because the peaks in the spectrum occur near the edgetone frequencies (see Fig. 41). Constants in the damping terms in the response function are selected to provide a predicted spectrum that matches the WICS spectrum (experi-

mental data) at Mach number 0.6. The basic parameter in the model is the ratio of a specified frequency to each of the three acoustic natural frequencies of the cavity. If the specified frequency is equal to one of the acoustic natural frequencies, then the damping is small and a relatively high pressure peak is calculated. Since the overall rms pressure level is known from the mixing analysis, then the absolute pressure level of the spectrum can be determined. The following flow chart of the method illustrates the approach:

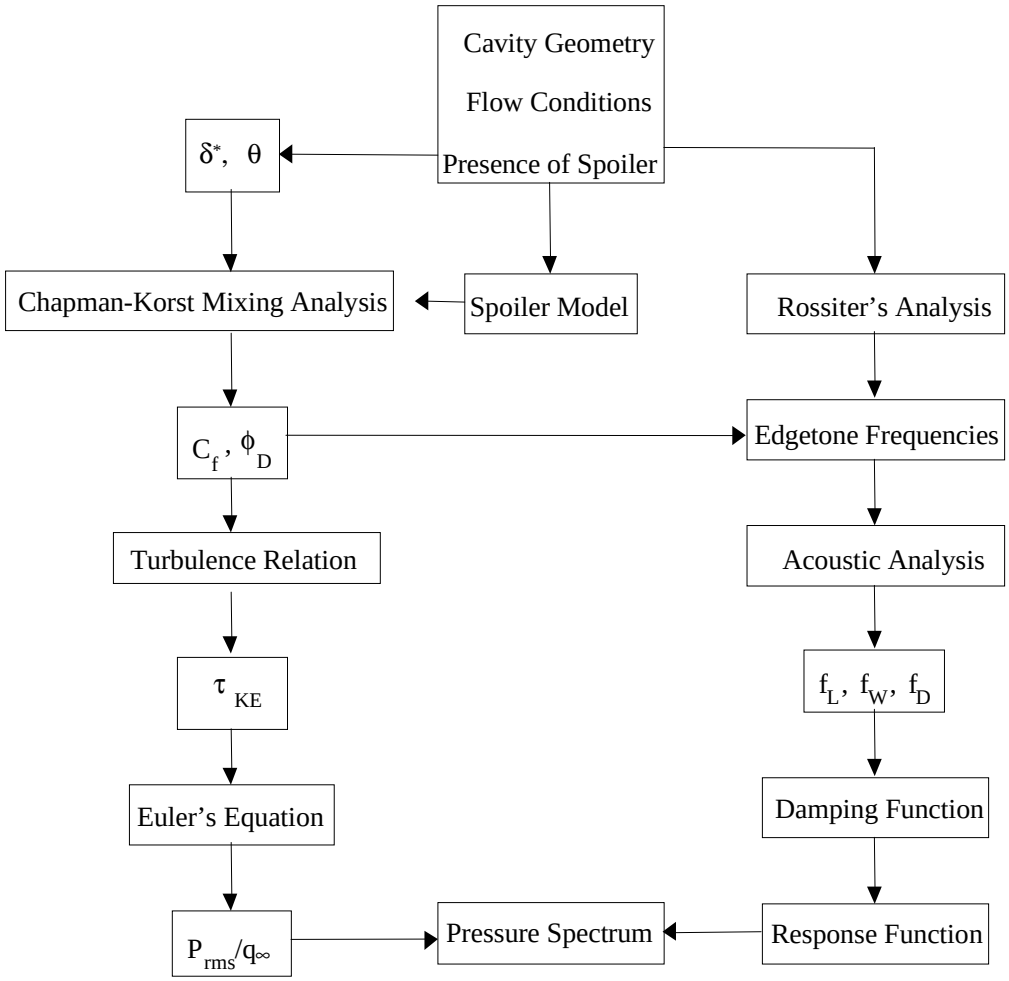

The analytical models for the various components of the theory modeled by the CAP2 code are presented in the Appendix.

5.3 APPLICATION OF THE CAP2 CODE – EDGETONE FREQUENCIES

As discussed in Section 5.1.1, the equation most often used for estimating the edgetone frequencies was developed by Rossiter (Ref. 12). Several investigators have used Rossiter's relationship in the analysis of their data, making adjustments as they believed necessary, produc-

ing the widely used version cited in Section 5.1.1 as Eq. (10). In the CAP2 Code, the present investigators have also made an adjustment, replacing the constant 0.57 with concepts taken from mixing theory. Specifically, it is asserted that the acoustic waves emanating from the downstream corner of the cavity are assumed to be moving through the low-velocity region inside the cavity at a velocity based on the freestream total temperature. Rossiter's equation is modified by assuming that the vortex convection velocity across the opening of the cavity is the velocity along the dividing streamline in a turbulent mixing zone, ϕ_d. Then Rossiter's equation becomes

$$f_{E_m} = \frac{V_\infty (m - \gamma_R)}{L\left[M_\infty \frac{\alpha_\infty}{\alpha_t} + \frac{1}{\phi_D}\right]} \tag{11}$$

The assumption can be verified by experiment since, for any two measured edgetone frequencies, it is possible to formulate two statements of Rossiter's equation and solve for the two unknowns, the phase constant, γ_R, and the vortex convection velocity, ϕ_D. Results calculated for the WICS data are presented in Fig. 42 for the phase constant, γ_R, and in Fig. 42 for the vortex convection velocity, ϕ_D. The results from the CAP2 Code are based on the calculated initial boundary-layer thicknesses shown in Fig.15, and have been verified by experiment at the higher Mach numbers. In Fig. 43, the phase constant, γ_R, is shown to be independent of Mach number. The values of 0.3 and 0.6 for cavities of L/D ratio of 4.5 and 9 agree well with those obtained by Rossiter (Ref. 12), and Dobson (Ref. 22). There is no theory for estimating the phase constant, γ_R, so the following empirical equation is used in developing the CAP2 Code:

$$\gamma_R = 0.062\frac{L}{D} \tag{12}$$

The vortex convection velocity ratio, ϕ_D, as illustrated in Fig. 43b, does vary with Mach number, and the theoretical dividing streamline velocity ratio agrees well with the experimental results of both the WICS program and Kaufman, et al., (Ref. 23).

5.4 APPLICATION OF THE CAP2 CODE – SCALING ACOUSTIC PREDICTIONS

In theory, the most important parameter that affects the vortex convection velocity is the size and shape of the initial boundary-layer profile. In the WICS experiment, the boundary layer was only about 0.25 in. thick, and the length of the cavity was 18 in. As a result, the turbulent mixing was essentially fully developed, and the dividing streamline velocity ratio was at its maximum value of between 0.6 and 0.7. In Rossiter's experiment, however, the initial boundary layer was 0.6 in., with a cavity length of 8 in., so Rossiter's value of 0.57 for the convection velocity is lower than for the WICS experiment because of the influence of the initial boundary layer. Using the CAP2 Code, a value of 0.52 is predicted for Rossiter's experiment. As mentioned in Section 5.1.1, East identified a range of from 0.35 to 0.65 for the vortex convection velocity, depending on the boundary-layer thickness (Ref. 14). Unfortunately, neither Rossiter's nor East's experiments are sufficiently documented to allow an analysis similar to that applied to the WICS data.

The theoretical variation of the dividing streamline velocity ratio with the ratio of mixing distance to initial boundary-layer thickness, L/δ, is compared with the data of Shaw, Ref. 24, in Fig. 42 for $M_\infty = 0.6$. Shaw's data were obtained from a wind tunnel experiment accomplished as a continuation of the last WICS test in AEDC Tunnel 4T. The same generic cavity model and test conditions were used, but with a series of u-shaped boxes that were inserted into the largest WICS cavity, producing smaller size cavities, but with the same ratios of length to width and length to depth of $L/D = L/W = 4.5$. The inserts were designed to shorten the cavity from the downstream end, leaving the upstream edge unchanged, thereby maintaining the initial boundary-layer thickness at 0.2484 in. for all configurations. (Note, however, that Shaw's data included in the illustration were obtained from a transducer mounted in a block that could be inserted in the downstream wall of any of the cavity size-altering inserts. The block was always inserted near the floor of the cavity on the downstream wall rather than near the cavity opening at the top of the downstream wall, where the WICS data were obtained, and where the CAP2 Code predictions apply. The block and locations are illustrated in Fig. 44.) As shown in Fig. 42, the theoretical dividing streamline velocity ratio agrees well with the experimental values and is clearly dependent on L/δ. Rossiter's phase constant is shown in Fig. 42 to also be dependent on L/δ, whereas in Fig. 43, it is shown to be independent of Mach number.

Also illustrated in Fig. 42 is an indication of the effectiveness of the parameter L/δ in estimating the overall acoustic level in various sizes of an $L/D = 4.5$ cavity and a freestream Mach number of 0.60. Correlation with other published data from similar experiments is not possible because of the lack of complete information describing either the boundary-layer depth or the location of the measurement point. Correlation of the prediction made using the CAP2 Code with data from the Shaw's experiments. using size-reducing inserts in the WICS cavity (Ref. 23) is good. The importance of the approaching boundary layer in determining the overall acoustic amplitude in the cavity (at the top of the downstream wall) is apparent.

5.5 APPLICATION OF THE CAP2 CODE – PRESSURE SPECTRA

The CAP2 Code can only predict the pressure spectrum on the downstream wall of the cavity, where the turbulent mixing zone impinges. Consistently, in both the WICS database and the published literature, the maximum overall sound pressure level also occurs at the downstream wall, a point of practical interest for designing support systems for items in the cavity. Predicted spectra from the CAP2 Code are compared with the WICS data in Fig. 45 for Mach numbers 0.6 through 5.04. The theoretical results are similar to those from the CAP Code for Mach numbers less than 2.0, which is to be expected since the damping functions are the same. For Mach numbers greater than 2.0, an error was found in the CAP Code that altered the results at the higher Mach numbers. In addition, the WICS data show that the edgetone frequencies do not occur for Mach numbers greater than 2.0, probably because the Mach number along the dividing streamline becomes supersonic for freestream Mach numbers greater than 2.0. As a result, in the CAP2 Code, the damping is increased; hence, modal peaks do not appear in the spectrum. Included in Fig. 45 are the acoustic natural frequencies for length, width, and depth to illustrate that the modal peaks in the spectrum occur at edgetone frequencies that are close to the acoustic natural frequencies for length and depth. These results illustrate that the CAP2 Code provides a good estimate of the pressure spectrum and the maximum overall sound pressure level on the downstream wall of the cavity.

5.6 APPLICATION OF THE CAP2 CODE – ACOUSTIC ATTENUATION (SPOILERS)

A boundary layer-altering device, or spoiler, mounted upstream of a cavity reduces the modal peak pressures and overall sound pressure level (OASPL) in the spectrum associated with the cavity. An option was included in the CAVA Code to predict the OASPL that would result from use of a spoiler. In Fig. 46, with the 0.45-in. spoiler mounted upstream of the leading edge of the cavity opening at X/L = –0.20, the measured decrease in P_{rms}/q_∞ and the decrease predicted by the CAP2 Code as a function of L/δ are illustrated for $M_\infty = 0.6$ and L/D = 4.5. Again, as discussed in Section 5.2.3.8, it should be noted that Shaw's data included in the illustration were obtained from a transducer mounted in a different location from that used in the WICS experiments. Consequently, the location of the transducer in Shaw's experiment varied from Z/D = 0.9 to Z/D = 0.7. Near the bottom of the downstream wall, the OASPL is generally lower by a value on the order of 2 db, as illustrated in Fig. 28, produced from the WICS database. The effect on the OASPL of the presence of the spoiler – both measured and predicted using the CAP2 Code – is illustrated in Fig. 47 for a range of freestream Mach number.

In the WICS program, three sawtooth spoilers were tested with heights of 0.15, 0.30, and 0.45 in. at various Mach numbers (Fig. 7). The CAP2 Code predicts the boundary-layer thicknesses for these spoilers to be 0.74, 1.55, and 2.44 in., respectively, at $M_\infty = 0.60$, and an upstream boundary-layer thickness of 0.2484 in. (i.e., the WICS boundary layer, predicted using the SWIM Code, Ref. 6). The most effective of the spoilers in causing an attenuation of the OASPL was the 0.45-in.-tall spoiler. It is important to note that a 12-percent error in P_{rms}/q_∞ results in only a 1.0-db error in the OASPL for levels in the 160- to 180-db range.

A more effective spoiler is bleed flow upstream of the cavity that not only increases the initial boundary-layer thickness, but also changes its shape to a near-linear profile that has a much larger momentum thickness compared to 1/7 to 1/9 profile shapes downstream of a typical flat-plate spoiler. Vakili, Ref. 25, studied this type of spoiler experimentally and concluded that both the boundary-layer thickness and its shape determine the OASPL. The Chapman-Korst mixing theory also predicts this result. Since there is no simple way to determine the profile shape produced by bleed flow, the N factor in CAVA is set equal to 1.6 when bleed flow is present. Results from CAVA are compared with Vakili's experiments in Fig. 47, where it is clear that bleed flow is very effective as a means of decreasing the OASPL.

6.0 CONCLUSIONS

Aerodynamic loads acting on models of 13 missile configurations mounted in and near a generic flat plate and three rectangular weapons cavities were recorded during a series of wind tunnel tests at Mach numbers from 0.60 to 5.04. Both static and fluctuating pressures acting on the surfaces of the plate and cavity were also measured and recorded. Static and fluctuating pressures acting on a model of a generic ogive-cylinder store were measured, and 134 separation trajectories were simulated using the CTS technique. Loads and pressure data were assembled in a database that can be used at a personal computer. The following conclusions concerning the

aeroacoustic flow environment in and near the WICS generic cavity can be drawn from analysis of the data:

1. Because of the fundamental influence of the boundary layer at the leading edge of the cavity, acoustic data from separate data bases cannot be compared without knowledge of the character of that boundary layer. Hundreds of publications document acoustic spectra, but few provide detailed information about the boundary layer. Comparison with one database from the National Aeronautics and Space administration, however, using models and flow conditions that approximate those of the WICS tests, reveal qualitative agreement via the acoustic scaling parameter, Strouhal number.

2. A rectangular cavity of length-to-depth and length-to-width ratio of 4.5 responds like an open organ pipe at freestream Mach numbers up to 5.0, and classical organ pipe formulae can be used to predict the natural frequencies in length, depth, and width.

3. In addition to the customary longitudinal (or length) modes in a cavity of length-to-depth and length-to-width ratio of 4.5, clear evidence was also observed of the existence of both depth and width modes at all Mach numbers up to 5.0.

4. An existing empirical technique of predicting the resonant frequencies of a rectangular cavity, the modified Rossiter equation, provided good results for the first three acoustic modes in the Mach number range for which the equation was formulated, i.e. $0.40 \leq M_\infty \leq 1.20$. Correlation of the predictions provided by the Rossiter equation with test data grew progressively worse for modes higher than 3, for Mach numbers greater than 1.20, and for a cavity of L/D = 14.4 because of a limitation of the Rossiter math model to only the longitudinal modes of the cavity response.

5. In deeper (L/D = 4.5) and transitional (L/D = 9.0) cavities, amplitudes of overall (rms) values of the fluctuating pressures increased with freestream Mach number in the subsonic regime, reached maximums in the transonic range at approximately $M_\infty = 1.20$, and abated as Mach number increased in the supersonic regime. As freestream Mach number increased beyond 2.75, overall amplitudes decreased to the same levels as in the subsonic regime. At freestream Mach numbers greater than 3.50, no discrete tones were observed – only broadband noise. Resonant tones did not exist in a shallow L/D = 14.4 cavity at any freestream Mach number.

6. The presence of a sting-supported store in the cavity caused a 50- to 100-Hz increase in modal frequencies sensed by transducers on the store body and cavity surfaces. When the observed values of the reduced frequencies were substituted into the Rossiter equation, an effective cavity length was calculated that was less than the actual cavity length by approximately the diameter of the sting. Therefore, the presence of a sting near the downstream wall of the cavity effectively shortened the cavity with respect to acoustic response.

7. Spectral frequencies sensed at all stations along the store surface were the same on both the cavity side of the store and the side facing the freestream at all Mach numbers.

8. With a store inside the cavity, the relationship of amplitudes sensed at the store surface and amplititudes sensed on the centerline of the cavity floor varied as a function of location along the length of the store. In the quieter regions of the cavity, i.e., the upstream end of the cavity, amplitudes sensed on the store were less than amplitudes sensed at the cavity surface. In the noisier regions of the cavity (downstream half), amplitudes on both sides of the store essentially matched the cavity spectrum. In some cases, the transducers on the freestream side of the store sensed disturbances of greater amplitude than the transducers on the cavity side, indicating a shielding effects of the store body.

9. When a store was in the plane of the cavity opening, amplitudes were lower on the freestream side of the store than on the side facing the cavity by on the order of 5 db at the primary (longitudinal) modes. Greater differences in amplitude from cavity side to freestream side of the store existed in the broadband noise levels above 2000 Hz.

10. A store mounted just outside the cavity opening experienced higher amplitudes on the cavity side than on the freestream side, ranging from 10 to 20 db at the modal frequencies.

11. Using the assumed ejection conditions of 30 ft/sec downward velocity and −1 rad/sec (nose-down) pitching velocity, a store separating from two different cavities – length-to-depth ratio of 4.5 and 9.0 – was made to separate cleanly despite experiencing significant and generally sinusoidal variations in acceleration and velocity in passing through the shear layer. The combined effects of store inertia, damping coefficients, and short exposure time in passing through the shear layer made it possible to eject a store cleanly. However, structural and operational integrity of the stores after such an ejection could not be assessed from data contained in the database.

12. When a store is released (end-of-ejector stroke) in or near the plane of the cavity opening, some or part of the fins of the store, if so equipped, could protrude into the freestream. Those areas would not be influenced by the shear layer, resulting in an unusual loading condition and pitching moment. Again, however, when the time required to traverse the shear layer is small, the inertia of the store prevents significant disturbance of the near-field trajectory.

13. While the dominant longitudinal modal frequencies in a rectangular cavity are predicted quite well using the modified Rossiter equation, corresponding modal amplitudes are much more difficult to predict. Fundamental fluid dynamic relations can be (and have been) used in conjunction with the Chapman-Korst mixing analysis to develop an analytical method for predicting modal amplitudes. The

CAP2 Code produces results that are adequate for preliminary design analysis, but in the present state of development, some experimental data have been used to provide a basis for selection of constants that are needed to produce a spectrum in the frequency domain, i.e., to predict amplitudes at frequencies other than the primary first three or four edgetone modes.

14. An important parameter in scaling overall acoustic levels in a cavity is the ratio of cavity length to the boundary-layer depth, L/δ.

REFERENCES

1. Suhs, N. E. "Transonic Flow Calculations for a Cavity With and Without a Store." AEDC-TR-92-4, September 1992.

2. Rizzeta, D. P. "Numerical Simulation of Supersonic Flow Over a Three-Dimensional Cavity." AIAA-87-1288, June 1987.

3. Bauer, R. C. and Dix, R. E. "Engineering Model of Unsteady Flow in a Cavity." AEDC-TR-91-17 (AD-A243636), December 1991.

4. Dix, R. E. and Bauer, R. C. "Engineering Model Predictions of Aeroacoustic Amplitudes in a Weapons Cavity." AIAA-93-0858, 31st Aerospace Sciences Meeting & Exhibit, Reno, NV, January 11-14, 1993.

5. Carman, J. B., Jr., Hill, D. W., Jr., and Christopher, J. P. "Store Separation Testing Techniques at the Arnold Engineering Development Center, Volume II, Description of Captive Trajectory Store Separation Testing in the Aerodynamic Wind Tunnel (4T)." AEDC-TR-79-1 (AD-A087561), June 1980.

6. Whitfield, D. L. "Integral Solution of Compressible Turbulent Boundary Layers Using Improved Velocity Profiles." AEDC-TR-78-42 (AD-A062946), December 1978.

7. Beers, Yardley. *Introduction to the Theory of Error*. Addison-Wesley Publishing Company, Inc., Reading, MA, 1957, pp. 26-36.

8. Komerath, N. M. "Prediction and Measurement of Flows Over Cavities – A Survey." AIAA-87-0166, 25th Aerospace Sciences Meeting, Reno, NV, January 12-15, 1987.

9. Tracy, Maureen B. and Plentovich, E. B. "Cavity Unsteady-Pressure Measurements at Subsonic and Transonic Speeds." NASA Technical Paper 3669, December 1997.

10. Enkenhus, K. R. and Maher, E. F. "The Aerodynamic Design of Axisymmetric Nozzles for High-temperature Air." NAVWEPS Report 7395, Aeroballistics Report No. 137, 5 Feb 1962.

11. Credle, O. P. “Perforated Wall Noise in the AEDC-PWT 16-FT and 4-FT Transonic Tunnels.” AEDC-TR-71-216 (AD-841857), October 1971.

12. Rossiter, J. E. “Wind Tunnel Experiment on the Flow Over Rectangular Cavities at Subsonic and Transonic Speeds.” Ministry of Aviation, Aeronautical Research Council, Reports and Memoranda No. 3438, October 1964.

13. Heller, H. H., Holmes, G., and Covert, E. “Flow-Induced Pressure Oscillations in Shallow Cavities.” AFFDL-TR-70-104, (AD-880496), December 1970.

14. East, L. F. “Aerodynamically-Induced Resonance in Rectangular Cavities.” *Journal of Sound and Vibration*, Vol. 3, No. 3, 1966, pp. 277-287.

15. Smith, D. L. and Shaw, L. L. “Prediction of the Pressure Oscillations in Cavities Exposed to Aerodynamic Flow.” AFFDL-TR-75-34 (AD-A018518), October 1975.

16. Plumblee, H. E., Gibson, J. S., and Lassiter, L. W. “A Theoretical and Experimental Investigation of the Acoustic Response of Cavities in an Aerodynamic Flow.” WADD-TR-61-75 (AD-277803), March 1962.

17. Chapman, A. J. and Korst, H. H. “Free-jet Boundary with Consideration of Initial Conditions.” Proceedings of the 2nd U. S. National Congress of Applied Mechanics, June 14-18, 1954.

18. Bauer, R. C. “An Analysis of Two-Dimensional Laminar and Turbulent Compressible Mixing.” *AIAA Journal*, Vol. 4, No. 3, March 1966, pp. 392-395.

19. Bauer, R. C. “Another Estimate of the Similarity Parameter for Turbulent Mixing.” *AIAA Journal*, Vol. 6, No. 5, May 1968, pp. 925-927.

20. Lee, S. C. and Harsha, P. F. “Use of Turbulent Kinetic Energy in Free Mixing Studies.” *AIAA Journal*, Vol. 8, No. 6, June 1970.

21. Dobson, T. W., Jr. “Discrete Frequency Acoustics Correlation for Rectangular Cavities Exposed to High-Speed Flows.” University of Tennessee Space Institute Thesis, December 1990.

22. Kaufman, Louis G., II, Maciulaitus, Algirdas, and Clark, Rodney. L. “Mach 0.6 to 3.0 Flows Over Rectangular Cavities.” AFWAL-TR-82-3112 (AD-A134579), May 1983.

23. Shaw, L. L. “Scale Effect on the Flow-induced Acoustic Environment in Cavities - Wind Tunnel Results.” WRDC-TM-89-159-FIBG, 14 February 1989.

24. Vakili, Ahmad D. and Gauthier, Christian “Control of Cavity Flow by Upstream Mass Injection.” AIAA-91-1645, June 1991.

25. Bauer, R. C. “A Method of Calculating the Response Time of Pressure Measuring Systems.” AEDC-TR-56-7 (AD-T343), November 1956.

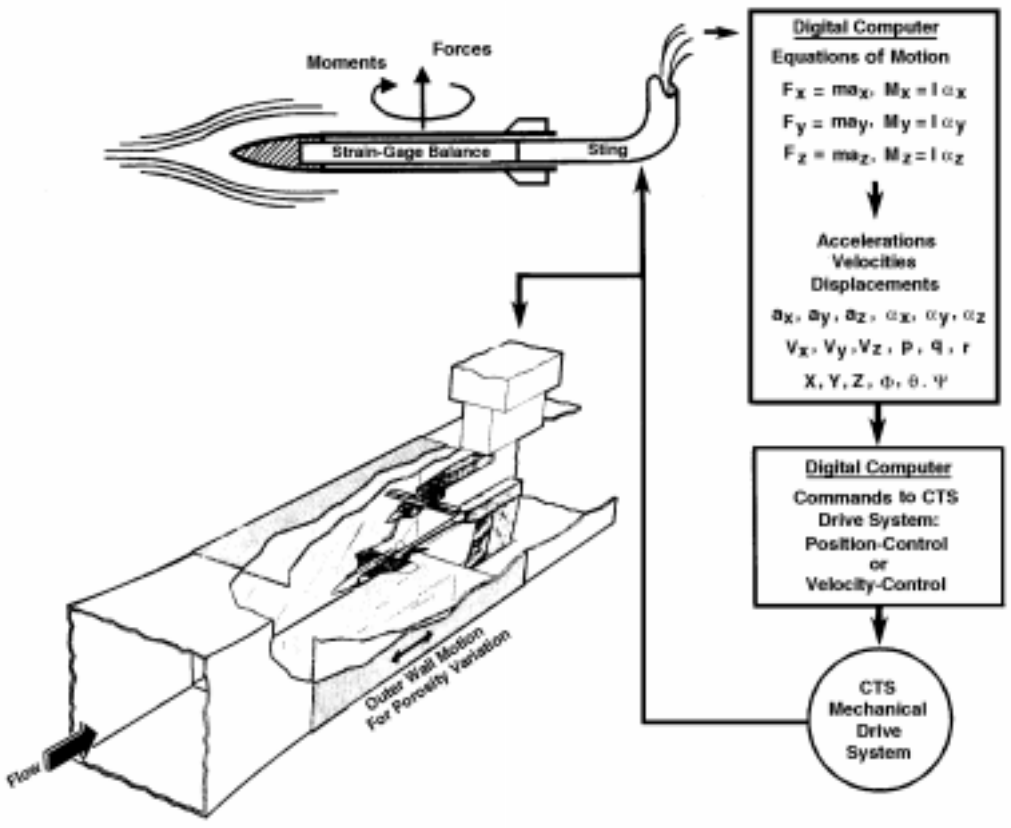

Figure 1. Schematic drawing of the Captive Trajectory Support System (CTS) in Tunnel 4T.

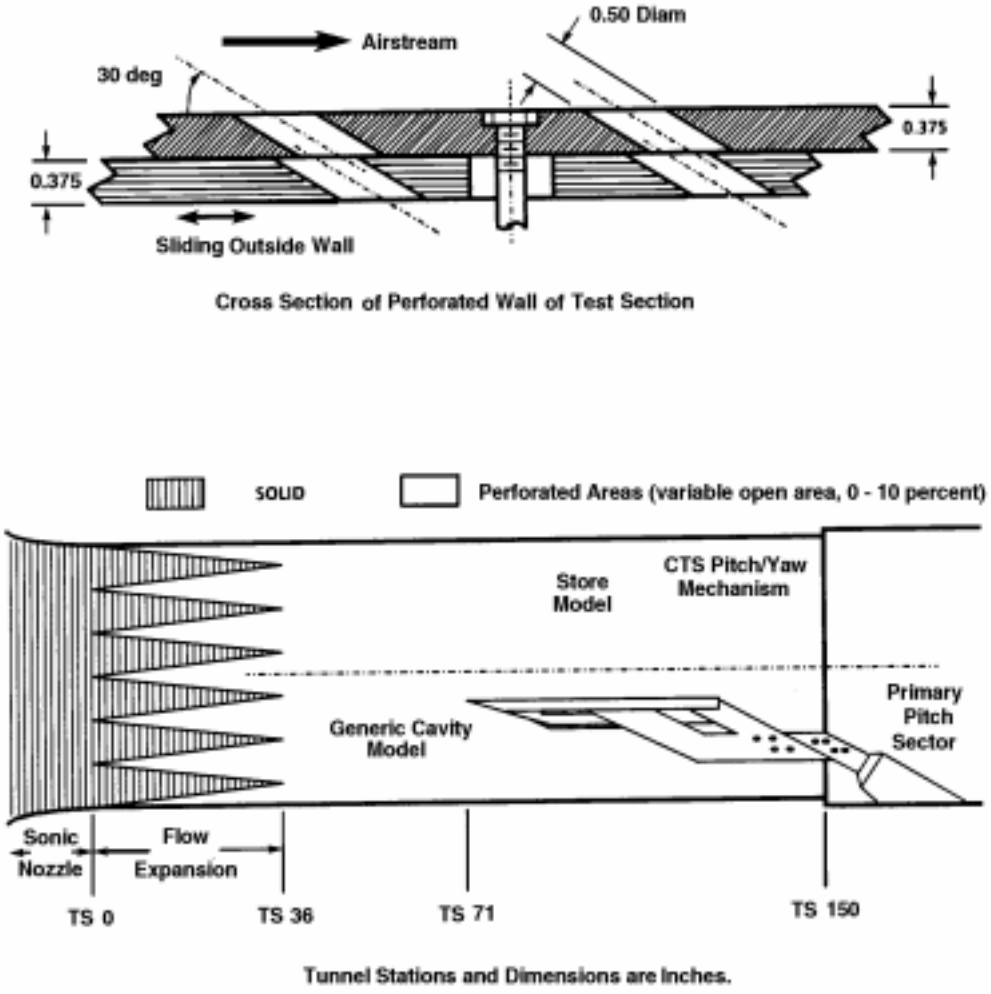

Figure 2. Sketch of the Tunnel 4T test section showing model location.

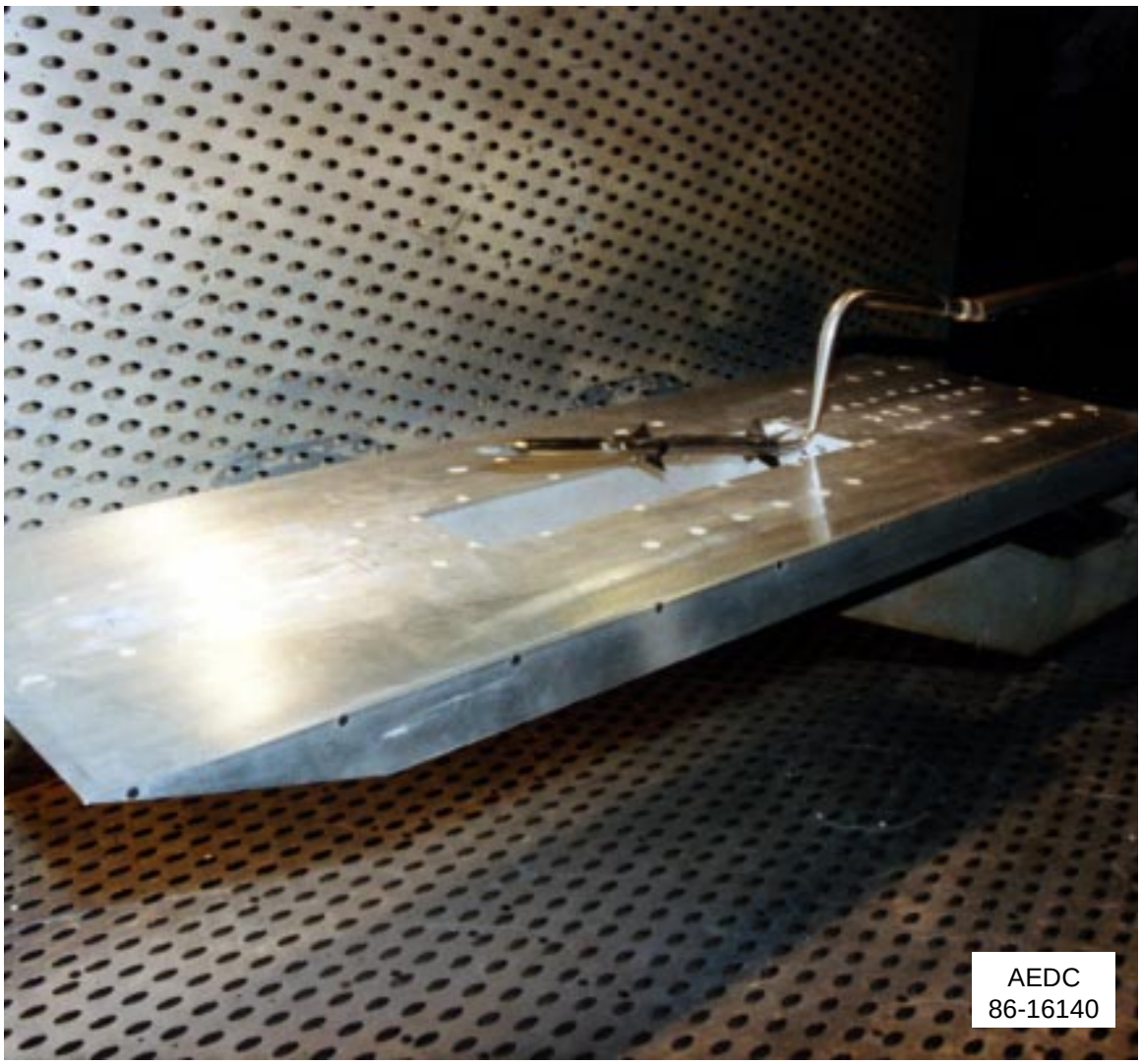

Figure 3. Photograph of WICS model installed in Tunnel 4T.

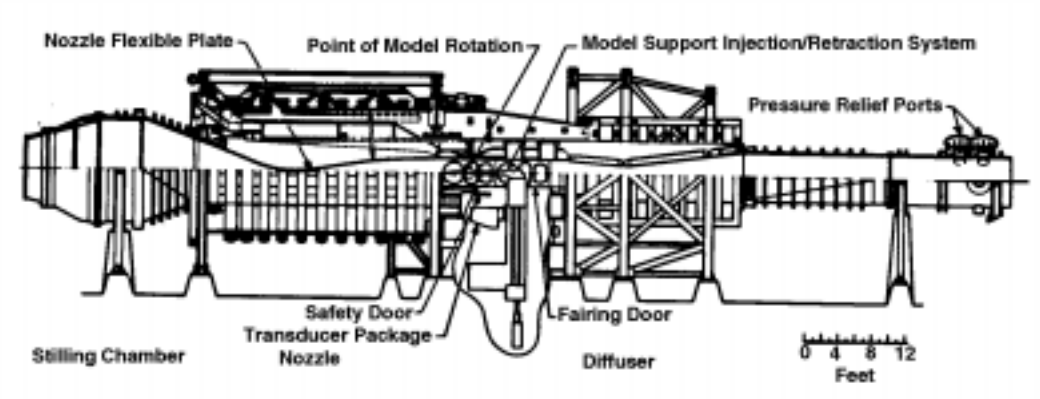

a. Tunnel assembly

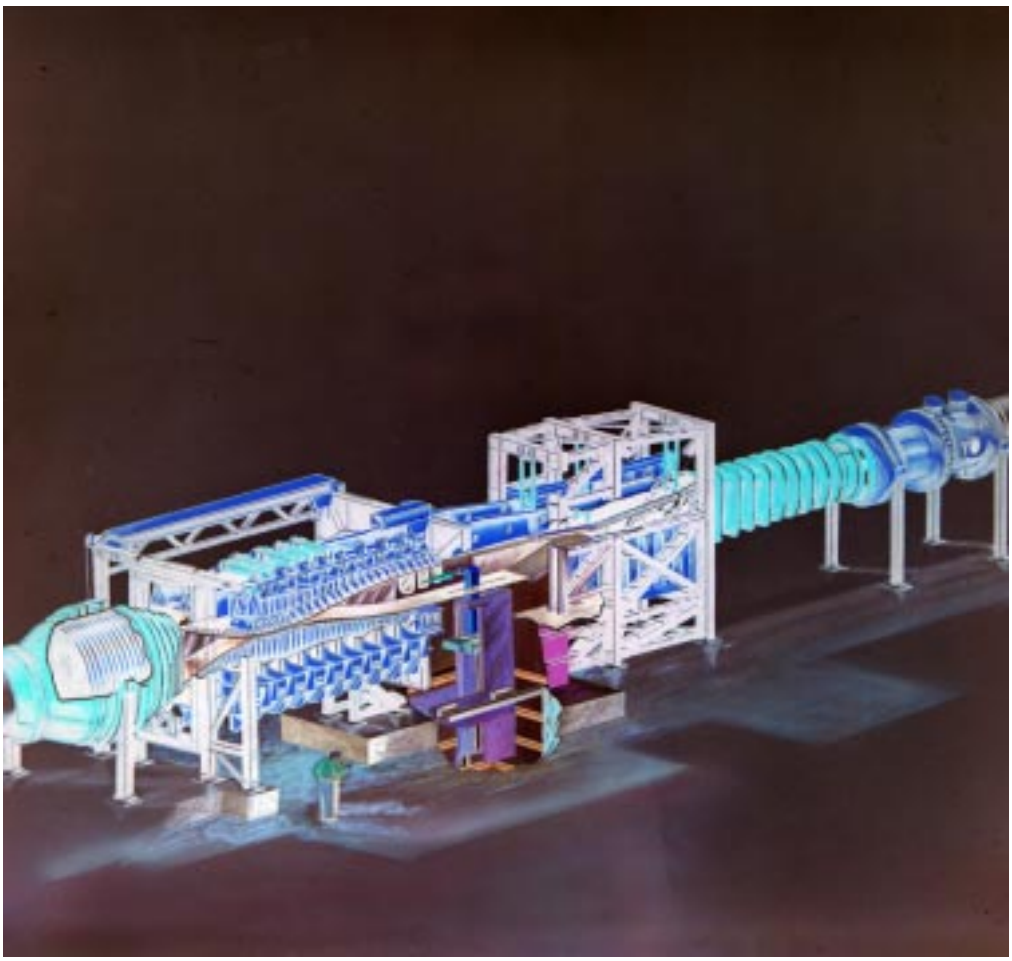

b. Tunnel test section

Figure 4. Sketches of Supersonic Tunnel A and the CTS system.

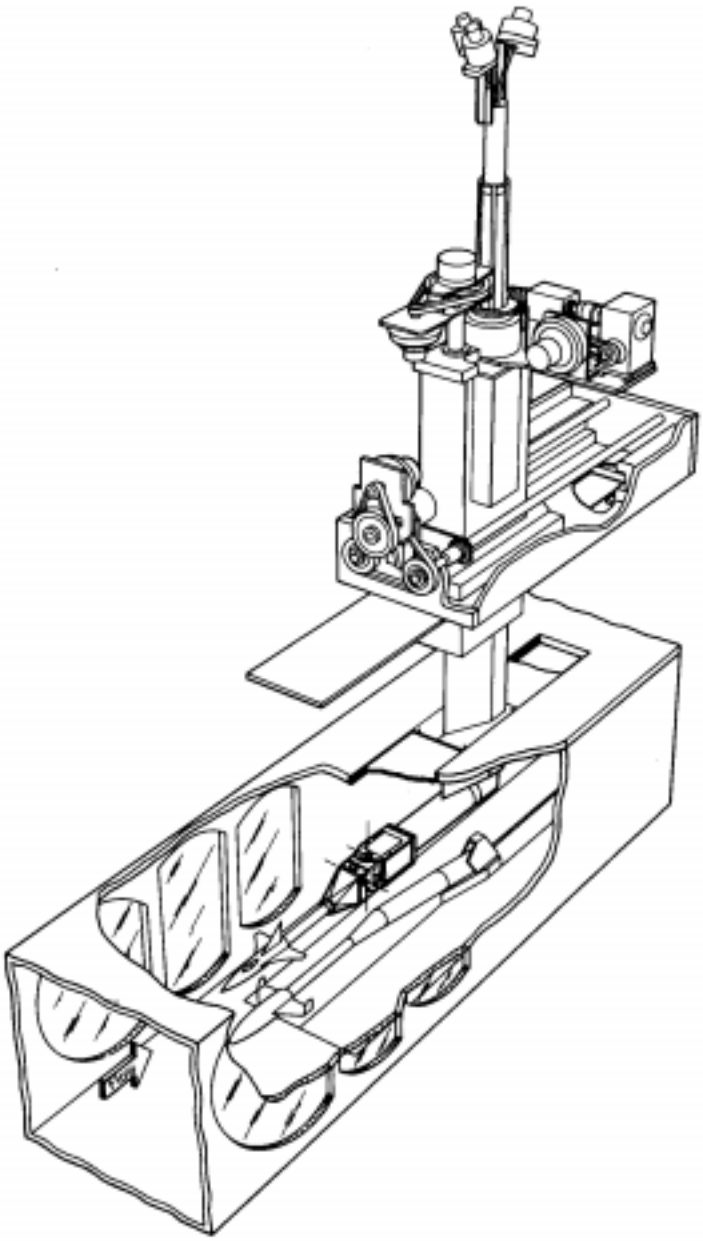

c. Tunnel A CTS system
Figure 4. Concluded.

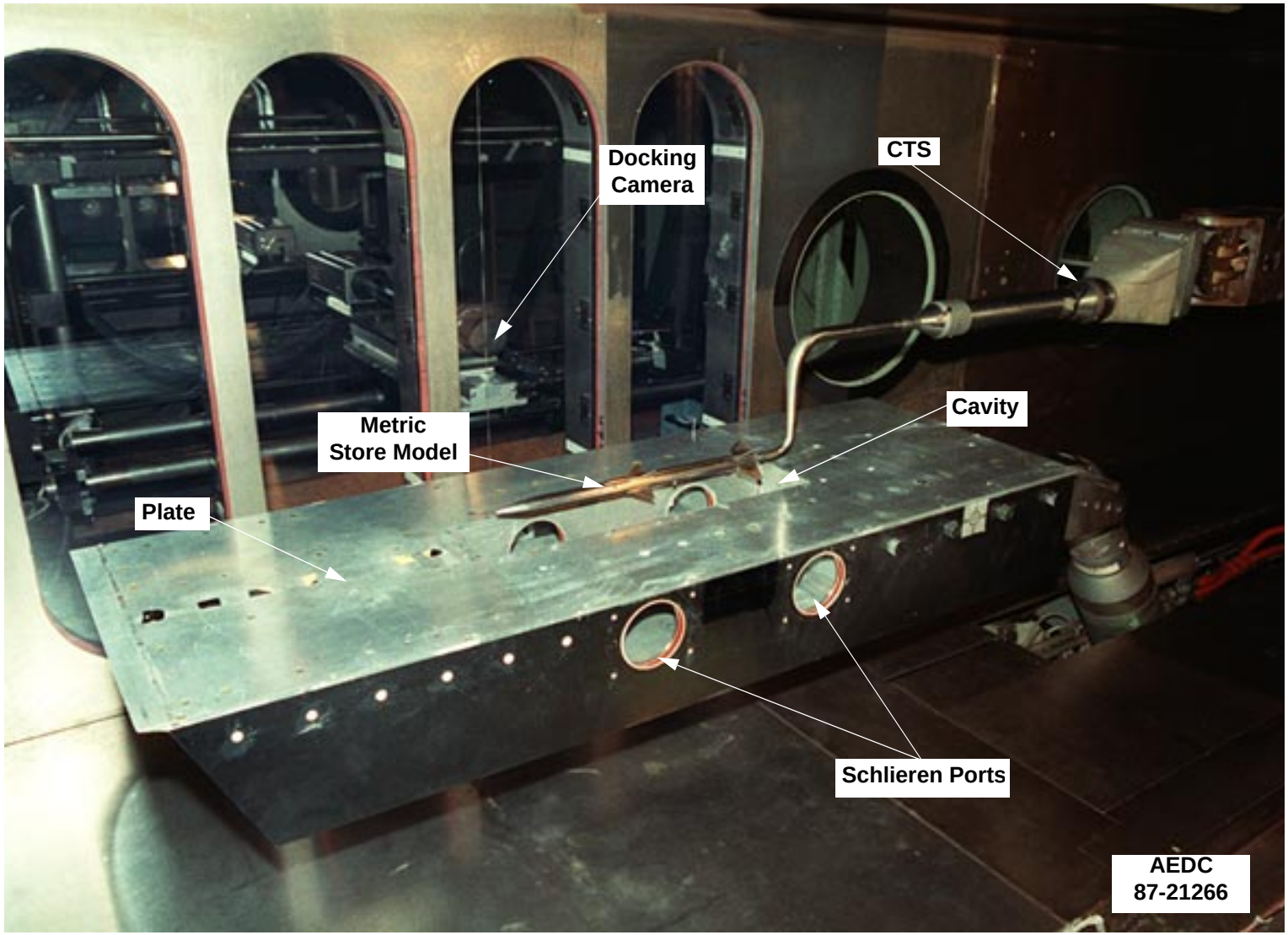

Figure 5. Photograph of WICS models installed in Tunnel A.

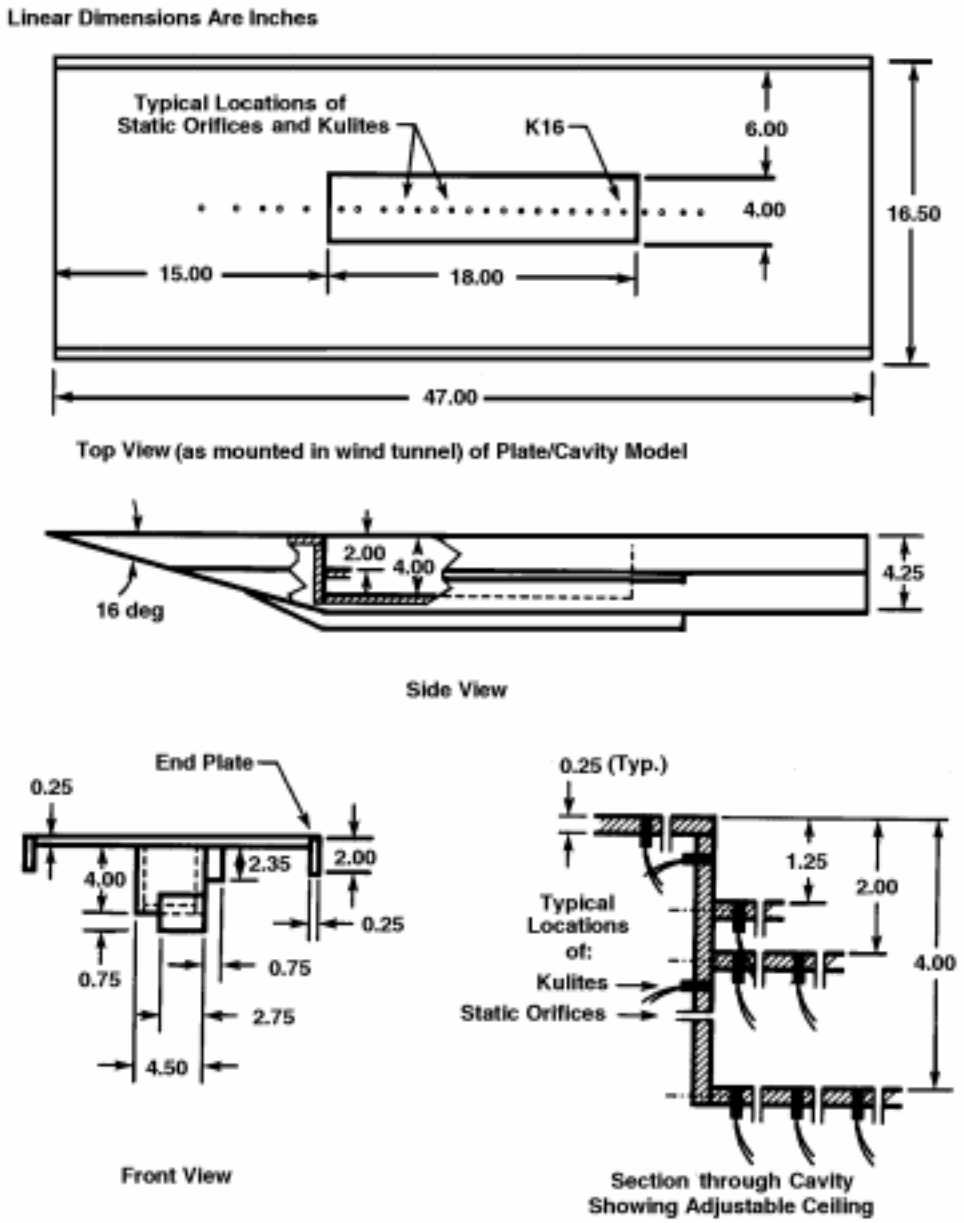

a. Model used in Tunnel 4T

Figure 6. Dimensions of the WICS flat-plate/cavity model.

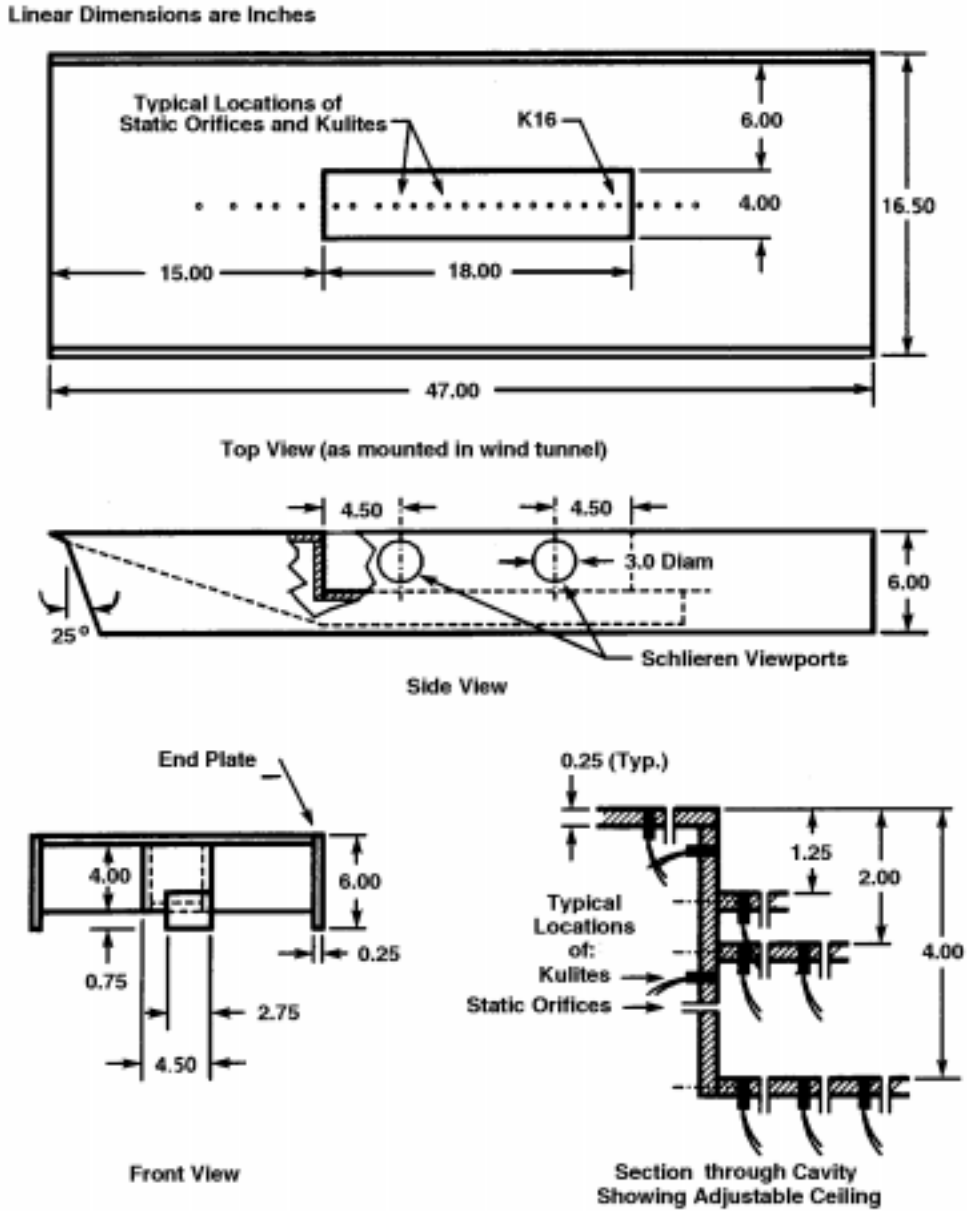

b. Model used in Tunnel A
Figure 6. Continued.

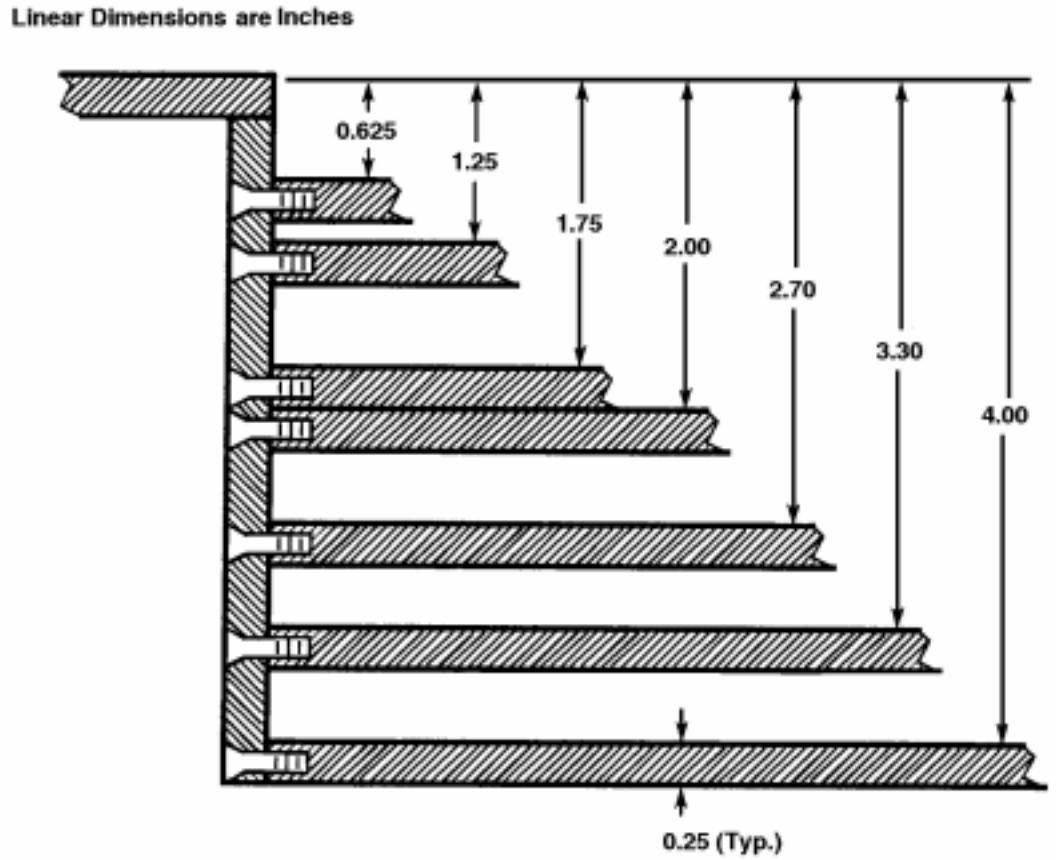

c. Generic cavity ceiling heights
Figure 6. Concluded.

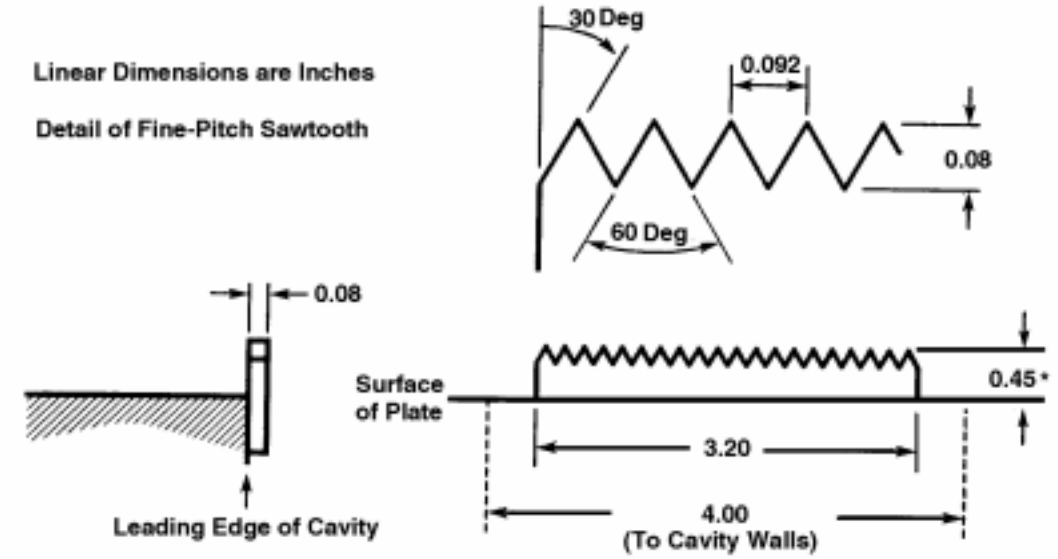

a. Sawtooth spoiler, fine pitch

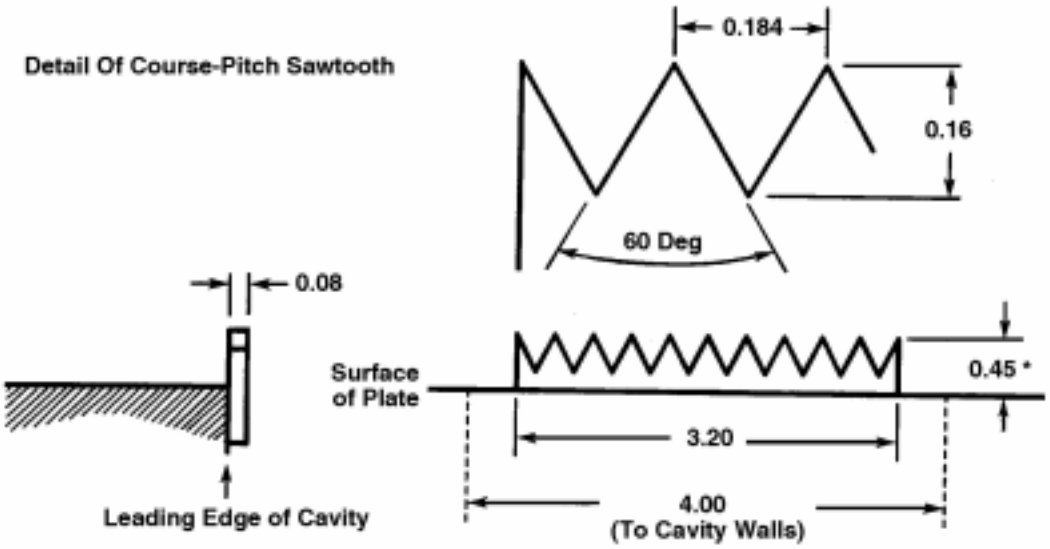

*Spoilers shown are 3δ (0.45-in.).
The 18 (0.15-in.) and 2δ (0.30-in.) spoilers differ in height only.

b. Sawtooth spoiler, coarse pitch

Figure 7. Spoiler model sketches.

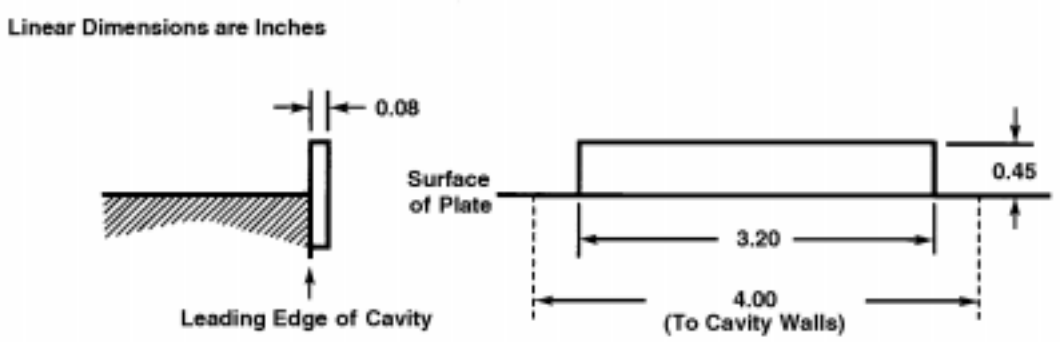

c. Solid spoiler

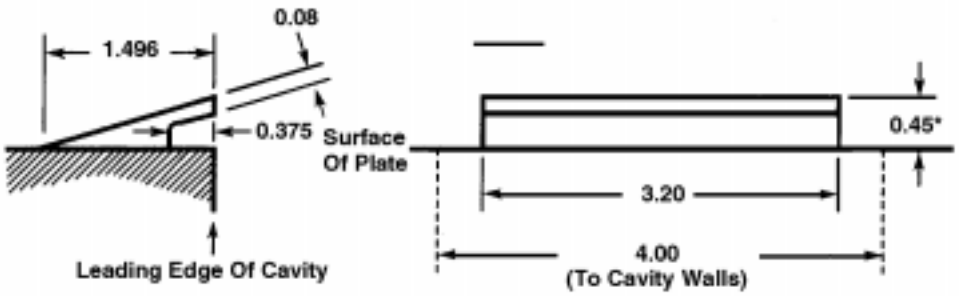

*Spoilers shown are 3δ (0.45-in.).
The 1δ (0.15-in.) and 2δ (0.30-in.) spoilers differ in height only.

d. Flap-type spoiler
Figure 7. Continued.

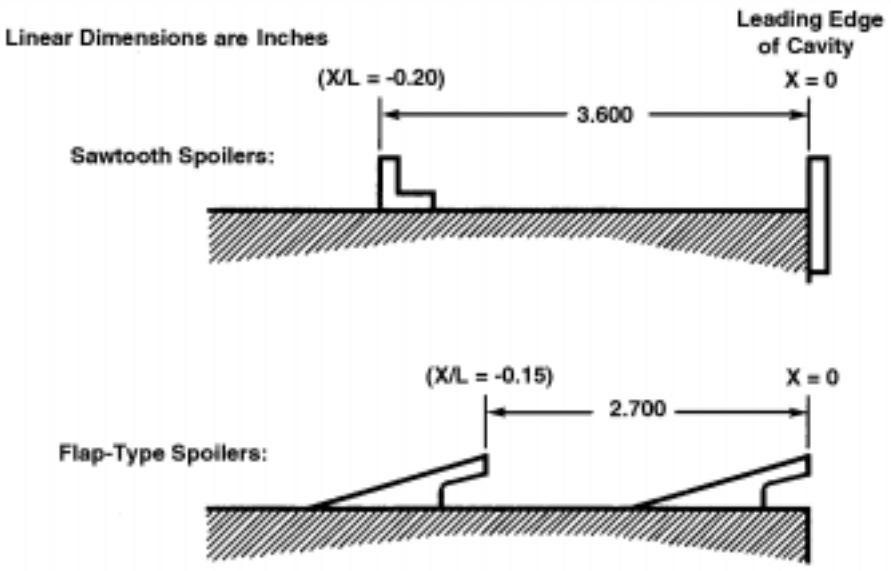

e. Alternate locations of spoilers
Figure 7. Concluded.

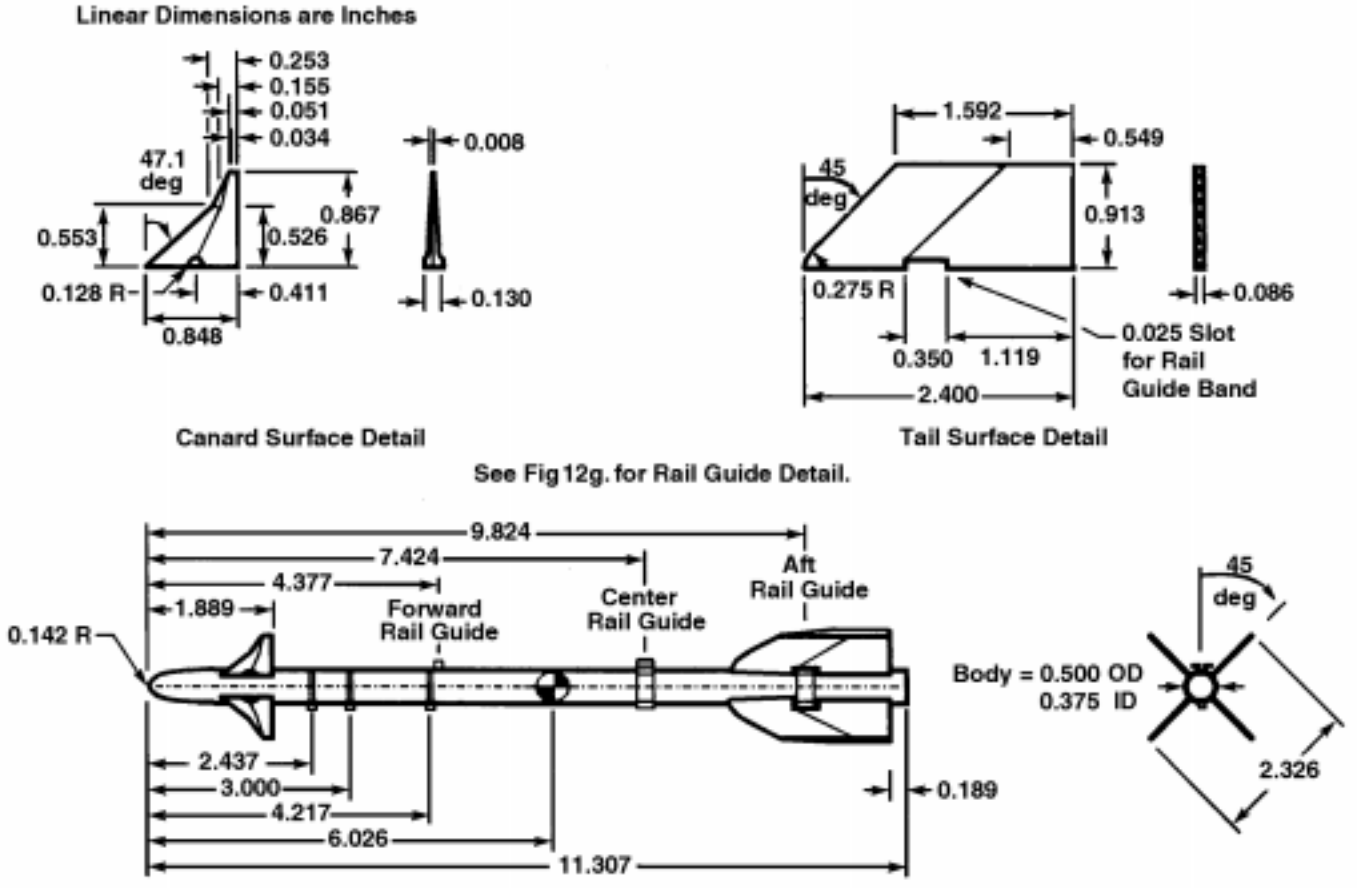

a. AIM-9L

Figure 8. Store model sketches.

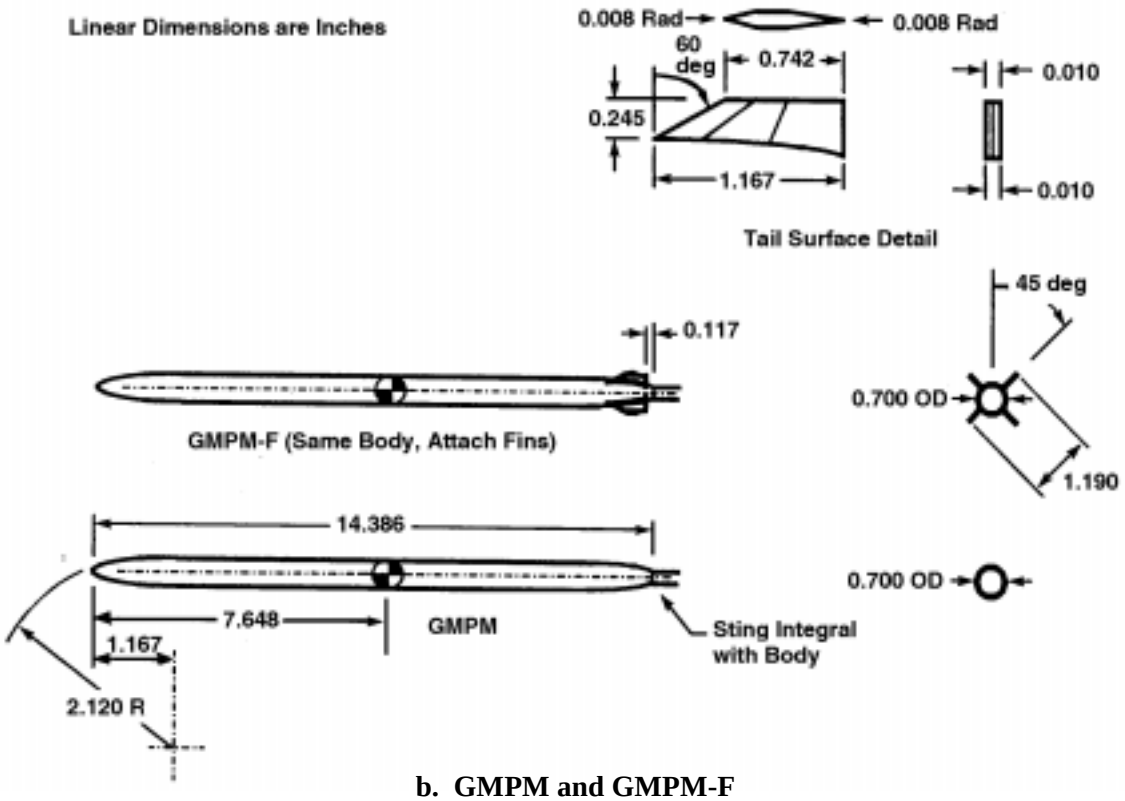

b. GMPM and GMPM-F

Figure 8. Concluded.

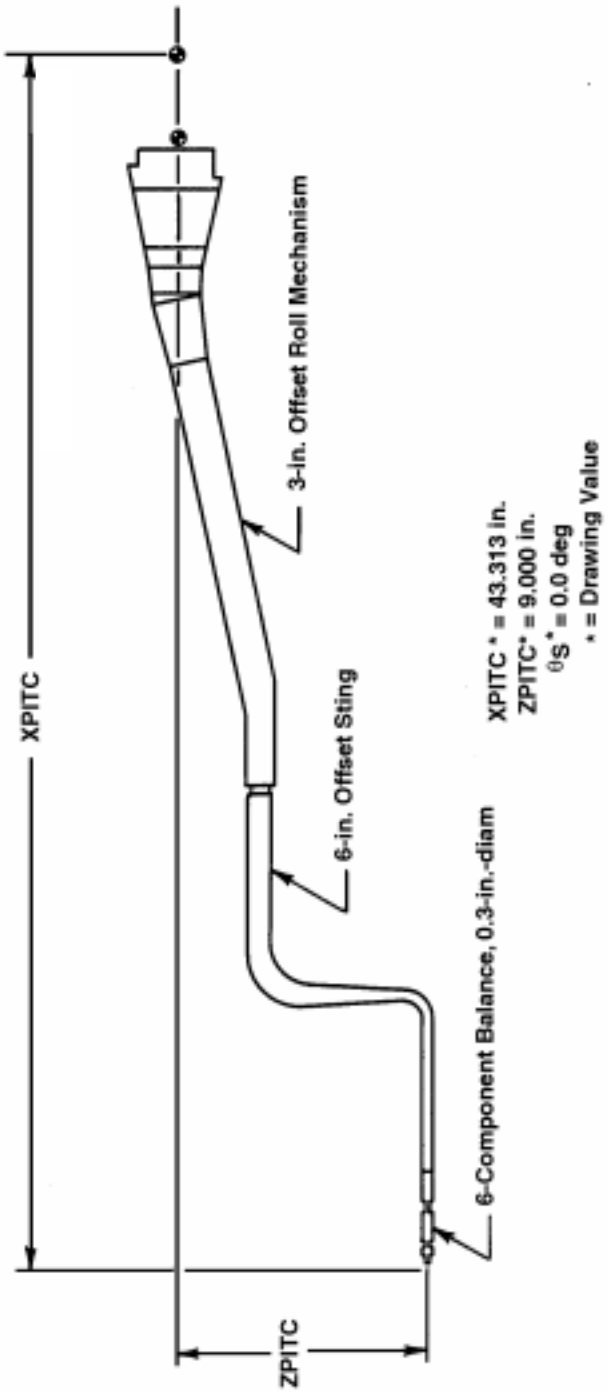

a. Sting used for AIM-96, AIM-9XX, and SPW

Figure 9. Dimensions of the stings used to support store models.

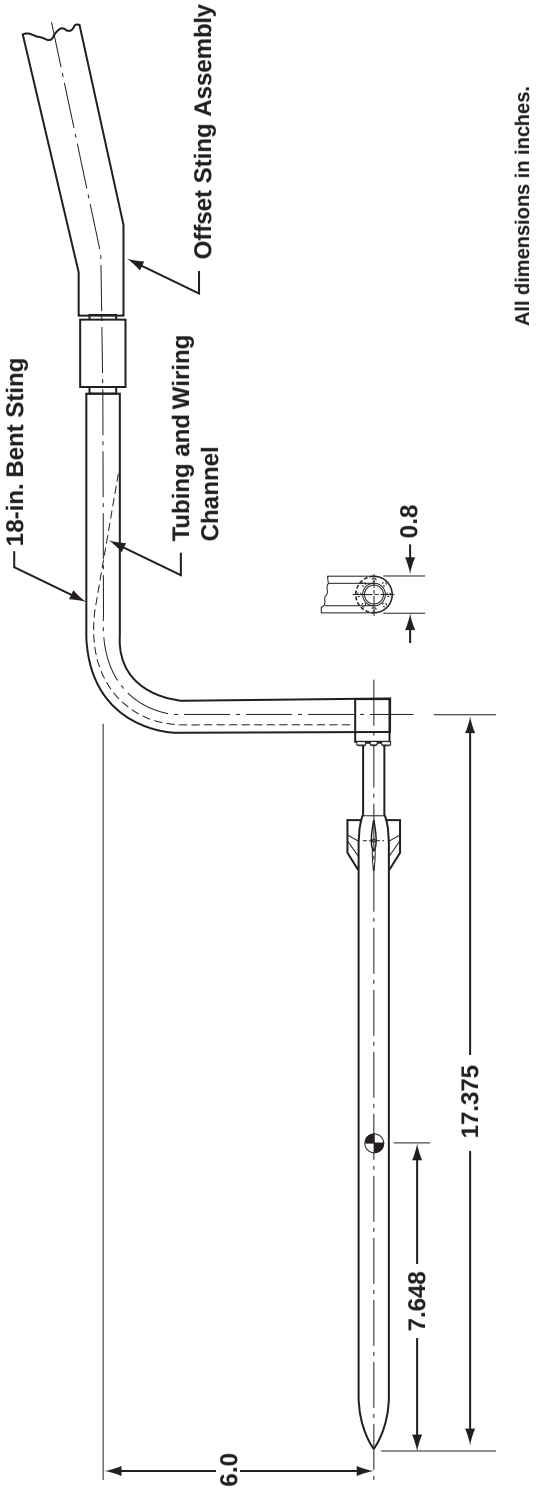

b. Pressure model and sting
Figure 9. Concluded.

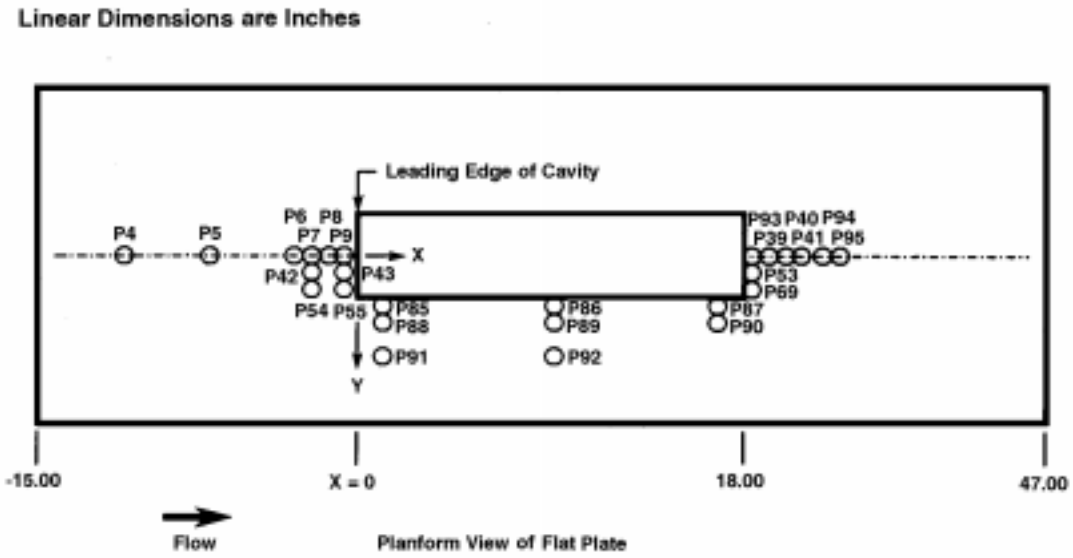

a. Location of static pressure orifices on the flat plate

Figure 10. Static pressure orifice locations.

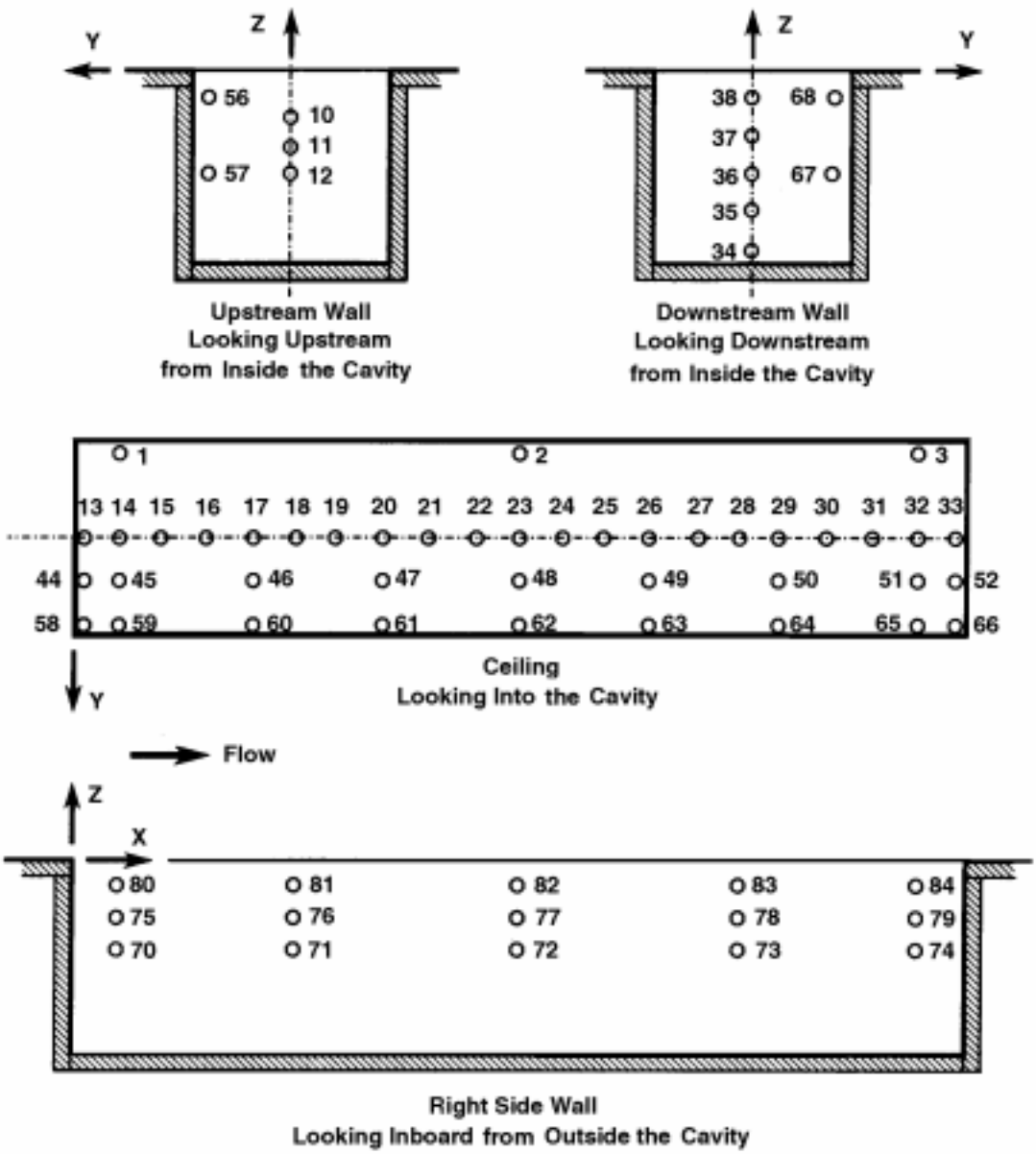

b. Location of static pressure orifices in the cavity
Figure 10. Continued.

Orifice Number	X Model, in.	X/L	Y Model, in.	Y/W/2	Z Model, in.	Orifice Number	X Model, in.	X/L	Y Model, in.	Y/W/2	Z Model, in.
1	0.9	0.05	–1.8	–0.90	-D	34	18.0	1.0	0	0	–3.75
2	9.0	0.50	–1.8	0.90	-D	35	18.0	1.0	0	0	–2.95
3	17.1	0.95	–1.8	0.90	-D	36	18.0	1.0	0	0	–2.15
4	–11.0	–0.611	0	0	0	37	18.0	1.0	0	0	–1.35
5	–7.0	–0.389	0	0	0	38	18.0	1.0	0	0	–0.55
6	–3.0	–0.167	0	0	0	39	18.7	1.039	0	0	0
7	–2.1	–0.117	0	0	0	40	19.2	1.067	0	0	0
8	–1.2	–0.067	0	0	0	41	20.1	1.117	0	0	0
9	–0.3	–0.017	0	0	0	42	–2.1	–0.117	0.9	0.45	0
10	0	0	0	0	–0.95	43	–0.3	–0.017	0.9	0.45	0
11	0	0	0	0	–1.55	44	0.1	0.006	0.9	0.45	–D
12	0	0	0	0	–2.15	45	0.9	0.050	0.9	0.45	–D
13	0.1	0.006	0	0	–D	46	3.6	0.200	0.9	0.45	–D
14	0.9	0.050	0	0	–D	47	6.3	0.350	0.9	0.45	–D
15	1.8	0.100	0	0	–D	48	9.0	0.500	0.9	0.45	–D
16	2.7	0.150	0	0	–D	49	11.7	0.650	0.9	0.45	–D
17	3.6	0.200	0	0	–D	50	14.4	0.800	0.9	0.45	–D
18	4.5	0.250	0	0	–D	51	17.1	0.950	0.9	0.45	–D
19	5.4	0.300	0	0	–D	52	17.9	0.994	0.9	0.45	–D
20	6.3	0.350	0	0	–D	53	18.7	1.039	0.9	0.45	0
21	7.2	0.400	0	0	–D	54	–2.1	–0.117	1.8	0.90	0
22	8.1	0.450	0	0	–D	55	–0.3	–0.017	1.8	0.90	0
23	9.0	0.500	0	0	–D	56	0	0	1.9	0.95	–0.55
24	9.9	0.550	0	0	–D	57	0	0	1.9	0.95	–2.15
25	10.8	0.600	0	0	–D	58	0.1	0.006	1.8	0.90	–D
26	11.7	0.650	0	0	–D	59	0.9	0.050	1.8	0.90	–D
27	12.6	0.700	0	0	–D	60	3.6	0.200	1.8	0.90	–D
28	13.5	0.750	0	0	–D	61	6.3	0.350	1.8	0.90	–D
29	14.4	0.800	0	0	–D	62	9.0	0.500	1.8	0.90	–D
30	15.3	0.850	0	0	–D	63	11.7	0.650	1.8	0.90	–D
31	16.2	0.900	0	0	–D	64	14.4	0.800	1.8	0.90	–D
32	17.1	0.950	0	0	–D	65	17.1	0.950	1.8	0.90	–D
33	17.9	0.994	0	0	–D	66	17.9	0.994	1.8	0.90	–D

c. Location of static pressure orifices

Figure 10. Continued.

Orifice Number	X Model, in.	X/L	Y Model, in.	Y/W/2	Z Model, in.
67	18.0	1.000	1.9	0.950	–2.15
68	18.0	1.000	1.9	0.950	–0.55
69	18.7	1.039	1.8	0.900	0
70	0.9	0.050	2.0	1.000	–1.95
71	4.5	0.250	2.0	1.000	–1.95
72	9.0	0.500	2.0	1.000	–1.95
73	13.5	0.750	2.0	1.000	–1.95
74	17.1	0.950	2.0	1.000	–1.95
75	-0.9	0.050	2.0	1.000	–1.15
76	4.5	0.250	2.0	1.000	–1.15
77	9.0	0.500	2.0	1.000	–1.15
78	13.5	0.750	2.0	1.000	–1.15
79	17.1	0.950	2.0	1.000	–1.15
80	0.9	0.050	2.0	1.000	–0.35
81	4.5	0.250	2.0	1.000	–0.35
82	9.0	0.500	2.0	1.000	–0.35
83	13.5	0.750	2.0	1.000	–0.35
84	17.1	0.950	2.0	1.000	–0.35
85	1.2	0.067	2.3	1.150	0
86	8.8	0.489	2.3	1.150	0
87	16.8	0.933	2.3	1.150	0
88	1.2	0.067	3.2	1.600	0
89	8.8	0.489	3.2	1.600	0
90	16.8	0.933	3.2	1.600	0
91	1.2	0.067	6.2	3.100	0
92	8.8	0.489	6.2	3.100	0
93	18.100	1.006	0	0	0
94	20.775	1.154	0	0	0
95	21.775	1.210	0	0	0

d. Location of static pressure orifices, concluded
Figure 10. Concluded.

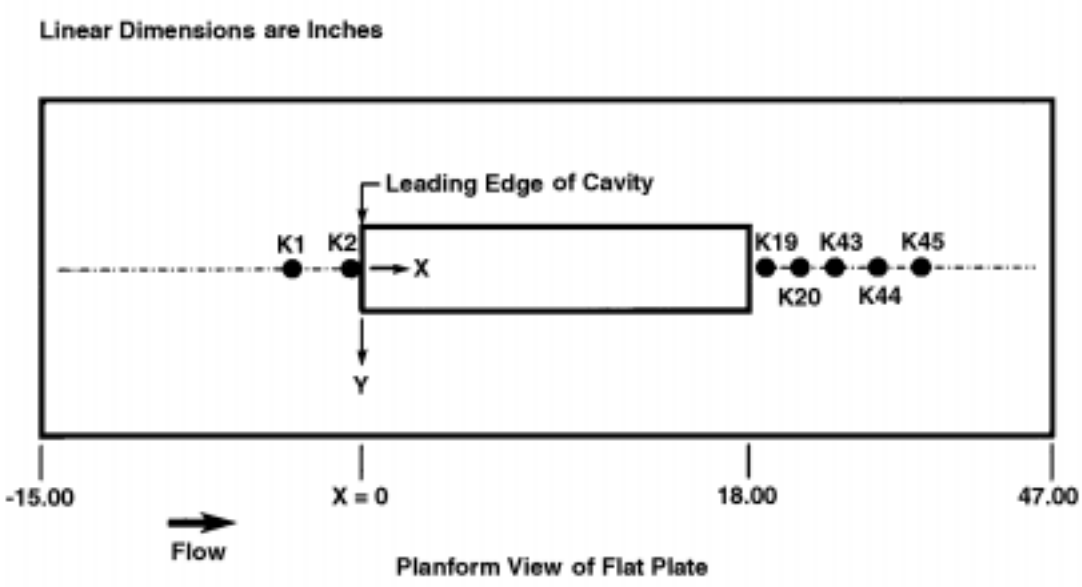

a. Location of dynamic pressure transducers on the flat plate

Figure 11. Dynamic pressure transducer locations.

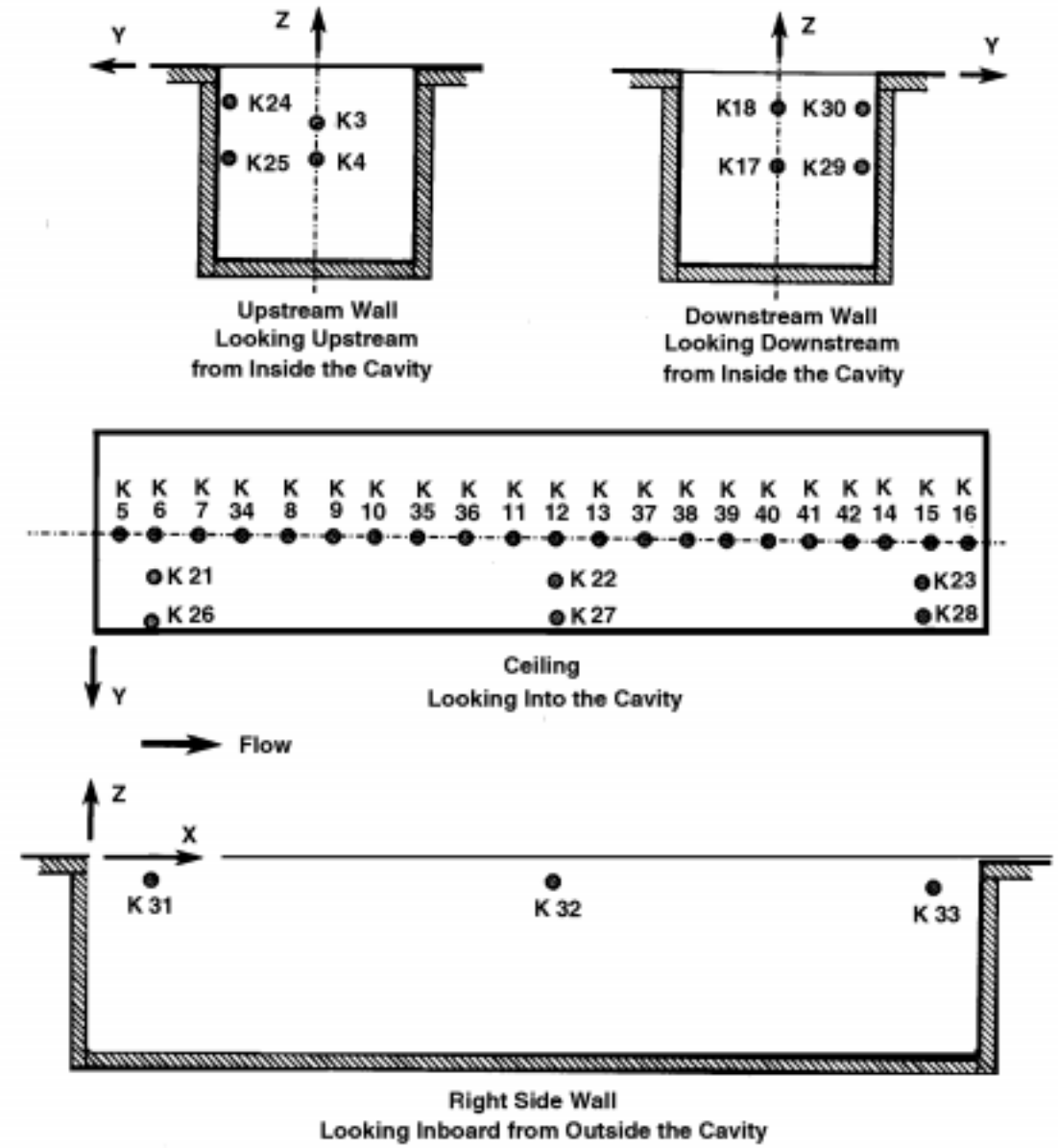

b. Location of dynamic pressure transducers in the cavity
Figure 11. Continued.

Transducer Number	X Model, in.	X/L	Y Model, in.	Y/W/2	Z Model, in.
K1	–3.175	–0.176	0	0	0
K2	–0.475	–0.026	0	0	0
K3	0	0	0	0	–1.125
K4	0	0	0	0	–1.975
K5	0.275	0.015	0	0	–D
K6	1.075	0.060	0	0	–D
K7	1.975	0.110	0	0	–D
K8	3.775	0.210	0	0	–D
K9	4.675	0.260	0	0	–D
K10	5.575	0.310	0	0	–D
K11	8.275	0.460	0	0	–D
K12	9.175	0.510	0	0	–D
K13	10.075	0.560	0	0	–D
K14	16.025	0.890	0	0	–D
K15	16.925	0.940	0	0	–D
K16	17.725	0.985	0	0	–D
K17	18.000	1.000	0	0	–1.975
K18	18.000	1.000	0	0	–0.725
K19	18.875	1.049	0	0	0
K20	20.275	1.126	0	0	0
K21	1.075	0.060	0.9	0.45	–D
K22	9.175	0.510	0.9	0.45	–D
K23	16.925	0.940	0.9	0.45	–D
K24	0	0	1.9	0.95	–0.725
K25	0	0	1.9	0.95	–1.975

Transducer Number	X Model, in.	X/L	Y Model, in.	Y/W/2	Z Model, in.
K26	1.075	0.060	1.8	0.90	-D
K27	9.175	0.510	1.8	0.90	-D
K28	16.925	0.940	1.8	0.90	-D
K29	18.000	1.000	1.9	0.95	–1.975
K30	18.000	1.000	1.9	0.95	–0.725
K31	1.075	0.060	2.0	1.00	–0.35
K32	9.175	0.510	2.0	1.00	–0.35
K33	16.925	0.940	2.0	1.00	–D
K34	2.875	0.160	0	0	–D
K35	6.475	0.360	0	0	–D
K36	7.375	0.410	0	0	–D
K37	10.975	0.610	0	0	–D
K38	11.875	0.660	0	0	–D
K39	12.775	0.710	0	0	–D
K40	13.675	0.760	0	0	–D
K41	14.575	0.810	0	0	–D
K42	15.475	0.860	0	0	–D
K43	21.950	1.219	0	0	0
K44	23.950	1.331	0	0	0
K45	25.950	1.442	0	0	0
K46	Tunnel Wall				
K101	GMPM Store Model (See Fig. 11)				
K106					

c. Dynamic pressure transducer locations

Figure 11. Concluded.

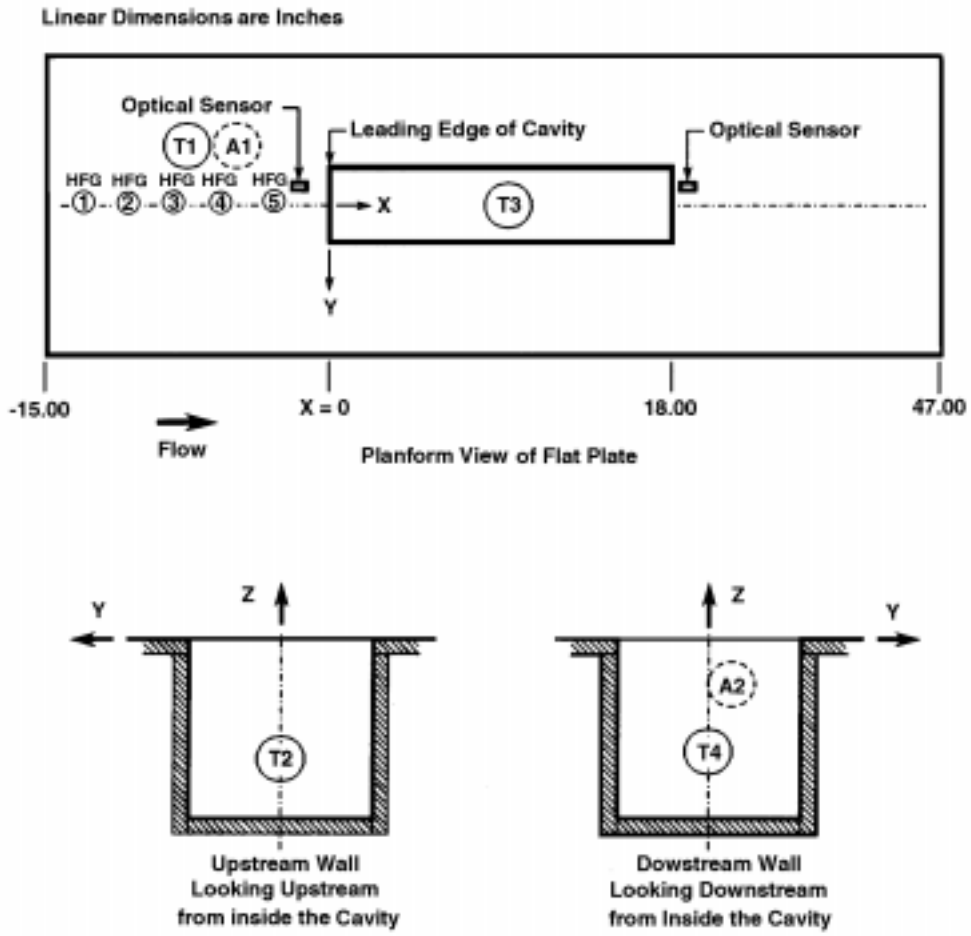

a. Instrument locations

Figure 12. Locations of other sensors.

Instrument	X Model, in.	X/L	Y Model, in.	Y/W/2	Z Model, in.
Hot-Film Gages:					
HFG 1	–11.0	–0.722	0.25	0.125	0
HFG 2	–7.0	–0.389	0.25	0.125	0
HFG 3	–3.0	0.167	0.25	0.125	0
HFG 4	-1.262	0.070	0.25	0.125	0
HFG 5	-0.388	0.022	0.25	0.125	0
Thermocouples:					
T1	–4.5	–0.25	–0.5	–0.25	-0.2
T2	–0.1	–0.01	–0.5	–0.25	-0.2
T3	9.0	0.50	–0.5	–0.25	–(D + 0.2)
T4	18.1	1.01	–0.5	–0.25	0
Accelerometers:					
A1	-6.0	–0.33	–0.5	–0.25	–0.25
A2	18.0	1.00	0.5	0.25	–1.0
Inclinometer:	–9.0	–0.50	0	0	0.25
Optical Sensor:	–2.85	–0.158	–1.0	–0.50	0
	18.6	1.028	-1.0	–0.50	0

b. Instrument summary
Figure 12. Concluded.

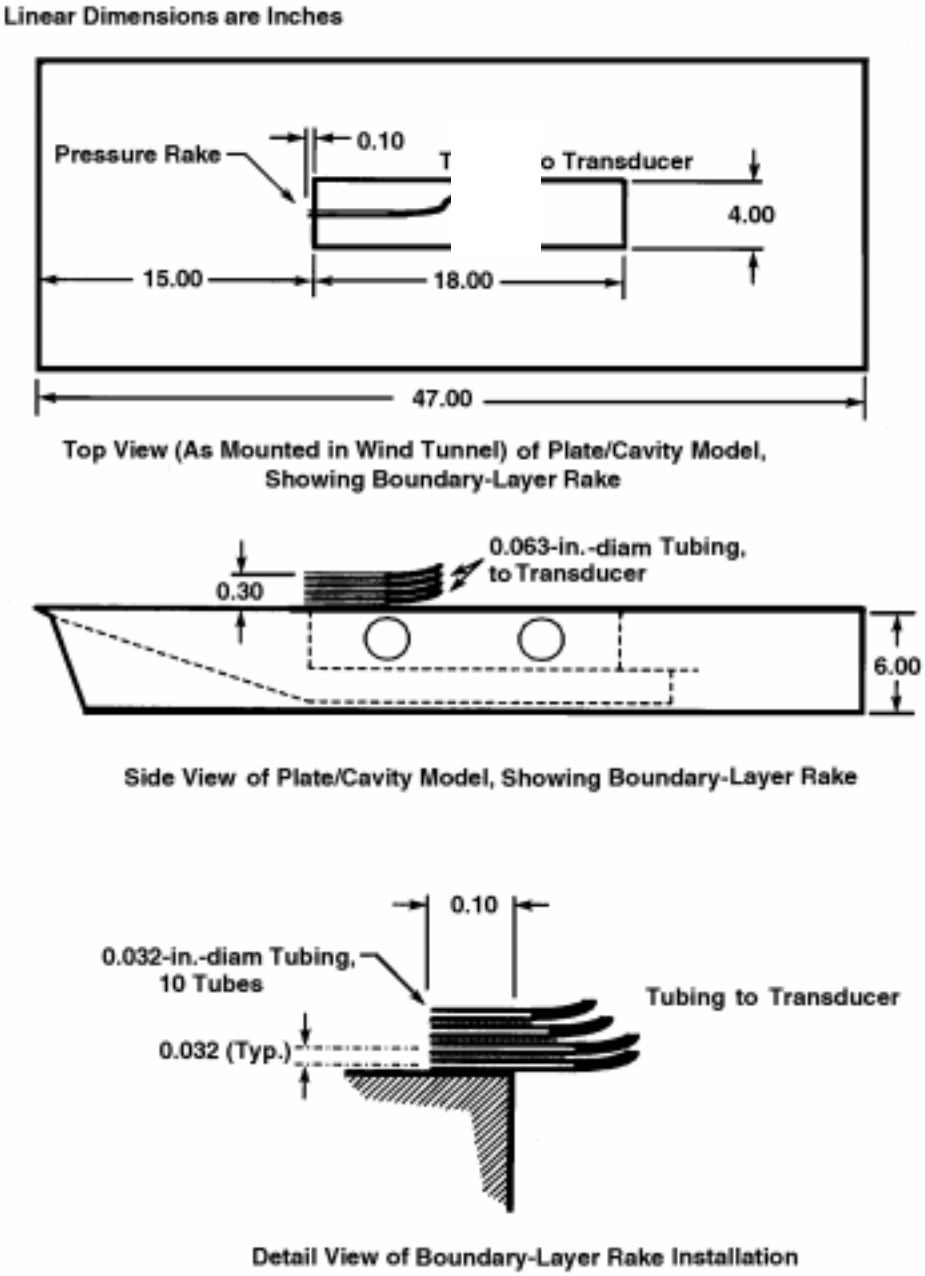

Figure 13. Sketch of the boundary-layer rake.

Orifice No.	MS, in.	X/L	ϕ, deg	Orifice No.	MS, in.	X/L	ϕ, deg	Orifice No.	MS, in.	X/L	ϕ, deg	Orifice No.	MS, in.	X/L	ϕ, deg
P101	0.205	0.03	0	P111	3.447	0.218	0	P121	8.447	0.695	0	P131	13.447	0.773	0
P102	0.205	0.03	180	P112	3.447	0.218	180	P122	8.447	0.695	180	P132	13.447	0.773	180
P103	0.618	0.06	0	P113	4.447	0.273	0	P123	9.447	0.551	0	P133	14.095	0.809	0
P104	0.618	0.06	180	P114	4.447	0.273	180	P124	9.447	0.551	180	P134	14.095	0.809	180
P105	1.056	0.08	0	P115	5.447	0.329	0	P125	10.447	0.607	0	P135	12.697	0.732	225
P106	1.056	0.08	180	P116	5.447	0.329	180	P126	10.447	0.607	180	P136	12.697	0.732	315
P107	1.44	0.107	0	P117	6.447	0.384	0	P127	11.447	0.662	0	P137	12.697	0.732	45
P108	1.447	0.107	180	P118	6.447	0.384	180	P128	11.447	0.662	180	P138	12.697	0.732	135
p109	2.447	0.162	0	P119	7.447	0.460	0	P129	12.447	0.718	0				
P110	2.447	0.162	180	P120	7.447	0.460	180	P130	12.447	0.718	180				

Kulite® No.	MS, in.	X/L	ϕ, deg	Kulite® No.	MS, in.	X/L	ϕ, deg	Kulite® No.	MS, in.	X/L	ϕ, deg
K101	4.147	0.257	0	K103	6.147	0.368	0	K105	8.147	0.479	0
K102	3.747	0.239	180	K104	5.747	0.345	180	K106	7.747	0.457	180

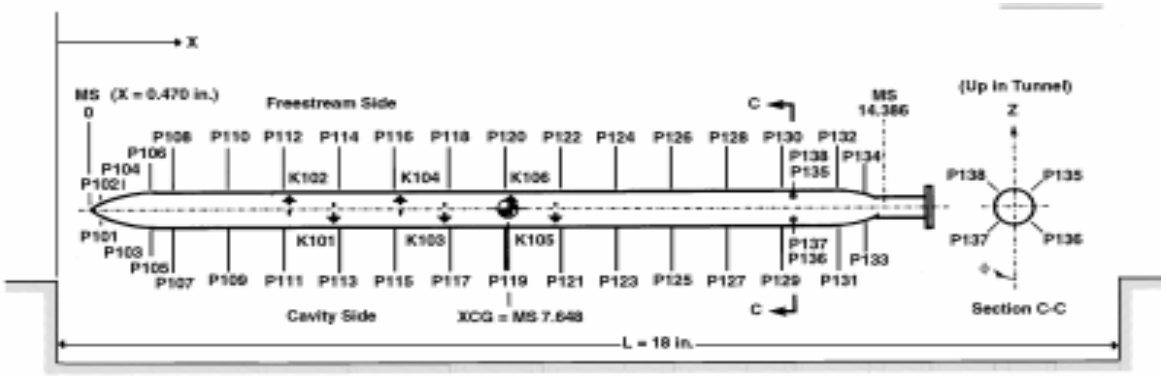

Figure 14. Points of measurement of static and dynamic pressures on the GMPM model.

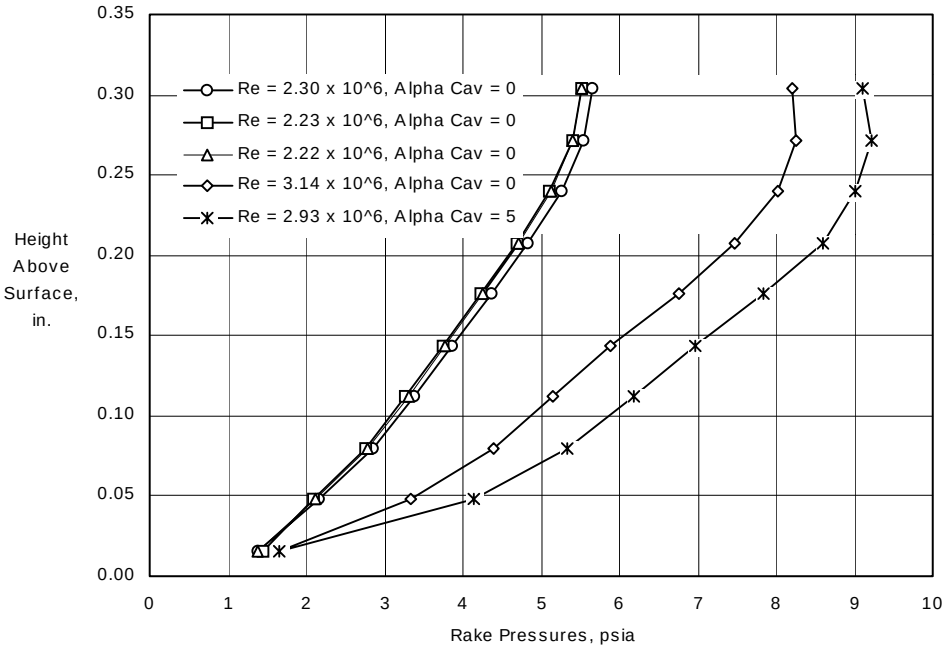

a. M_∞ = 2.50

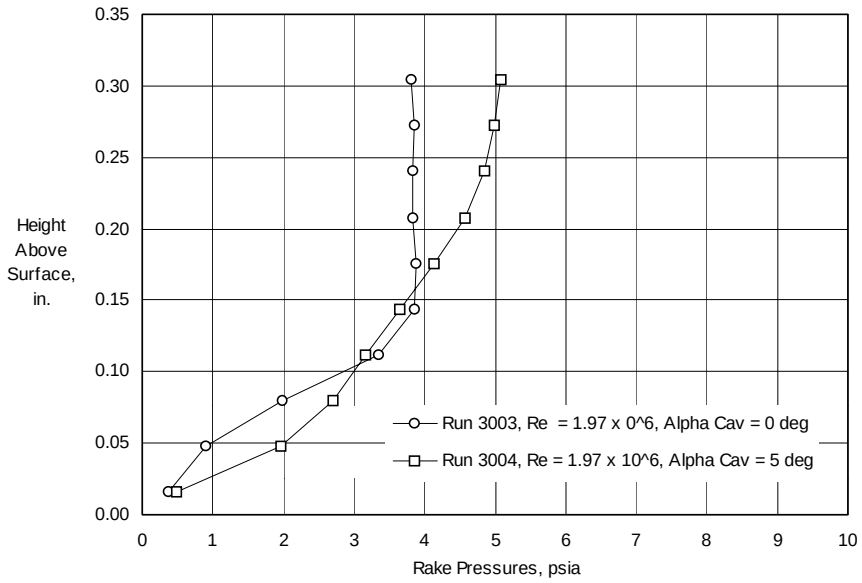

b. M_∞ = 3.51

Figure 15. Measured boundary-layer profiles at the leading edge of the cavity.

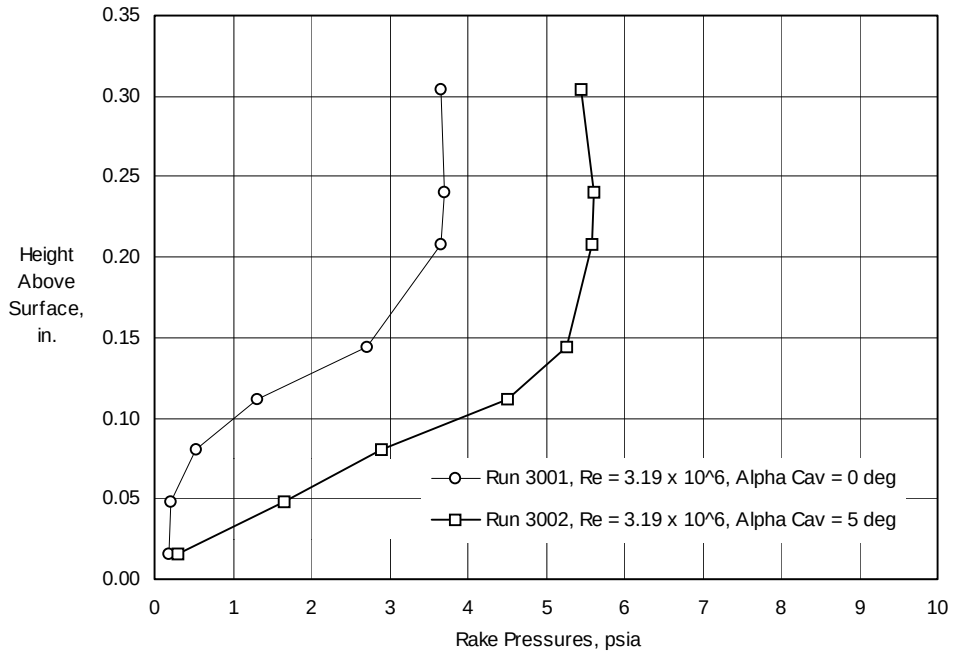

c. $M_\infty = 5.04$

Figure 15. Concluded.

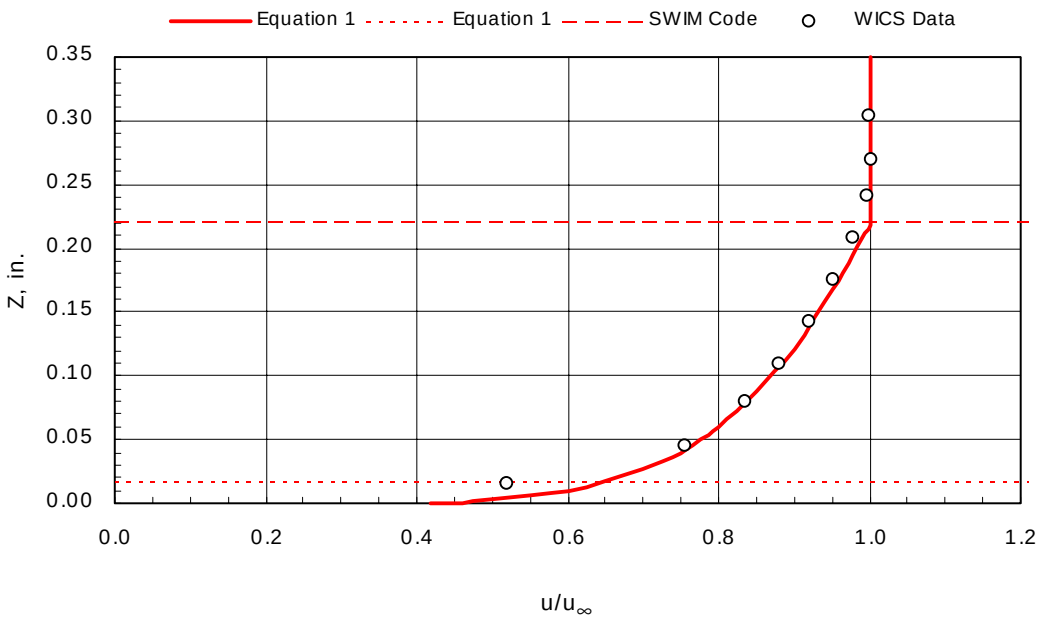

a. $M_\infty = 2.5$, $Re = 3 \times 10^6$

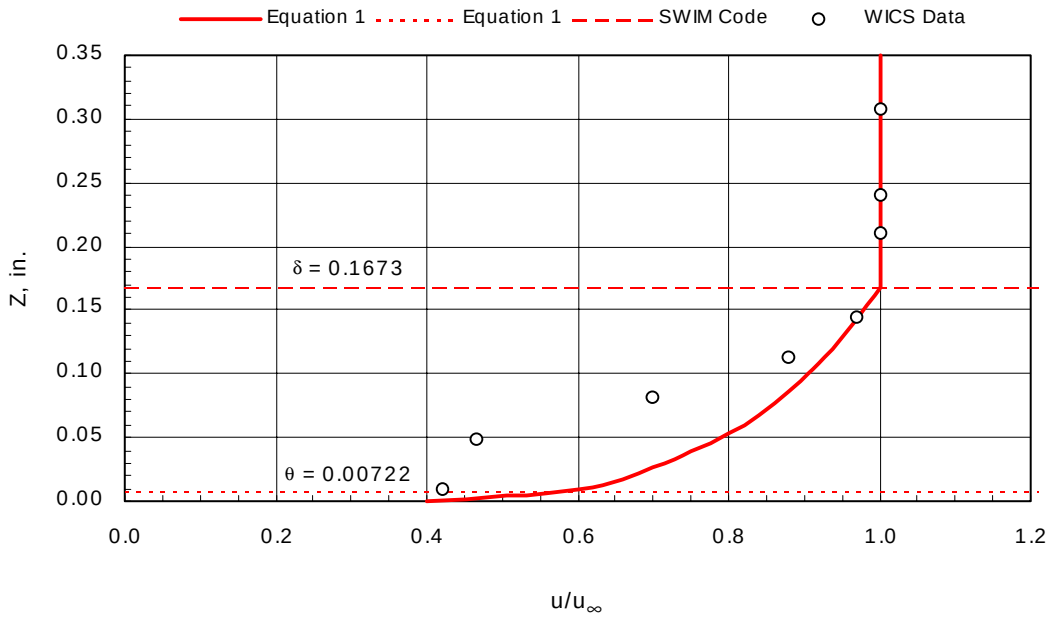

b. $M_\infty = 5.0$, $Re = 3 \times 10^6$

Figure 16. Comparison of measured and predicted boundary-layer velocity profiles.

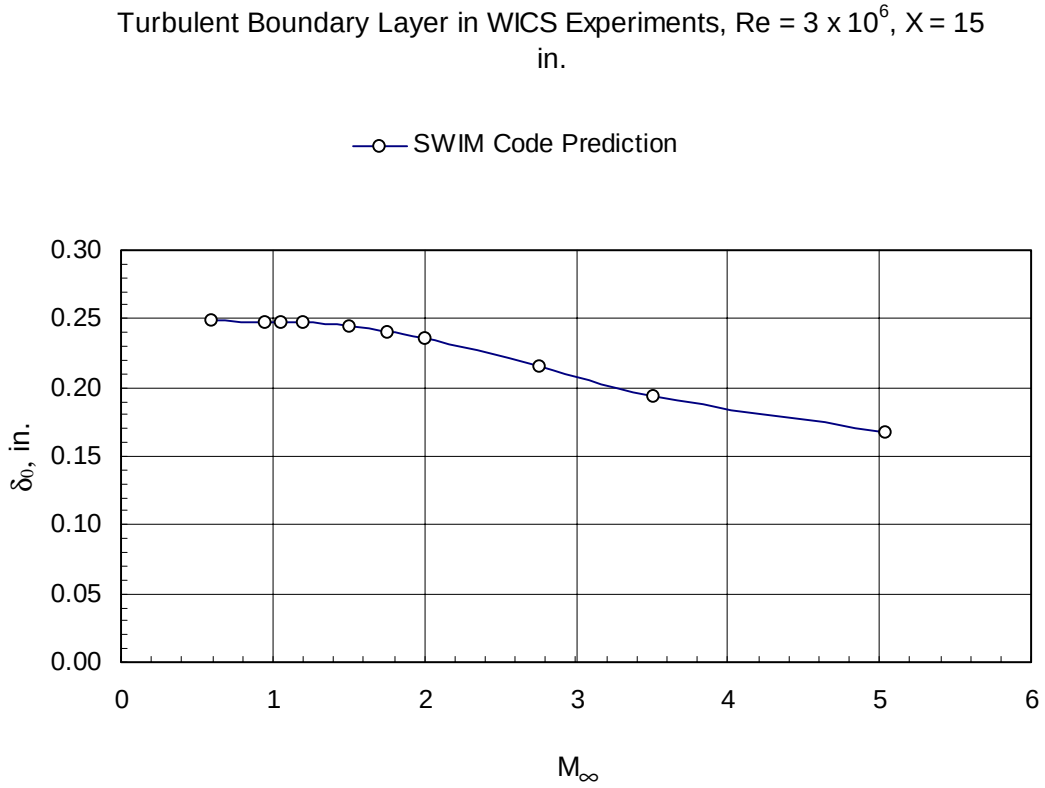

Figure 17. Predicted height of the boundary layer at the leading edge of the cavity.

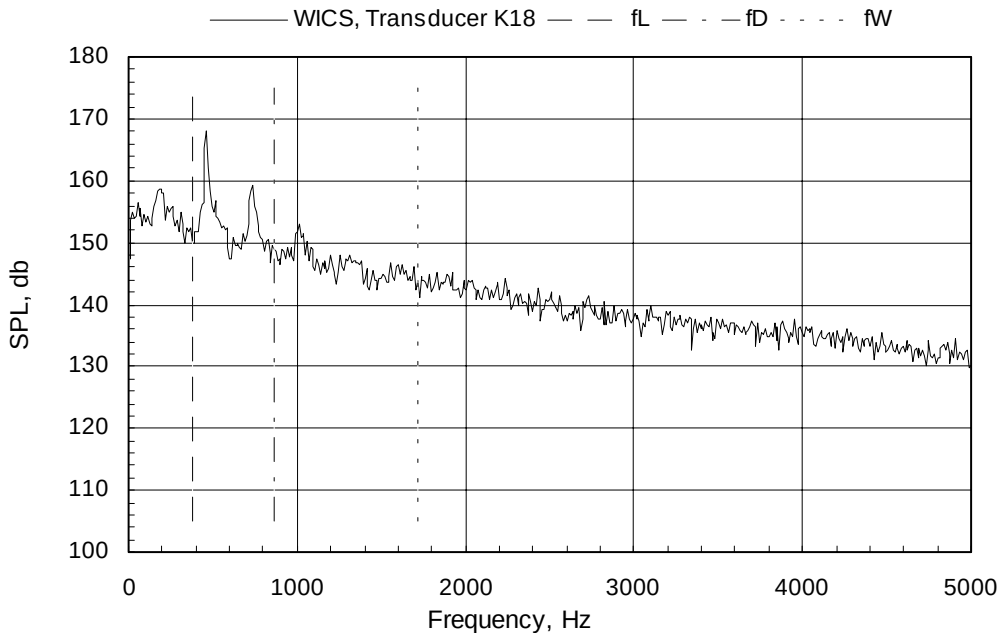

a. M_∞ = 0.60

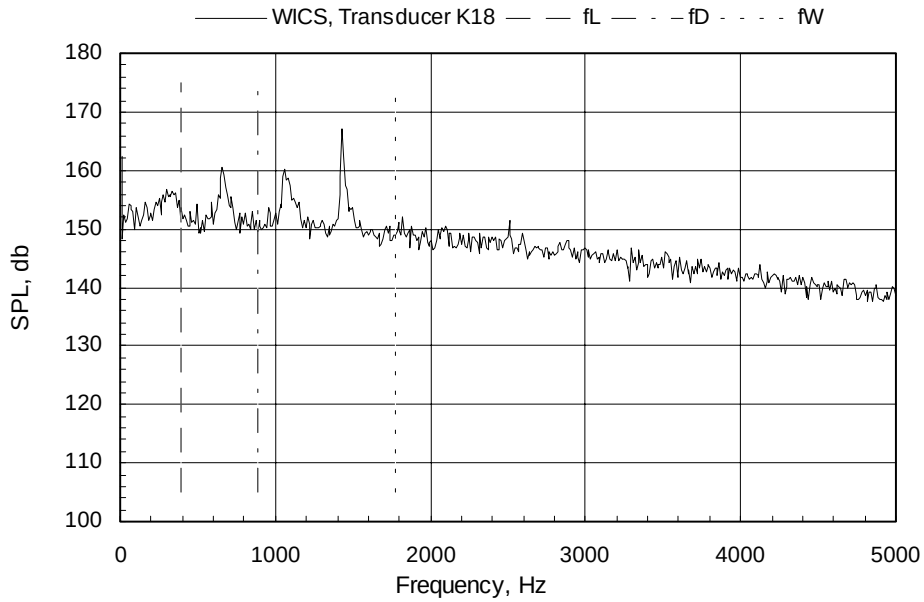

b. M_∞ = 0.95

Figure 18. Comparison of measured and natural acoustic (open organ pipe) modal frequencies for the WICS cavity, L/.D = 4.5.

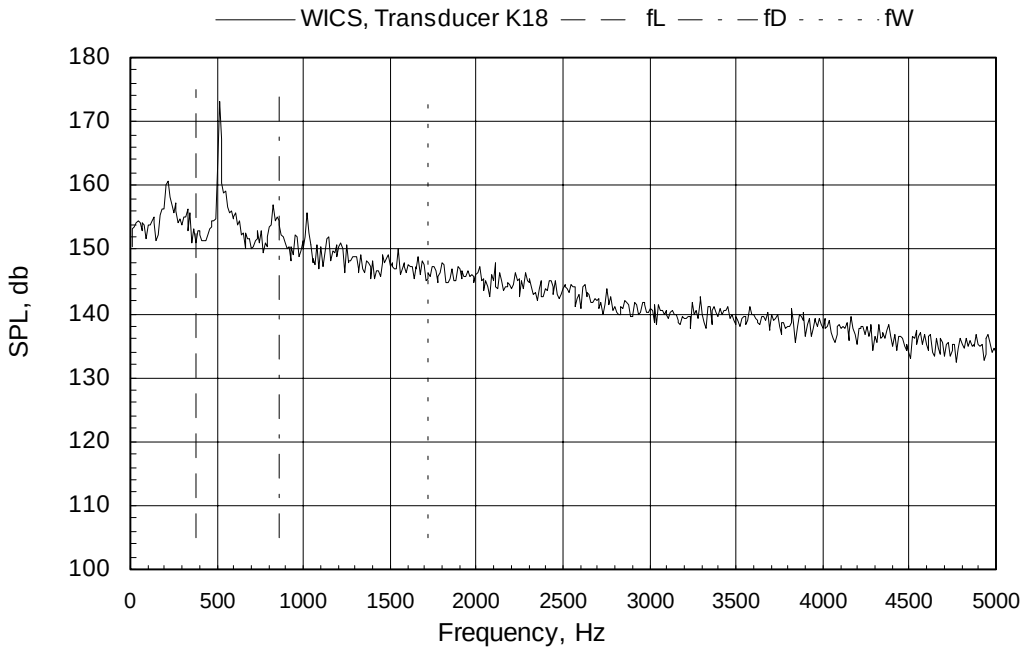

c. M_∞ = 1.20

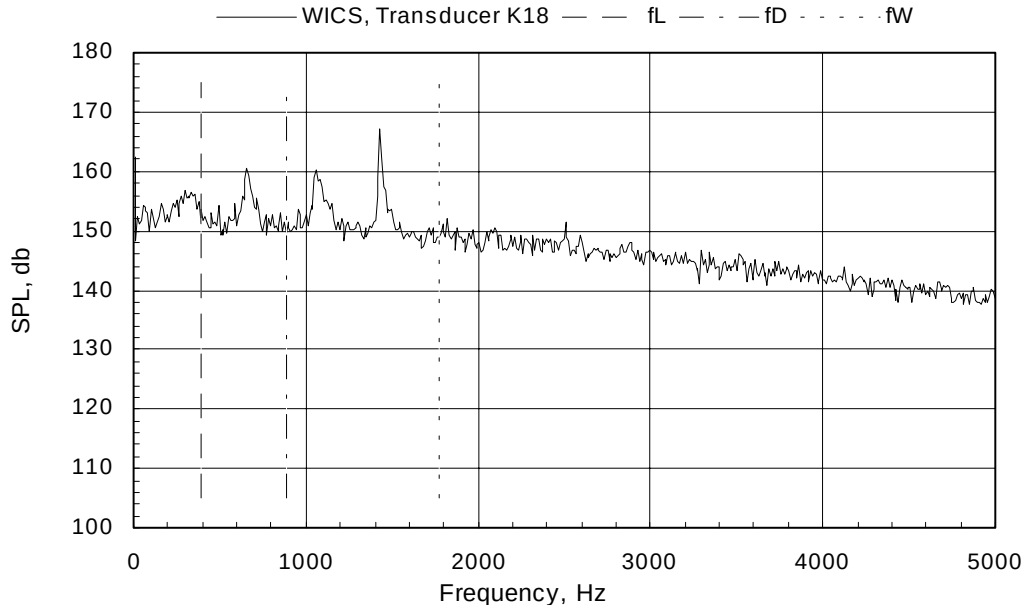

d. M_∞ = 2.00

Figure 18. Continued.

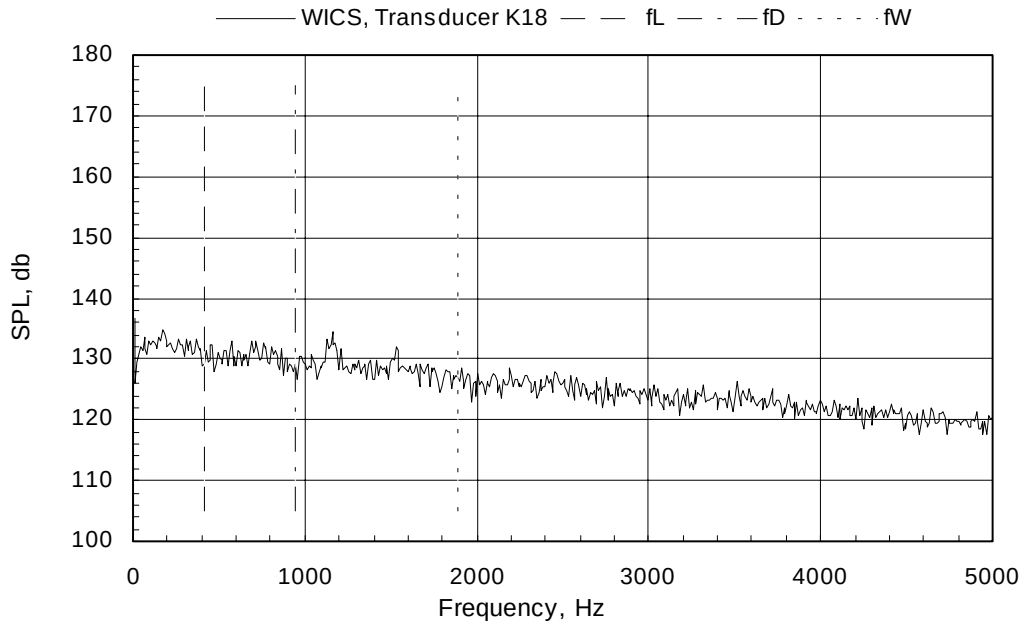

e. M_∞ = 3.51

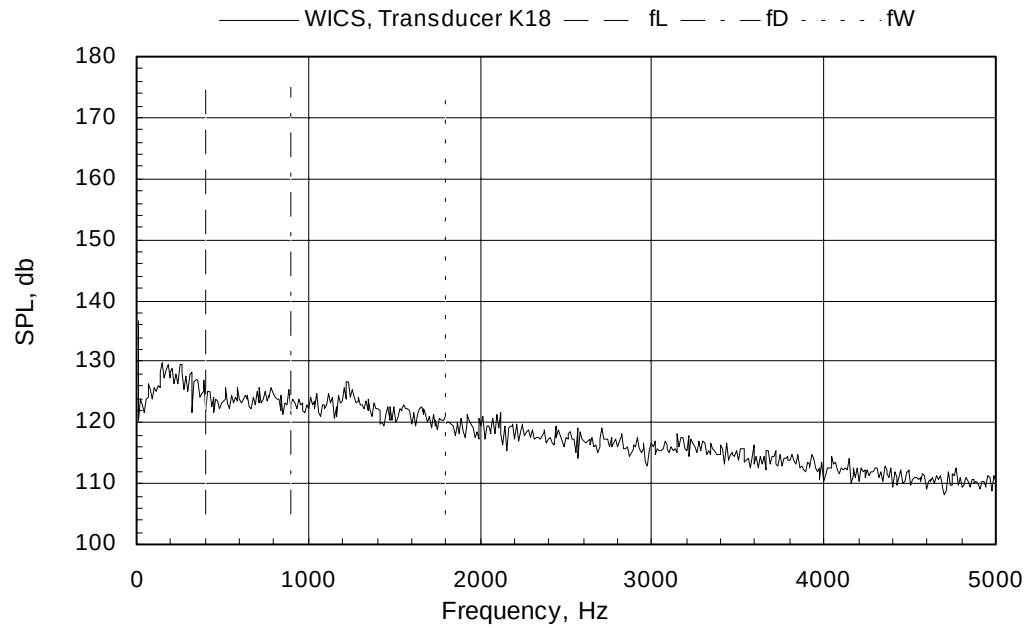

f. M_∞ = 5.04

Figure 18. Concluded.

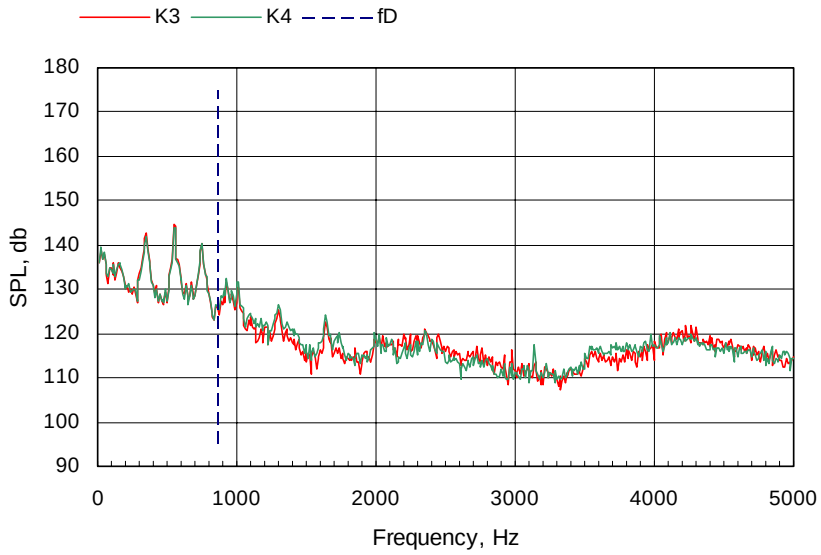

a. M_∞ = 0.60, Y = 0

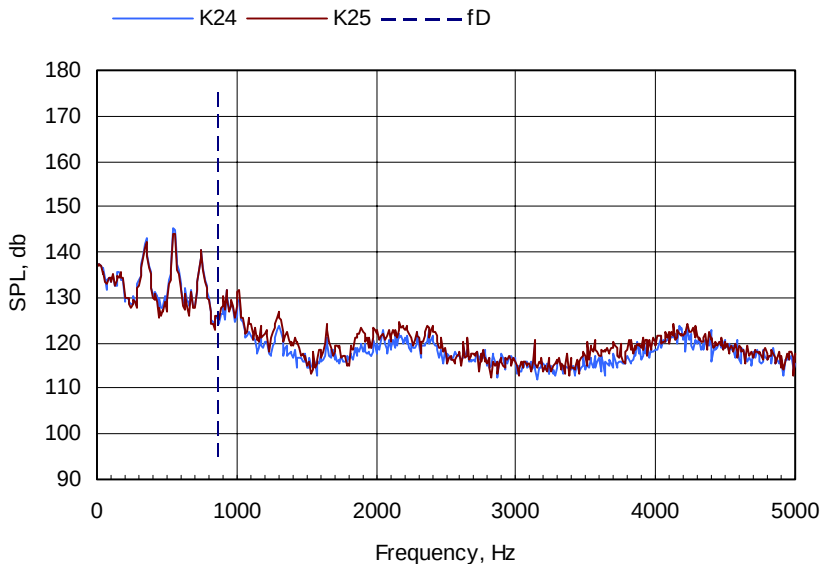

b. M_∞ = 0.60, 2Y/W = 0.95

Figure 19. Measured spectra along vertical planes on the upstream wall, L/D = 4.5.

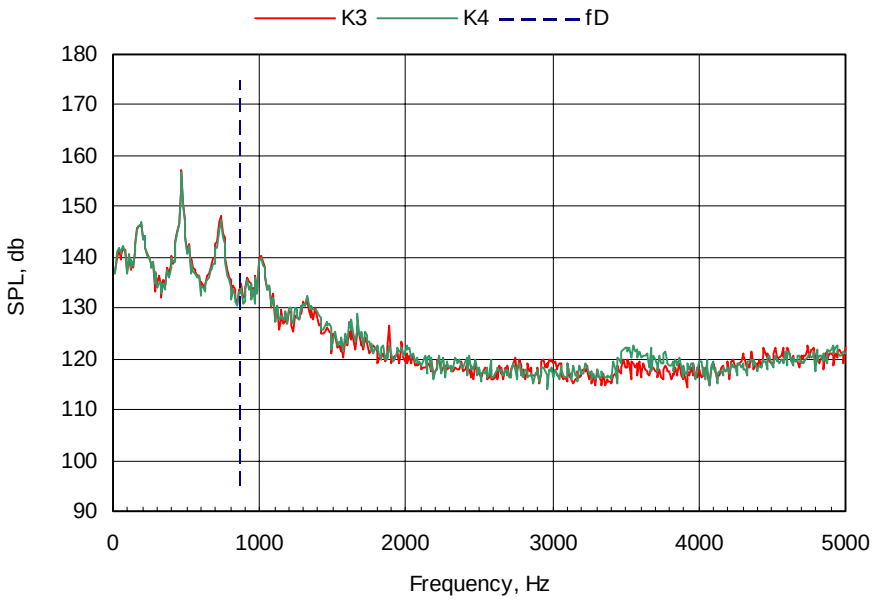

c. M_∞ = 0.95, Y = 0.95

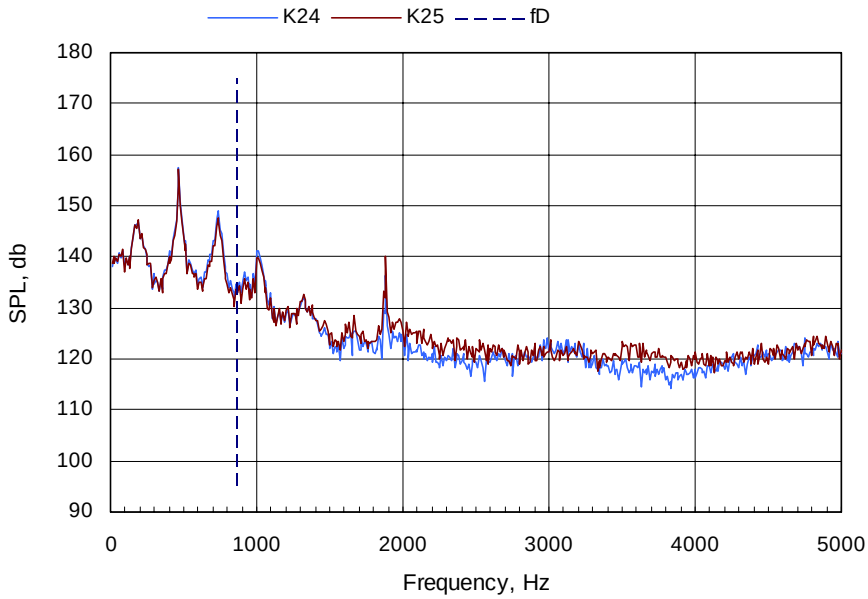

d. M_∞ = 0.95, 2Y/W = 0.95

Figure 19. Continued.

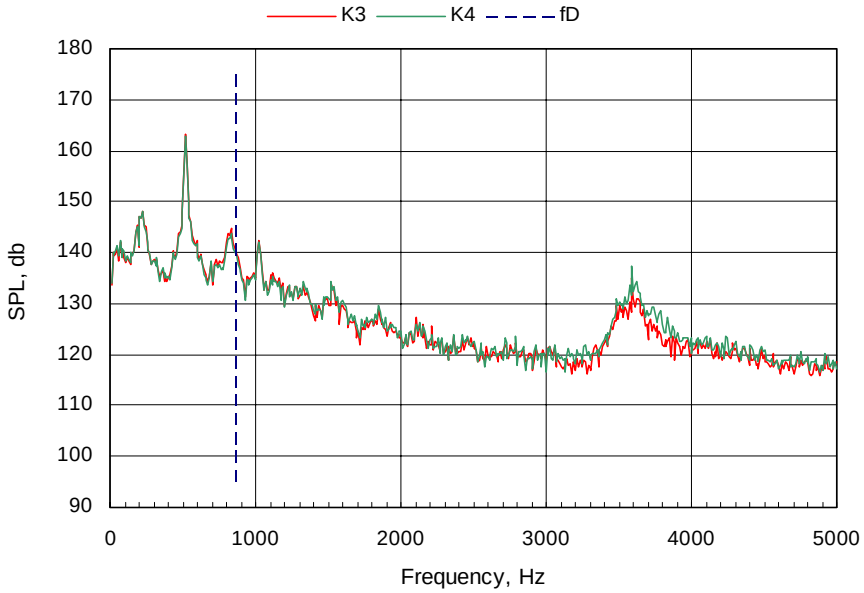

e. M_∞ = 1.20, Y = 0

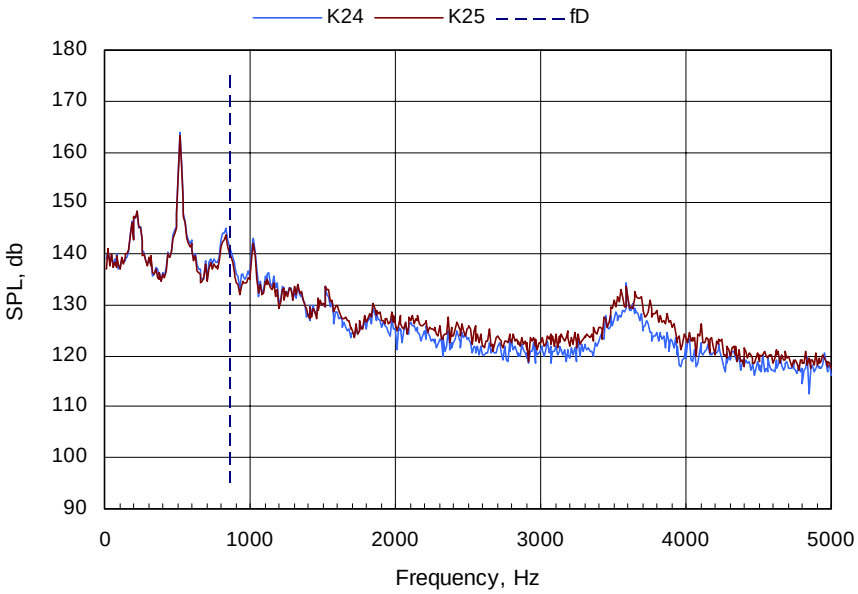

f. M_∞ = 1.20, 2Y/W = 0.95

Figure 19. Continued.

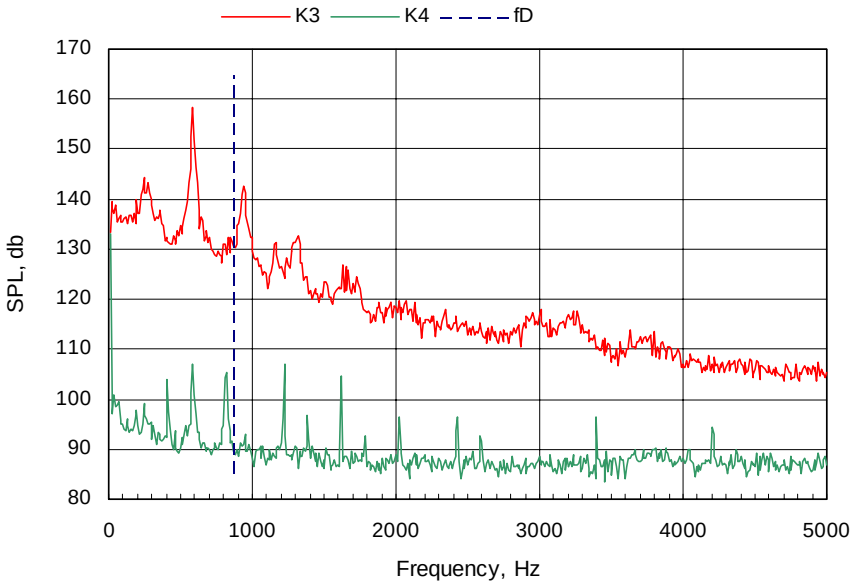

g. M_∞ = 1.50, Y = 0

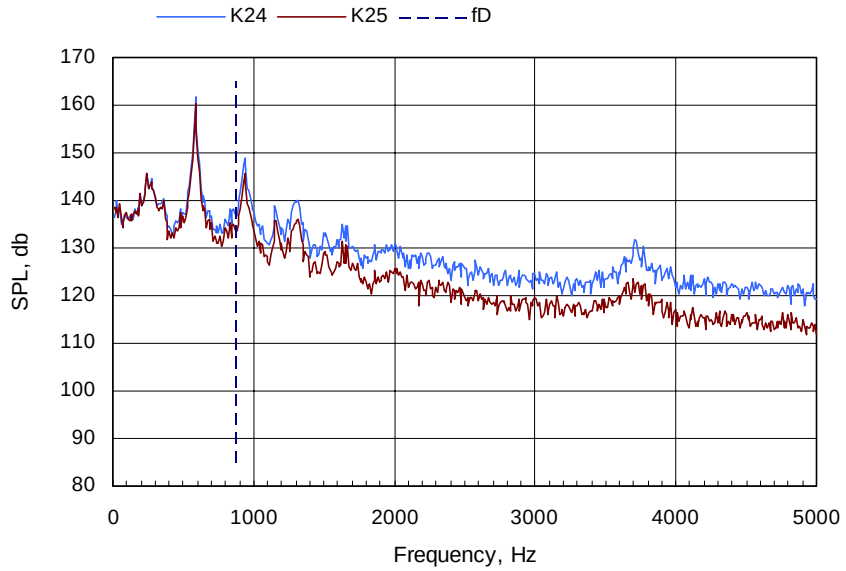

h. M_∞ = 1.50, 2Y/W = 0.95

Figure 19. Continued.

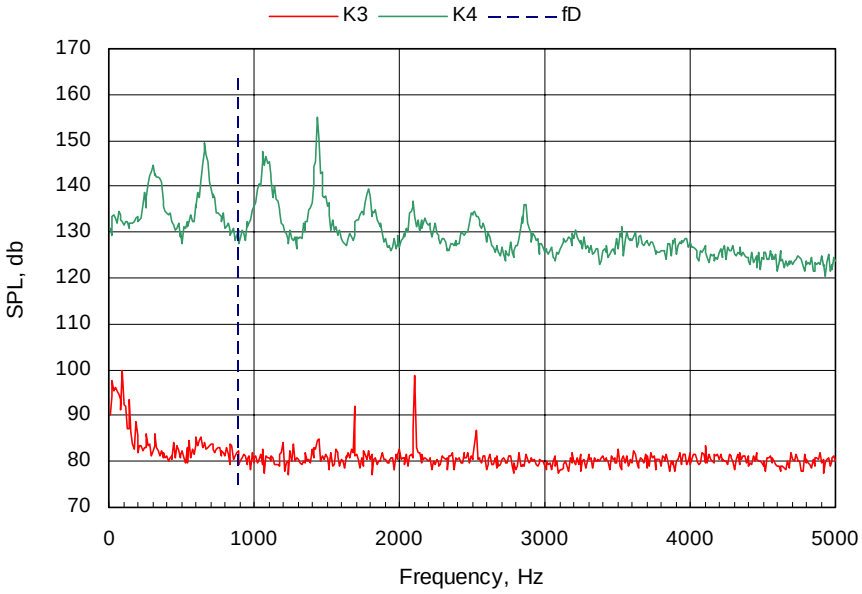

i. M_∞ = 2.00, Y = 0

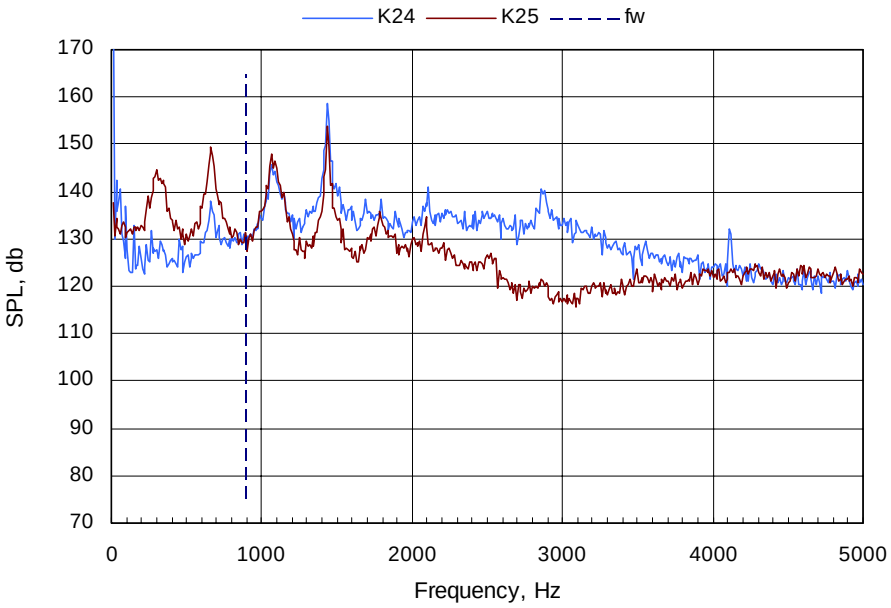

j. M_∞ = 2.00, 2Y/W = 0.95

Figure 19. Continued.

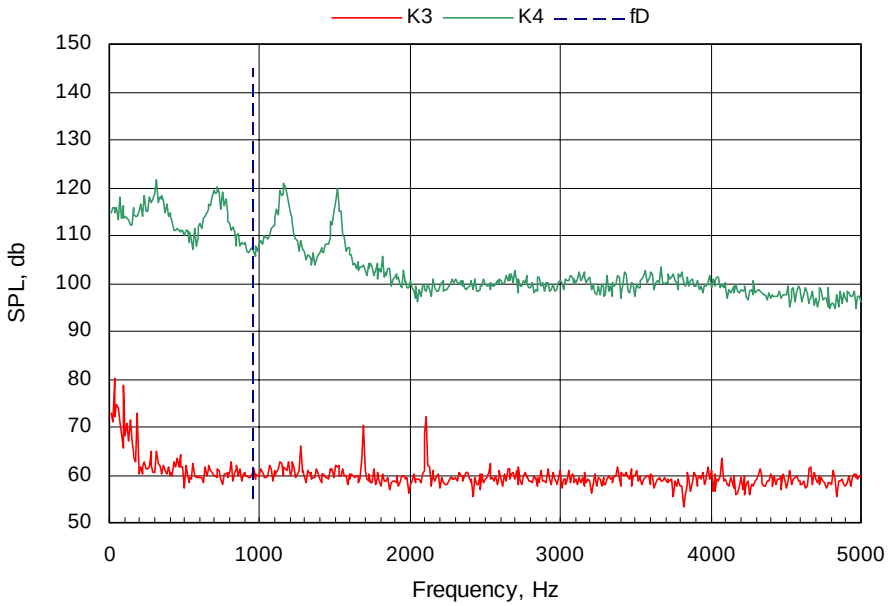

k. M_∞ = 3.51, Y = 0

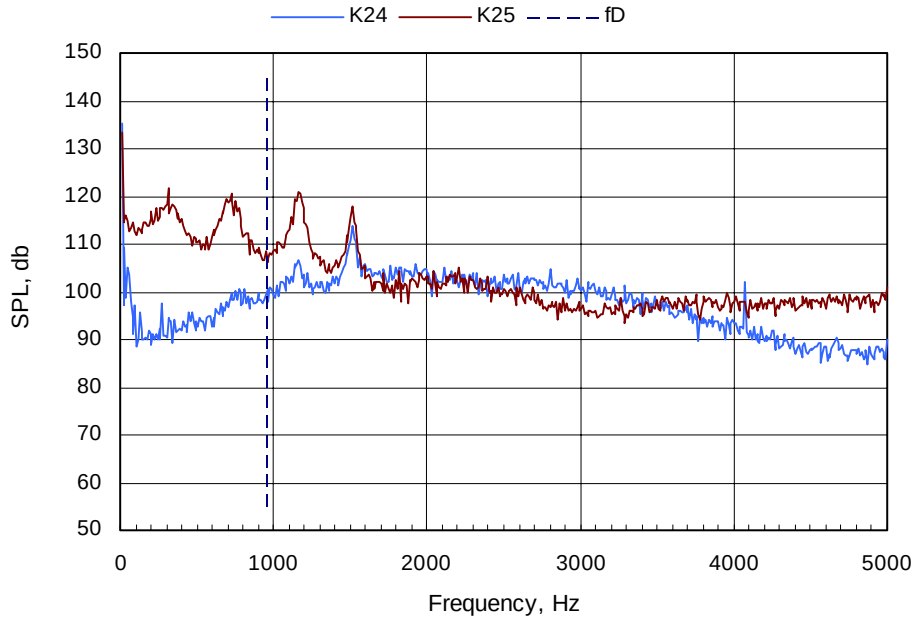

l. M_∞ = 3.51, 2Y/W = 0.95

Figure 19. Continued.

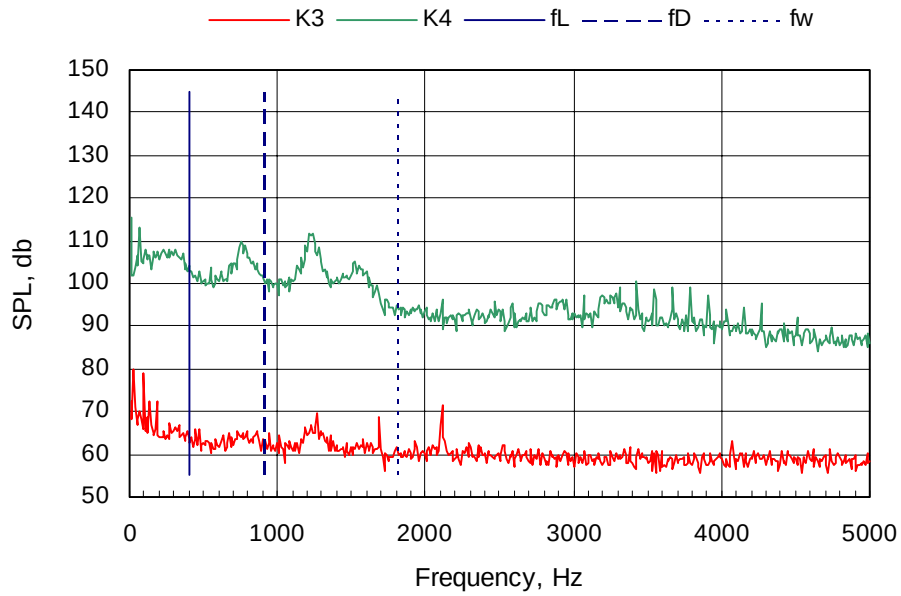

m. M_∞ = 5.04, Y = 0

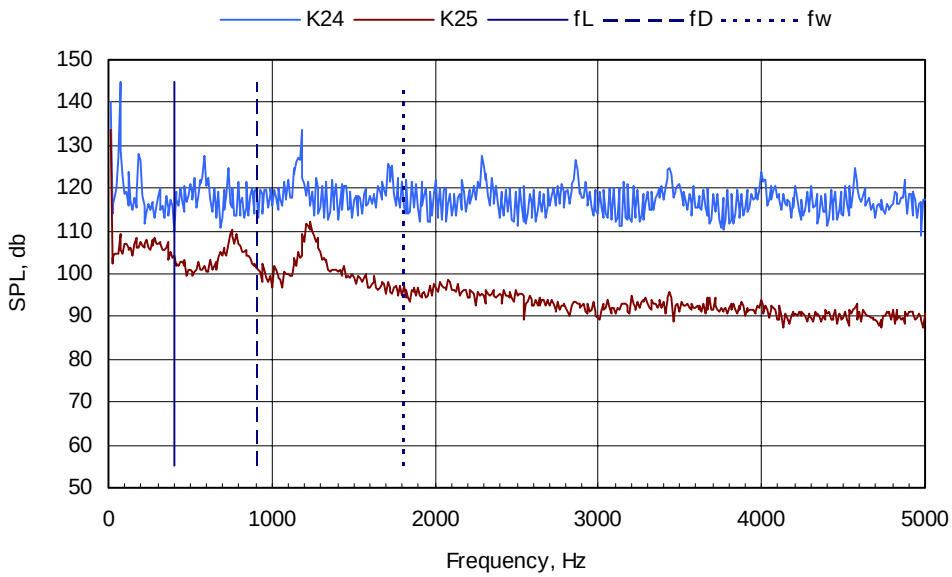

n. M_∞ = 5.04, 2Y/W = 0.95

Figure 19. Concluded.

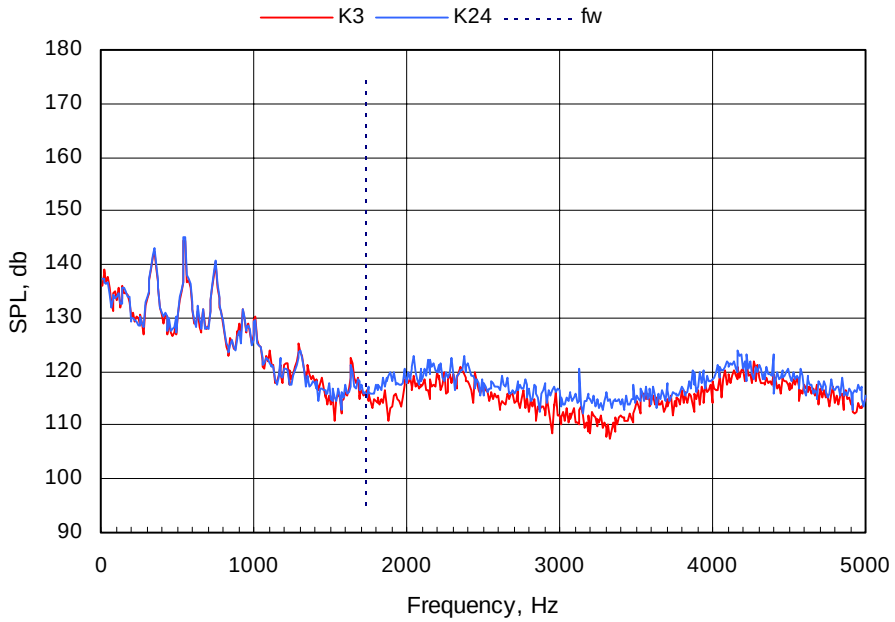

a. M_∞ = 0.60, Z/D = –0.2

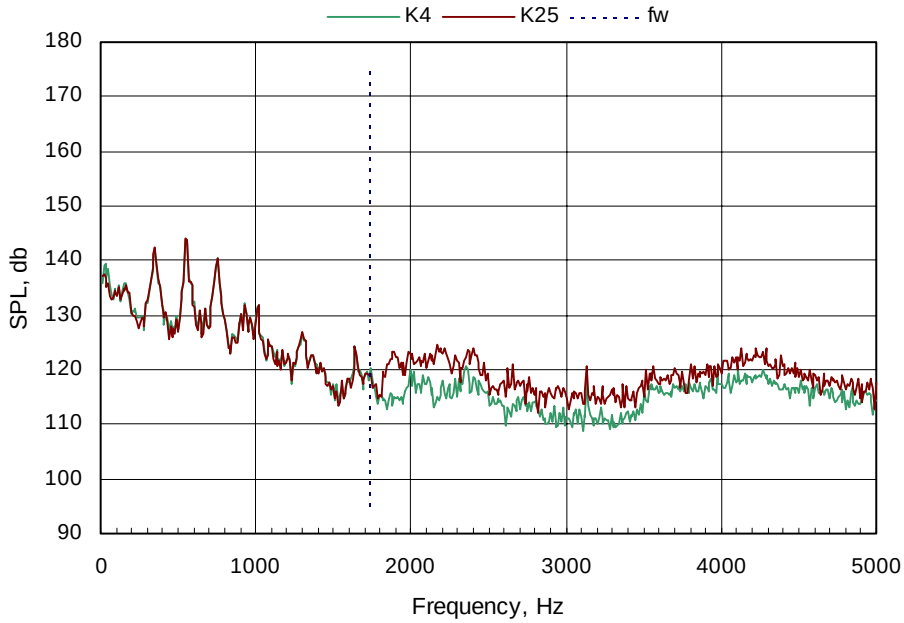

b. M_∞ = 0.60, Z/D = –0.49

Figure 20. Measured spectra in the Y direction on the upstream wall, L/D = 4.5.

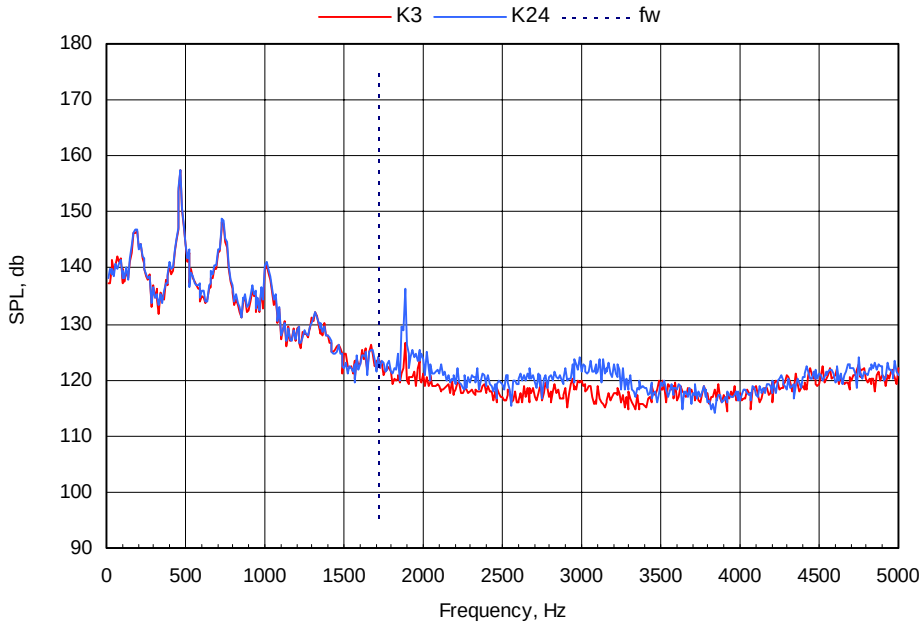

c. M_∞ = 0.95, Z/D = –0.2

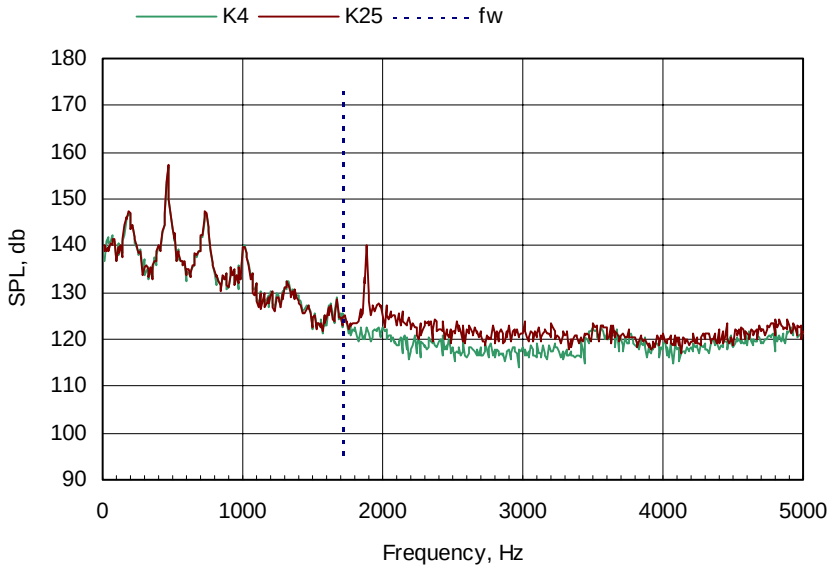

d. M_∞ = 0.95, Z/D = –0.49

Figure 20. Continued.

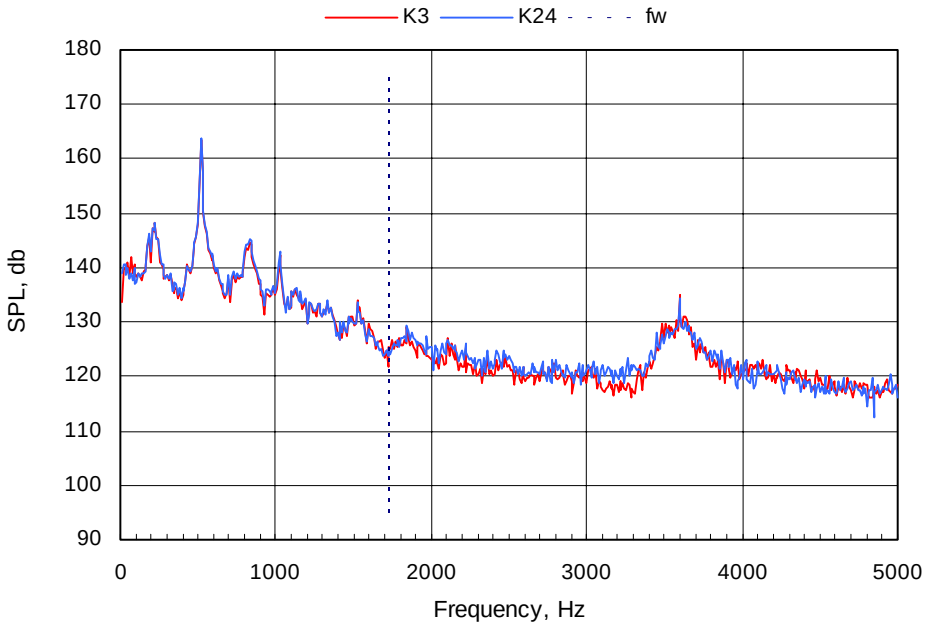

e. M_∞ = 1.20, Z/D = –0.2

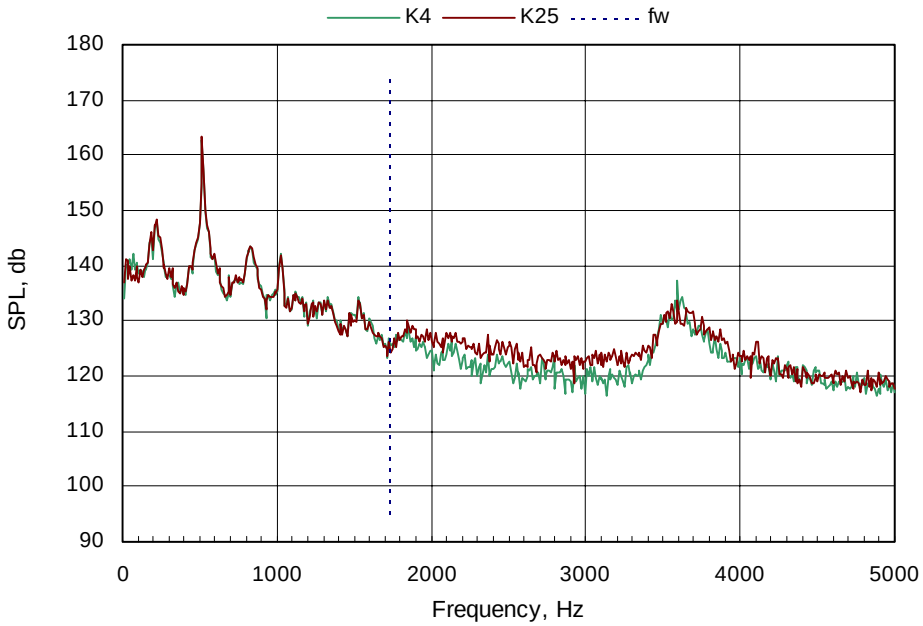

f. M_∞ = 1.20, Z/D = –0.49

Figure 20. Continued.

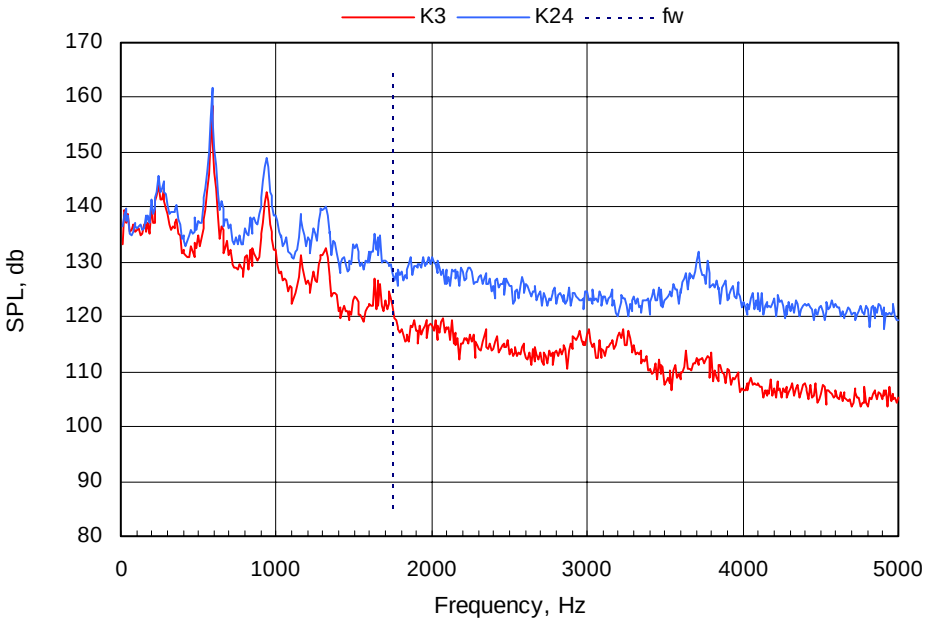

g. M_∞ = 1.50, Z/D = –0.2

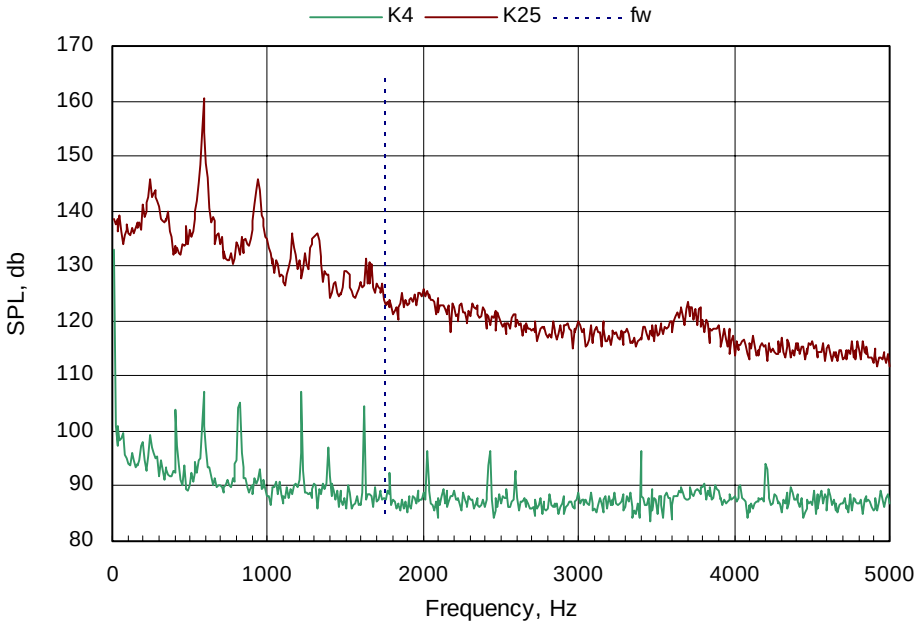

h. M_∞ = 1.50, Z/D = –0.49

Figure 20. Continued.

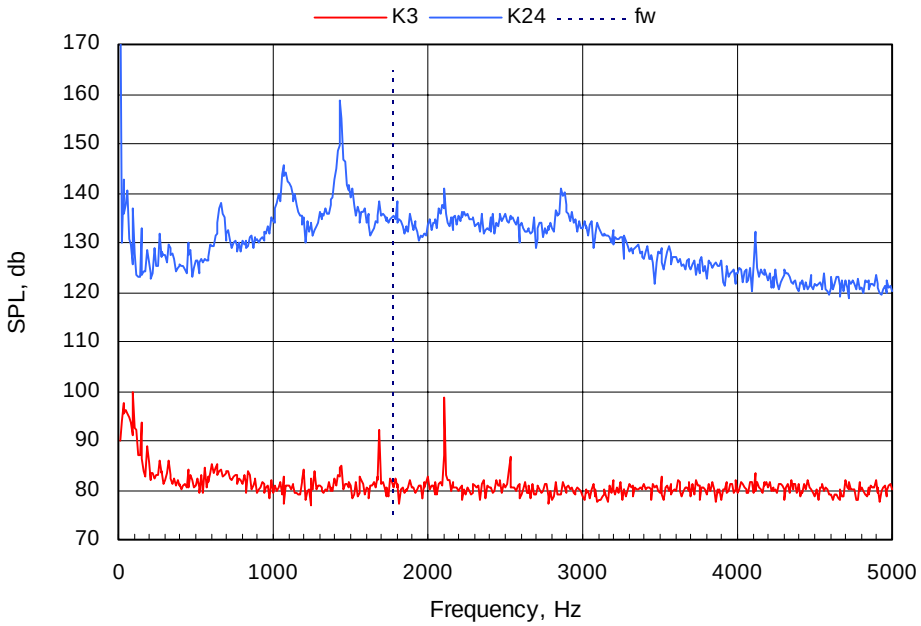

i. M_∞ = 2.00, Z/D = –0.2

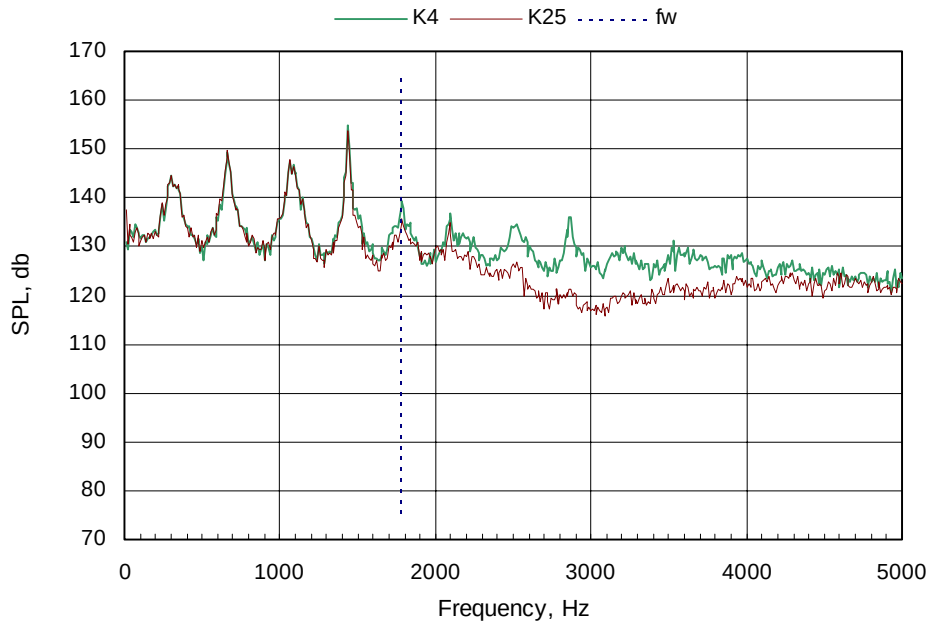

j. M_∞ = 2.00, Z/D = –0.49

Figure 20. Continued.

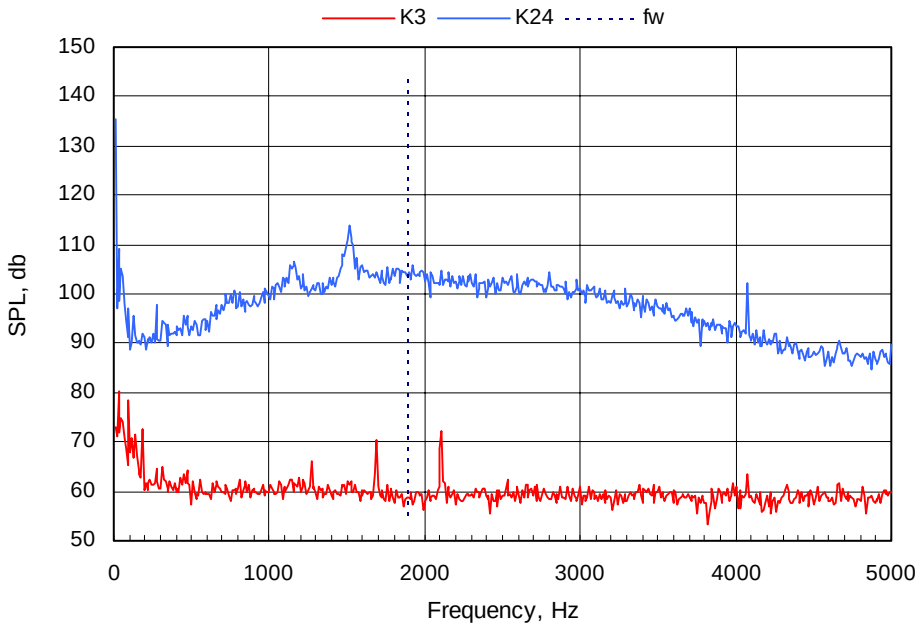

k. M_∞ = 3.51, Z/D = –0.2

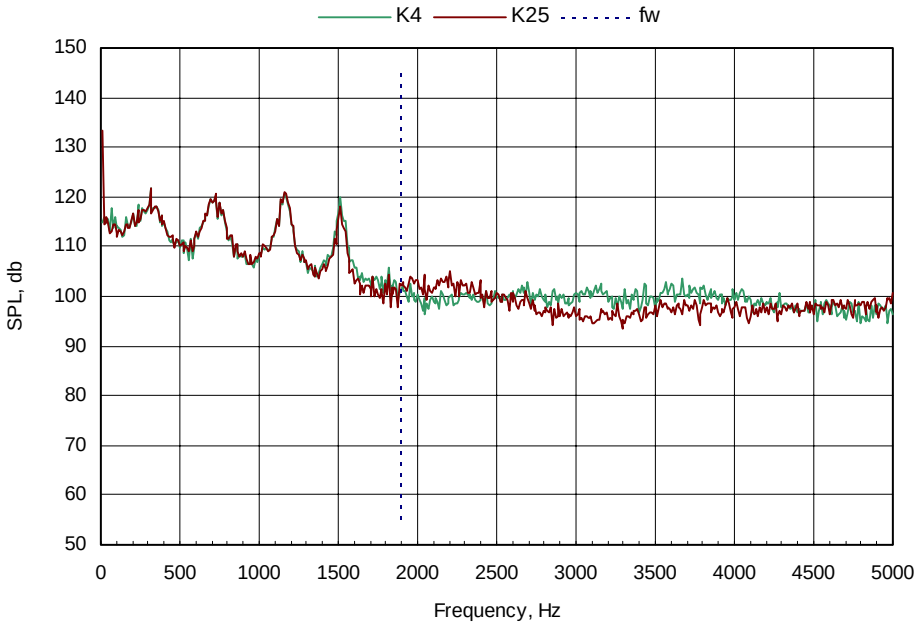

l. M_∞ = 3.51, Z/D = –0.49

Figure 20. Continued.

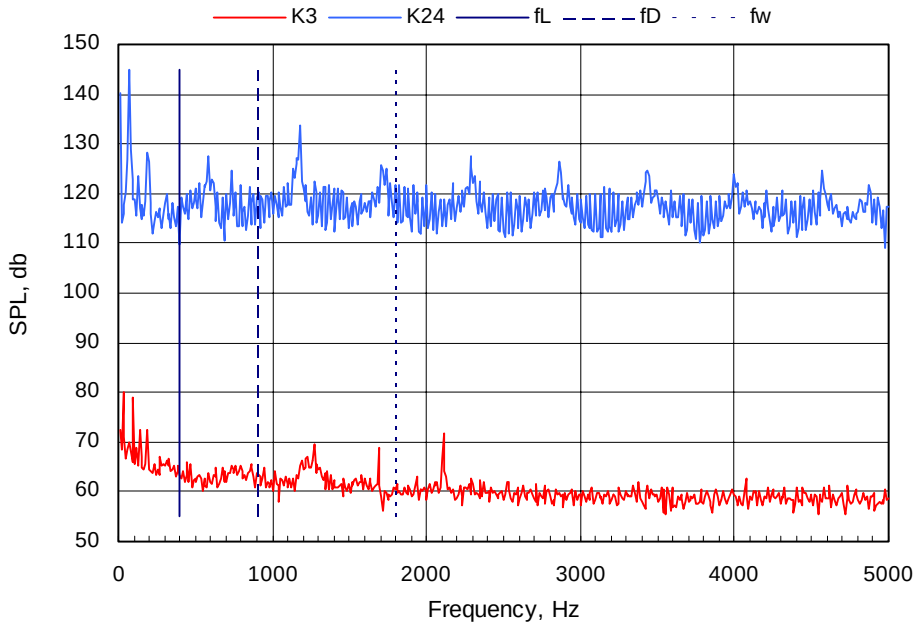

m. M_∞ = 5.04, Z/D = –0.2

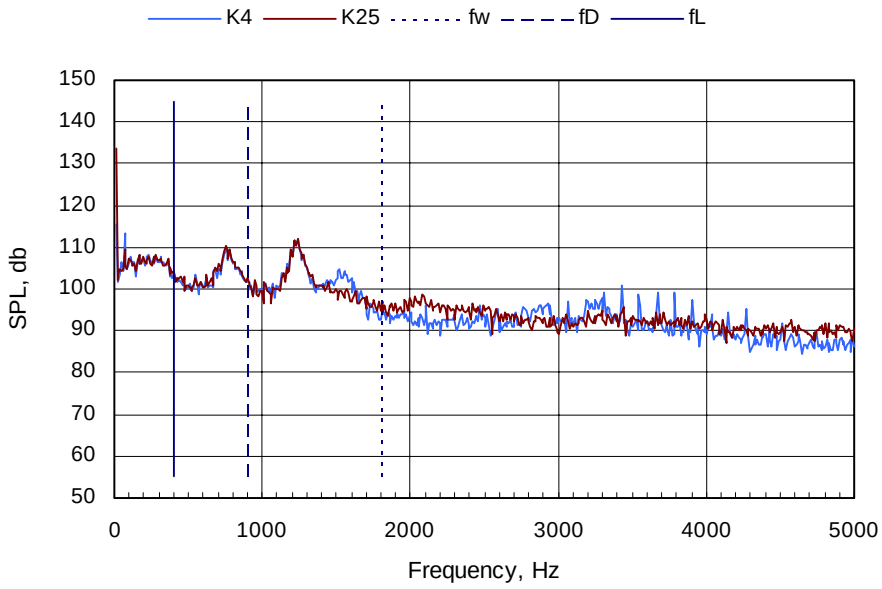

n. M_∞ = 5.04, Z/D = –0.49

Figure 20. Concluded.

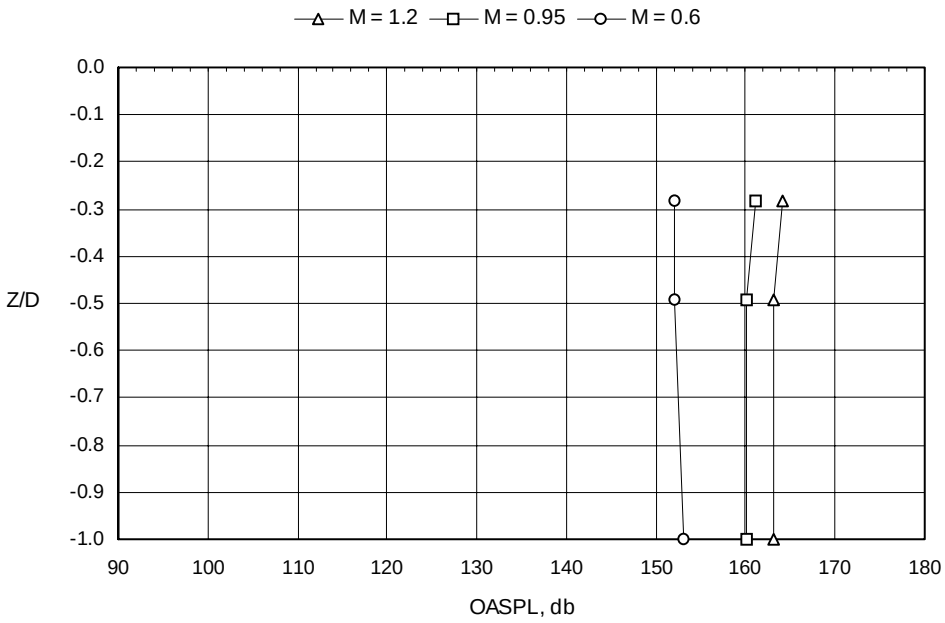

a. Along the vertical centerline, Y = 0

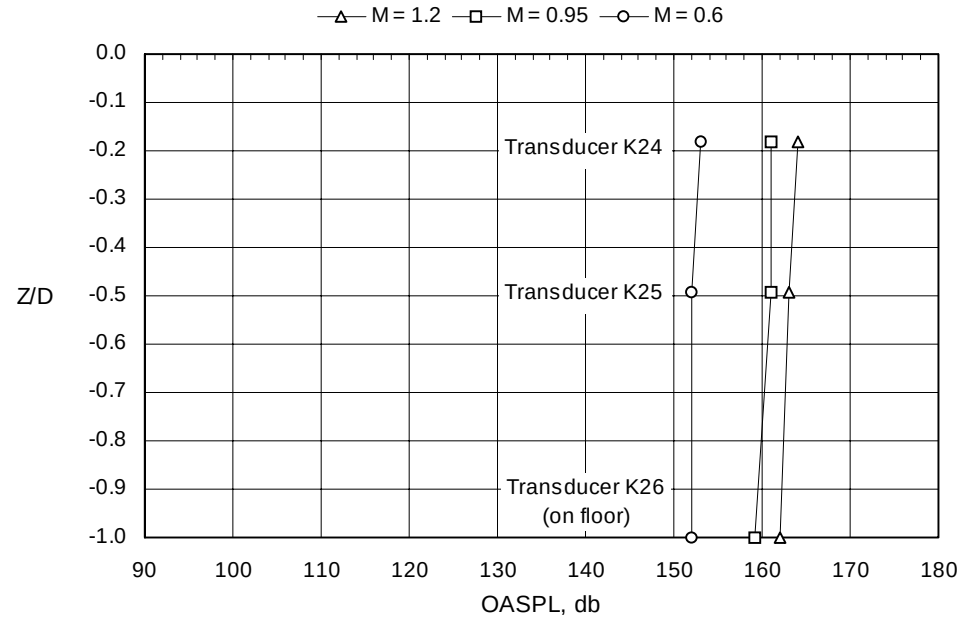

b. Along a vertical line near the corner, 2Y/W = 0.95

Figure 21. OASPL on the upstream wall of an L/D = 4.5 cavity.

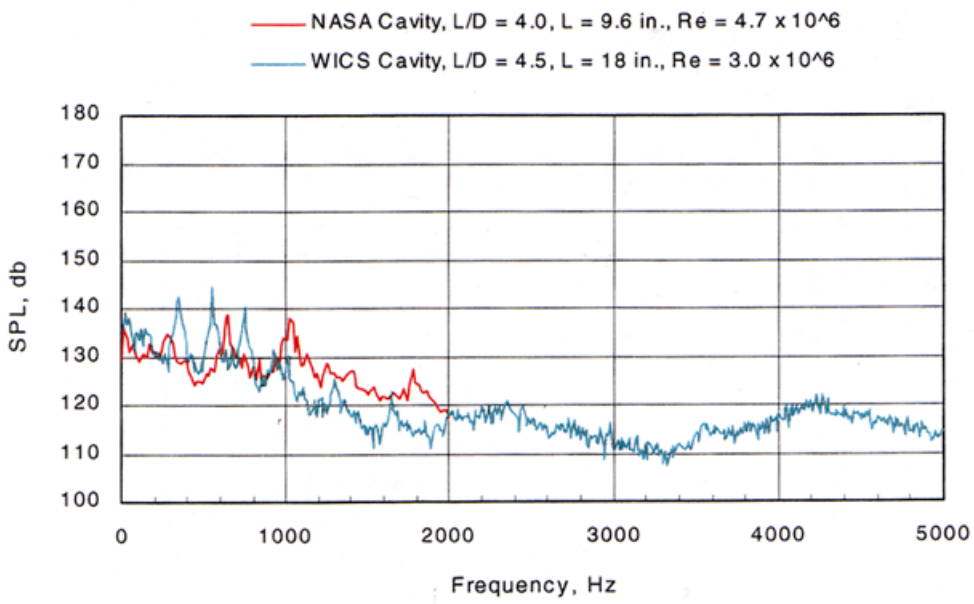

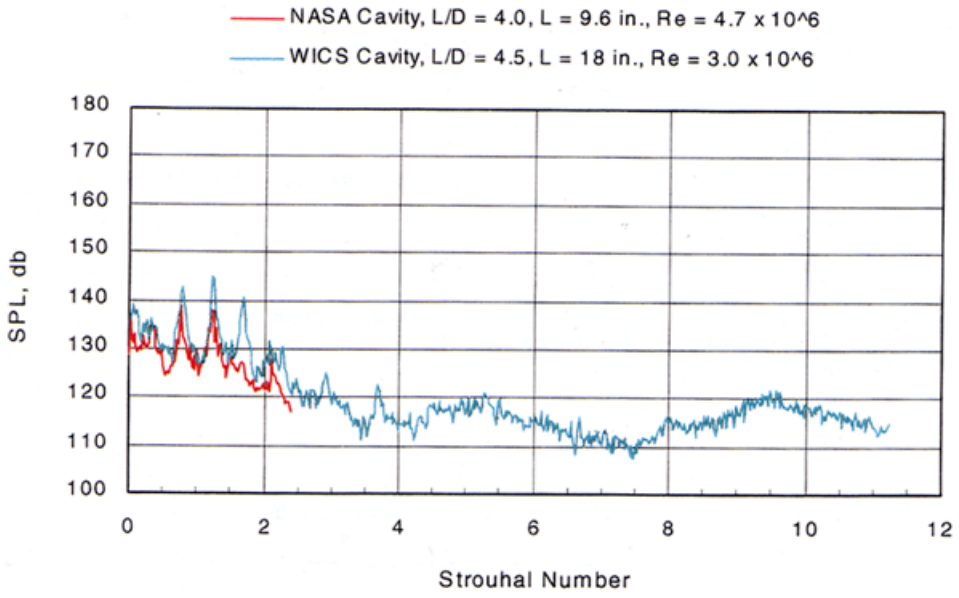

a. $M_\infty = 0.60$

Figure 22. Comparison of spectra on the upstream wall of two independent cavities.

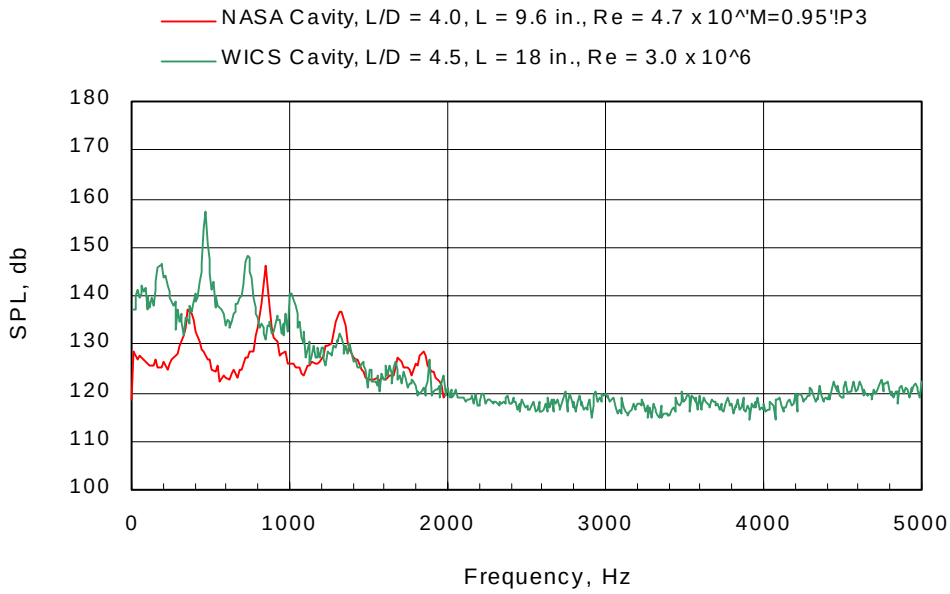

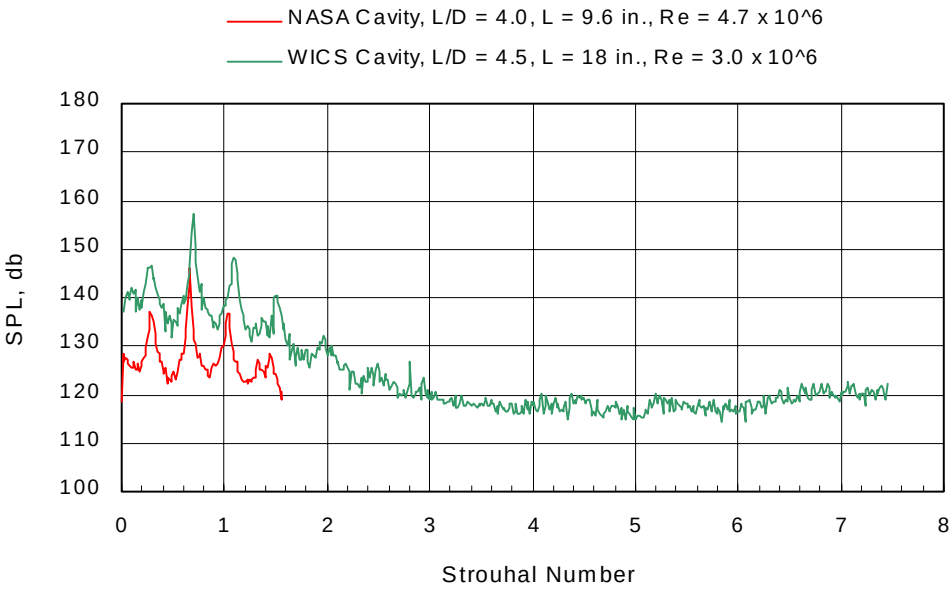

b. $M_\infty = 0.95$

Figure 22. Concluded.

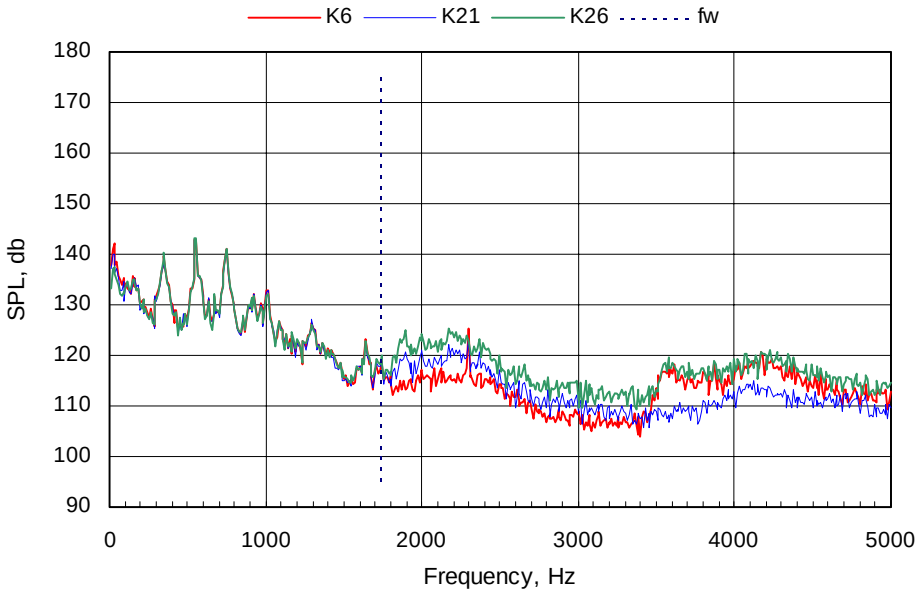

a. M_∞ = 0.60

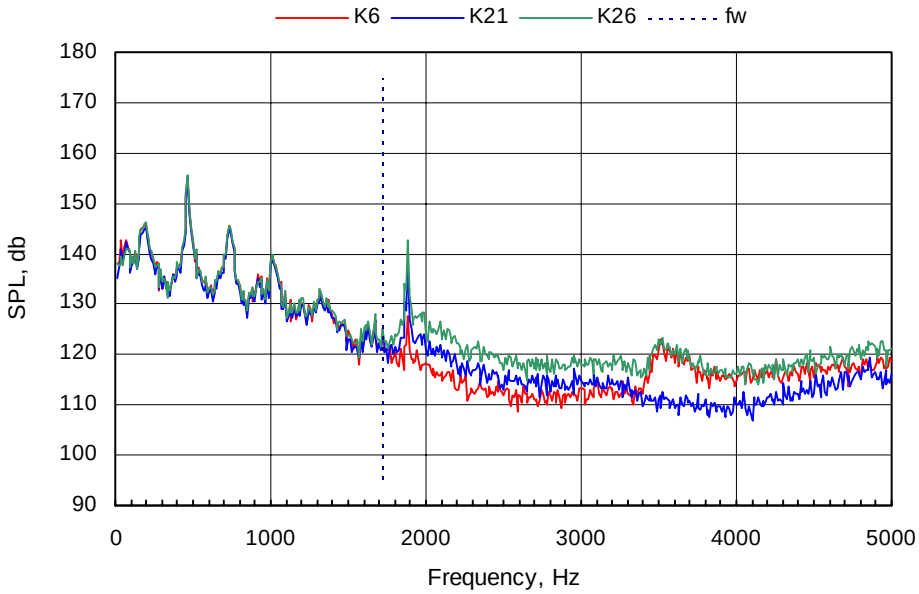

b. M_∞ = 0.95

Figure 23. Measured spectra along lateral planes on the floor of an L/D = 4.5 cavity, X/L = 0.06.

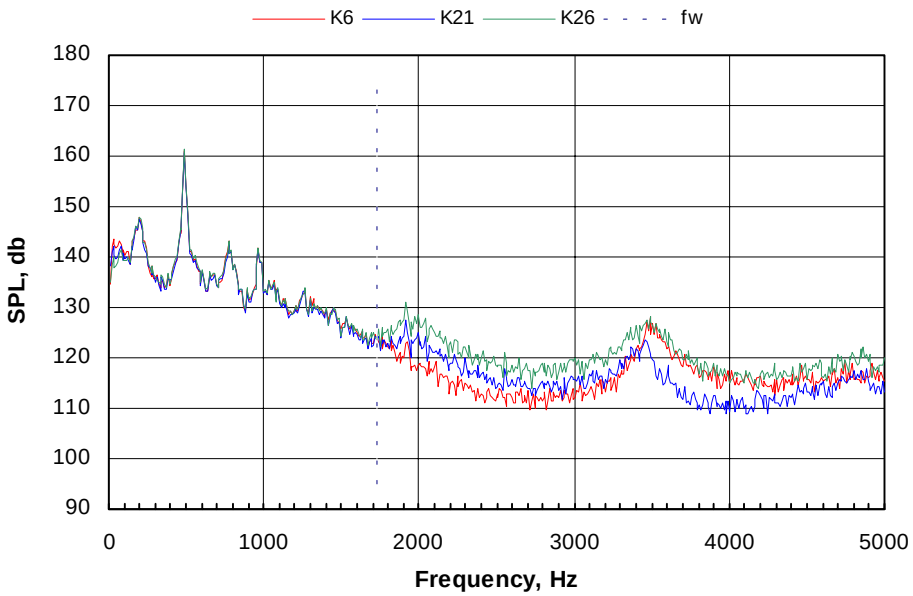

c. M_∞ = 1.05

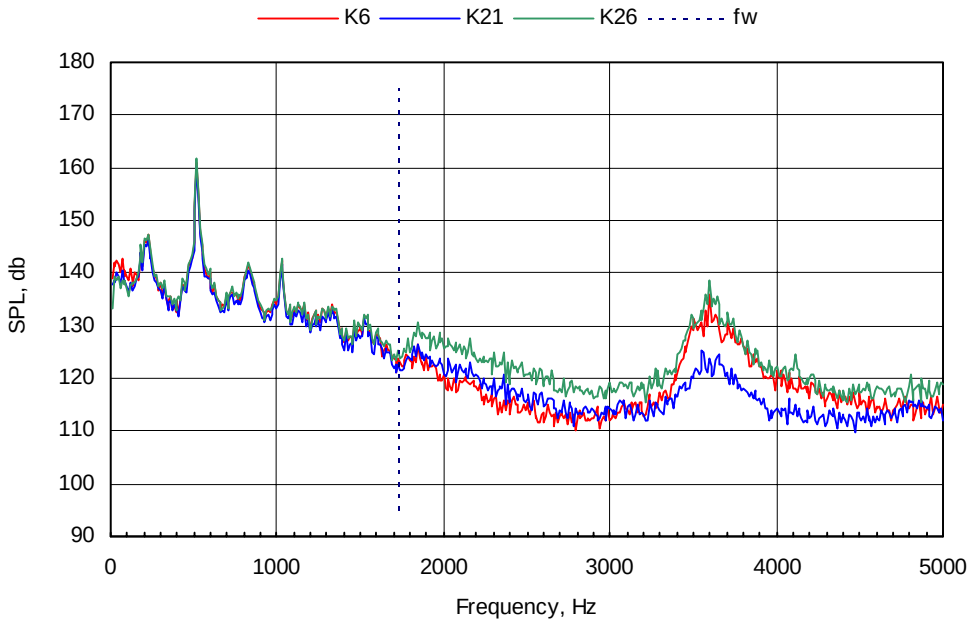

d. M_∞ = 1.20

Figure 23. Continued.

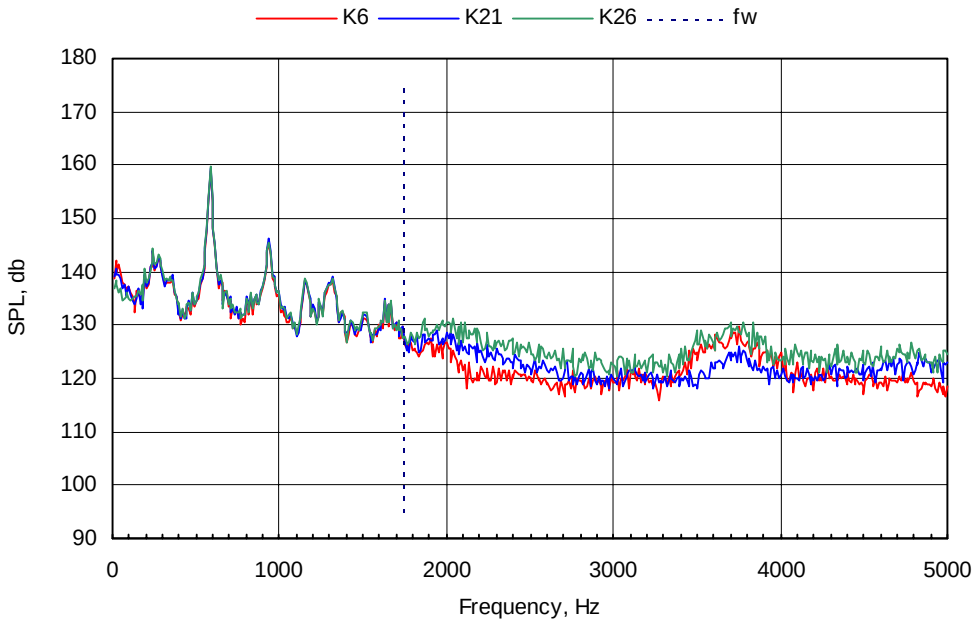

e. M_∞ = 1.50

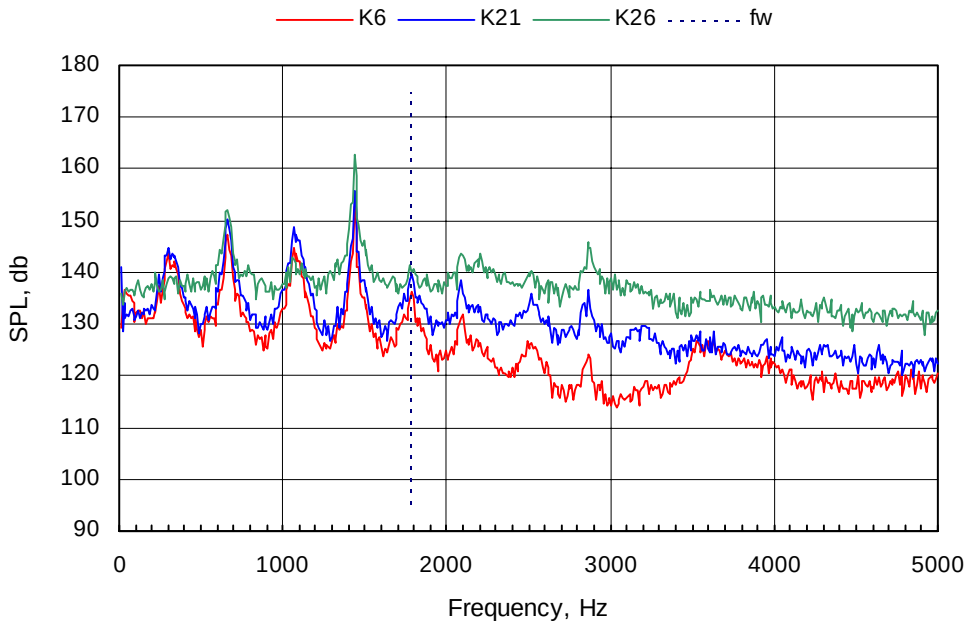

f. M_∞ = 2.00

Figure 23. Continued.

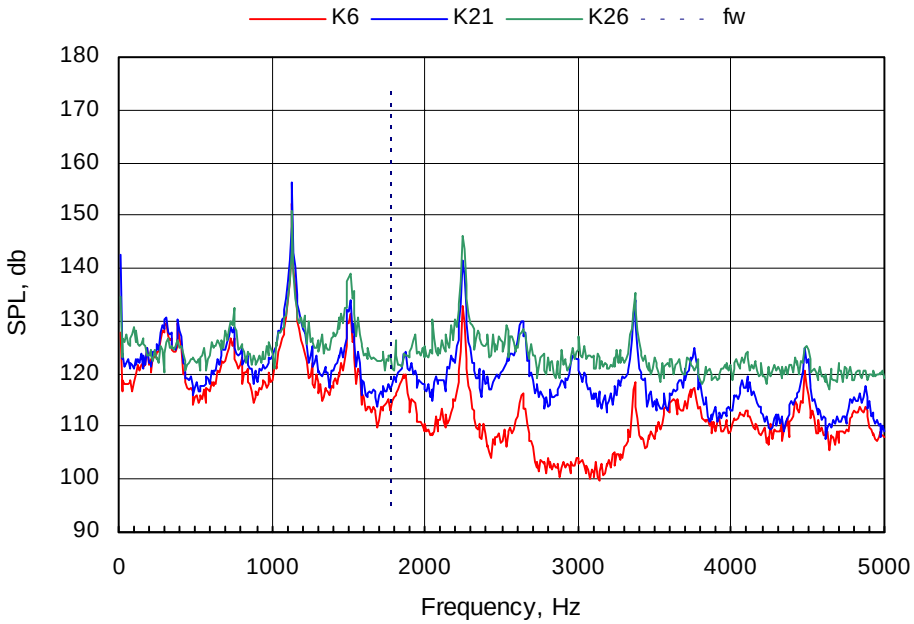

g. M_∞ = 2.75

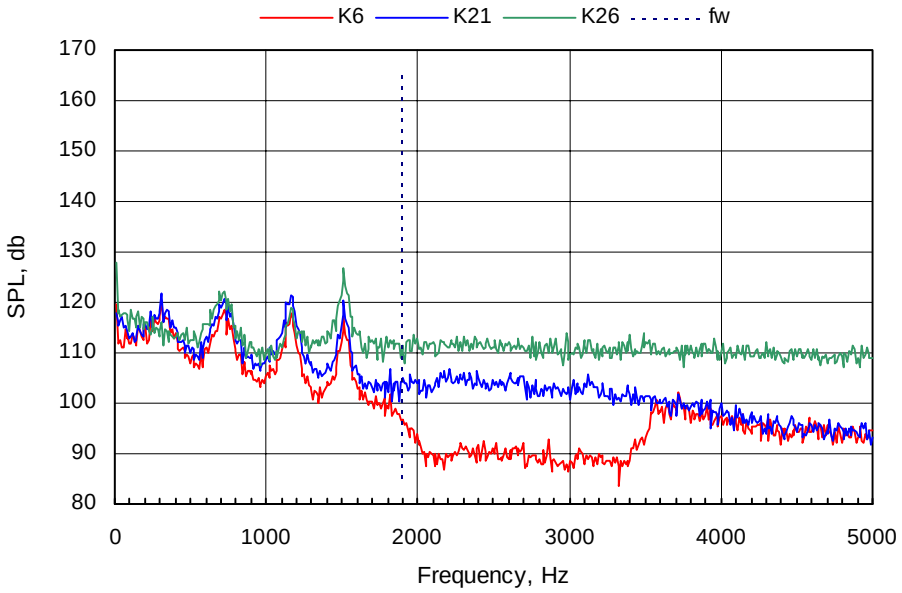

h. M_∞ = 3.51

Figure 23. Continued.

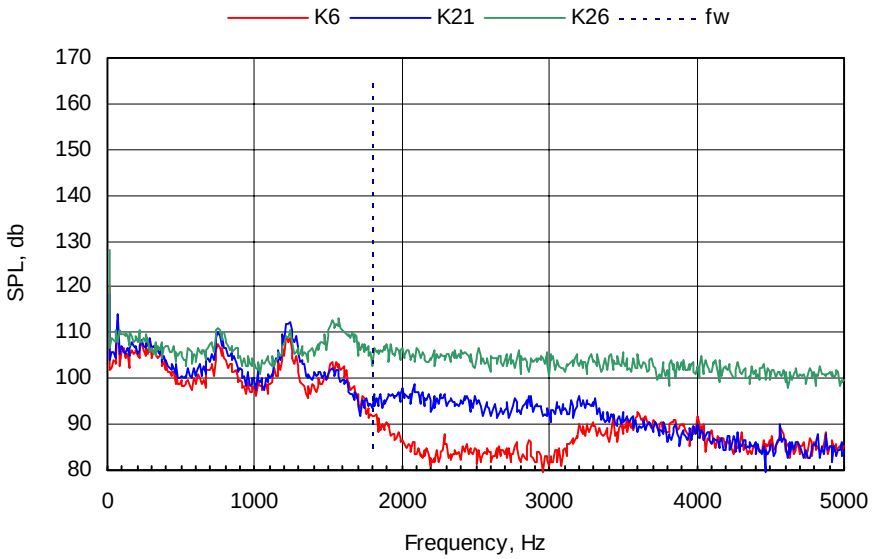

i. M_∞ = 5.04

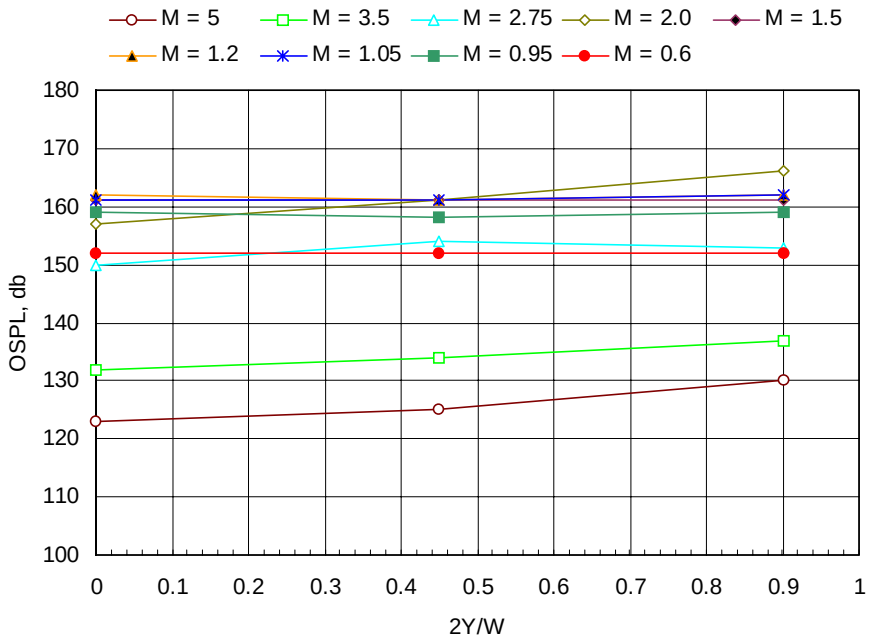

j. Overall sound pressure level laterally across the floor at X/L = 0.06

Figure 23. Concluded.

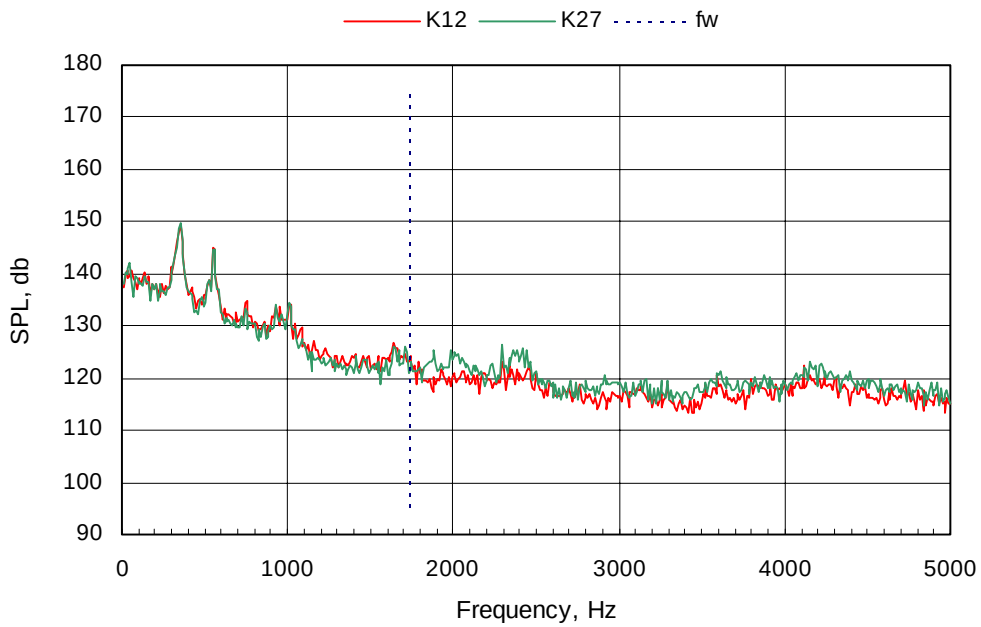

a. M_∞ = 0.60

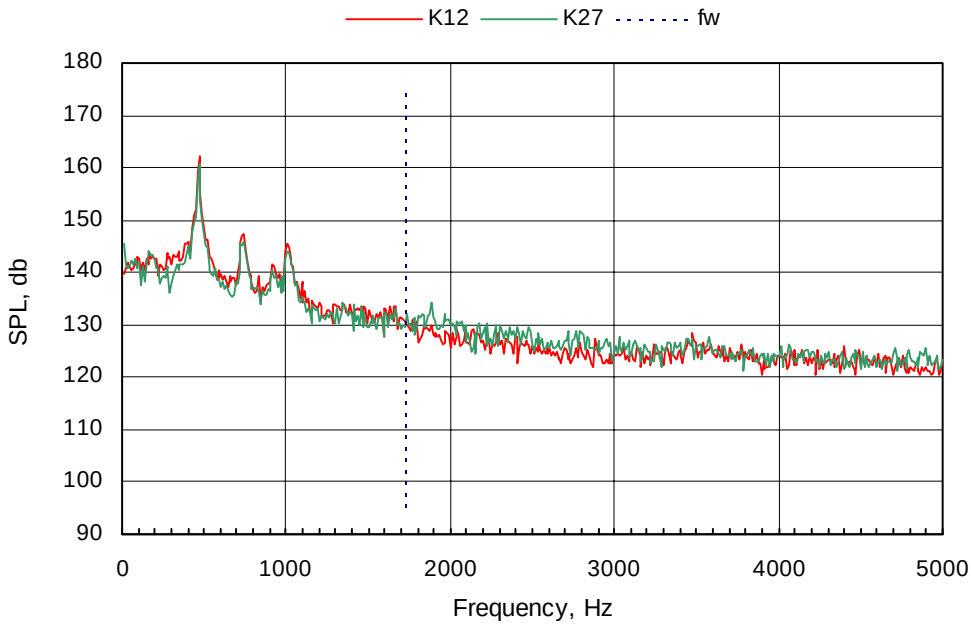

b. M_∞ = 0.95

Figure 24. Measured spectra along lateral planes on the floor of an L/D = 4.5 cavity, X/L = 0.51.

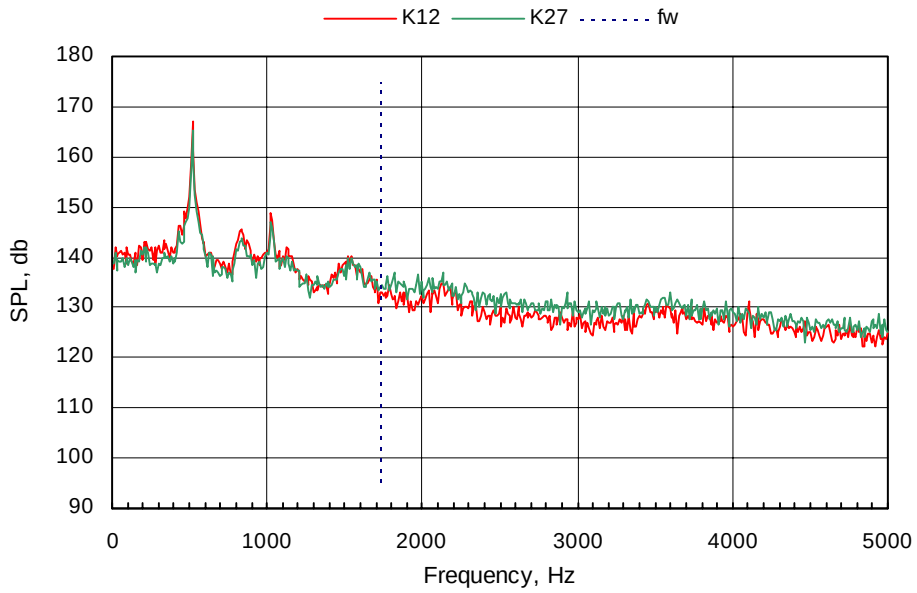

c. M_∞ = 1.05

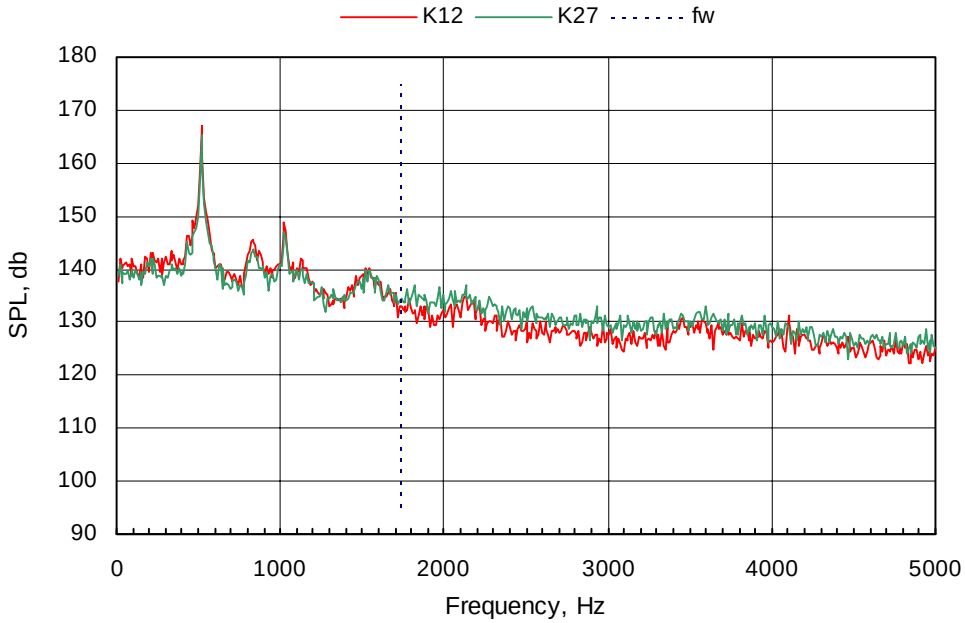

d. M_∞ = 1.20

Figure 24. Continued.

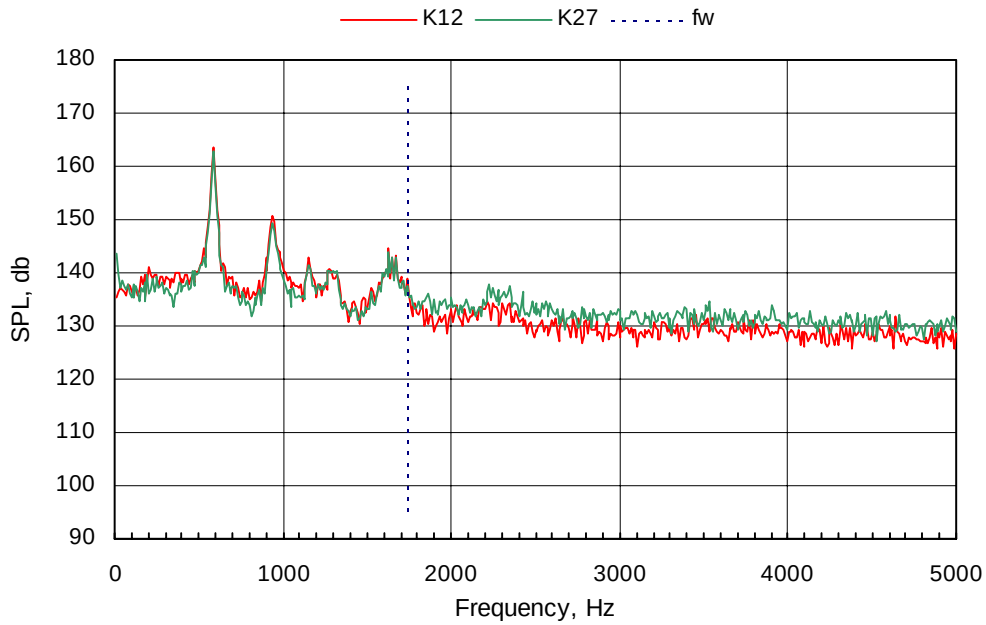

e. M_∞ = 1.50

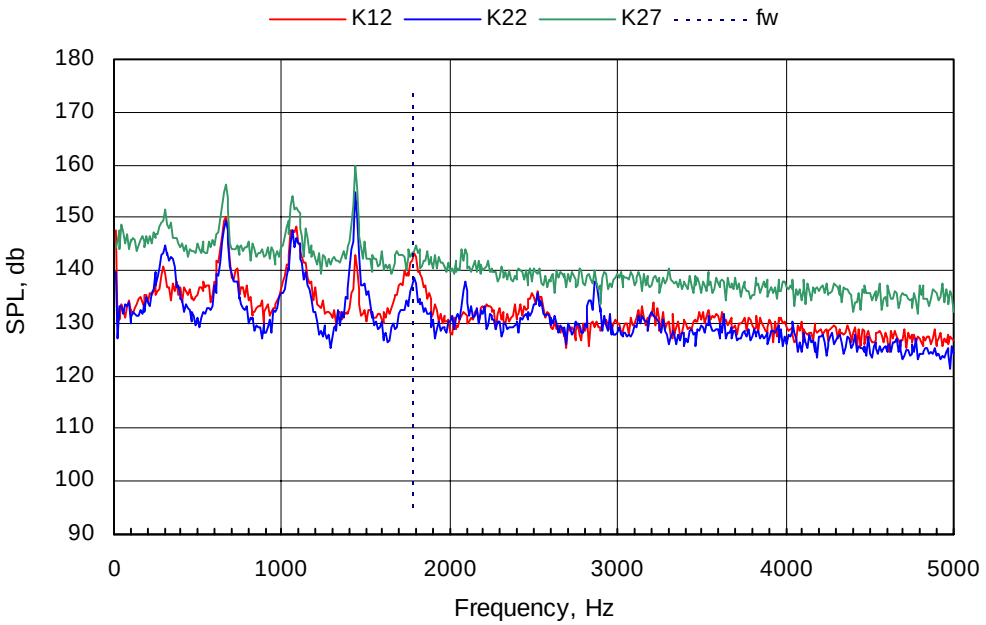

f. M_∞ = 2.00

Figure 24. Continued.

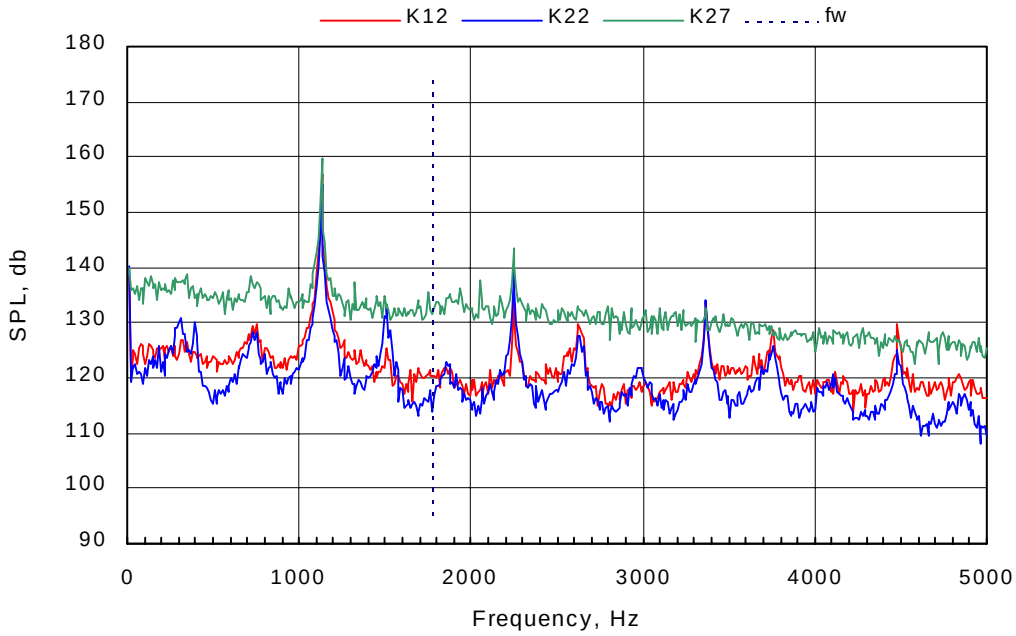

g. M_∞ = 2.75

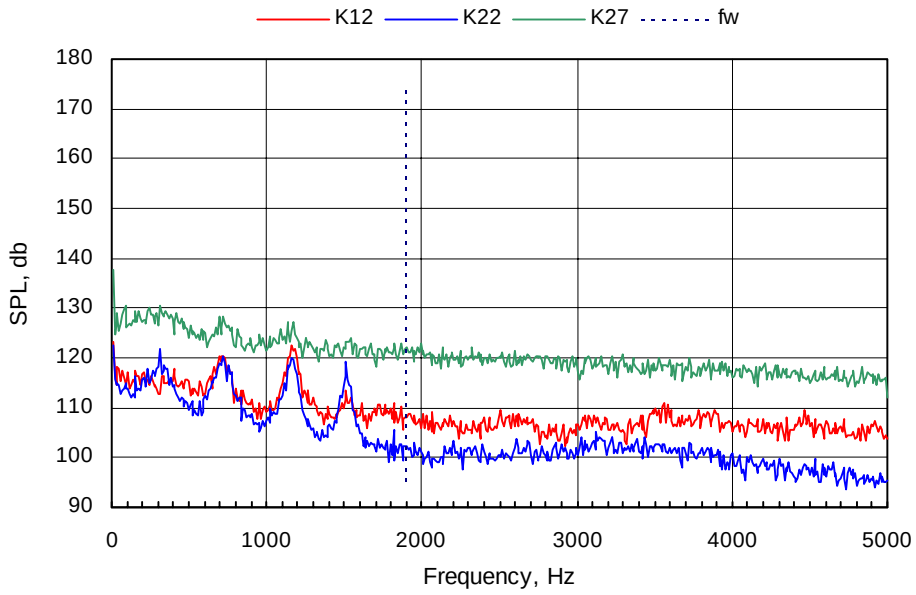

h. M_∞ = 3.51

Figure 24. Continued.

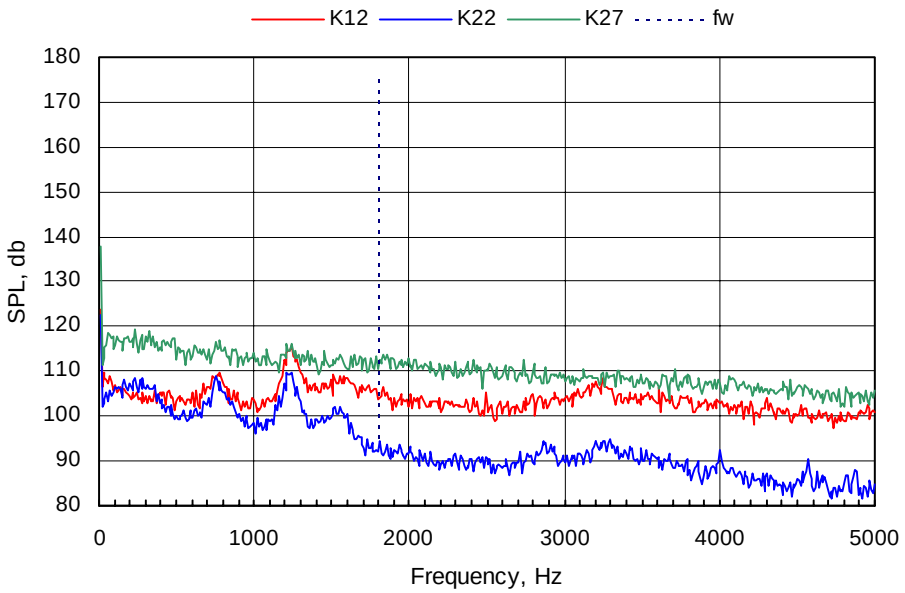

i. M_∞ = 5.04

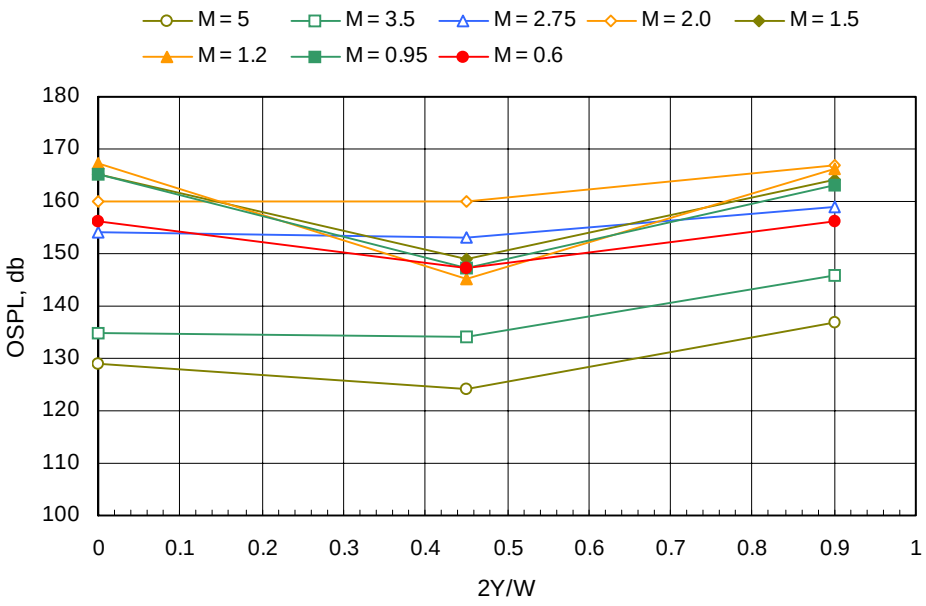

j. Overall sound pressure level laterally across the floor at X/L = 0.51

Figure 24. Concluded.

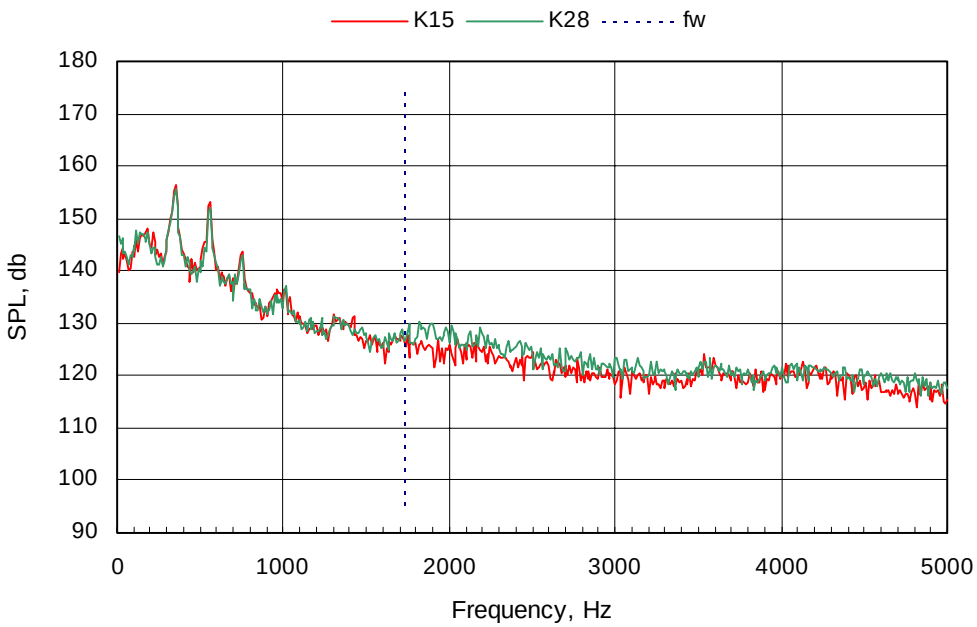

a. $M_\infty = 0.60$

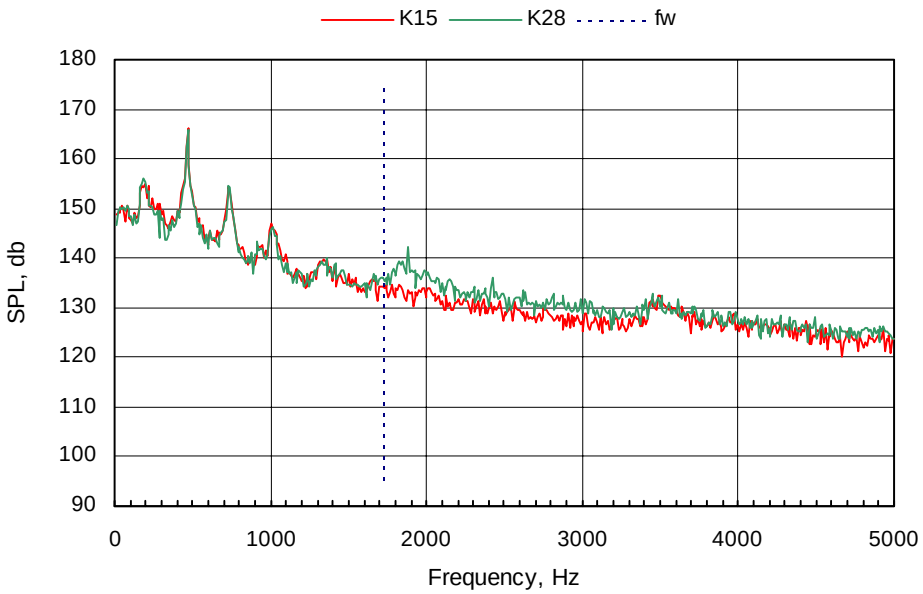

b. $M_\infty = 0.95$

Figure 25. Measured spectra along lateral planes on the floor of an L/D = 45 cavity, X/L = 0.94.

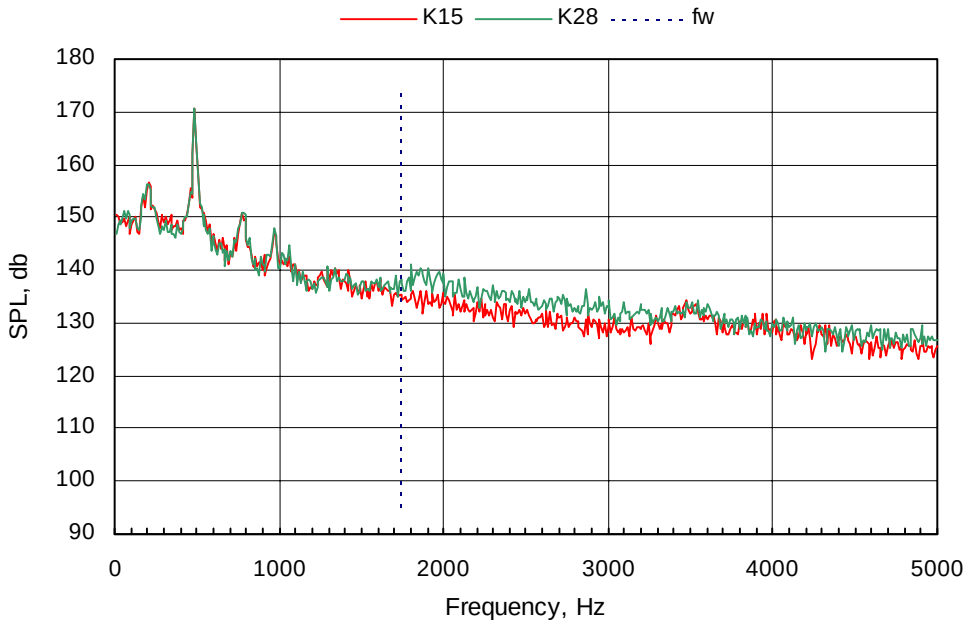

c. M_∞ = 1.05

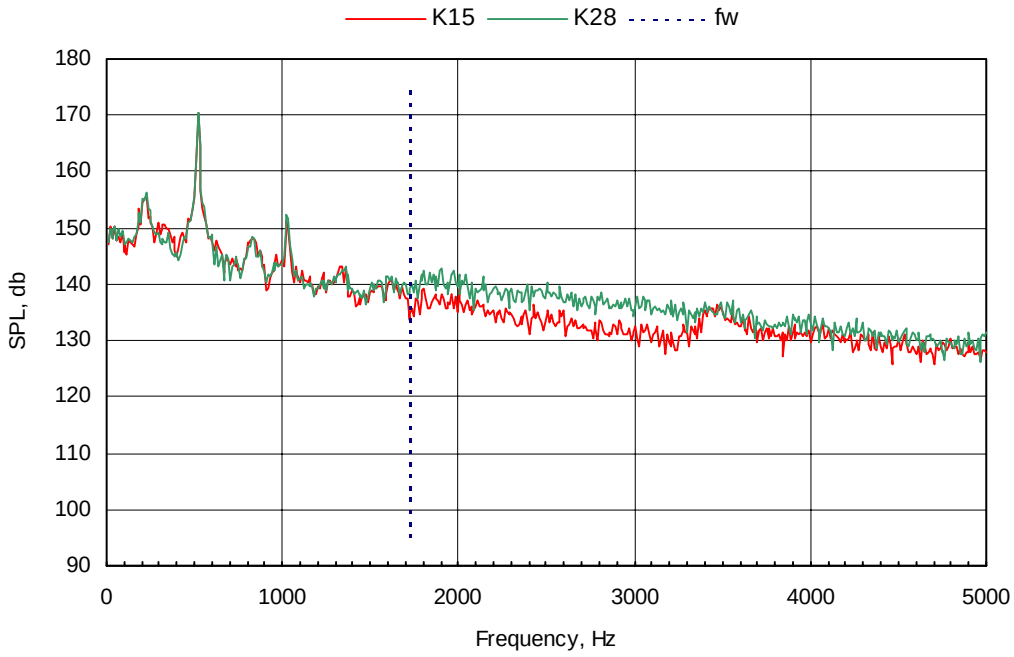

d. M_∞ = 1.20

Figure 25. Continued.

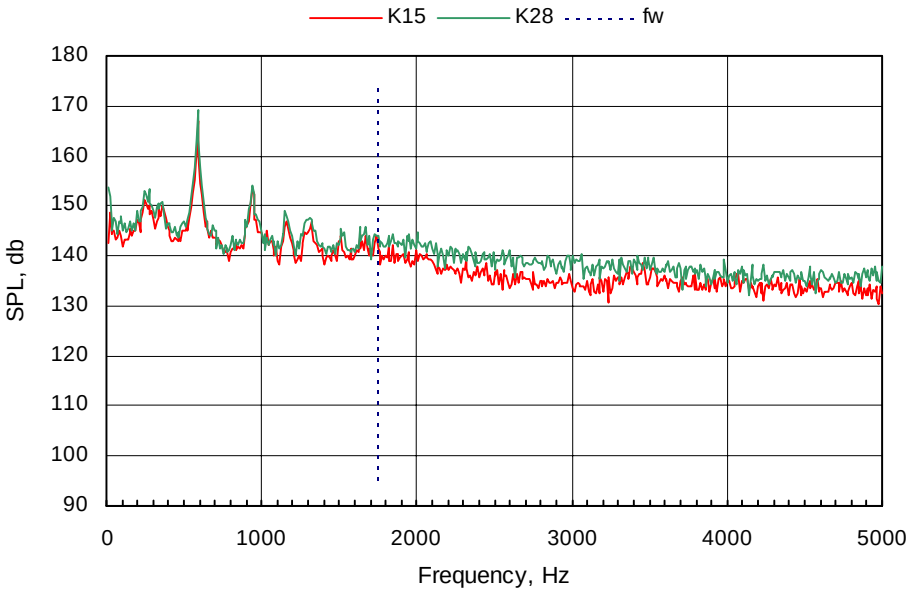

e. M_∞ = 1.50

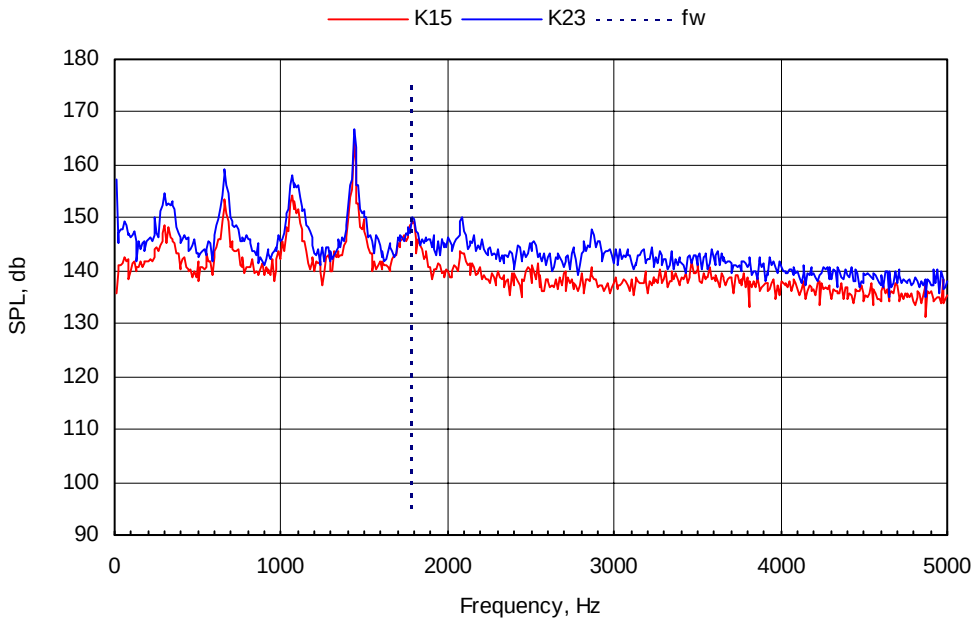

f. M_∞ = 2.00

Figure 25. Continued.

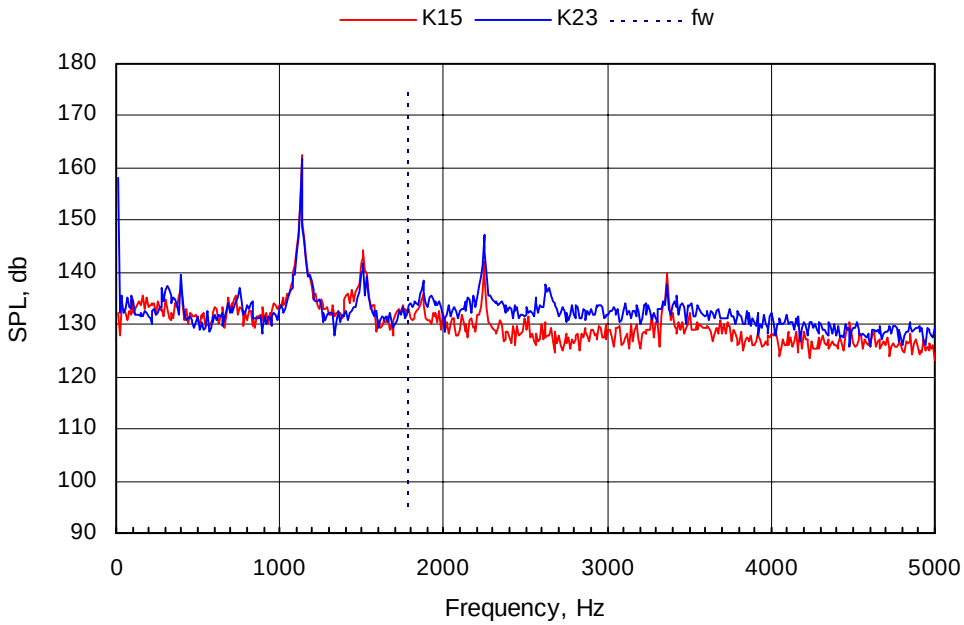

g. M_∞ = 2.75

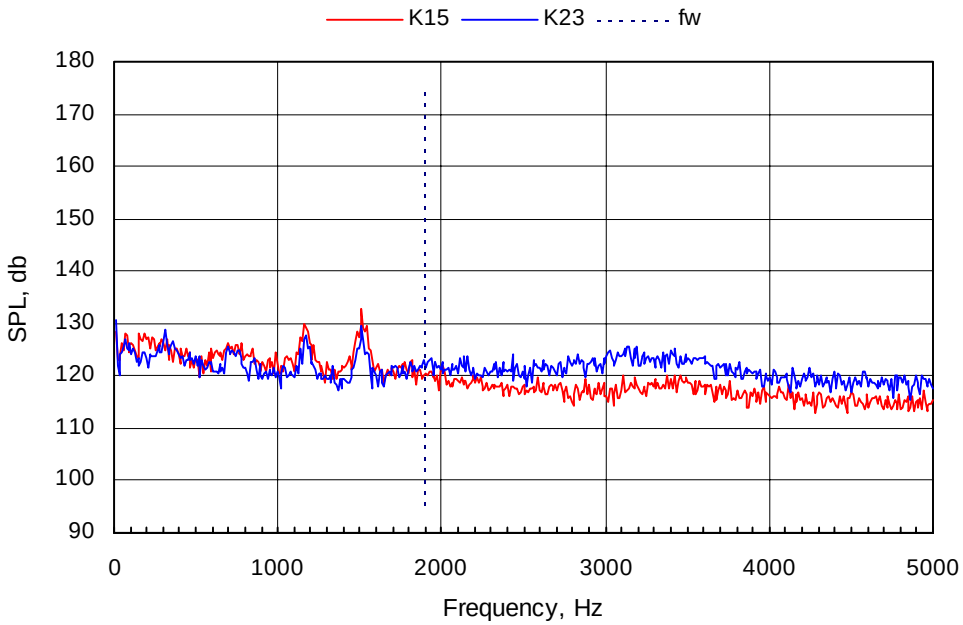

h. M_∞ = 3.51

Figure 25. Continued.

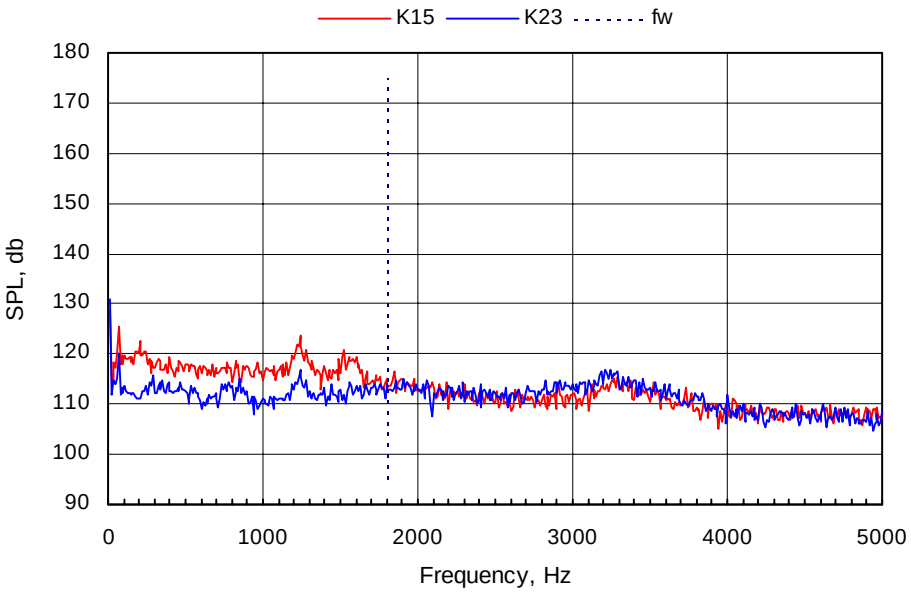

i. M_∞ = 5.04

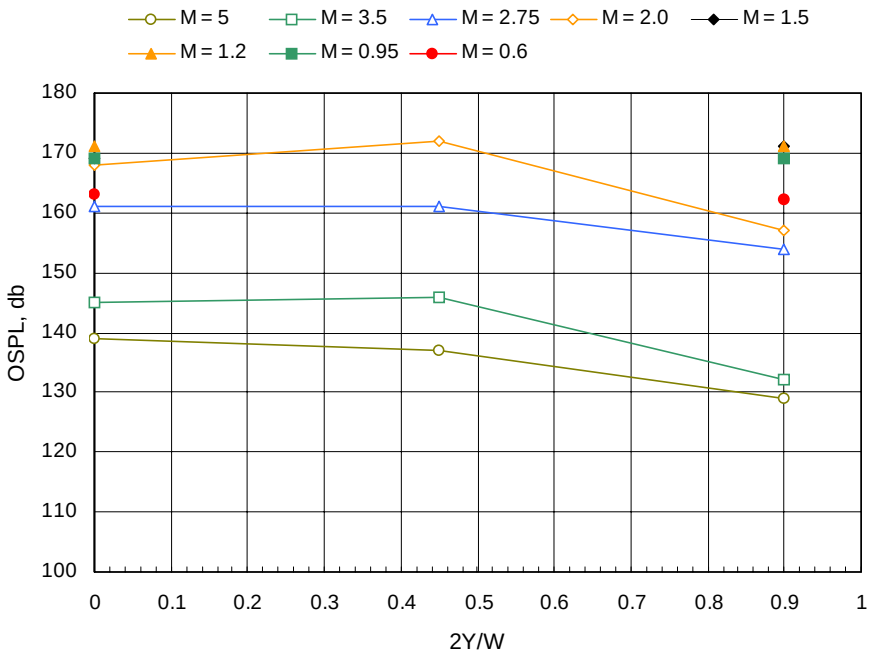

j. Overall sound pressure level laterally across the floor at X/L = 0.51

Figure 25. Concluded.

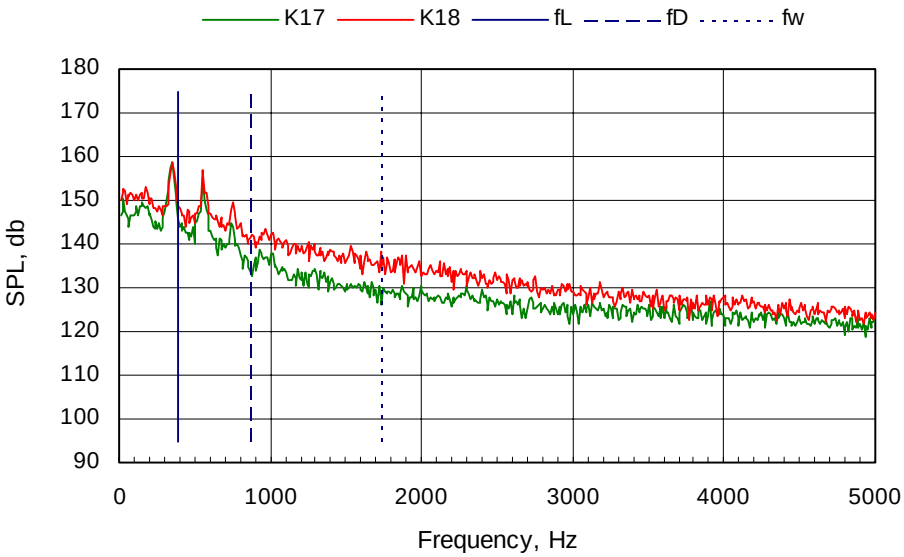

a. M_∞ = 0.60, transducers on cavity centerline (Y = 0)

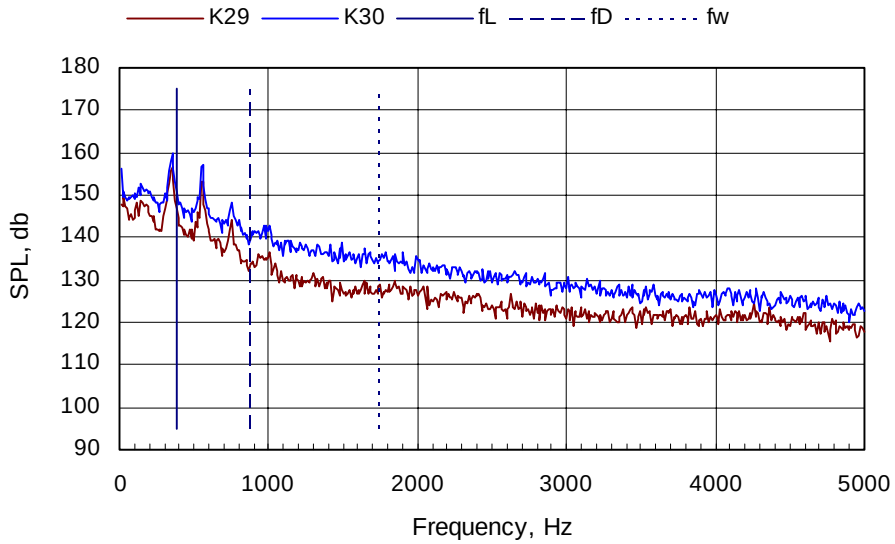

b. M_∞ = 0.60, transducers aligned vertically near the corner (2Y/W = 0.95)

Figure 26. Measured spectra along vertical planes on the downstream wall, L/D = 4.5, Re = 3×10^6.

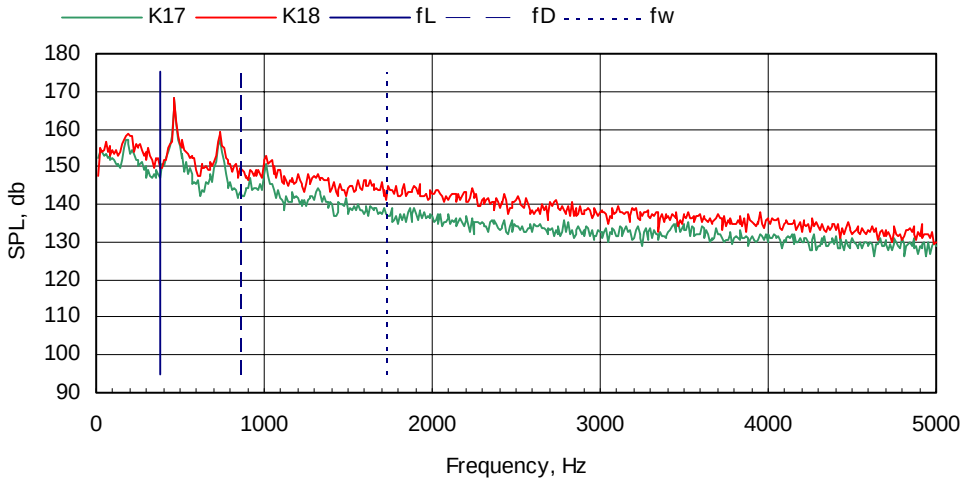

c. M_∞ = 0.95, transducers on cavity center (Y = 0)

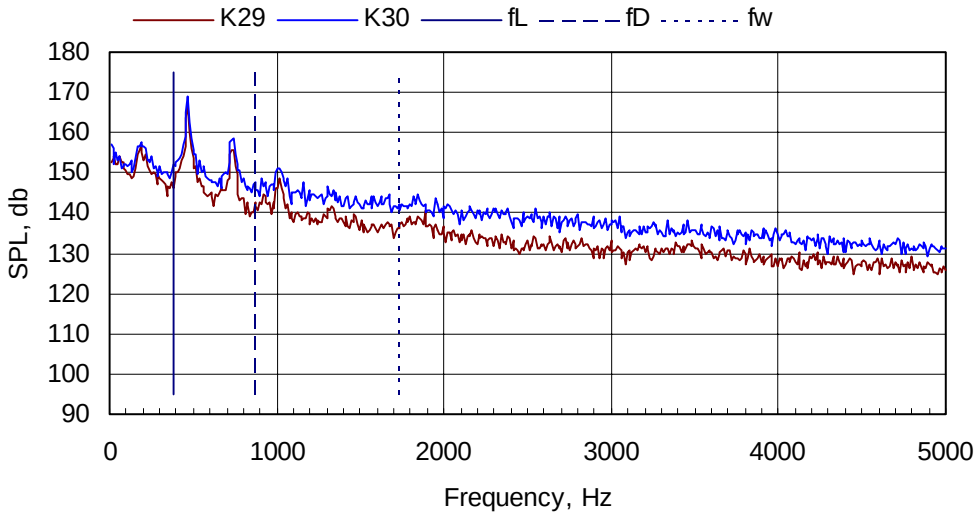

d. M_∞ = 0.95, transducers aligned vertically near the corner (2Y/W = 0.95)

Figure 26. Continued.

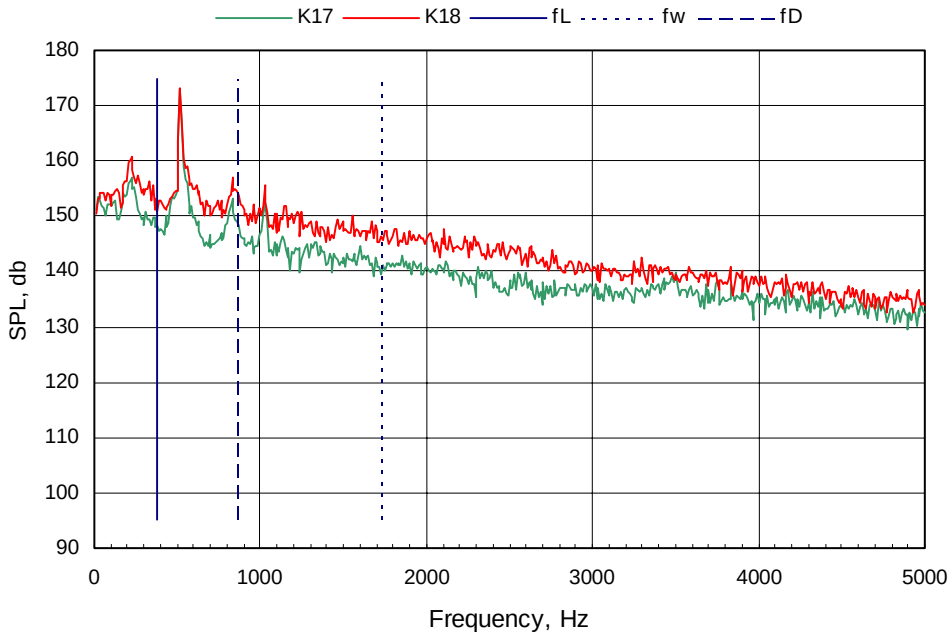

e. M_∞ = 1.20, transducers on cavity centerline (Y = 0)

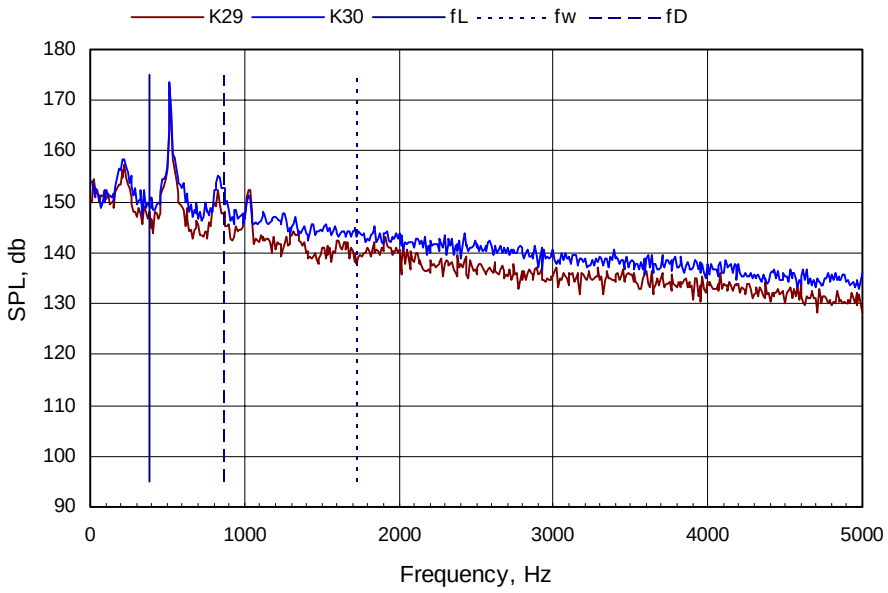

f. M_∞ = 1.20, transducers aligned vertically near the corner (2Y/W = 0.95)

Figure 26. Continued.

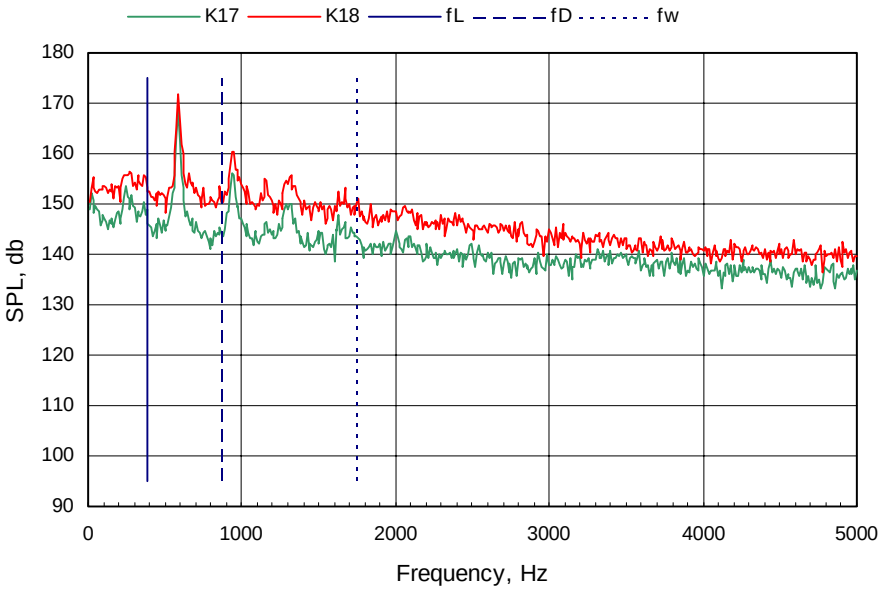

g. M_∞ = 1.50, transducers on cavity centerline (Y = 0)

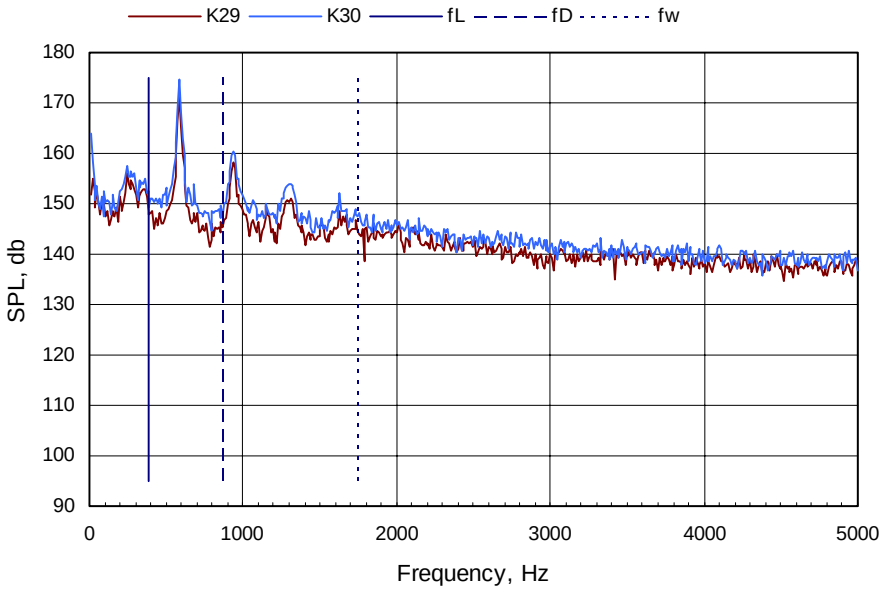

h. M_∞ = 1.50, transducers aligned vertically near the corner (2Y/W = 0.95)

Figure 26. Continued.

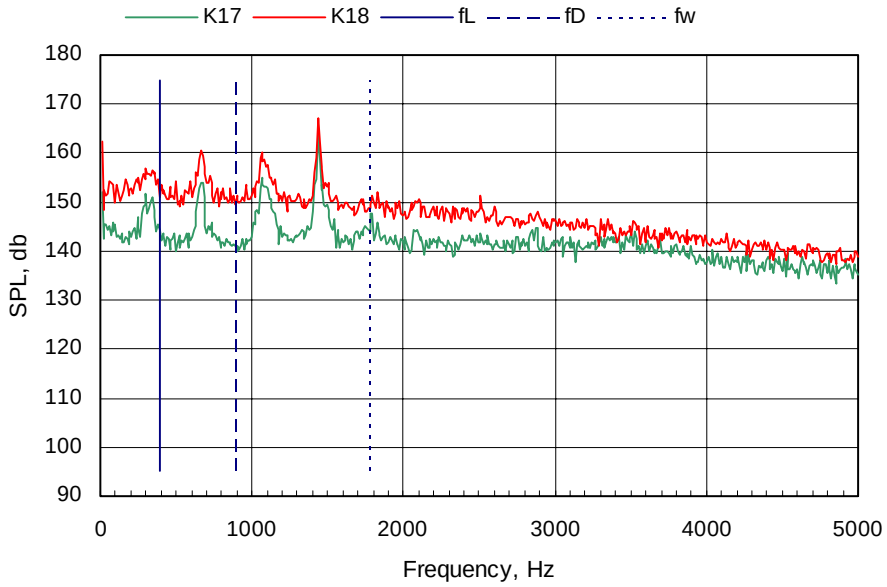

i. M_∞ = 2.00, transducers on cavity centerline (Y = 0)

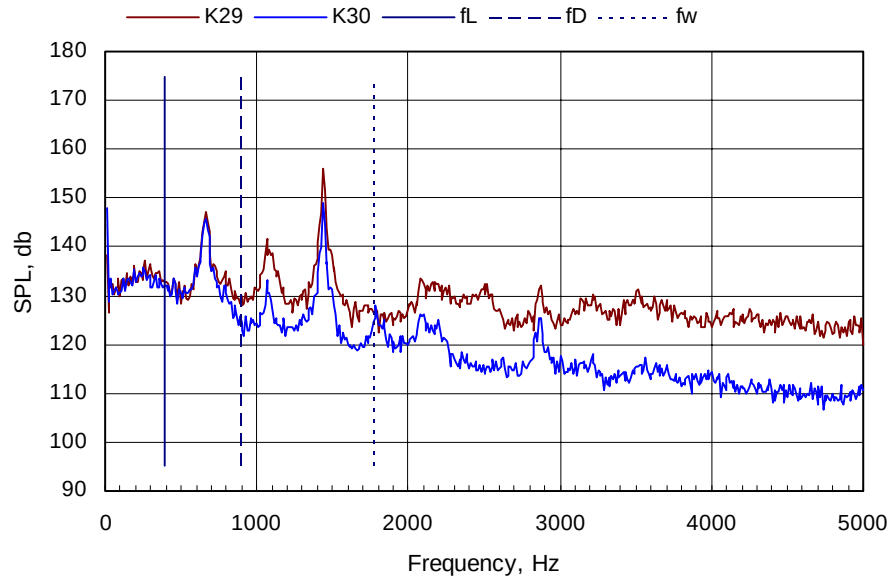

j. M_∞ = 1.50, transducers aligned vertically near the corner (2Y/W = 0.95)

Figure 26. Continued.

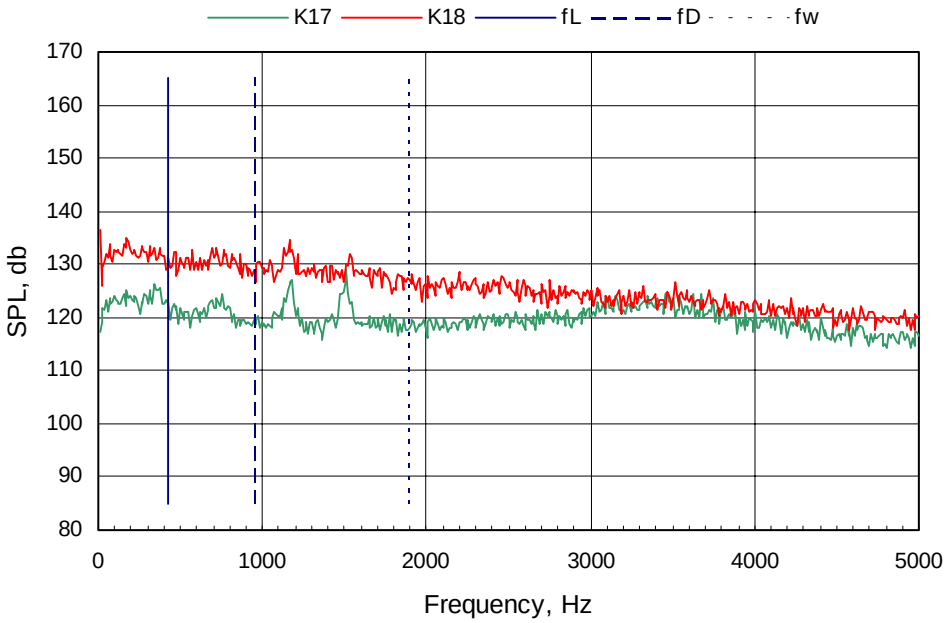

k. M_∞ = 3.51, transducers on cavity centerline (Y = 0)

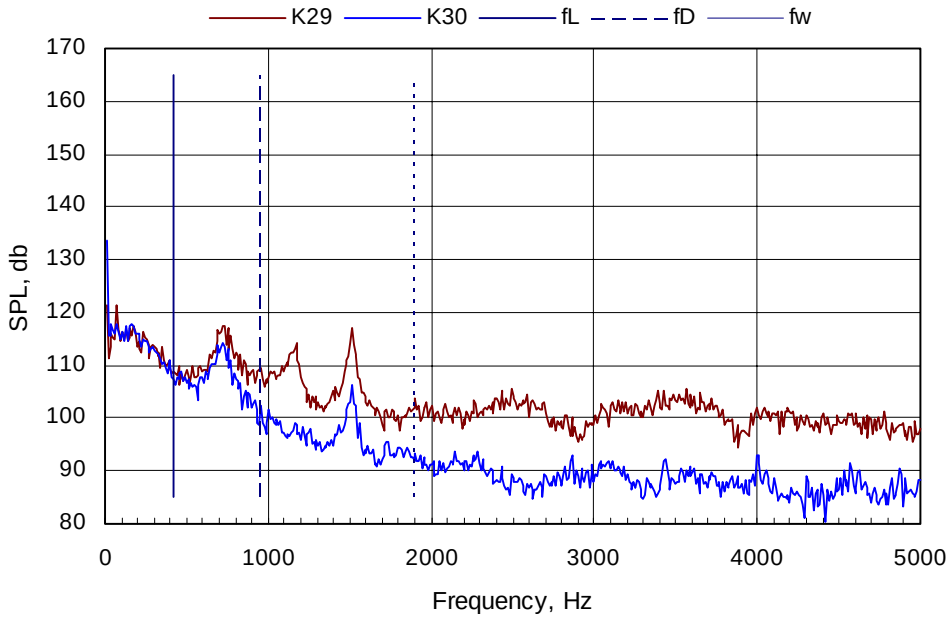

l. M_∞ = 3.51, transducers aligned vertically near the corner (2Y/W = 0.95)

Figure 26. Continued.

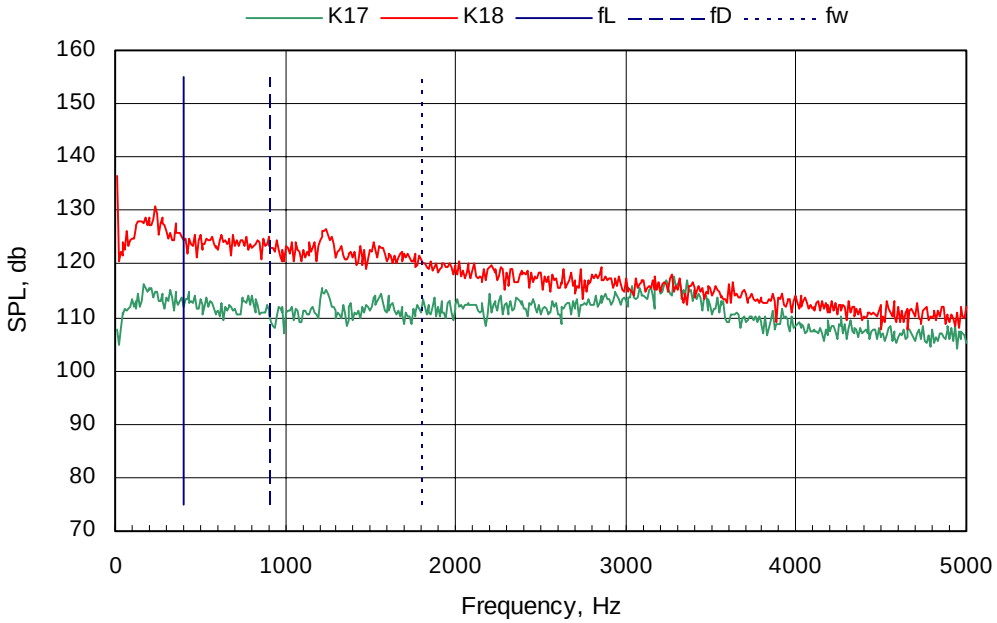

m. M_∞ = 5.04, transducers on cavity centerline (Y = 0)

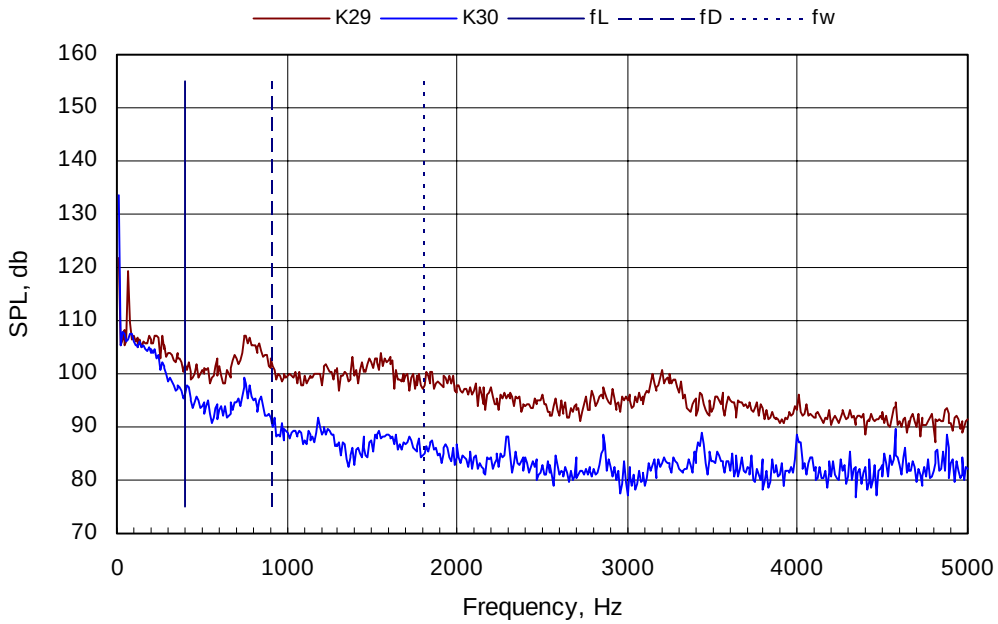

n. M_∞ = 5.04, transducers aligned vertically near the corner (2Y/W = 0.95)

Figure 26. Concluded.

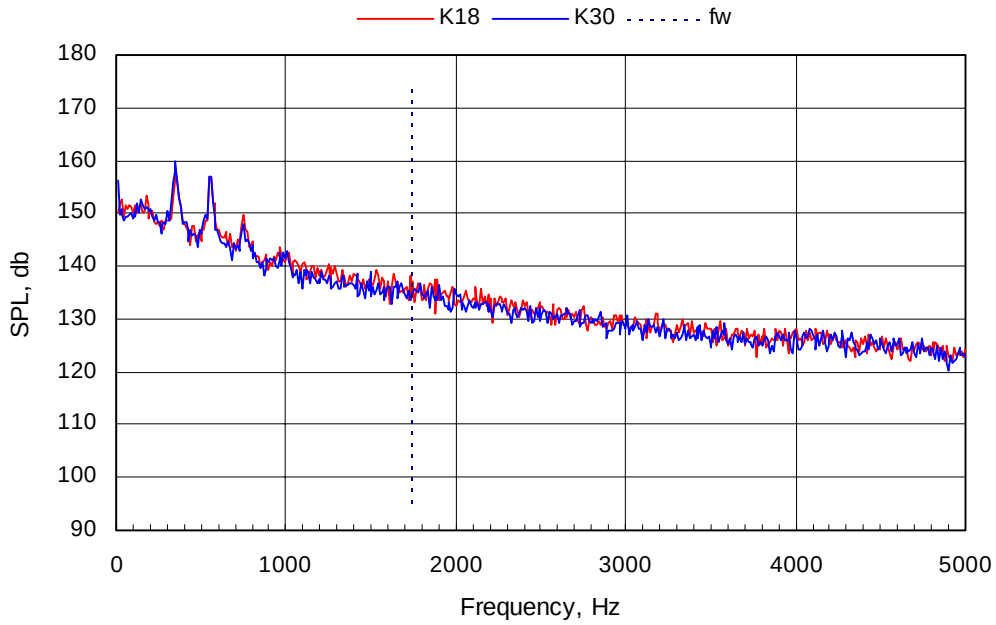

a. M_∞ = 0.60, transducers at Z/D = –0.18

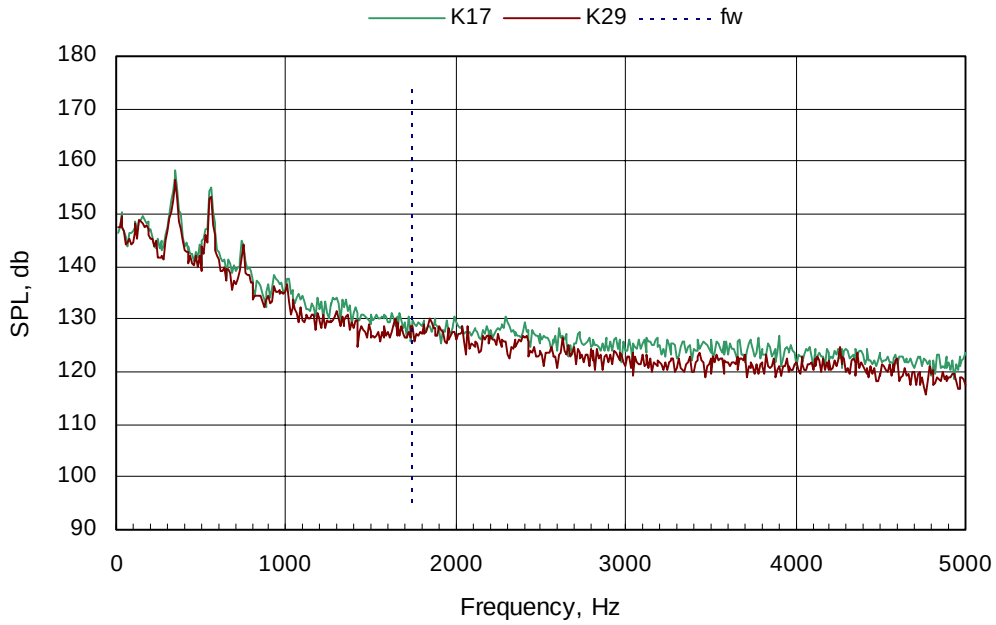

b. M_∞ = 0.60, transducers at Z/D = –0.49

Figure 27. Measured spectra along lateral planes on the downstream wall, L/D = 4.5, Re = 3×10^6.

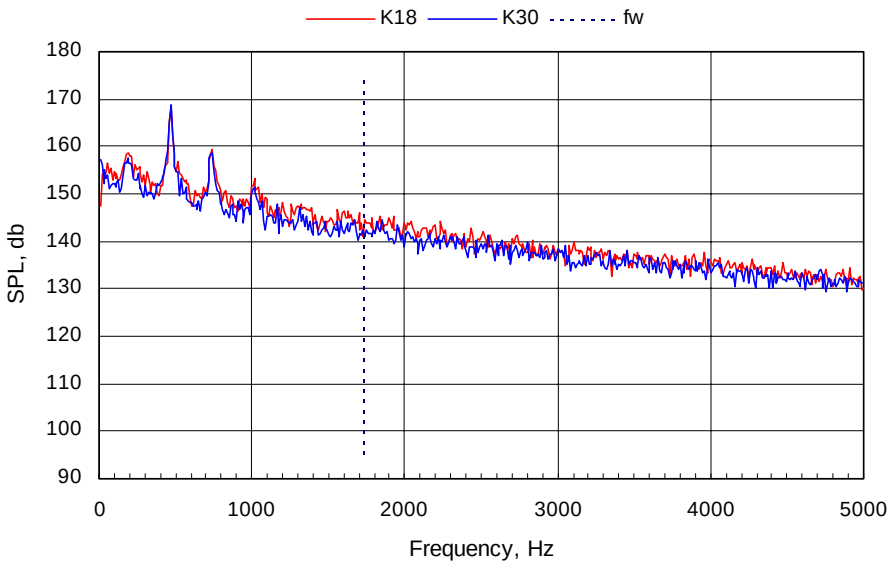

c. M_∞ = 0.95, transducers at Z/D = –0.18

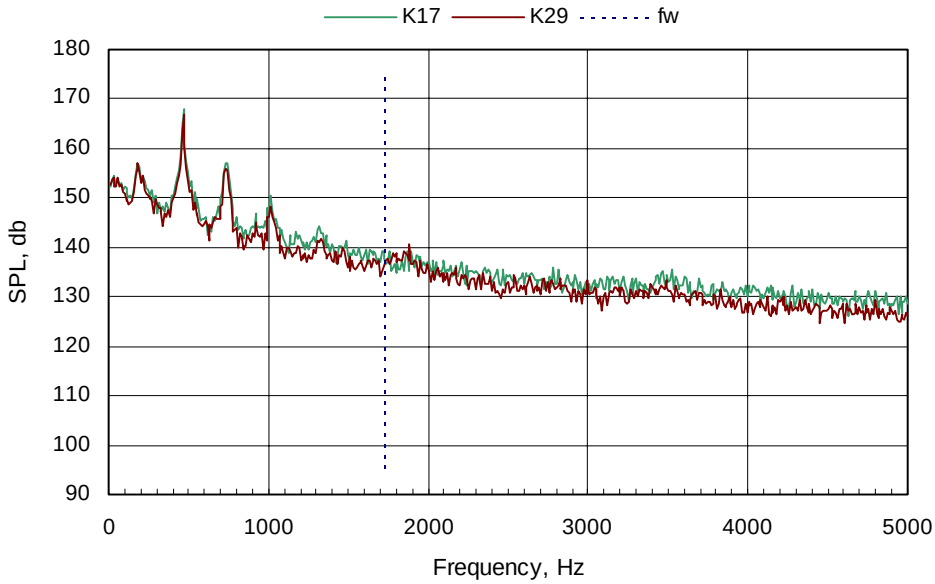

d. M_∞ = 0.95, transducers at Z/D = –0.49

Figure 27. Continued.

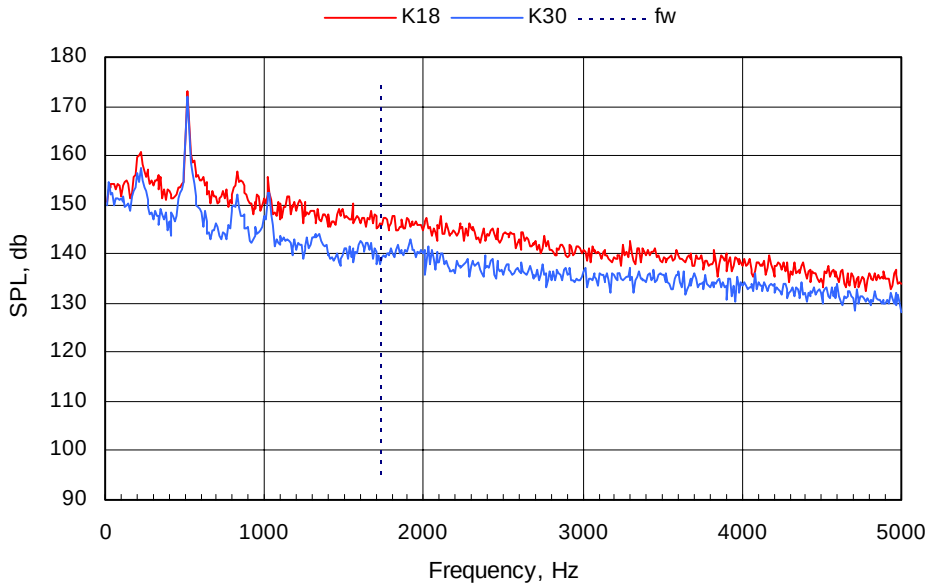

e. M_∞ = 1.20, transducers at Z/D = –0.18

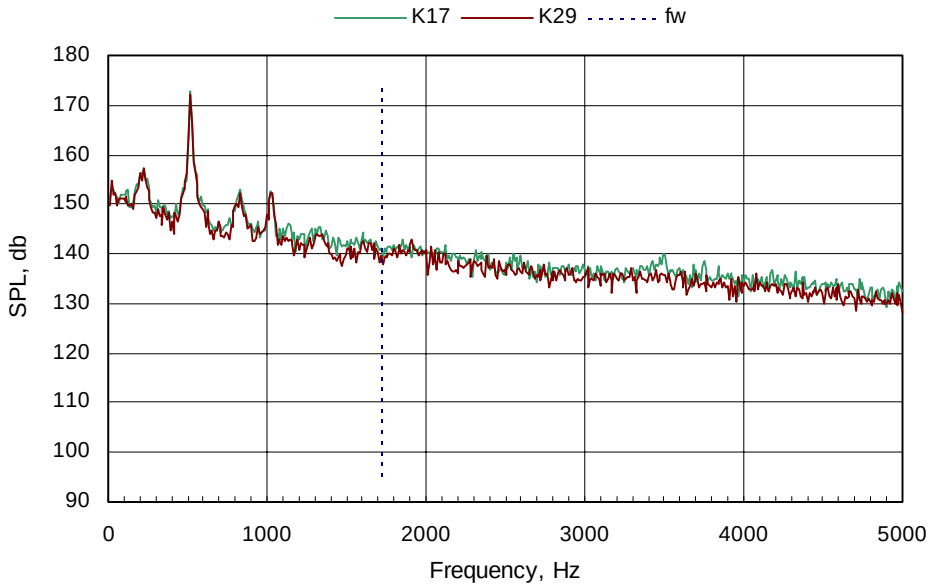

f. M_∞ = 1.20, transducers at Z/D = –0.49

Figure 27. Continued.

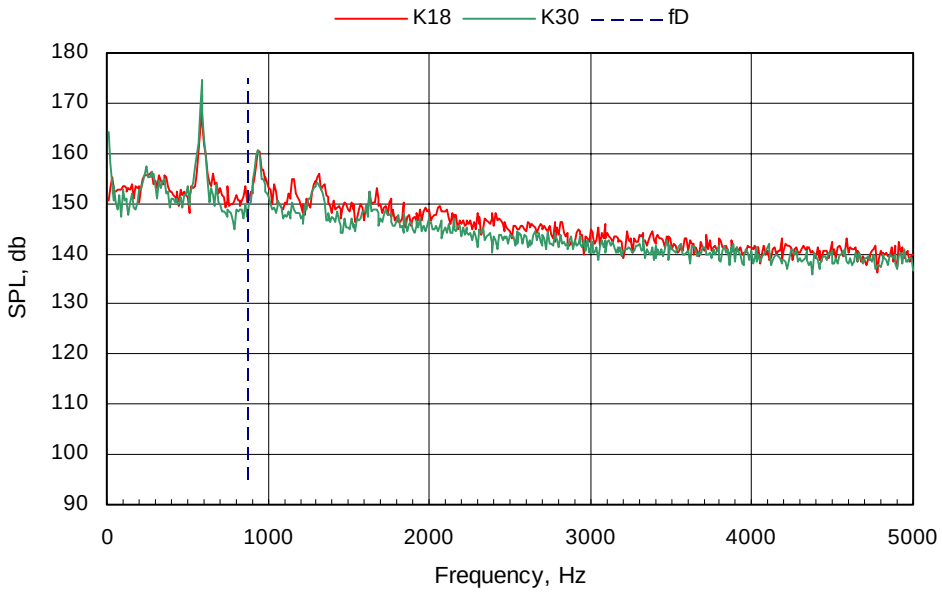

g. M_∞ = 1.50, transducers at Z/D = –0.18

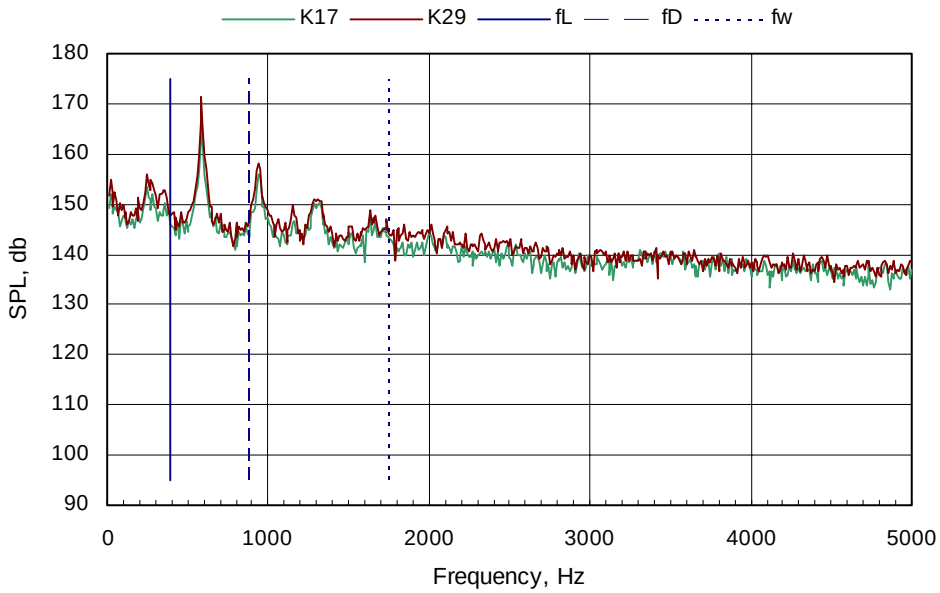

h. M_∞ = 1.50, transducers at Z/D = –0.49

Figure 27. Continued.

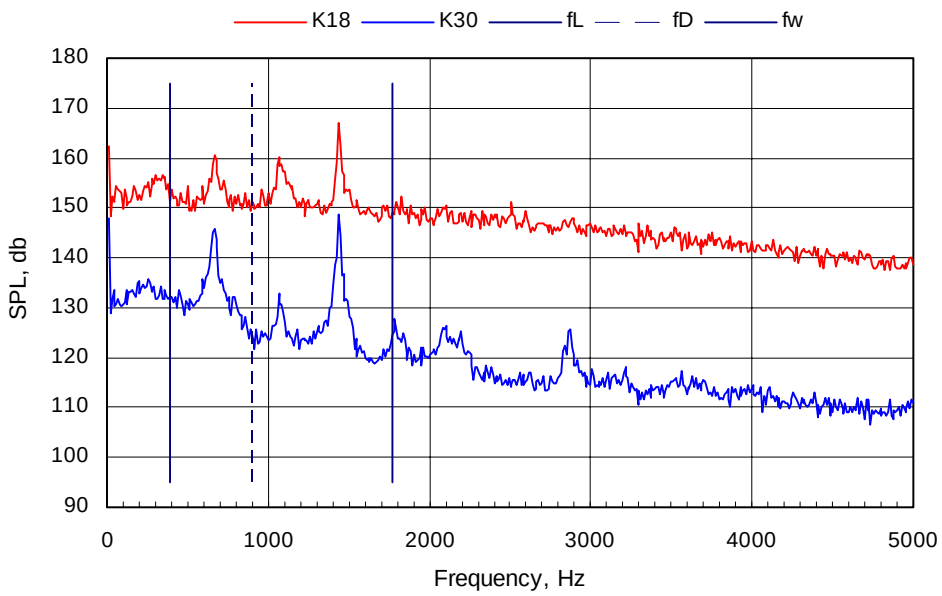

i. M_∞ = 2.00, transducers at Z/D = –0.18

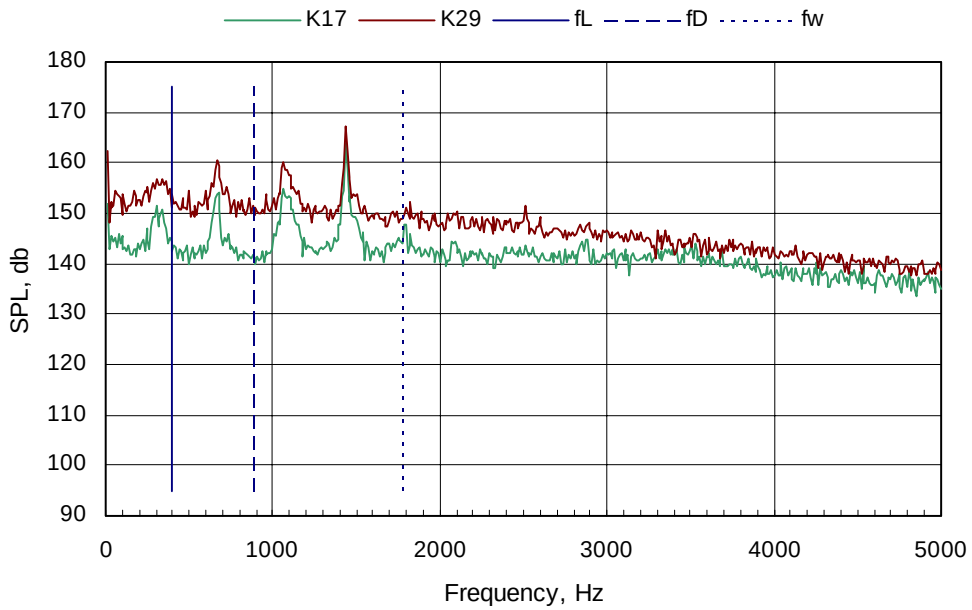

j. M_∞ = 2.00, transducers at Z/D = –0.49

Figure 27. Continued.

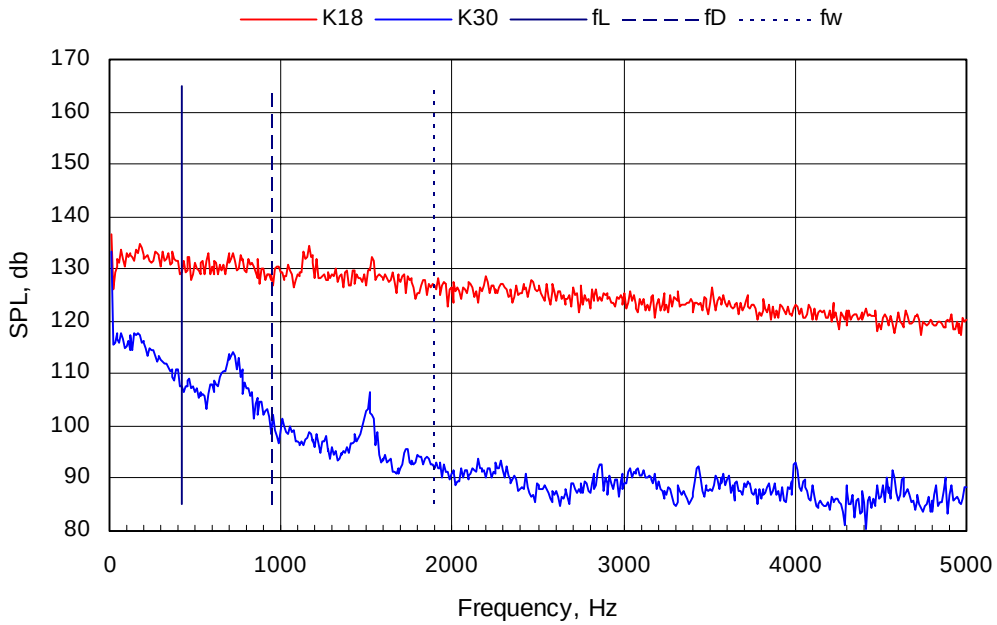

k. M_∞ = 3.51, transducers at Z/D = –0.18

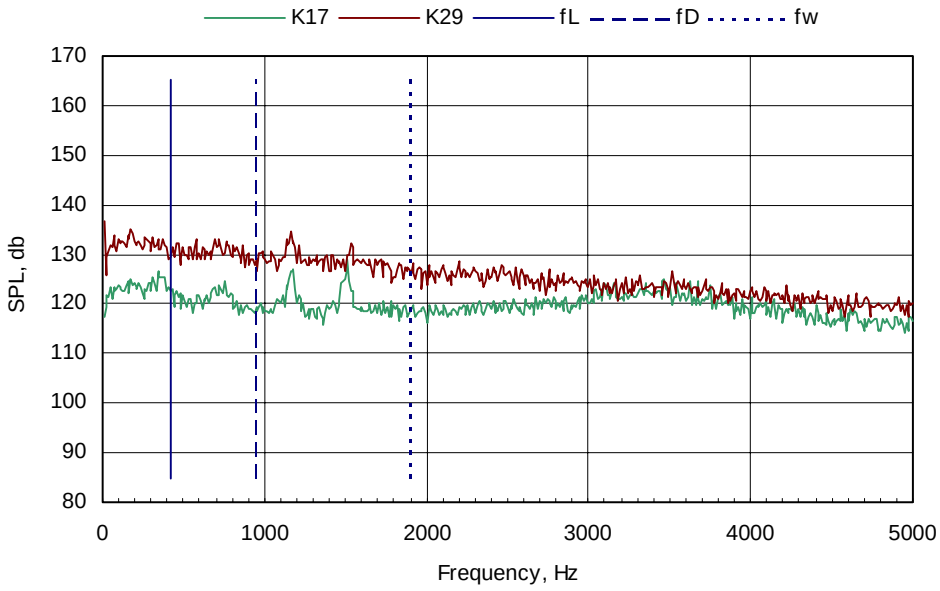

l. M_∞ = 3.51, transducers at Z/D = –0.49

Figure 27. Continued.

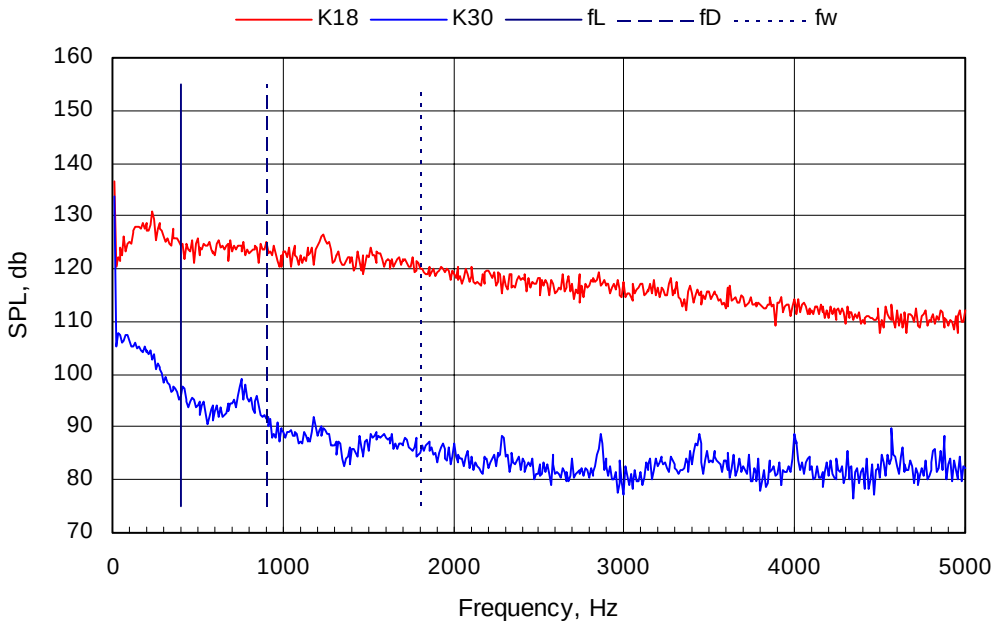

m. M_∞ = 5.04, transducers at Z/D = –0.18

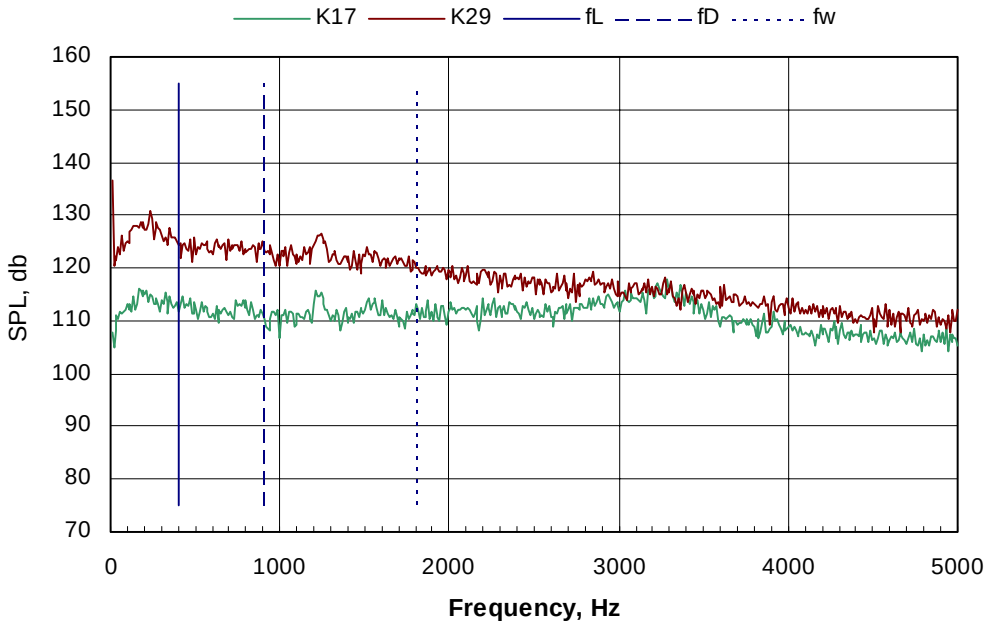

n. M_∞ = 5.04, transducers at Z/D = –0.49

Figure 27. Concluded.

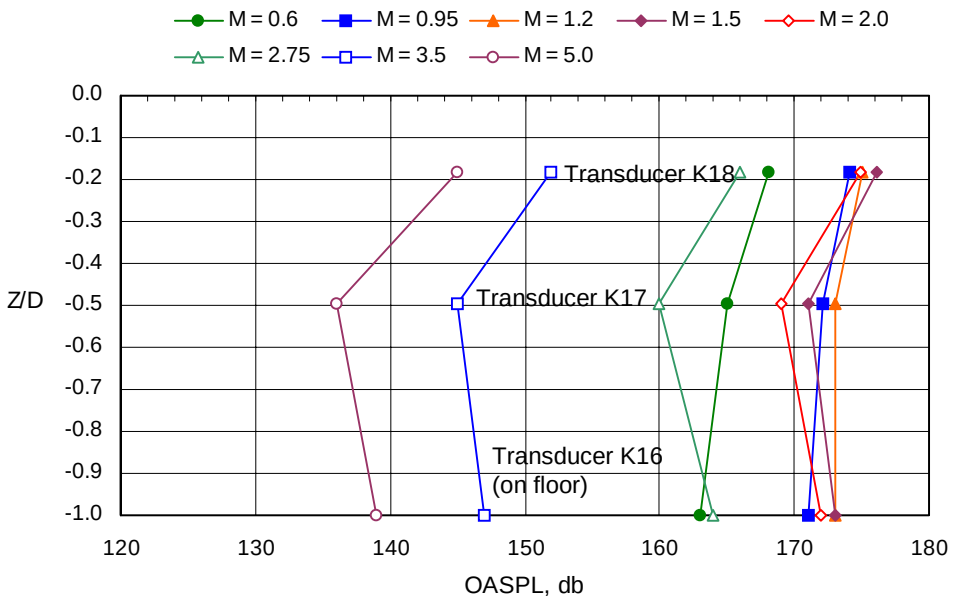

a. Transducers along the vertical centerline, Y = 0

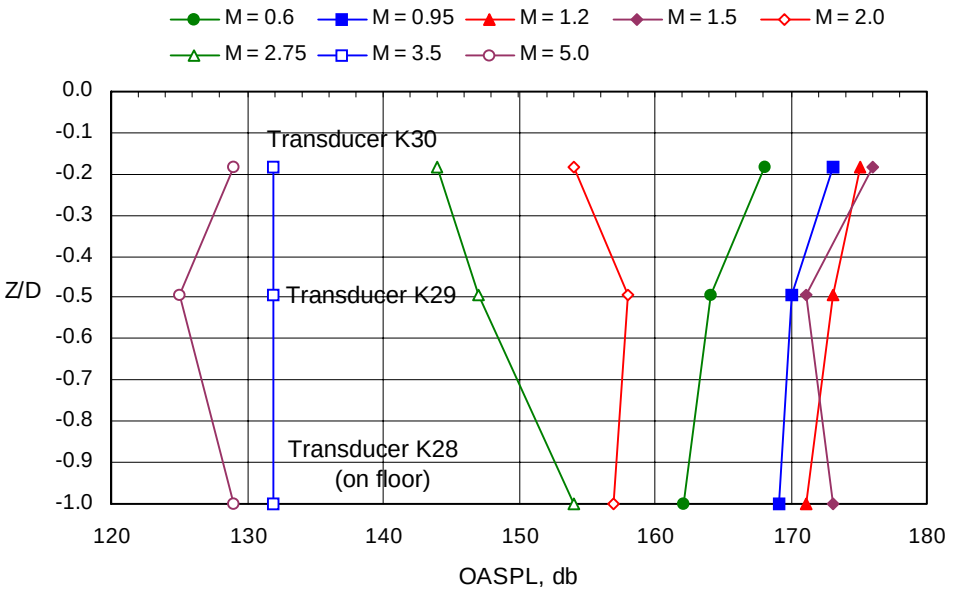

b. Transducers along a vertical line near the corner, 2Y/W = 0.95

Figure 28. OASPL on the downstream wall of an L/D = 4.5 cavity.

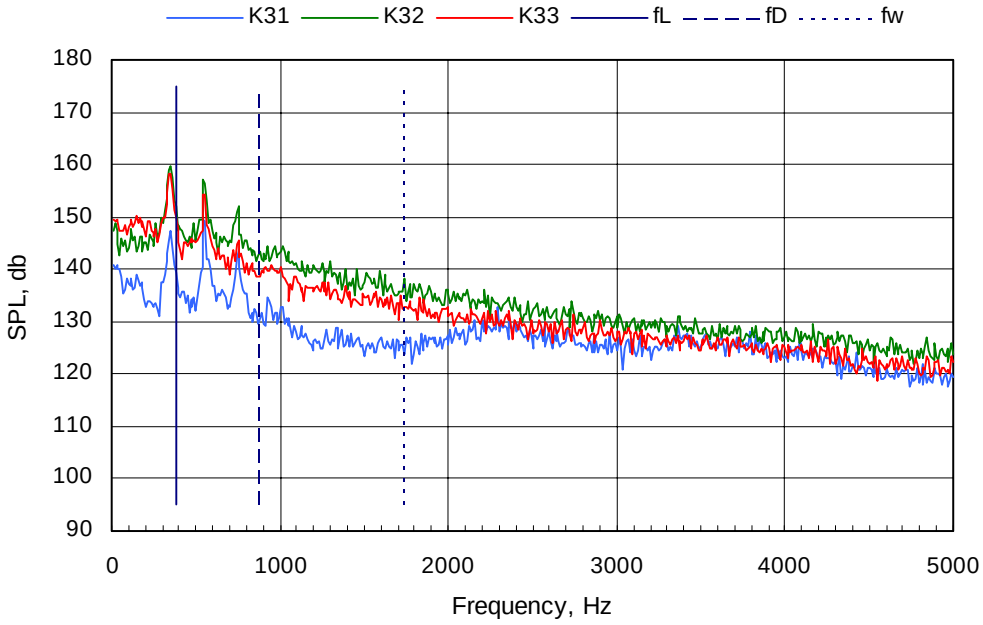

a. M_∞ = 0.60

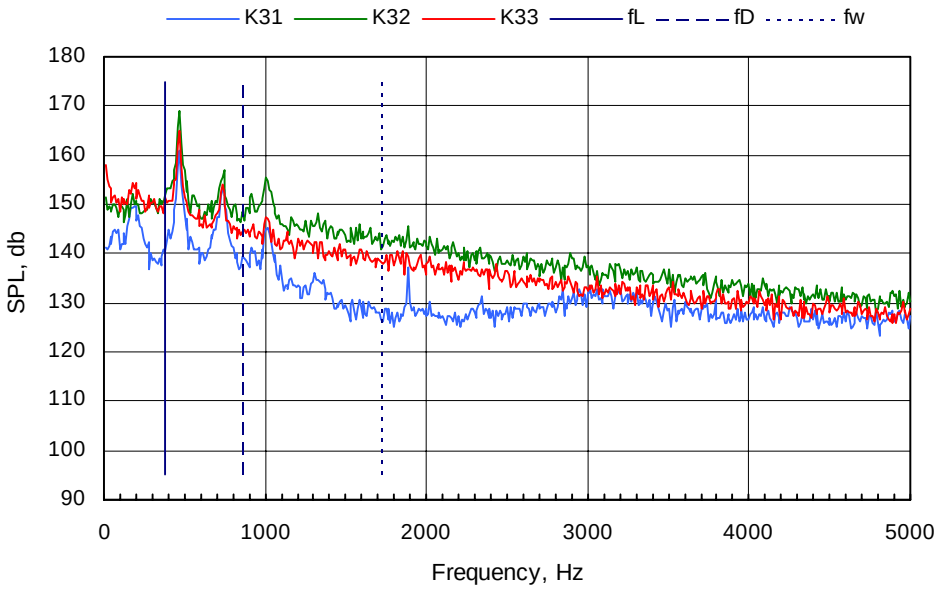

b. M_∞ = 0.95

Figure 29. Measured spectra along the top of the side wall of an L/D = 4.5 cavity.

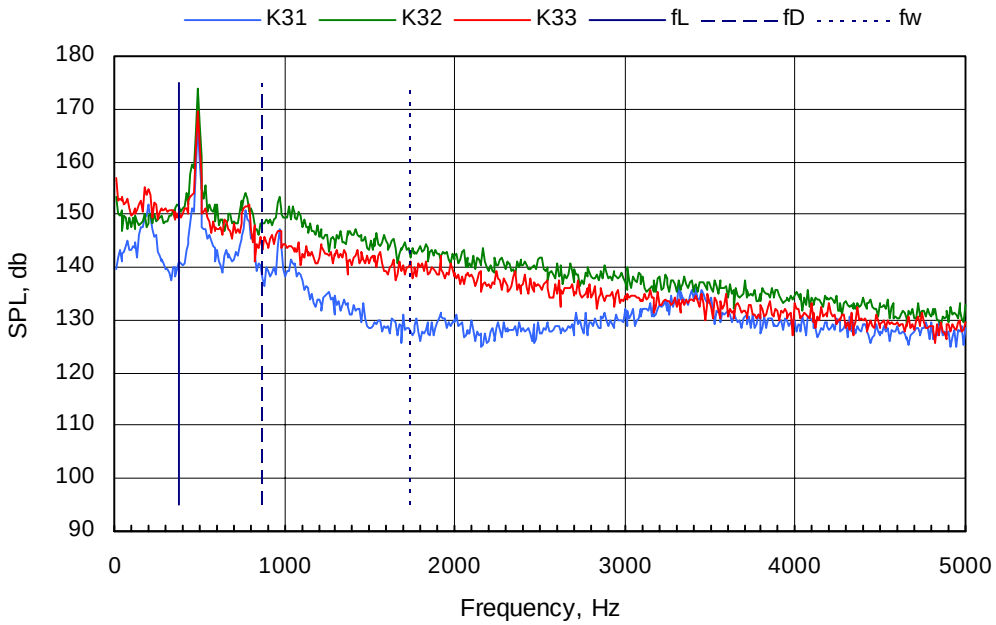

c. M_∞ = 1.05

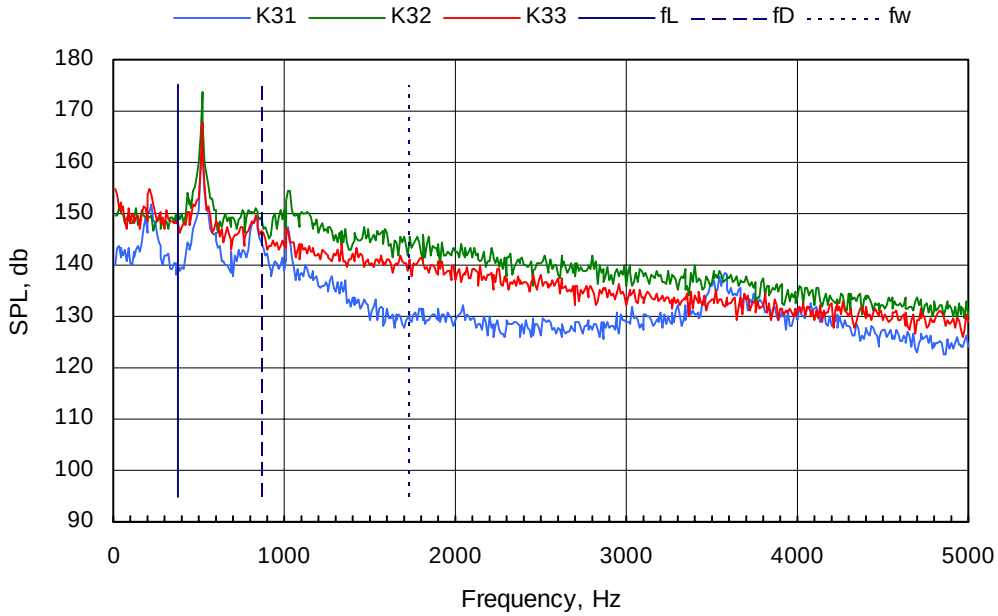

d. M_∞ = 1.20

Figure 29. Continued.

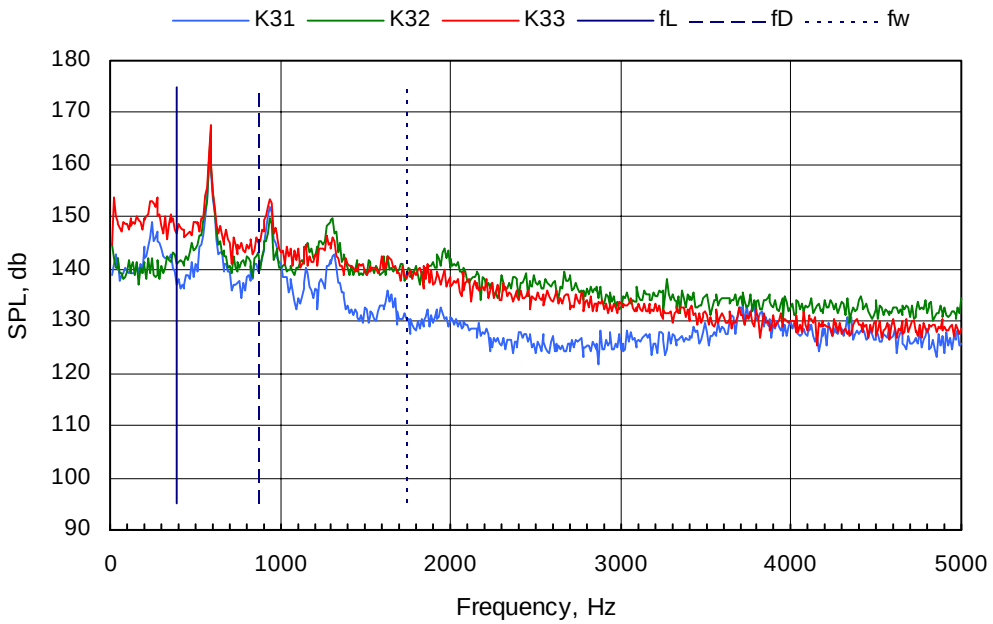

e. $M_\infty = 1.50$

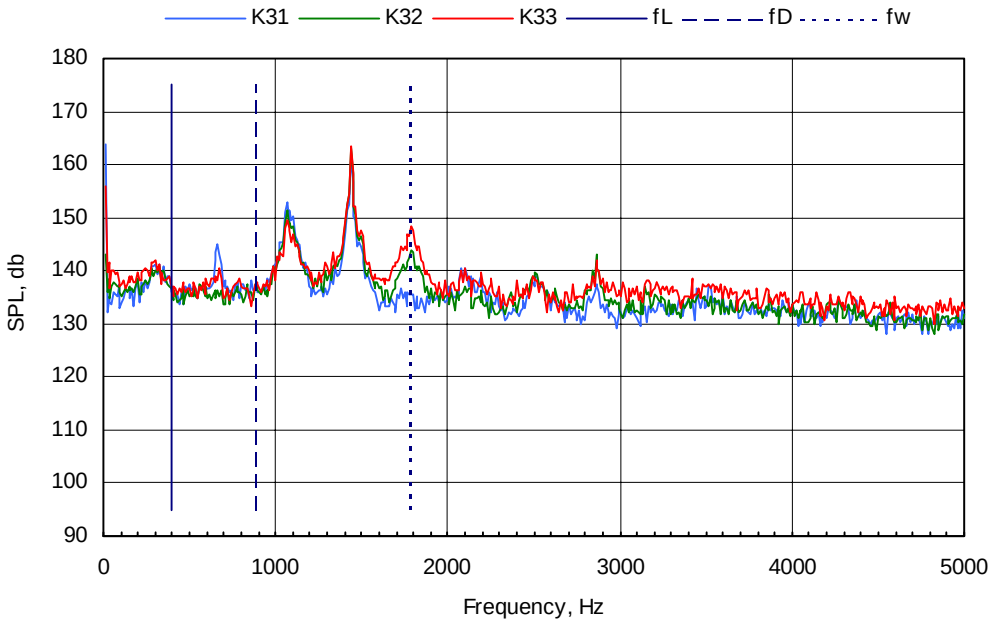

f. $M_\infty = 2.00$

Figure 29. Continued.

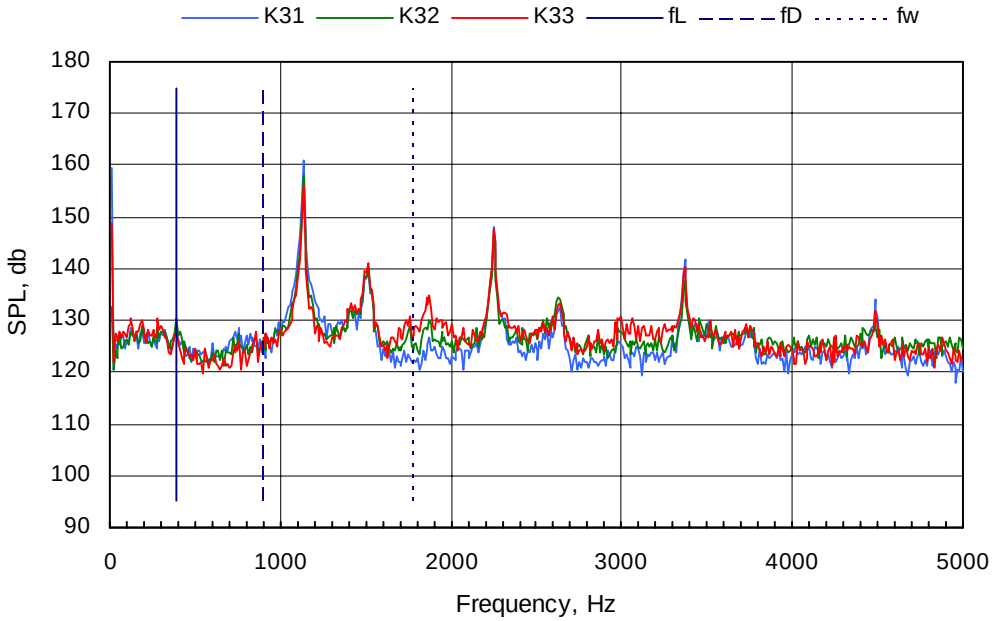

g. M_∞ = 2.75

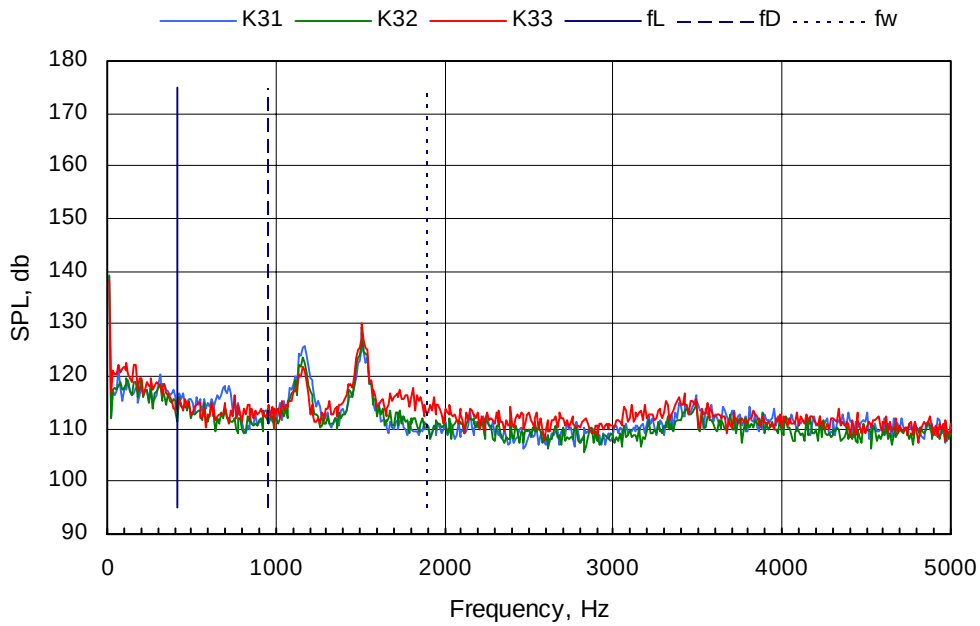

h. M_∞ = 3.51

Figure 29. Continued.

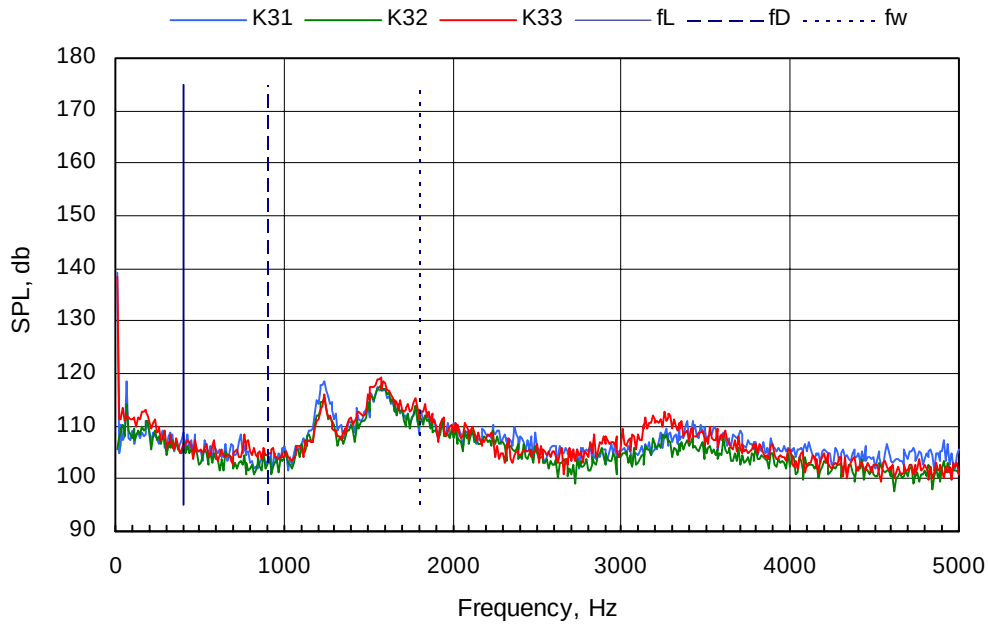

i. M_∞ = 5.04

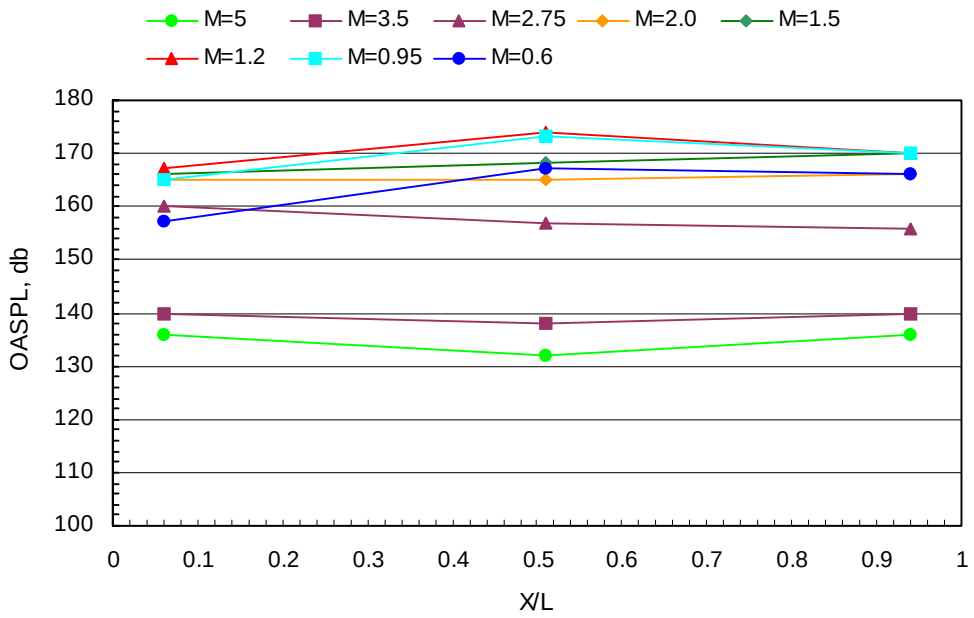

j. Overall sound pressure level along the top of the side wall

Figure 29. Concluded.

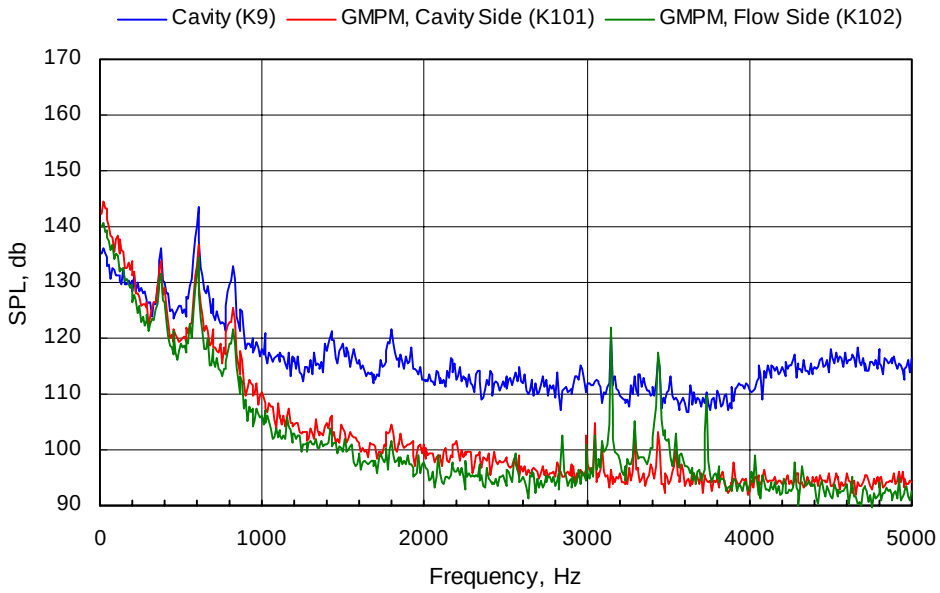

a. GMPM store model centerline at Z/D = –0.75, transducers at X/L = 0.26

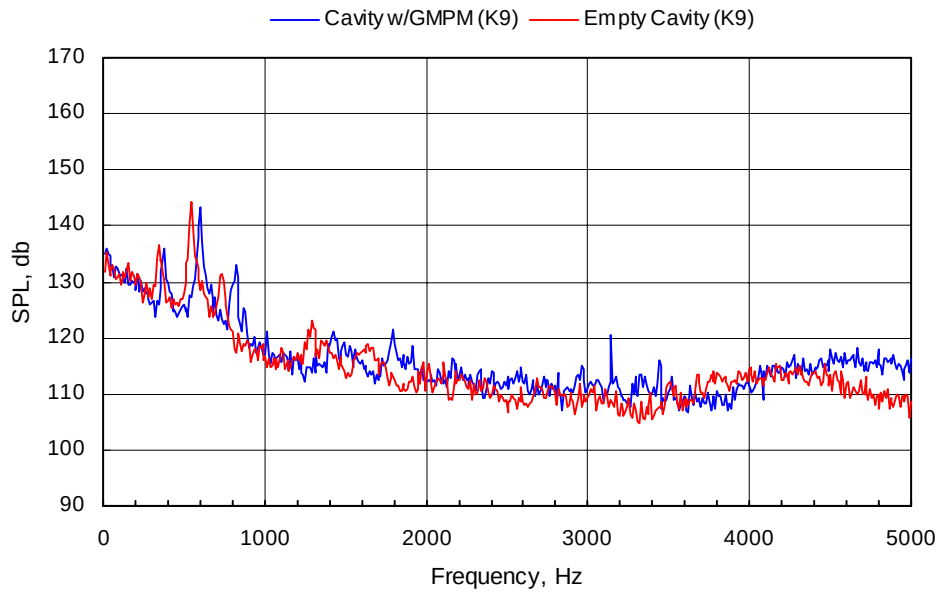

b. Comparison with and without the GMPM store model centerline at Z/D = –0.75, transducers at X/L = 0.26

Figure 30. Comparison of spectra sensed on the floor of an L/D = 4.5 cavity with spectra sensed on the body of a generic store model. M_∞ = 0.60.

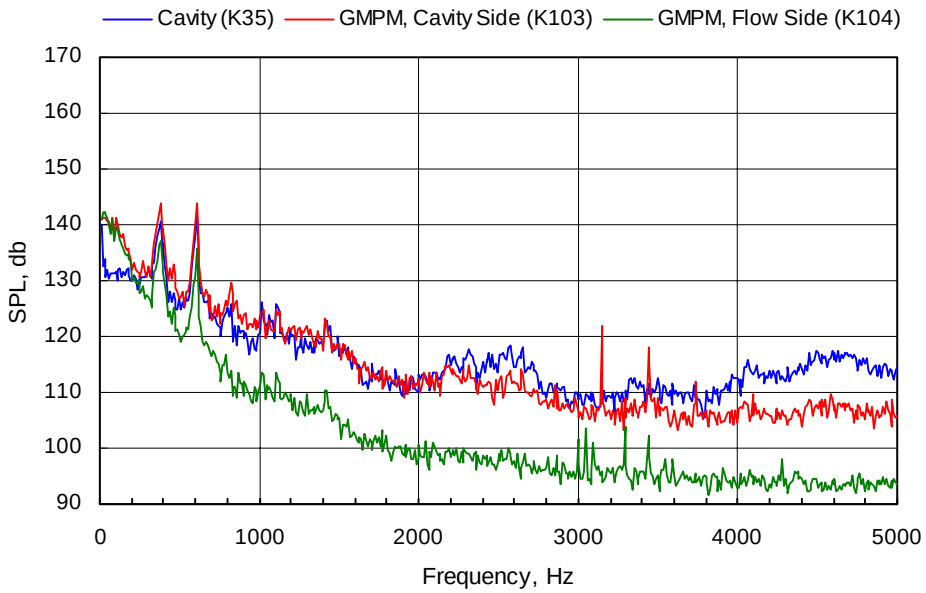

c. GMPM store model centerline at Z/D = –0.75, transducers at X/L = 0.36

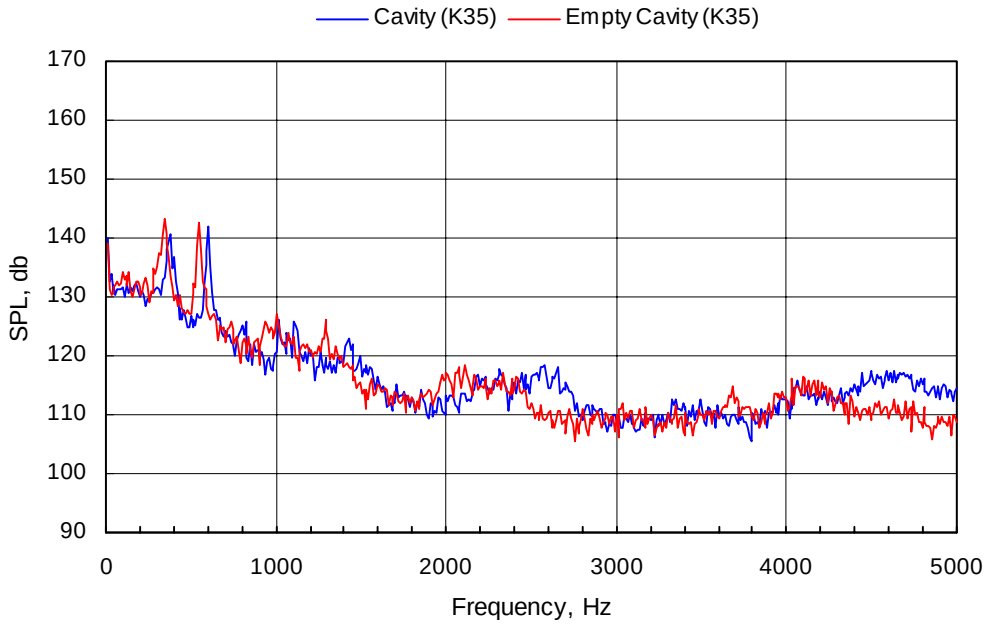

d. Comparison with and without the GMPM store model centerline at Z/D = –0.75, transducers at X/L = 0.36

Figure 30. Continued.

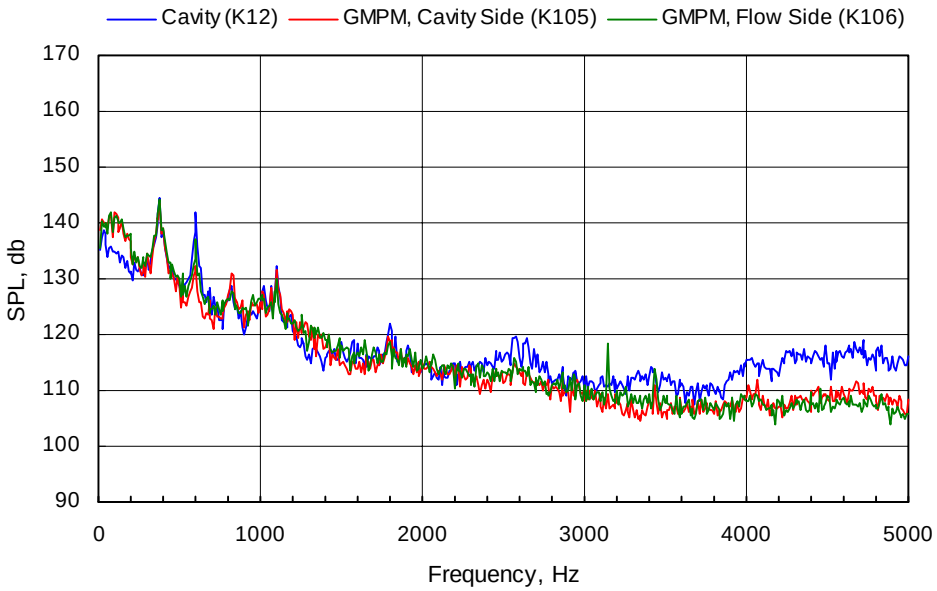

e. GMPM store model centerline at Z/D = –0.75, transducers at X/L = 0.51

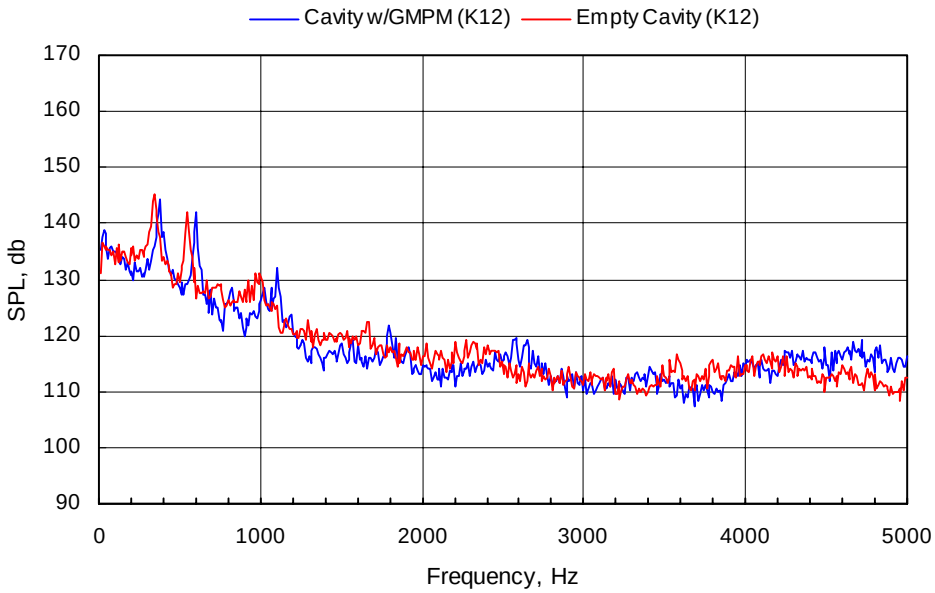

f. Comparison with and without the GMPM store model centerline at Z/D = –0.75, transducers at X/L = 0.51

Figure 30. Continued.

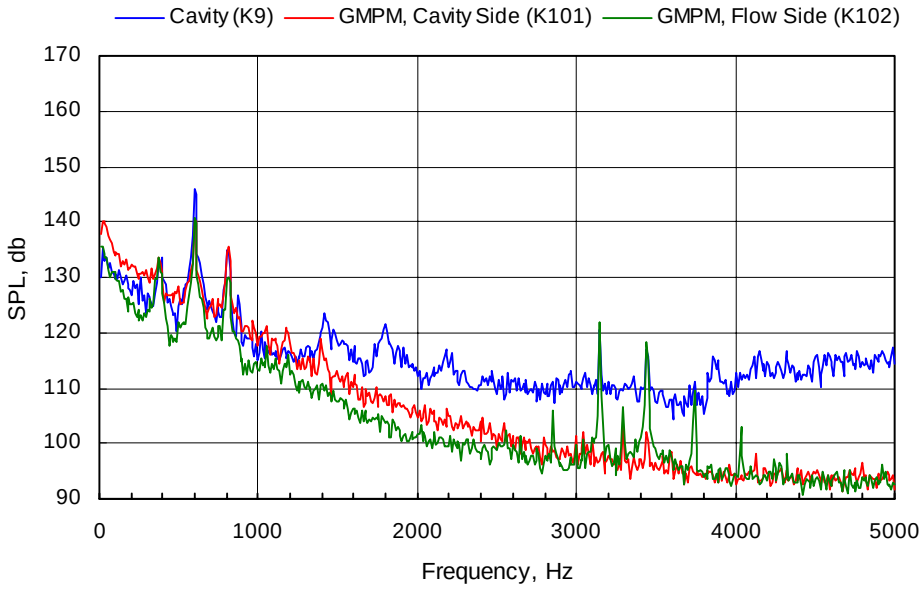

g. GMPM store model centerline at Z/D = 0, transducers at X/L = 0.26

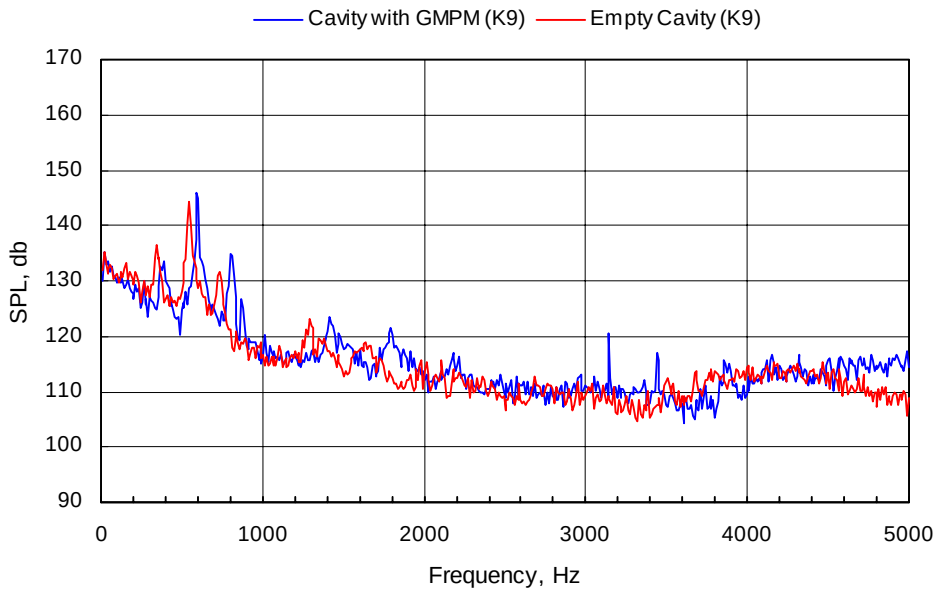

h. Comparison with and without the GMPM store model centerline at Z/D = 0, transducers at X/L = 0.26

Figure 30. Continued.

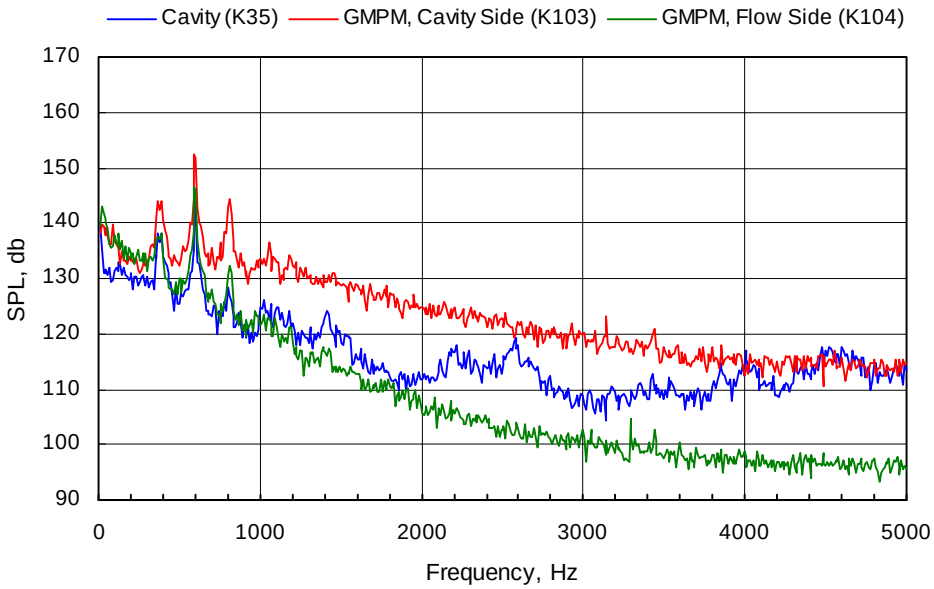

i. GMPM store model centerline at Z/D = 0, transducers at X/L = 0.36

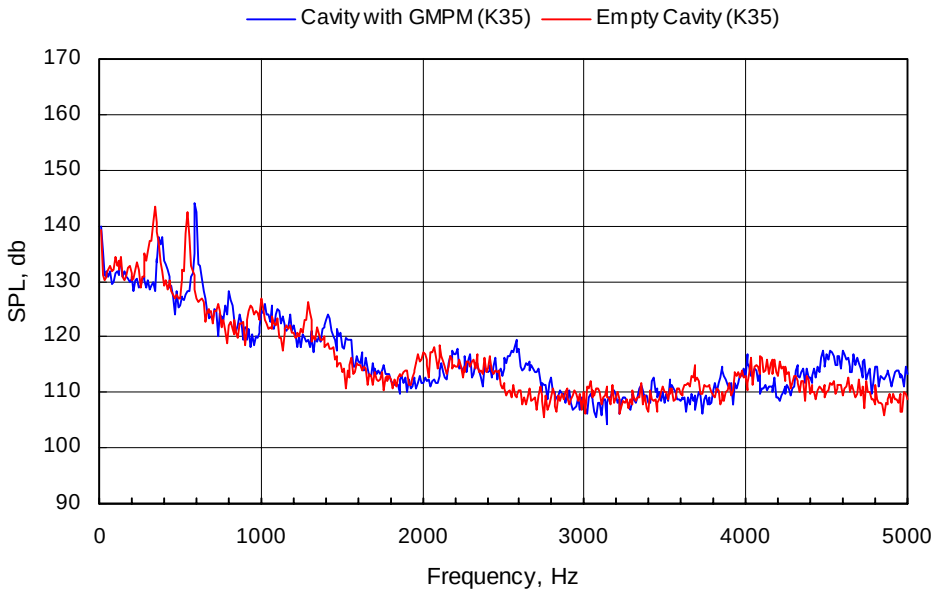

j. Comparison with and without the GMPM store model centerline at Z/D = 0, transducers at X/L = 0.36

Figure 30. Continued.

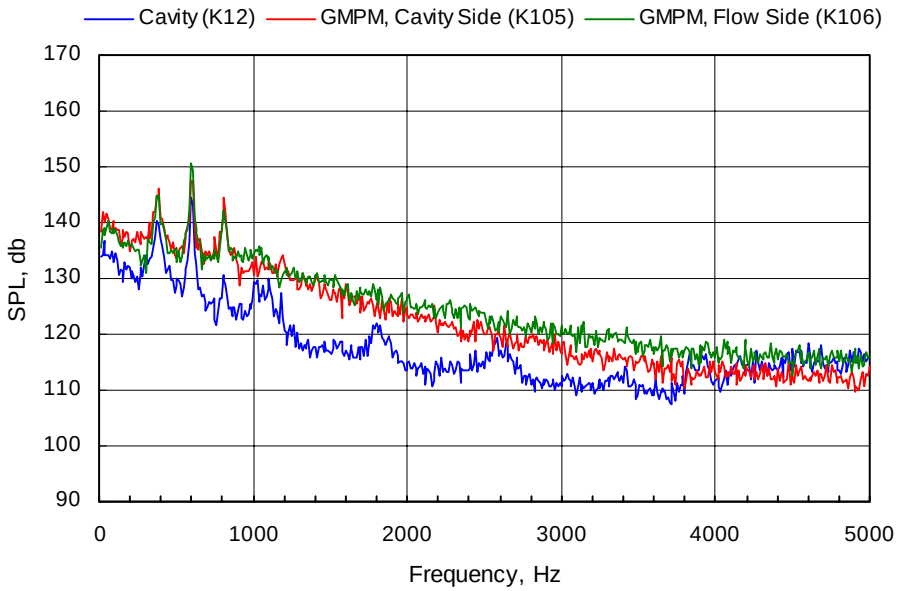

k. GMPM store model centerline at Z/D = 0, transducers at X/L = 0.51

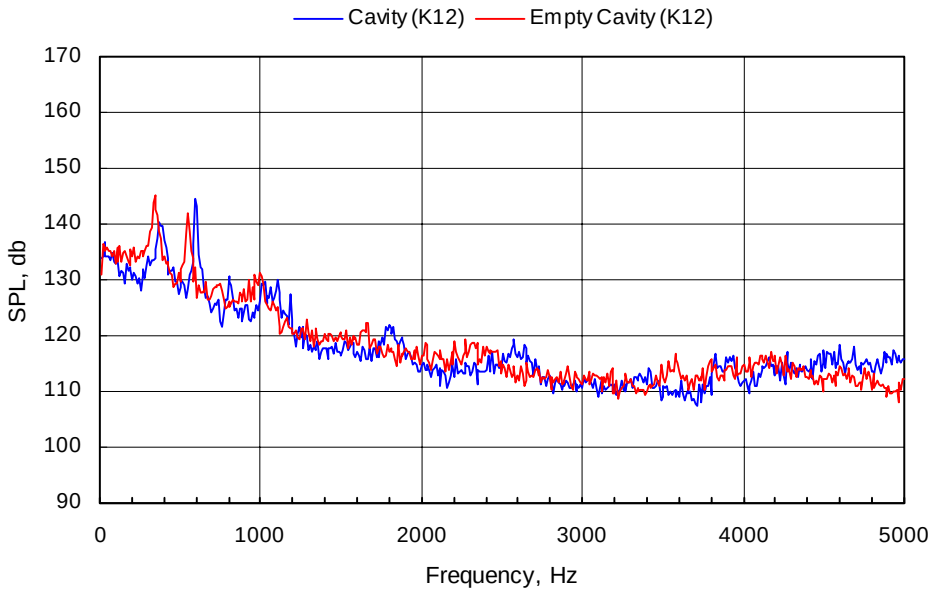

l. Comparison with and without the GMPM store model centerline at Z/D = 0, transducers at X/L = 0.51

Figure 30. Continued.

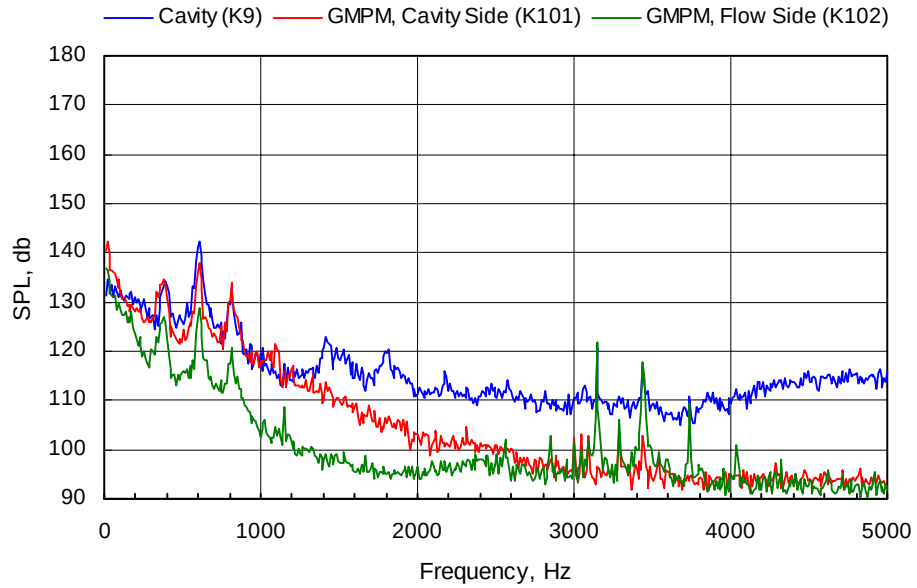

m. GMPM store model centerline at Z/D = 0.3, transducers at X/L = 0.26

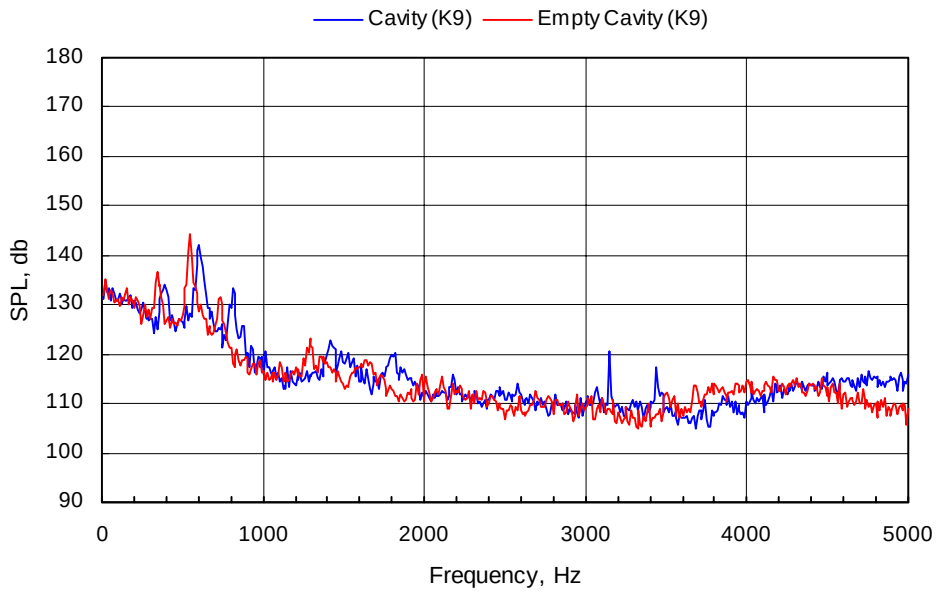

n. Comparison with and without the GMPM store model centerline at Z/D = 0.3, transducers at X/L = 0.26

Figure 30. Continued.

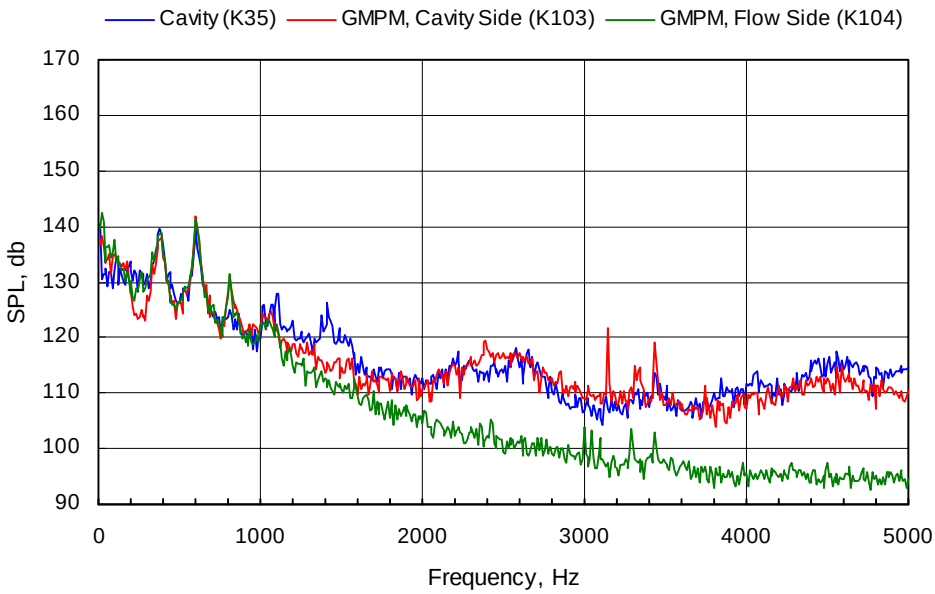

o. GMPM store model centerline at Z/D = 0.3, transducers at X/L = 0.36

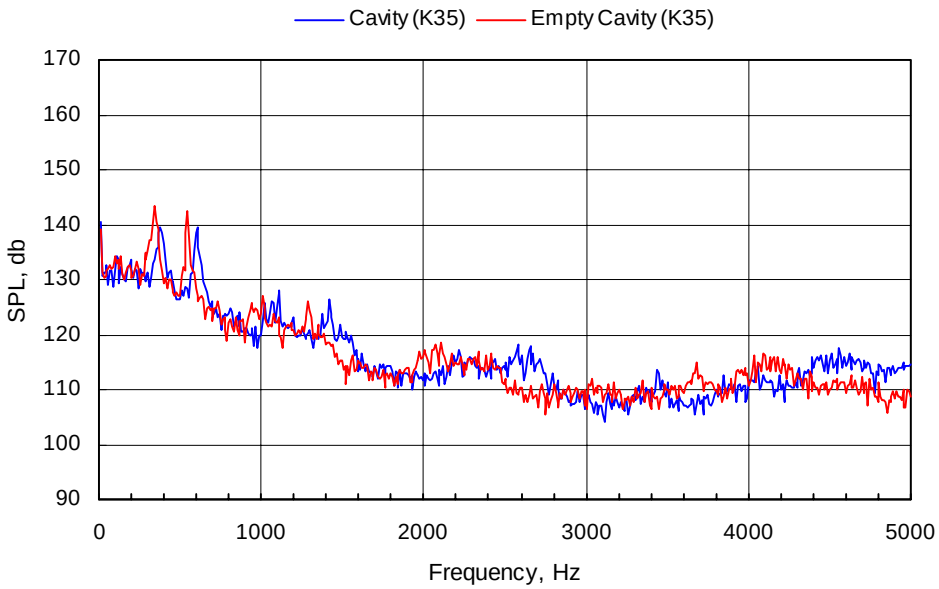

p. Comparison with and without the GMPM store model centerline at Z/D = 0.3, transducers at X/L = 0.36

Figure 30. Continued.

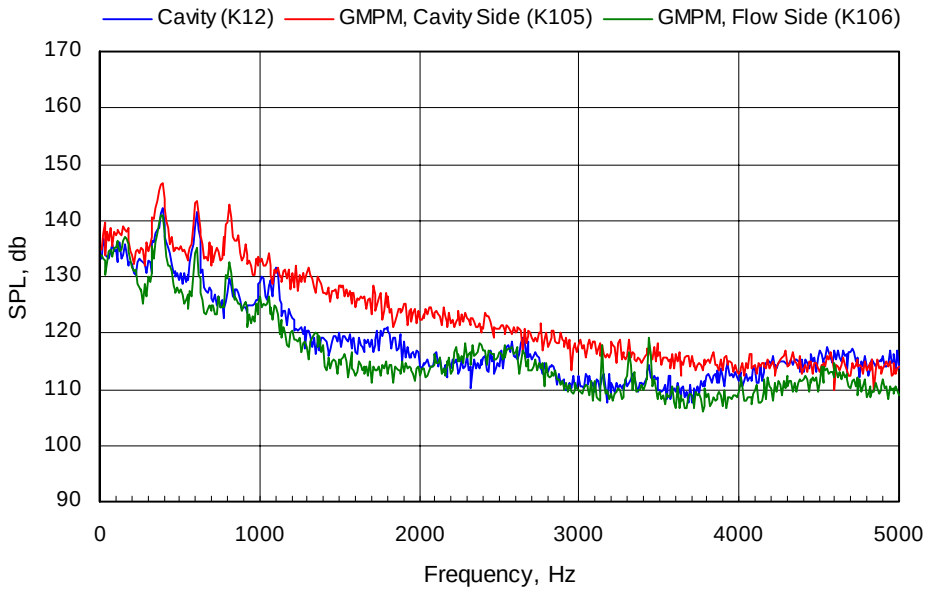

q. GMPM store model centerline at Z/D = 0.3, transducers at X/L = 0.51

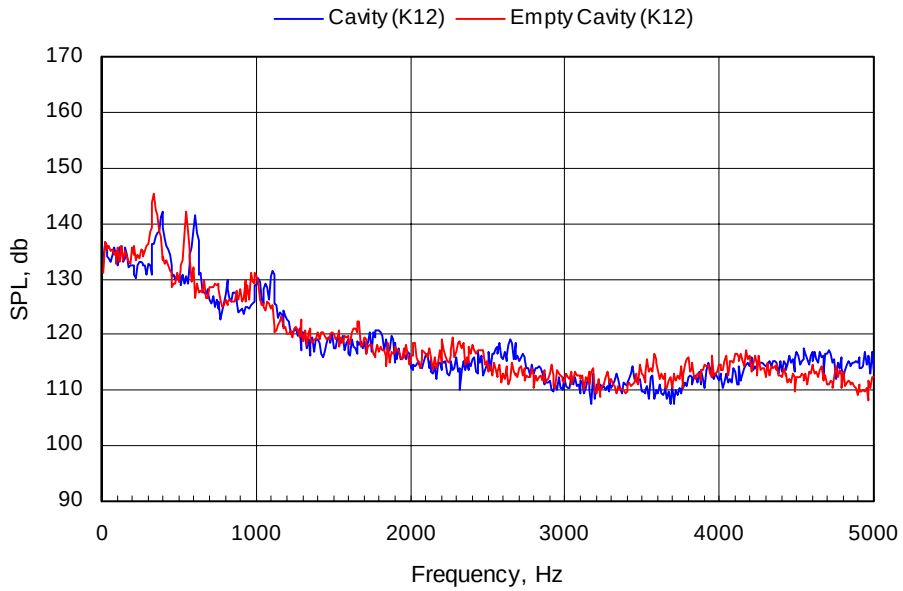

r. Comparison with and without the GMPM store model centerline at Z/D = 0.3, transducers at X/L = 0.51

Figure 30. Concluded.

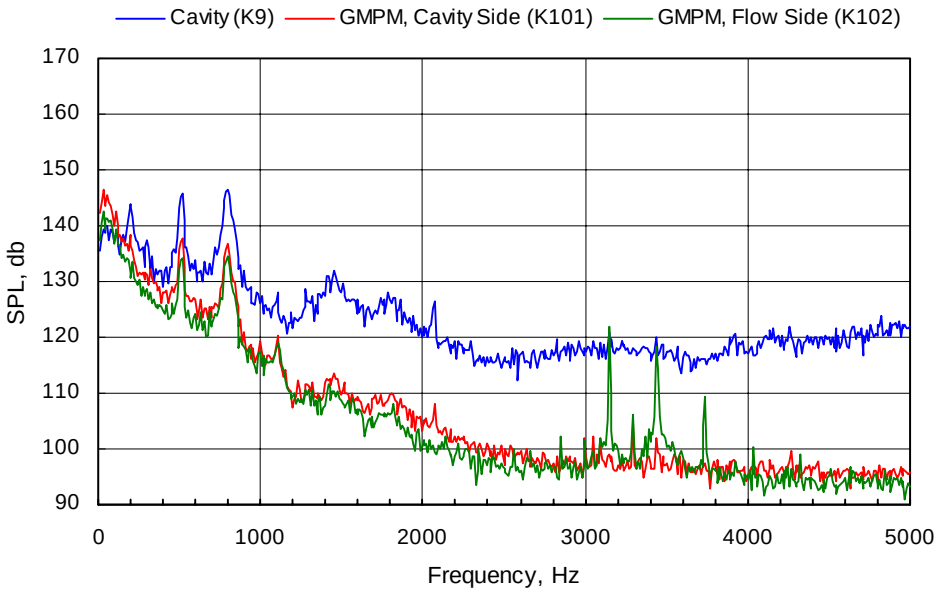

a. GMPM store model centerline at Z/D = –0.75, transducers at X/L = 0.26

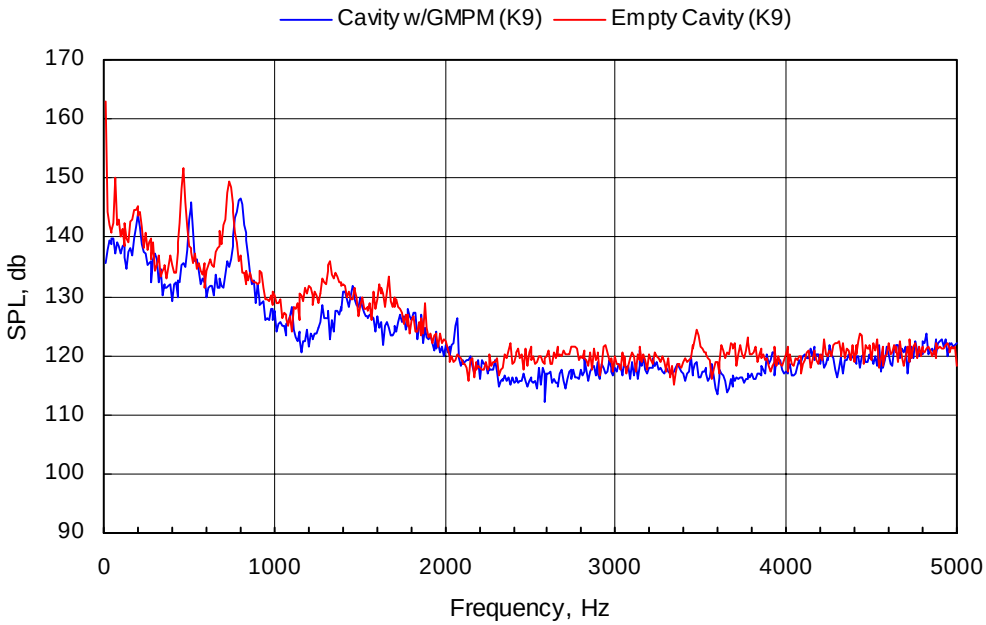

b. Comparison with and without the GMPM store model centerline at Z/D = –0.75, transducers at X/L = 0.26

Figure 31. Comparison of spectra sensed on the floor of an L/D = 4.5 cavity with spectra sensed on the body of a generic store model, M_∞ = 0.95.

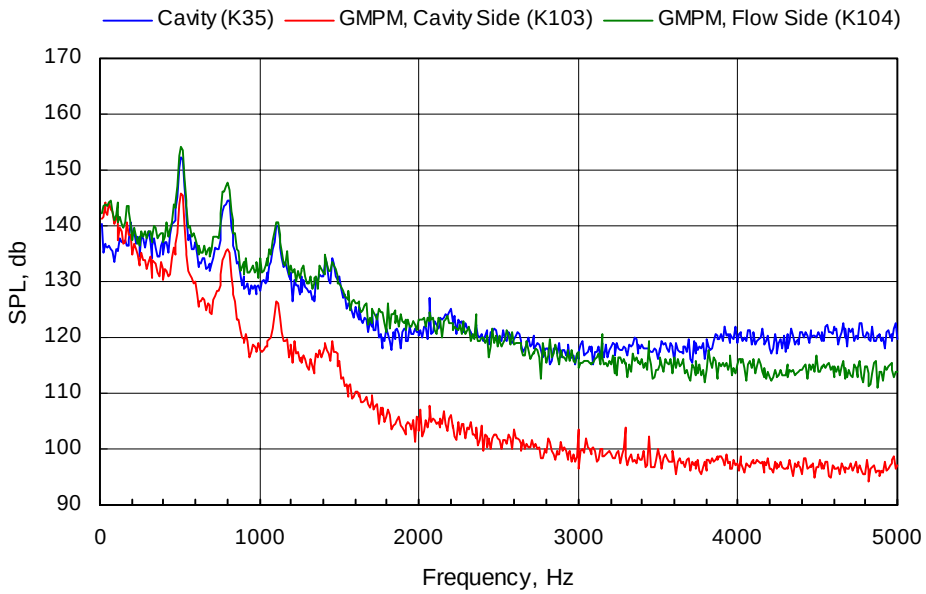

c. GMPM store model centerline at Z/D = –0.75, transducers at X/L = 0.36

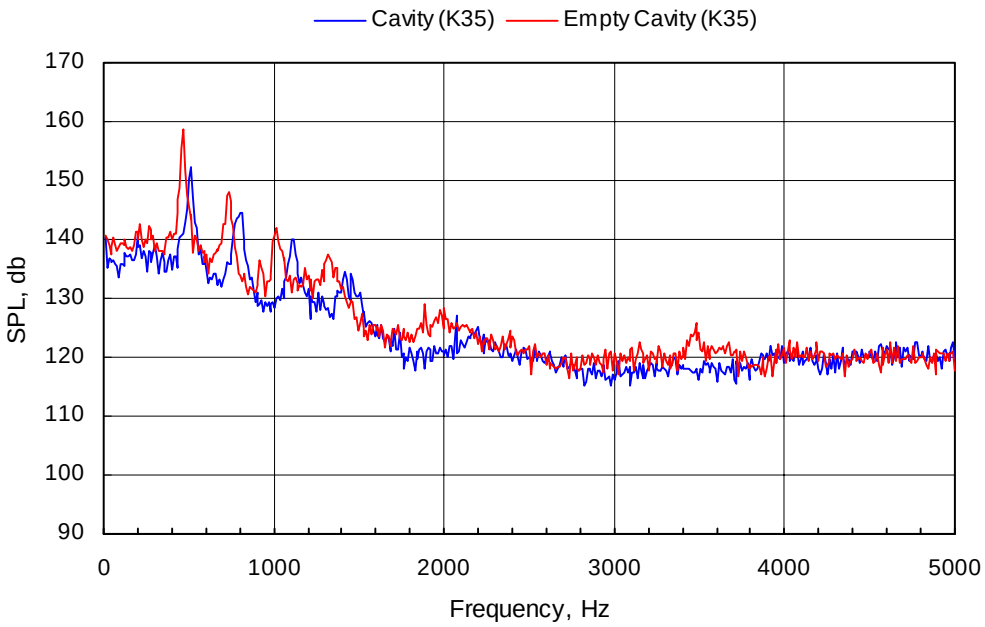

d. Comparison with and without the GMPM store model centerline at Z/D = –0.75, transducers at X/L = 0.36

Figure 31. Continued.

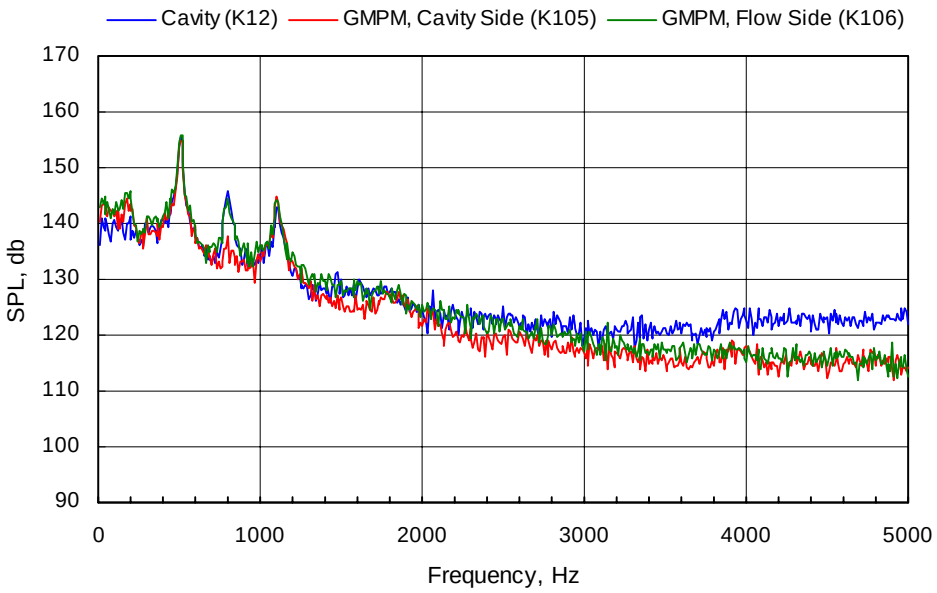

e. GMPM store model centerline at Z/D = –0.75, transducers at X/L = 0.51

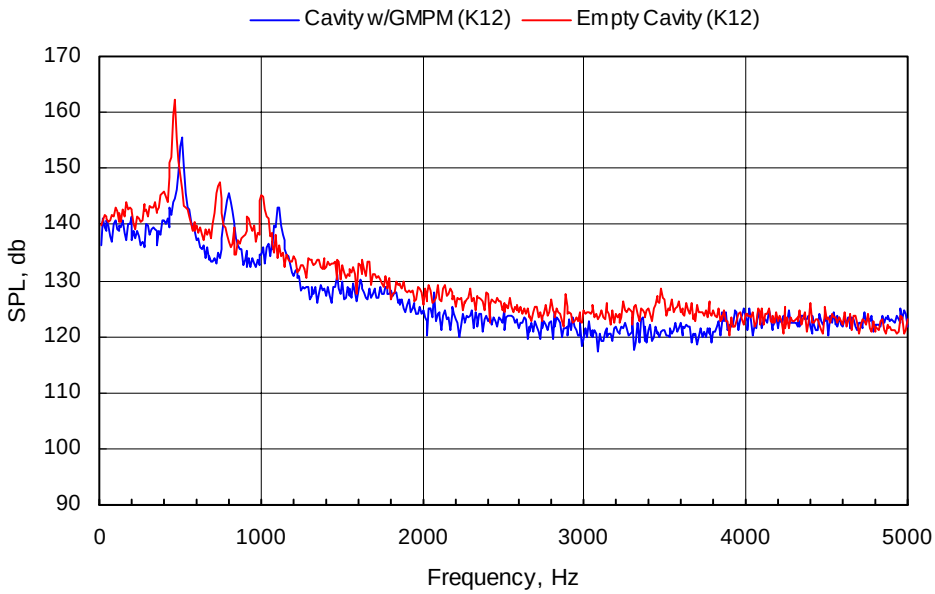

f. Comparison with and without the GMPM store model centerline at Z/D = –0.75, transducers at X/L = 0.51

Figure 31. Continued.

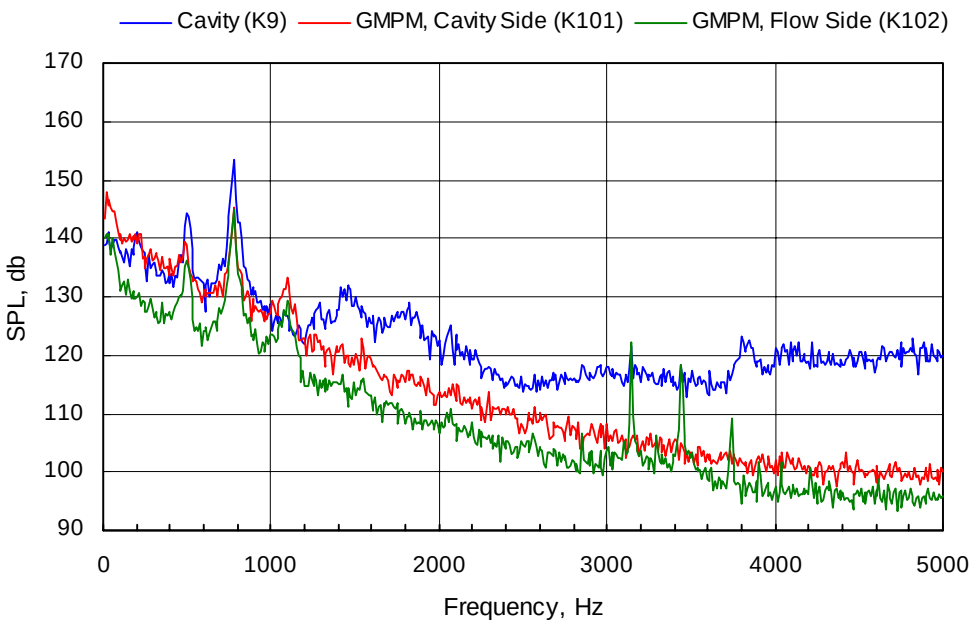

g. GMPM store model centerline at Z/D = 0, transducers at X/L = 0.26

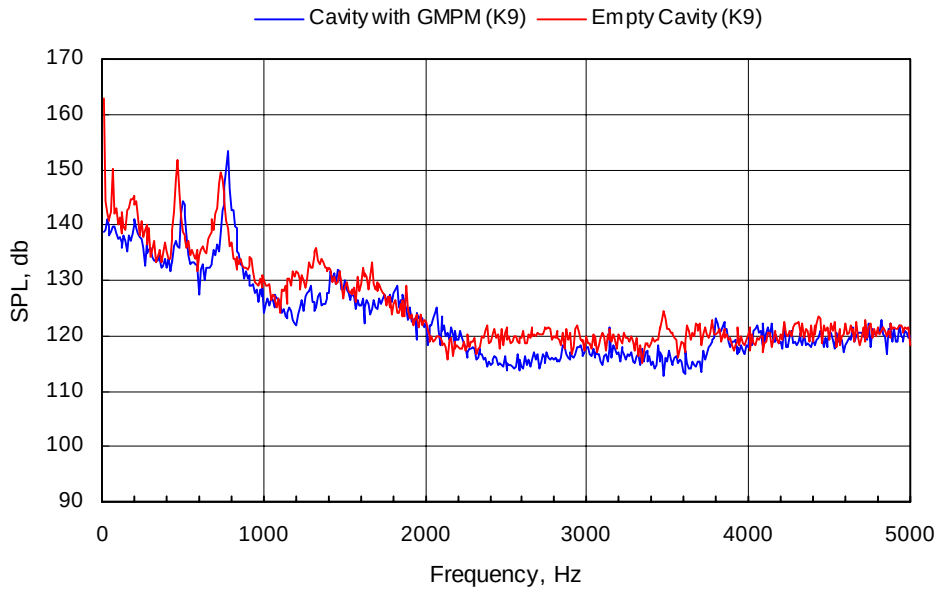

h. Comparison with and without the GMPM store model centerline at Z/D = 0, transducers at X/L = 0.26

Figure 31. Continued.

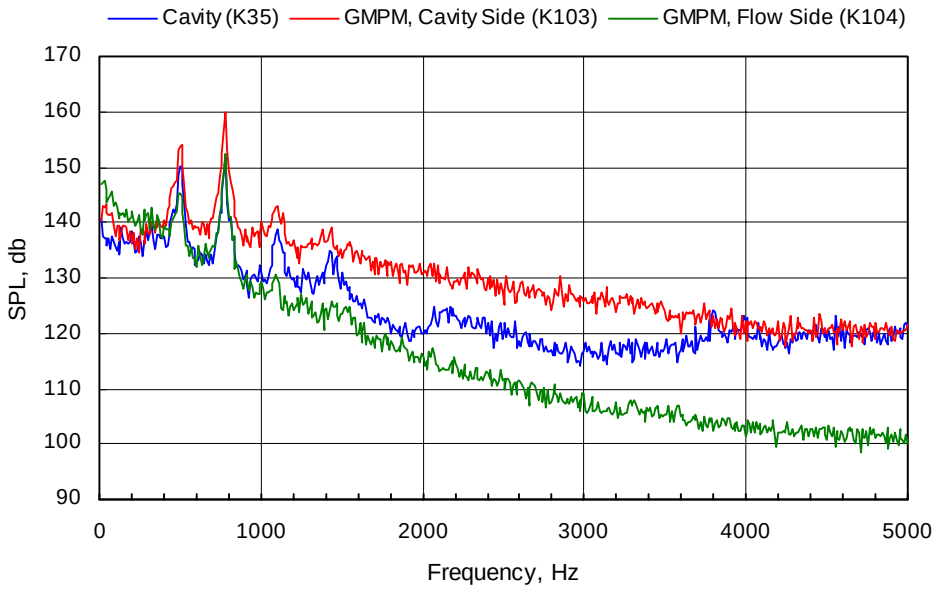

i. GMPM store model centerline at Z/D = 0, transducers at X/L = 0.36

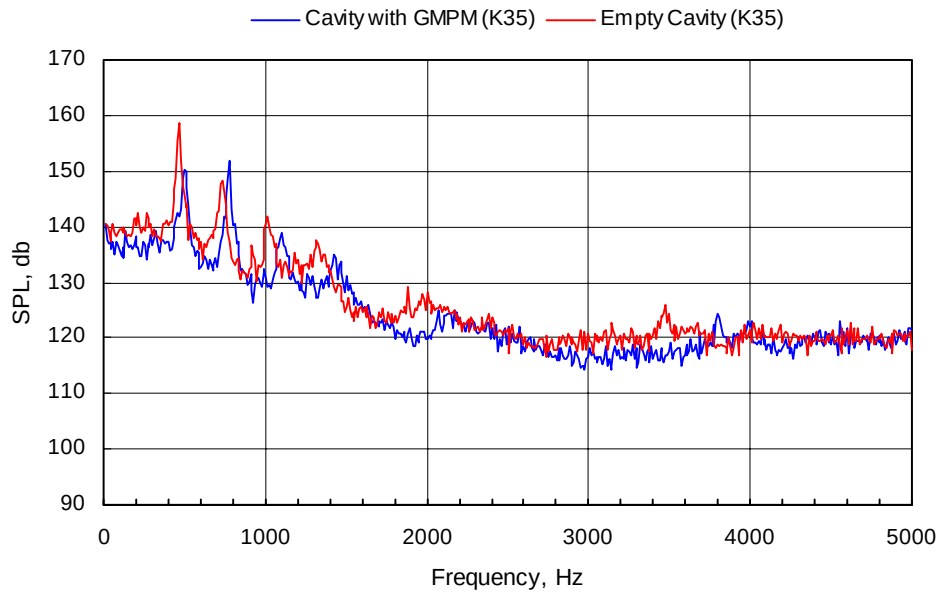

j. Comparison with and without the GMPM store model centerline at Z/D = 0, transducers at X/L = 0.36

Figure 31. Continued.

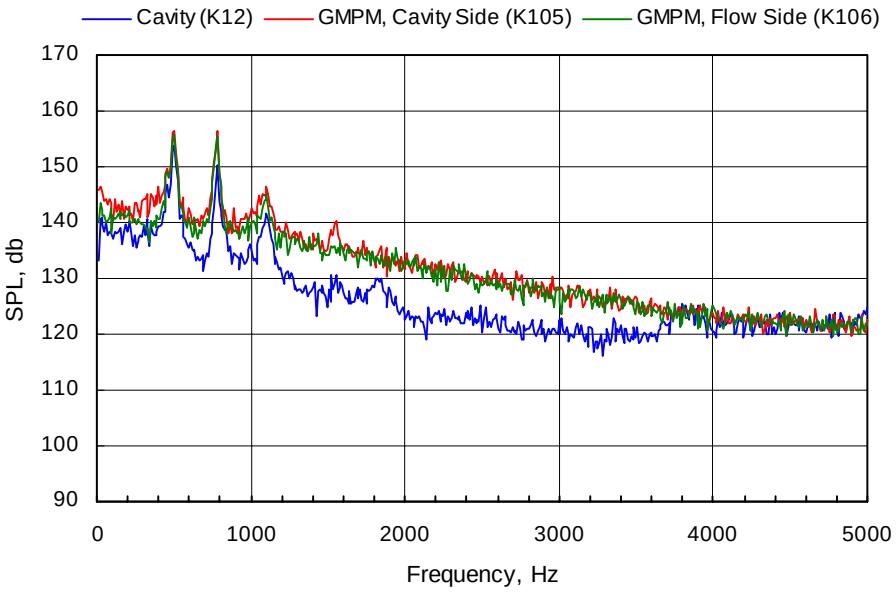

k. GMPM store model centerline at Z/D = 0, transducers at X/L = 0.51

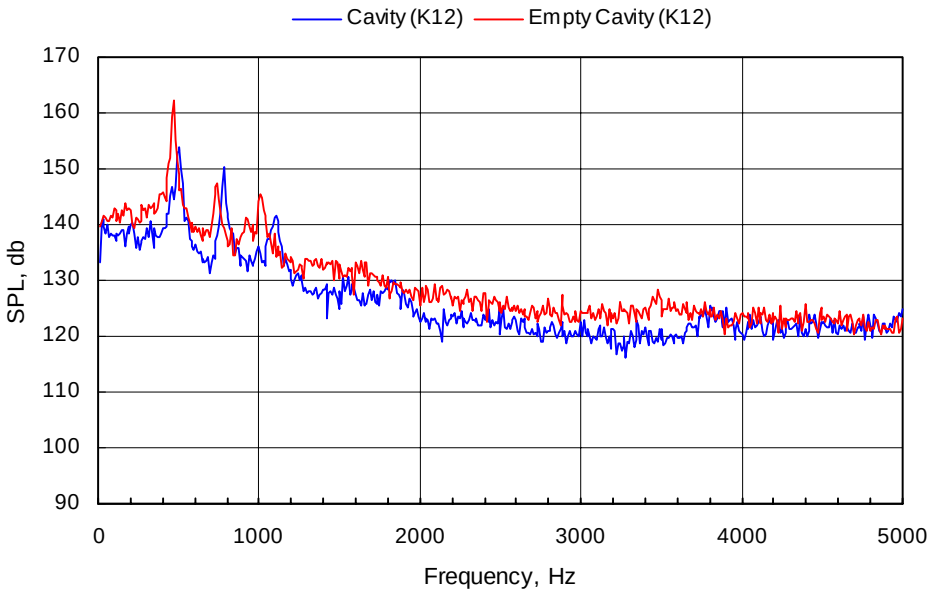

l. Comparison with and without the GMPM store model centerline at Z/D = 0, transducers at X/L = 0.51

Figure 31. Continued.

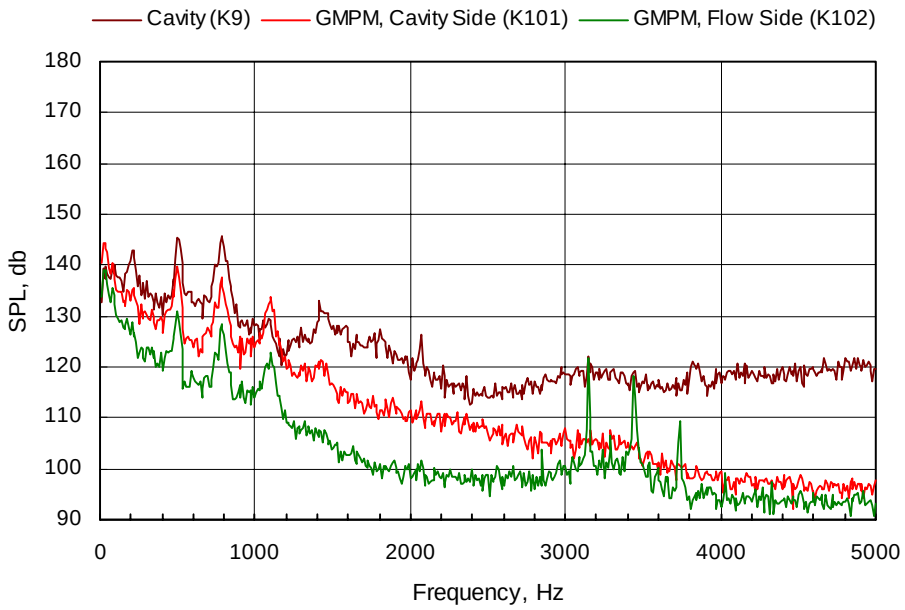

m. GMPM store model centerline at Z/D = 0.3, transducers at X/L = 0.26

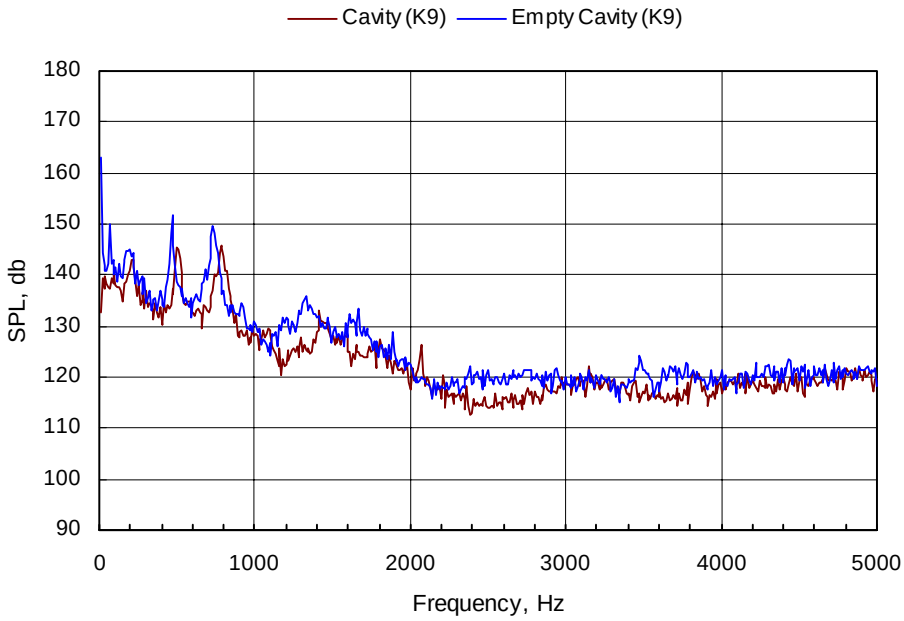

n. Comparison with and without the GMPM store model centerline at Z/D = 0.3, transducers at X/L = 0.26

Figure 31. Continued.

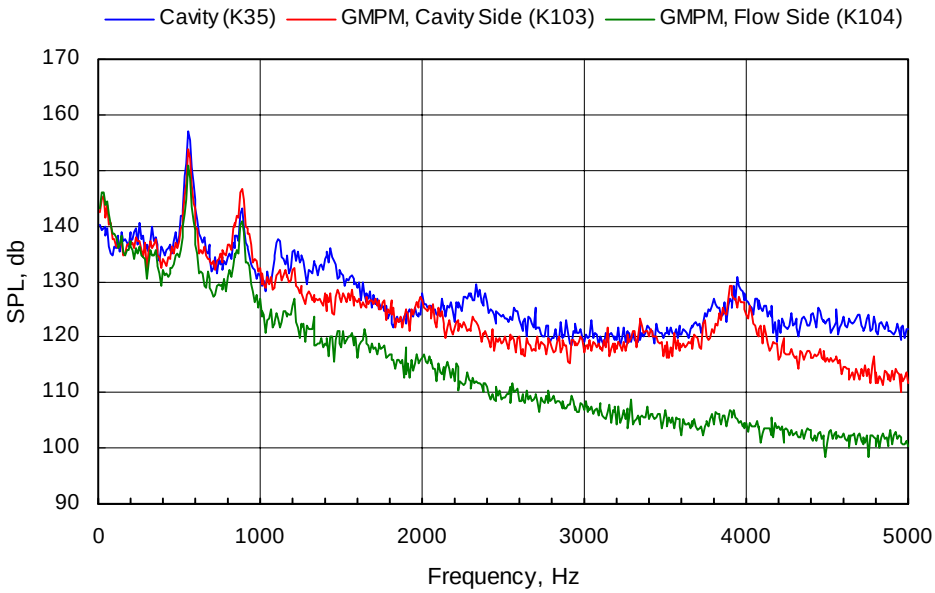

o. GMPM store model centerline at Z/D = 0.3, transducers at X/L = 0.36

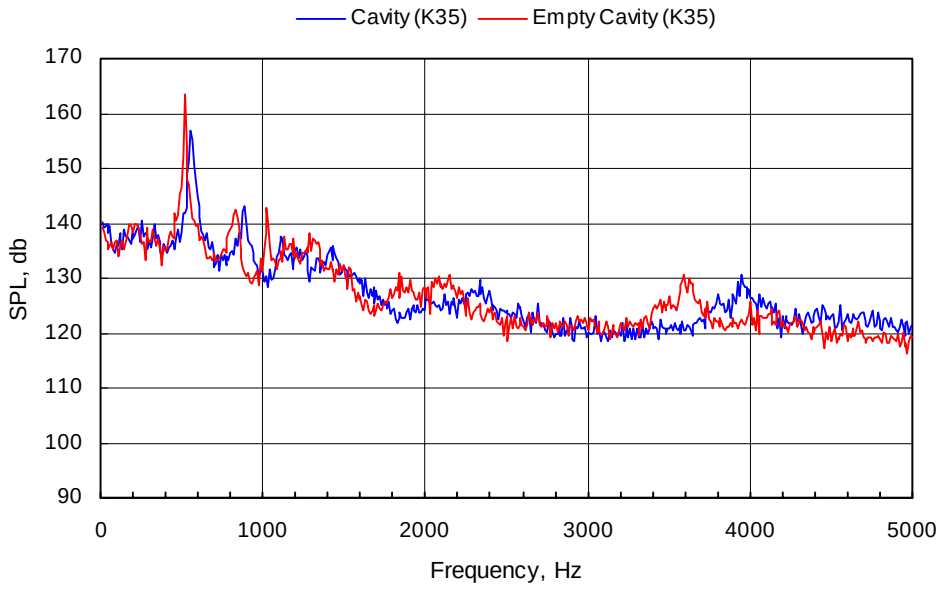

p. Comparison with and without the GMPM store model centerline at Z/D = 0.3, transducers at X/L = 0.36

Figure 31. Continued.

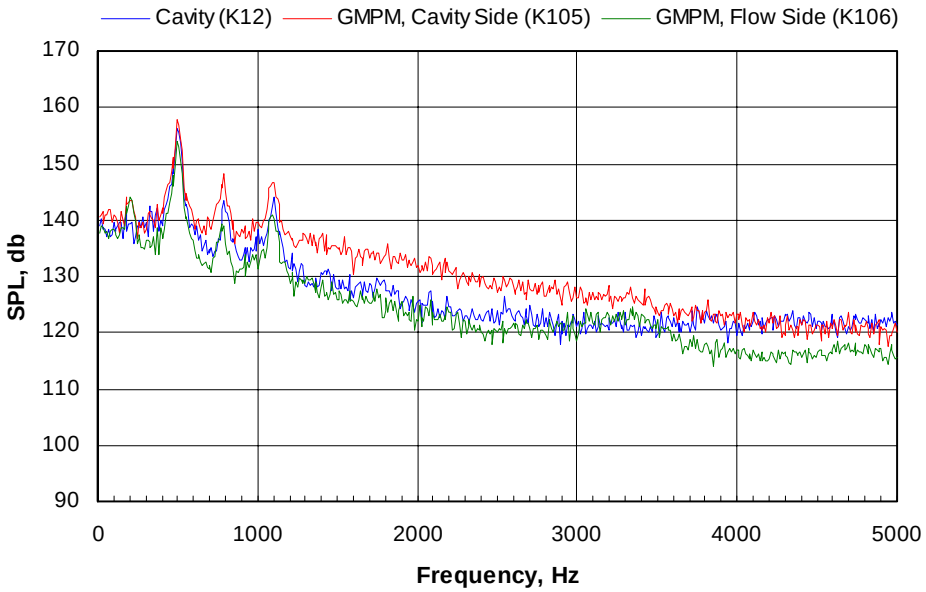

q. GMPM store model centerline at Z/D = 0.3, transducers at X/L = 0.51

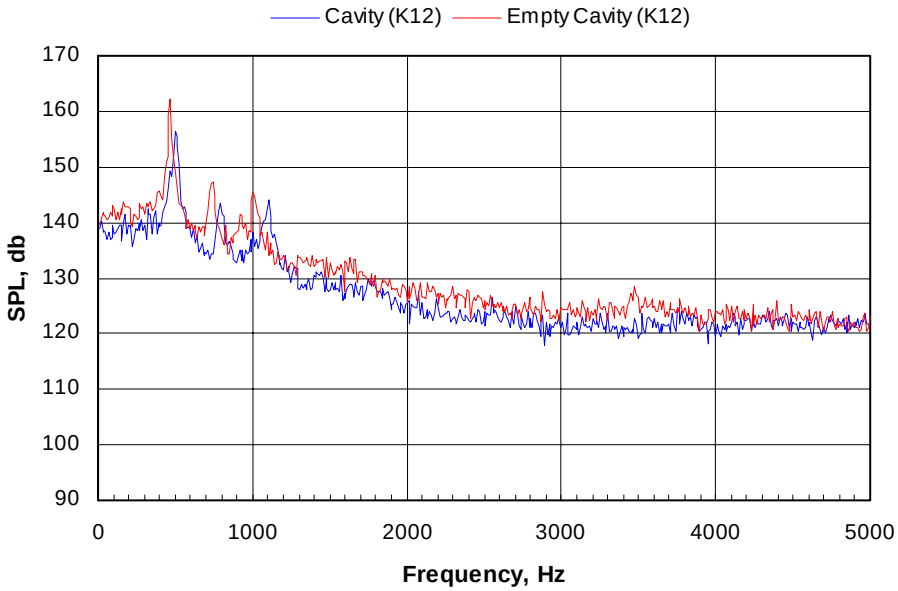

r. Comparison with and without the GMPM store model centerline at Z/D = 0.3, transducers at X/L = 0.51

Figure 31. Concluded.

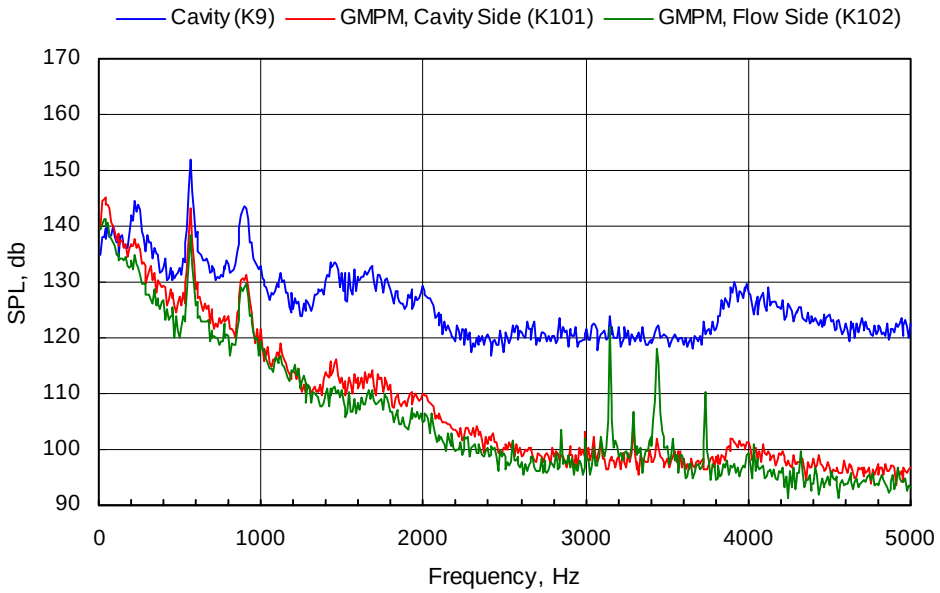

a. GMPM store model centerline at Z/D = –0.75, transducers at X/L = 0.26

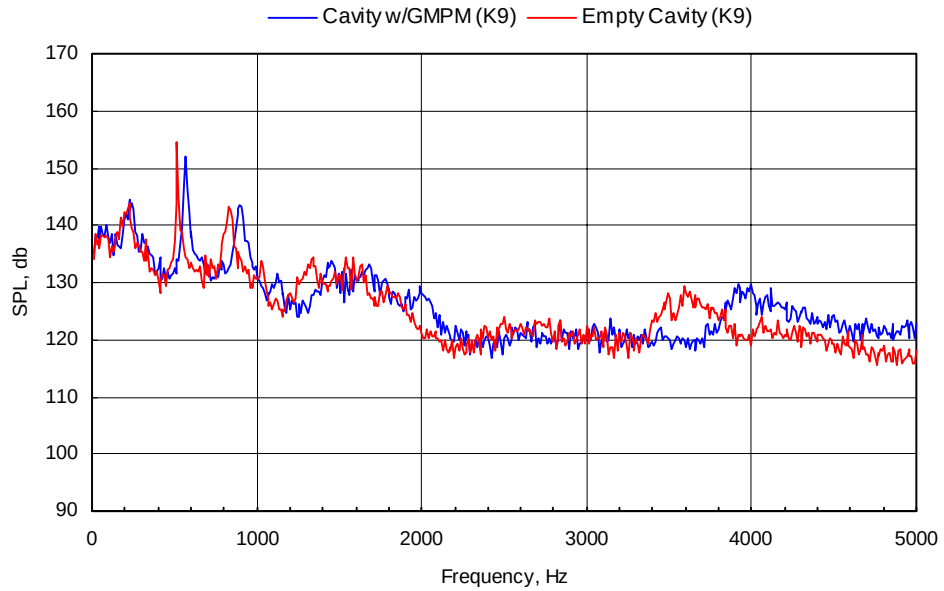

b. Comparison with and without the GMPM store model centerline at Z/D = –0.75, transducers at X/L = 0.26

Figure 32. Comparison of spectra sensed on the floor of an L/D = 4.5 cavity with spectra sensed on the body of a generic store model, M_∞ = 1.20.

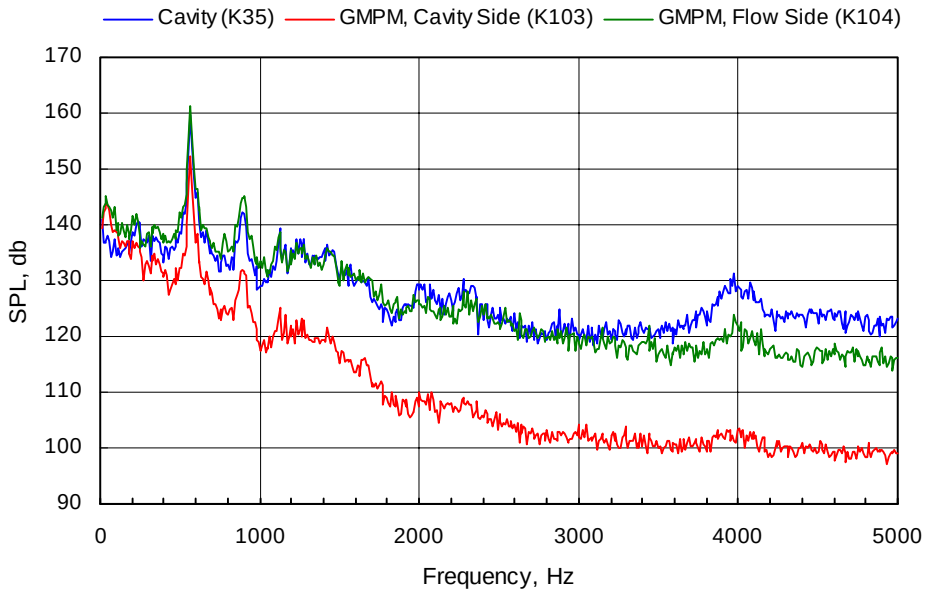

c. GMPM store model centerline at Z/D = –0.75, transducers at X/L = 0.36

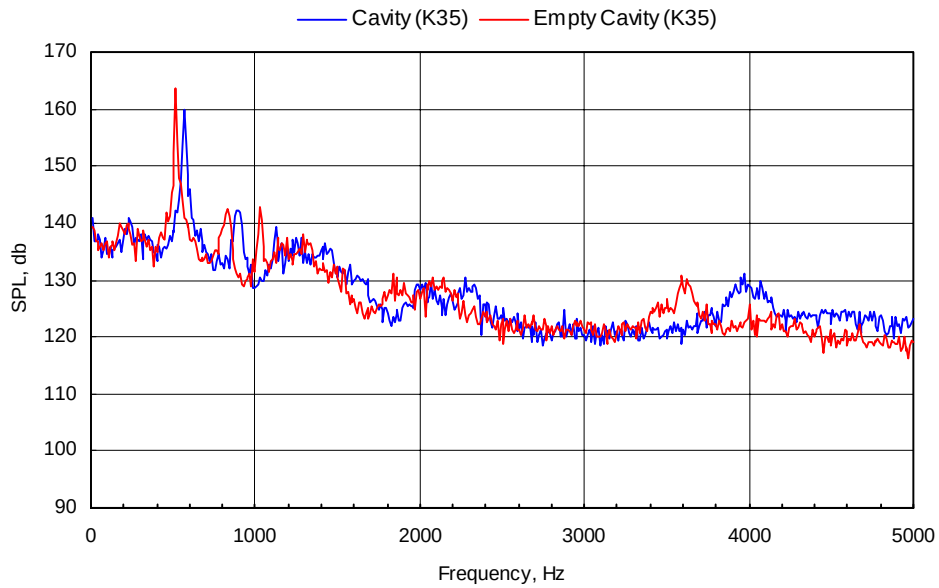

d. Comparison with and without the GMPM store model centerline at Z/D = –0.75, transducers at X/L = 0.36

Figure 32. Continued.

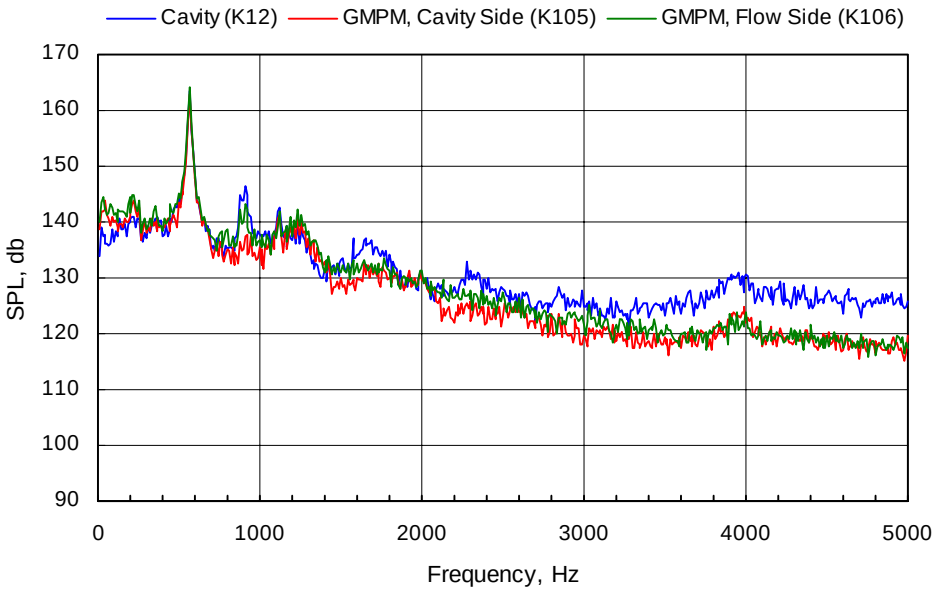

e. GMPM store model centerline at Z/D = –0.75, transducers at X/L = 0.51

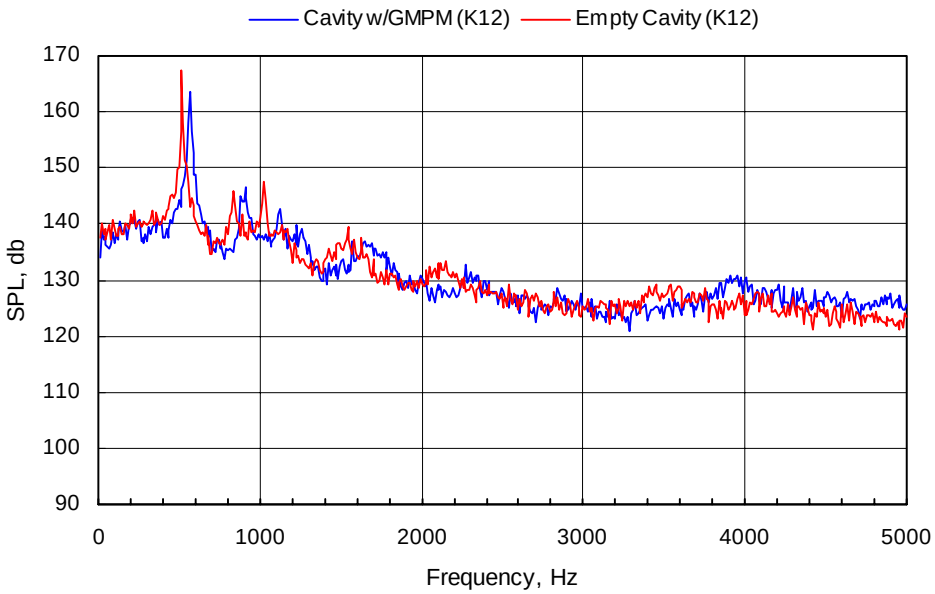

f. Comparison with and without the GMPM store model centerline at Z/D = –0.75, transducers at X/L = 0.51

Figure 32. Continued.

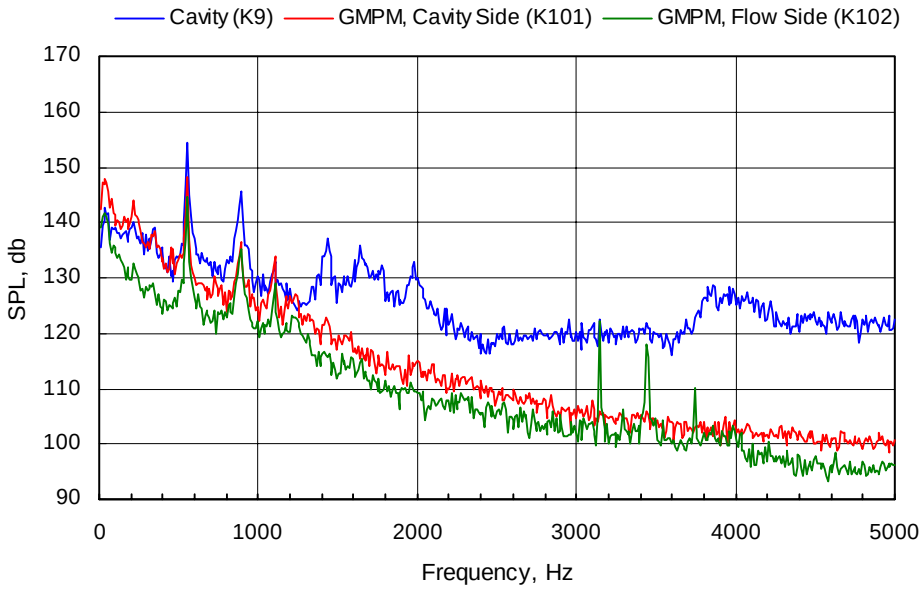

g. GMPM store model centerline at Z/D = 0, transducers at X/L = 0.26

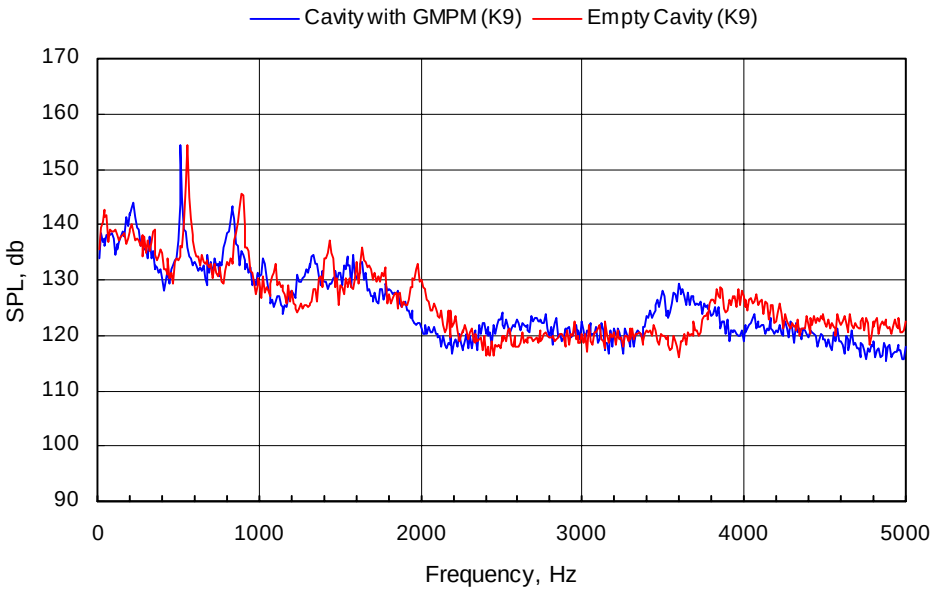

h. Comparison with and without the GMPM store model centerline at Z/D = 0, transducers at X/L = 0.26

Figure 32. Continued.

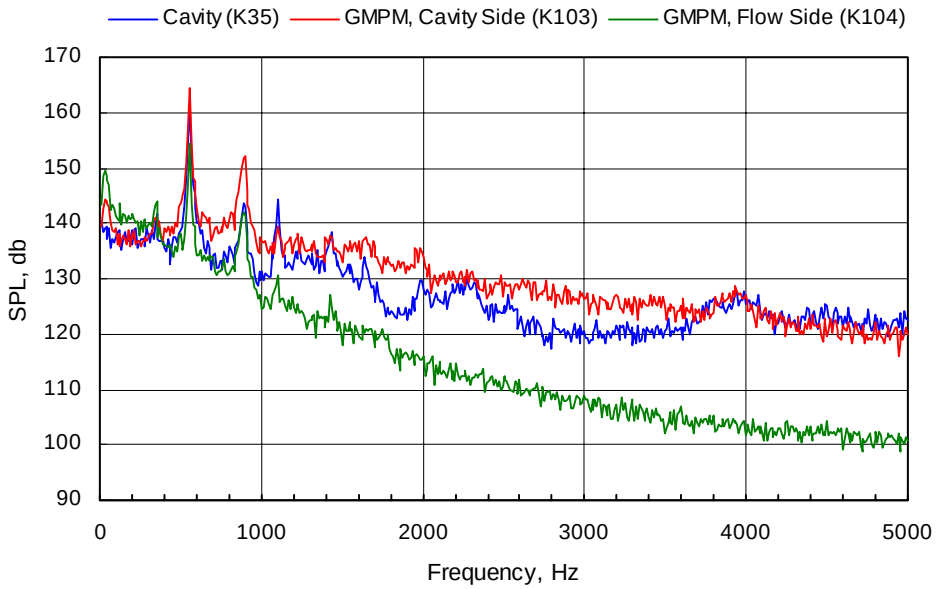

i. GMPM store model centerline at Z/D = 0, transducers at X/L = 0.36

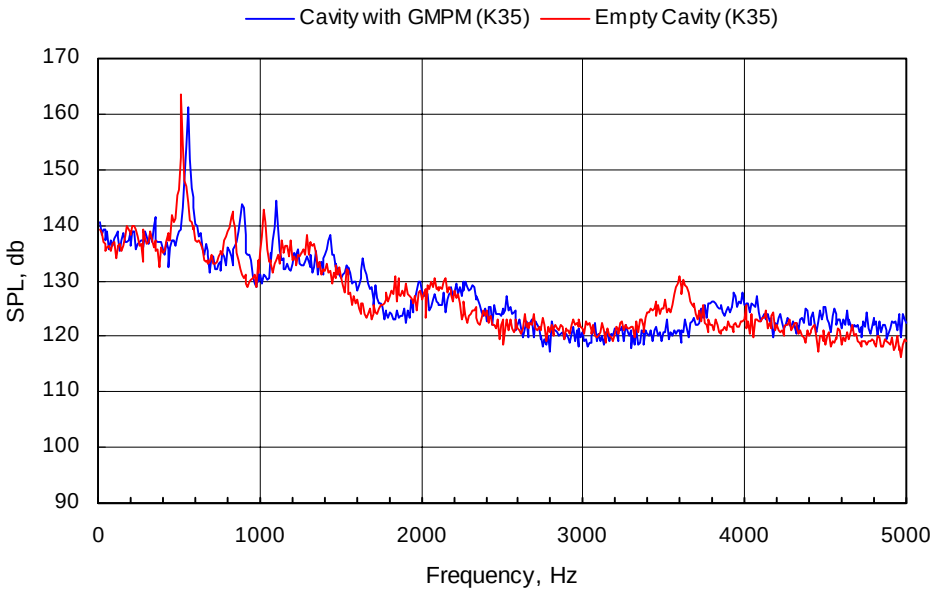

j. Comparison with and without the GMPM store model centerline at Z/D = 0, transducers at X/L = 0.36

Figure 32. Continued.

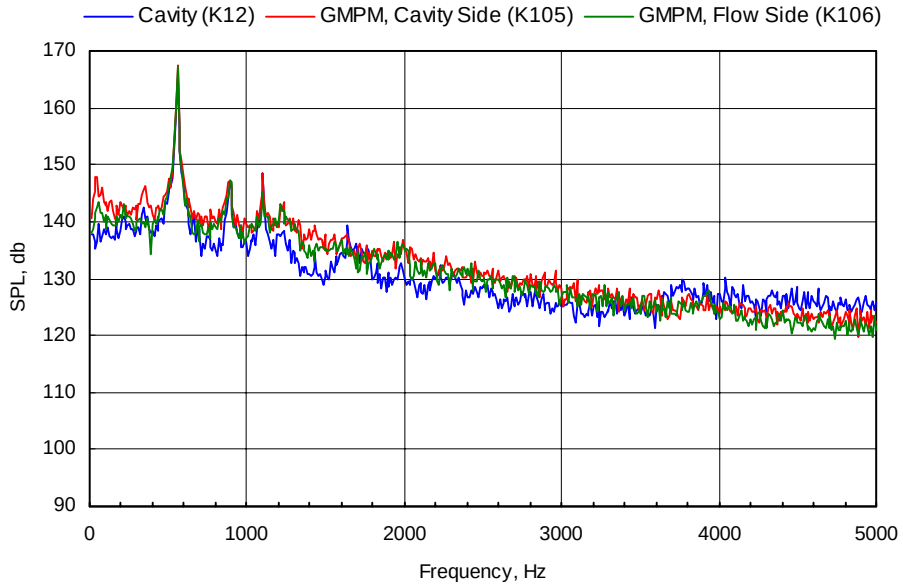

k. GMPM store model centerline at Z/D = 0, transducers at X/L = 0.51

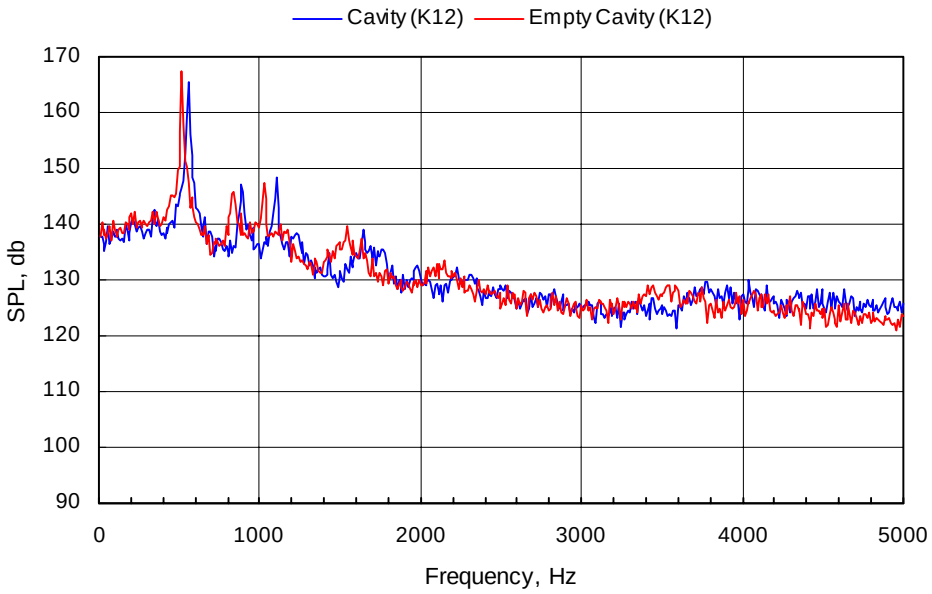

l. Comparison with and without the GMPM store model centerline at Z/D = 0, transducers at X/L = 0.51

Figure 32. Continued.

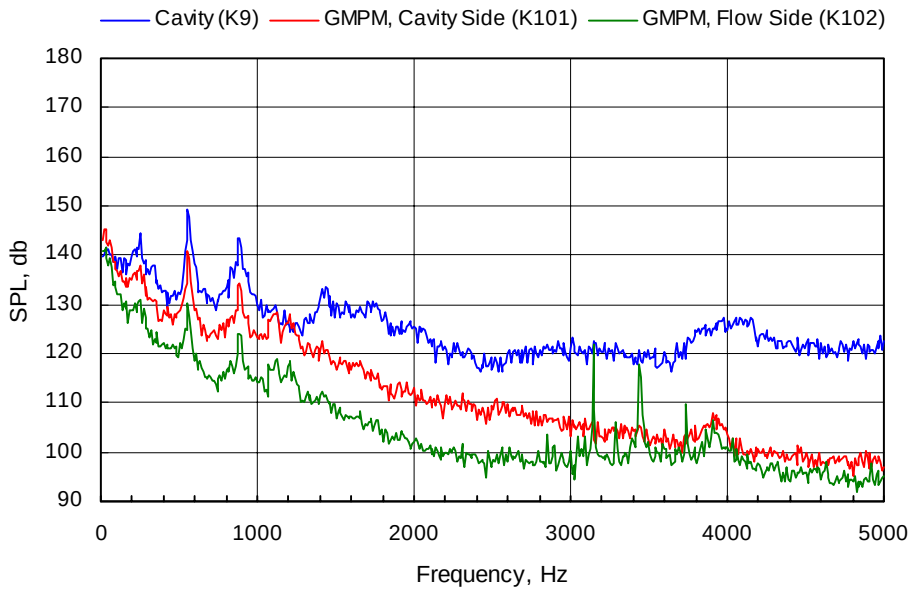

m. GMPM store model centerline at Z/D = 0.3, transducers at X/L = 0.26

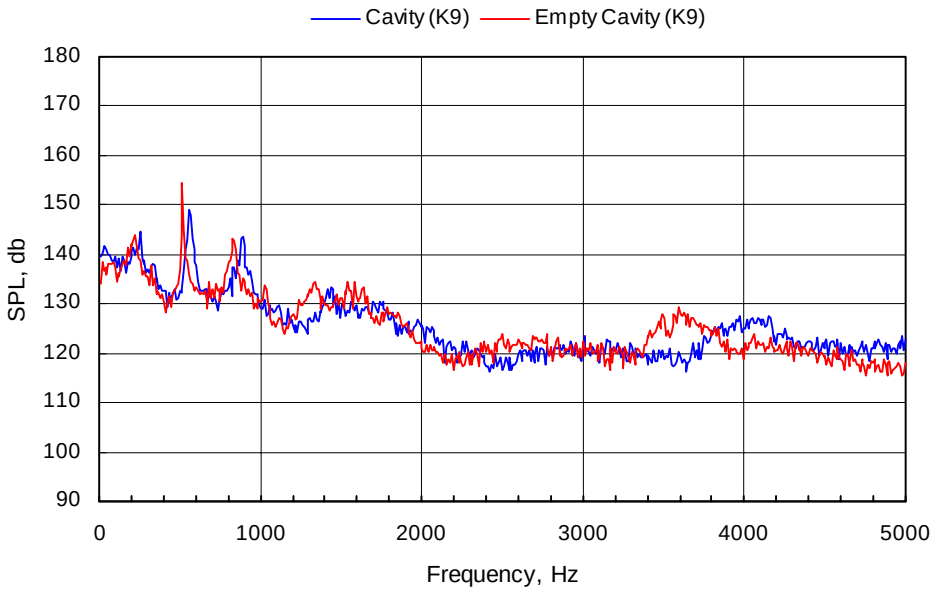

n. Comparison with and without the GMPM store model centerline at Z/D = 0.3, transducers at X/L = 0.26

Figure 32. Continued.

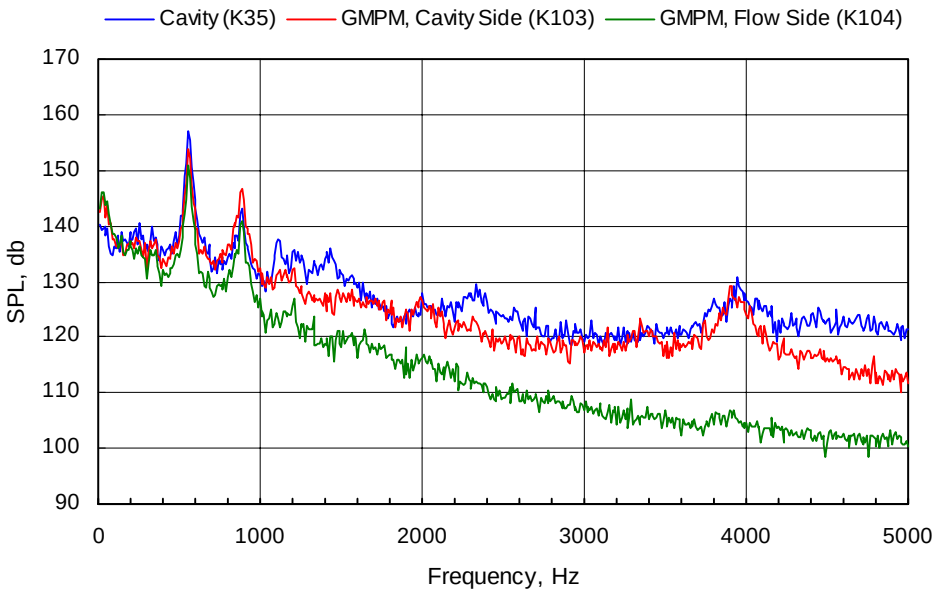

o. GMPM store model centerline at Z/D = 0.3, transducers at X/L = 0.36

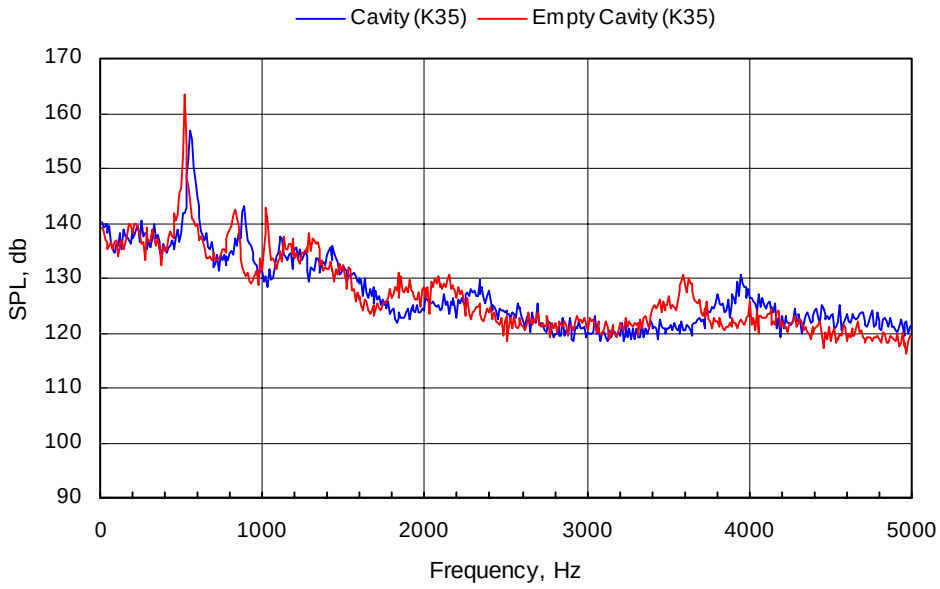

p. Comparison with and without the GMPM store model centerline at Z/D = 0.3, transducers at X/L = 0.36

Figure 32. Continued.

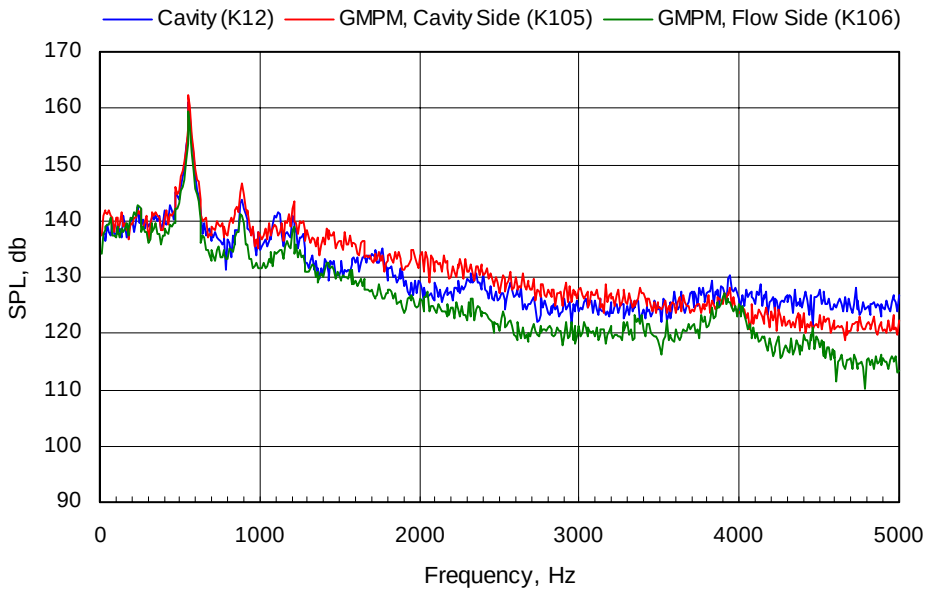

q. GMPM store model centerline at Z/D = 0.3, transducers at X/L = 0.51

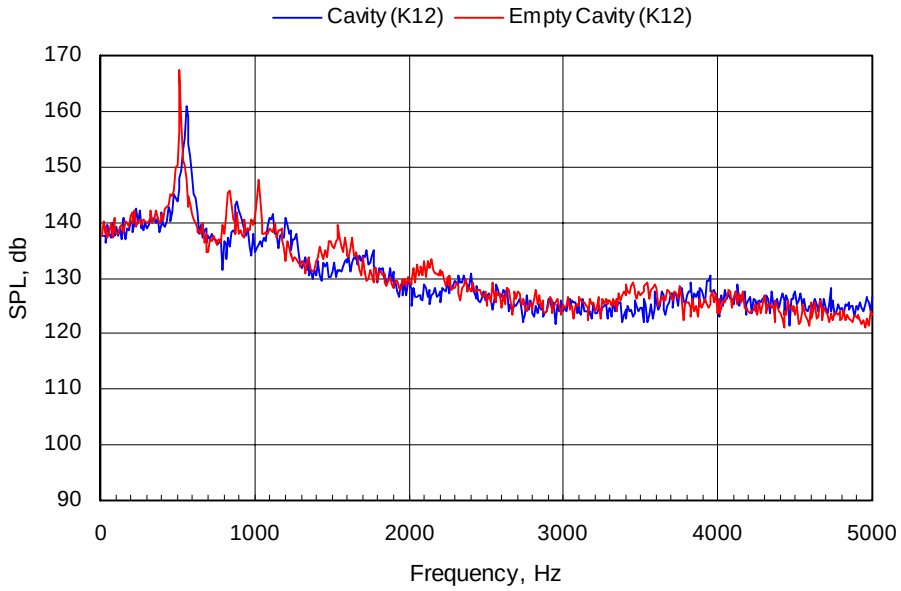

r. Comparison with and without the GMPM store model centerline at Z/D = 0.3, transducers at X/L = 0.51

Figure 32. Concluded.

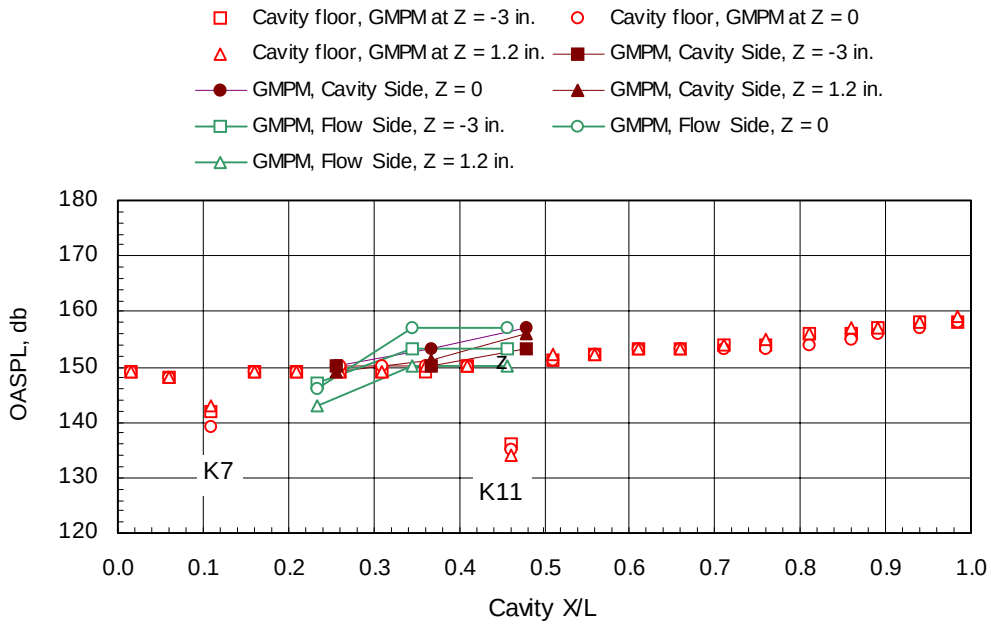

a. M_∞ = 0.60

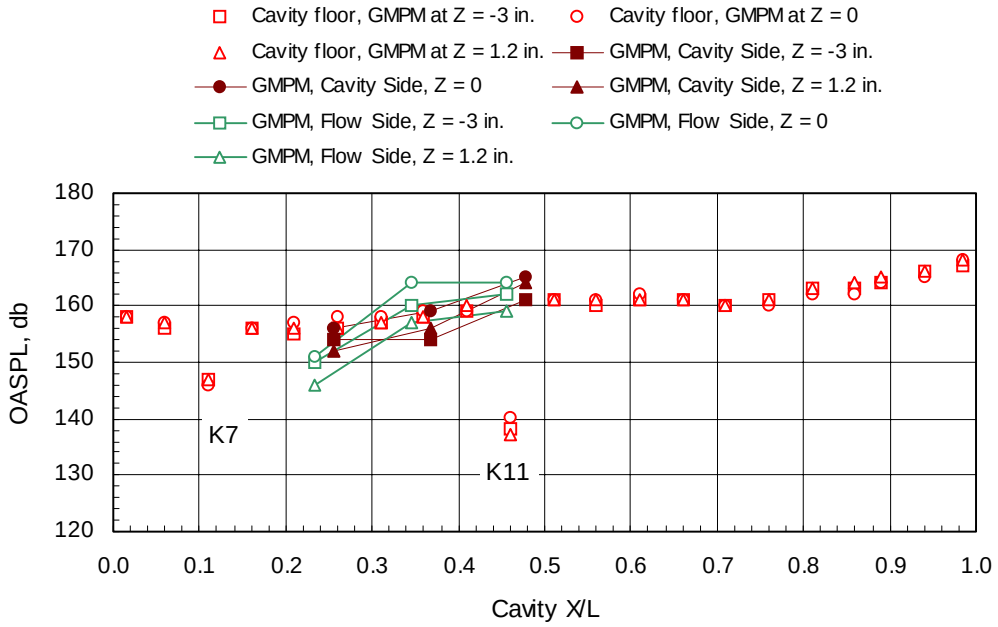

b. M_∞ = 0.95

Figure 33. Comparison of OASPL on the bottom of an L/D = 4.5 cavity and on the GMPM store model.

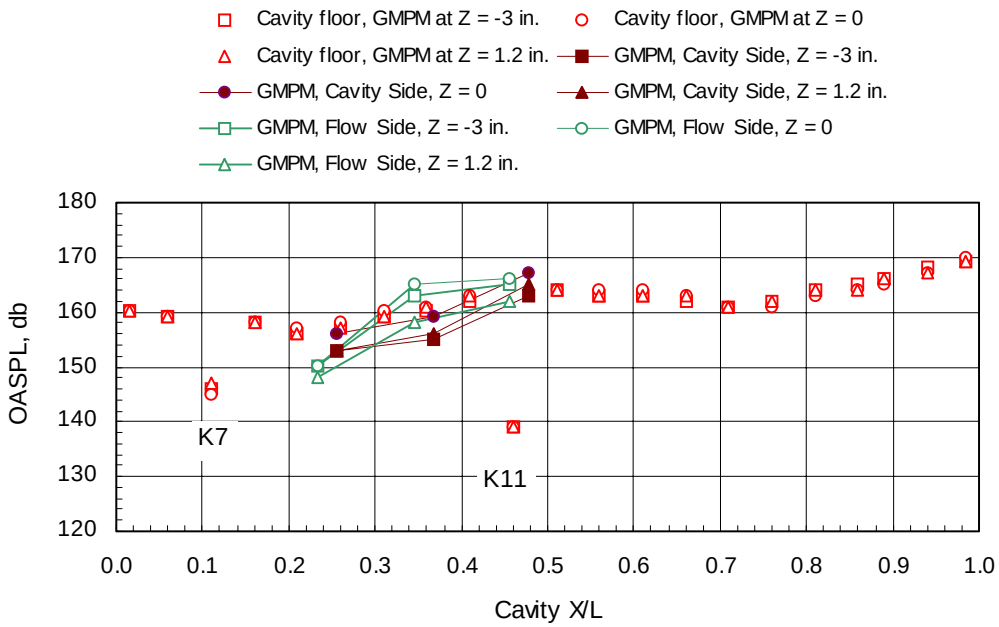

c. M_∞ = 1.05

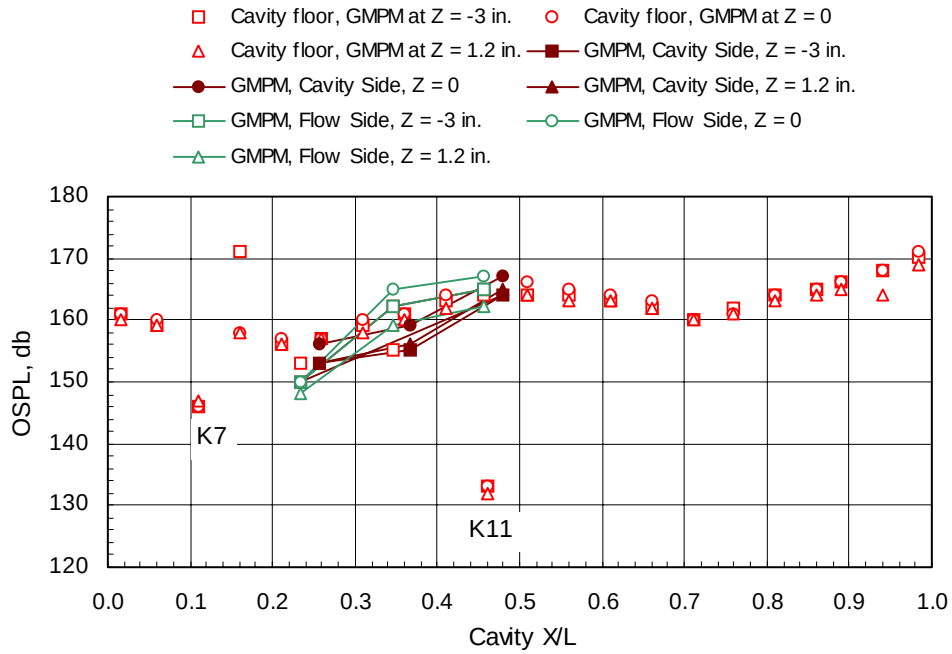

d. M_∞ = 1.20

Figure 33. Concluded.

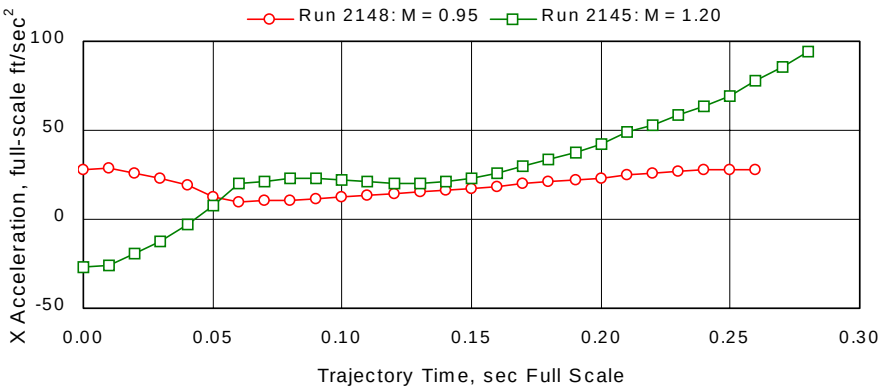

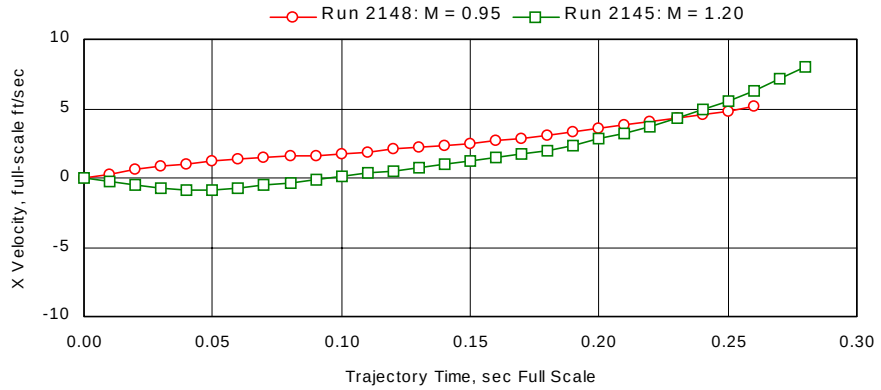

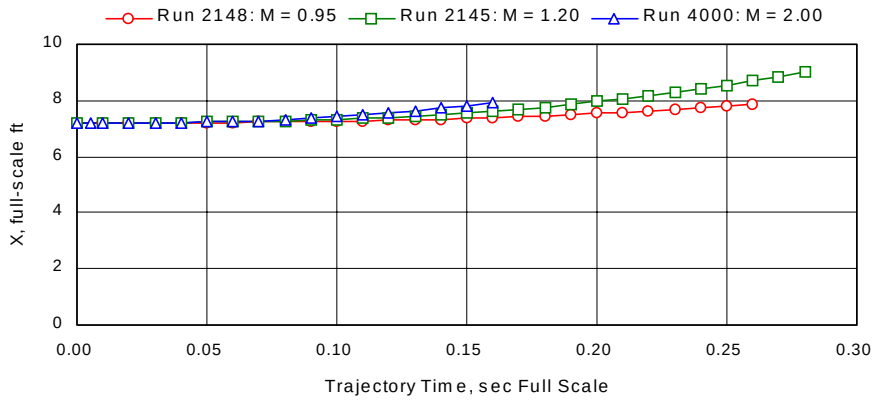

a. X-direction trajectory parameters

Figure 34. Separation trajectories of a store jettisoned from an L/D = 4.5 cavity at transonic and supersonic free-stream Mach numbers.

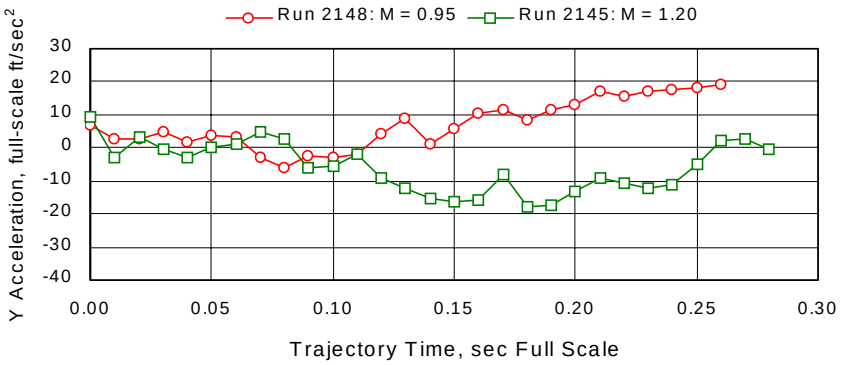

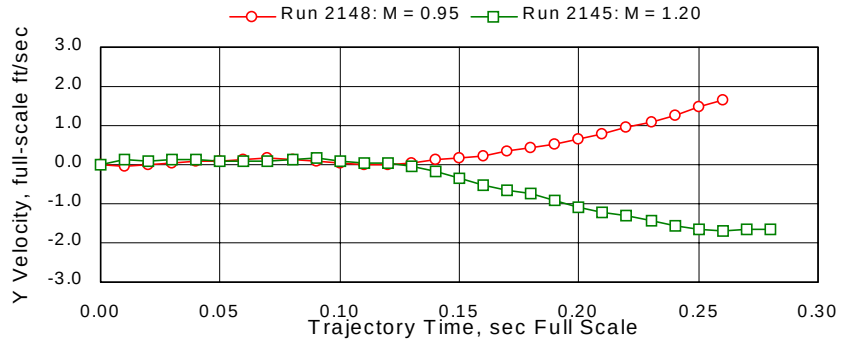

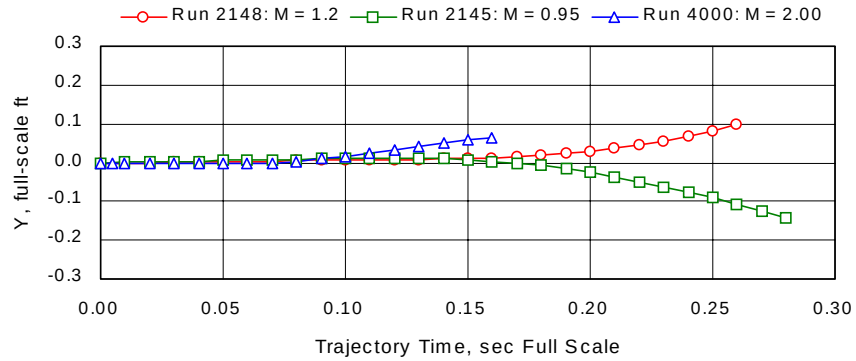

b. Y-direction trajectory parameters
Figure 34. Continued.

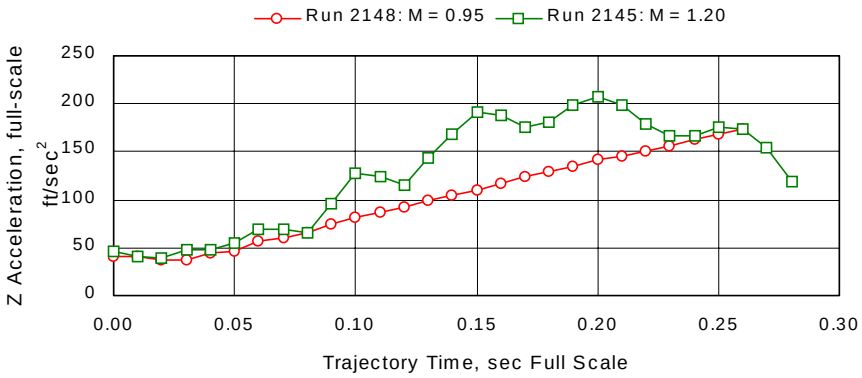

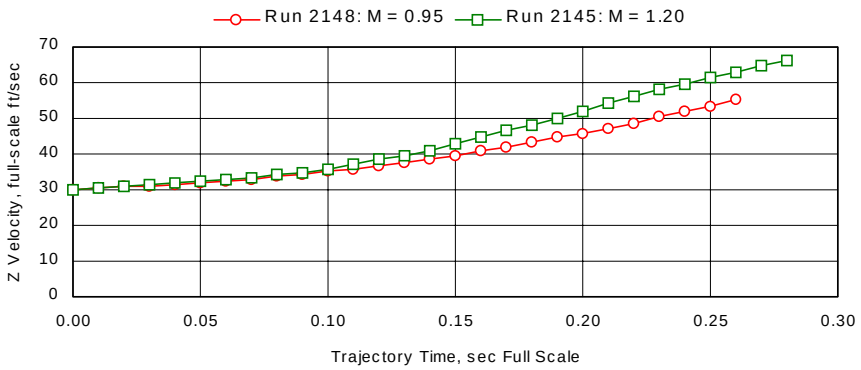

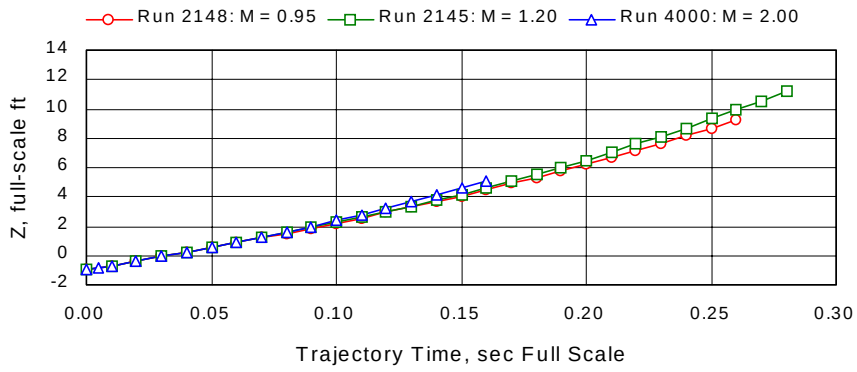

c. Z-direction trajectory parameters
Figure 34. Continued.

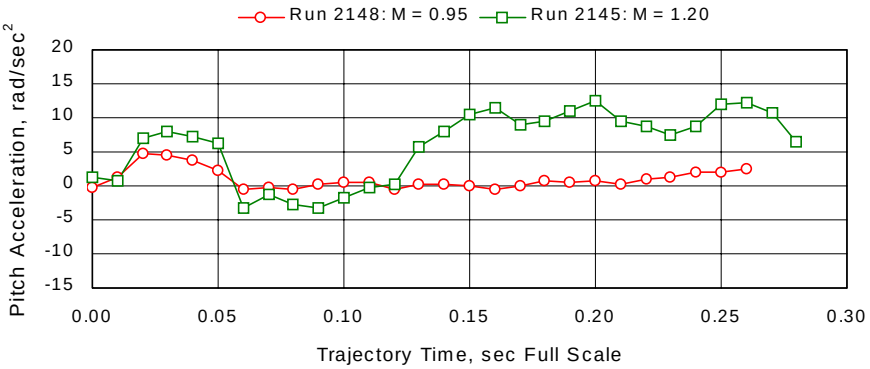

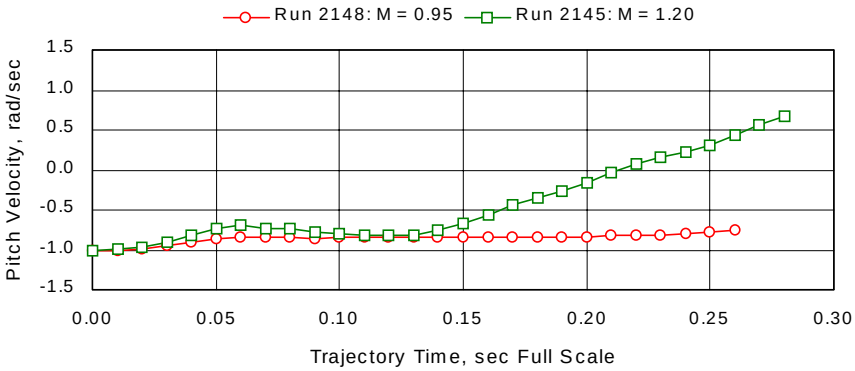

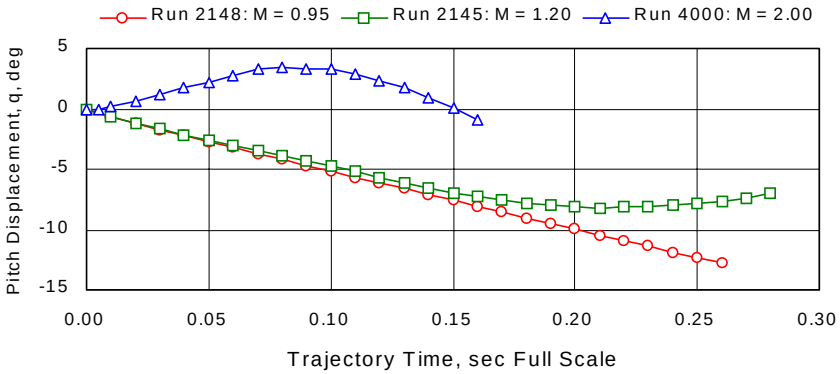

d. Pitching-motion trajectory parameters
Figure 34. Continued.

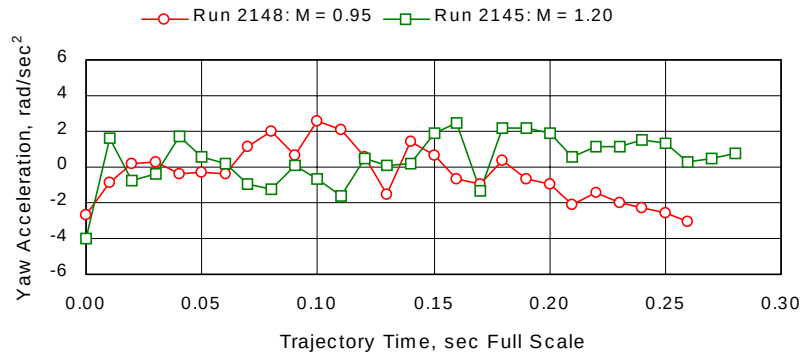

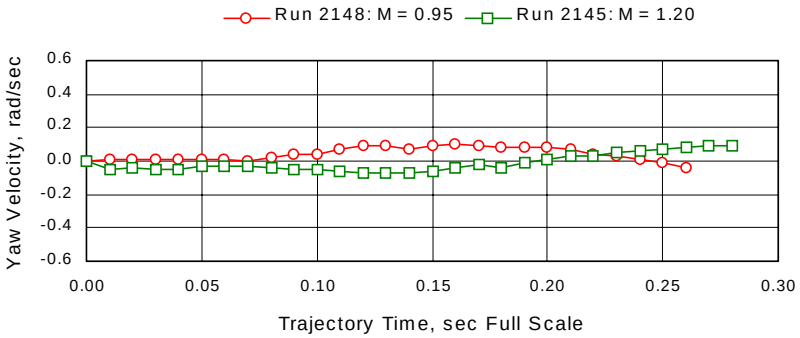

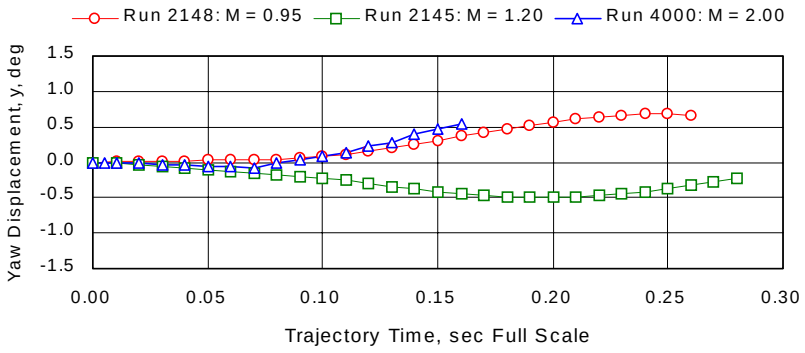

e. Yawing-motion trajectory parameters
Figure 34. Concluded.

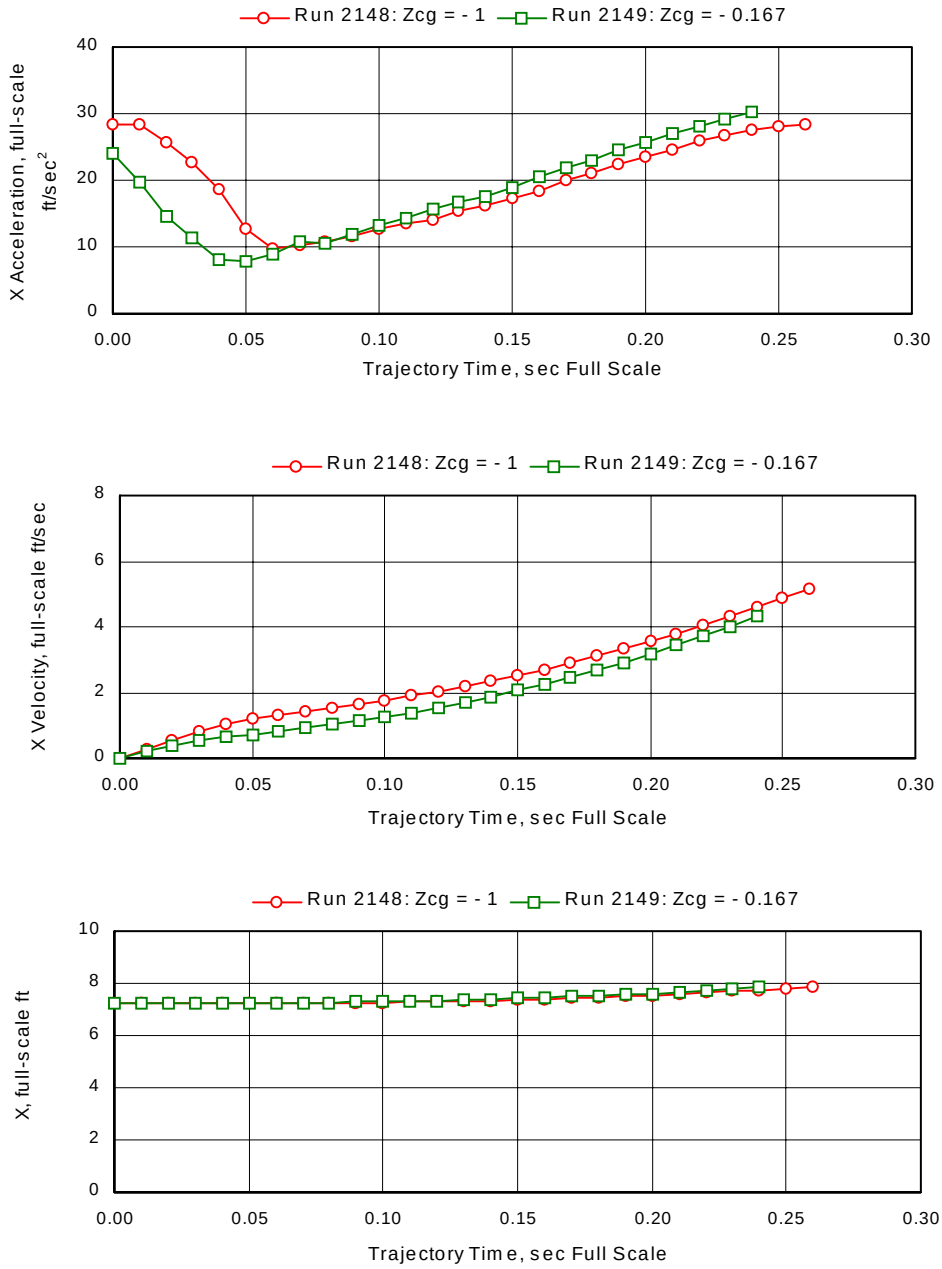

a. X-direction trajectory parameters

Figure 35. Separation trajectories of a store jettisoned from an L/D = 4.5 cavity at two difference release points, M_∞ = 0.95.

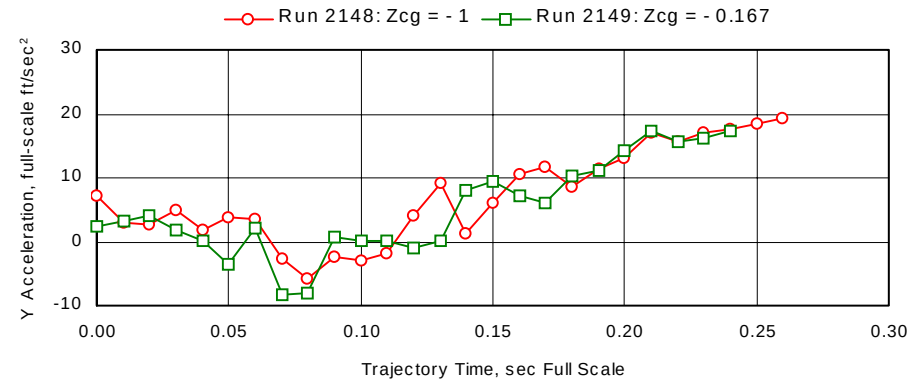

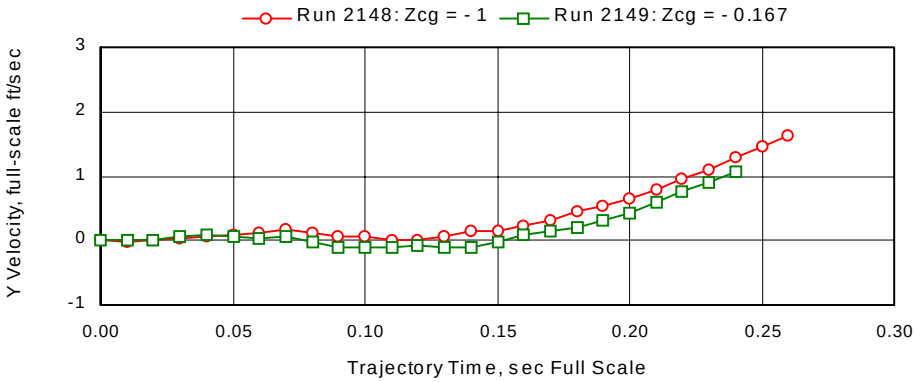

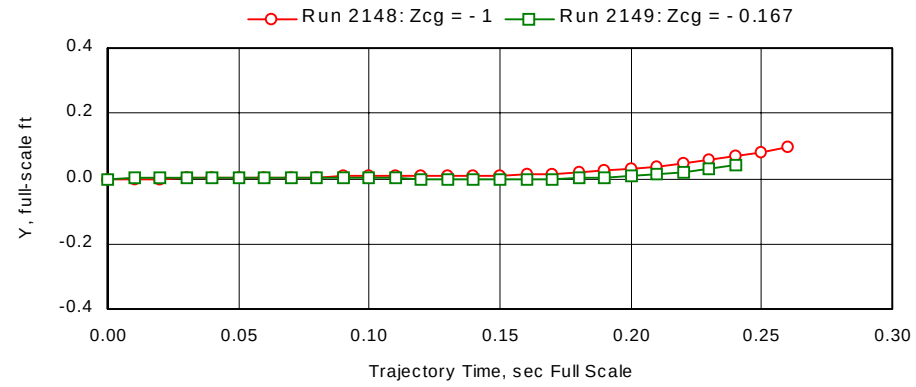

b. Y-direction trajectory parameters
Figure 35. Continued.

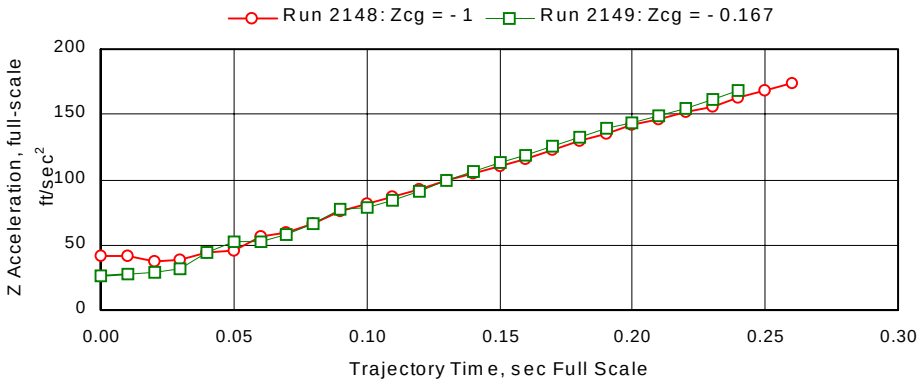

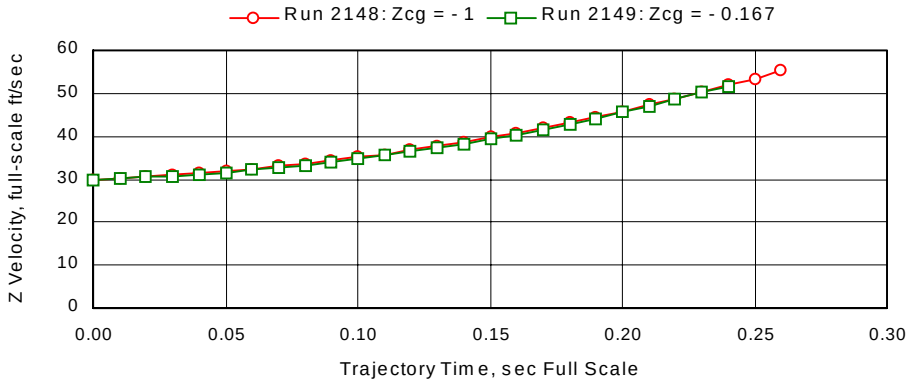

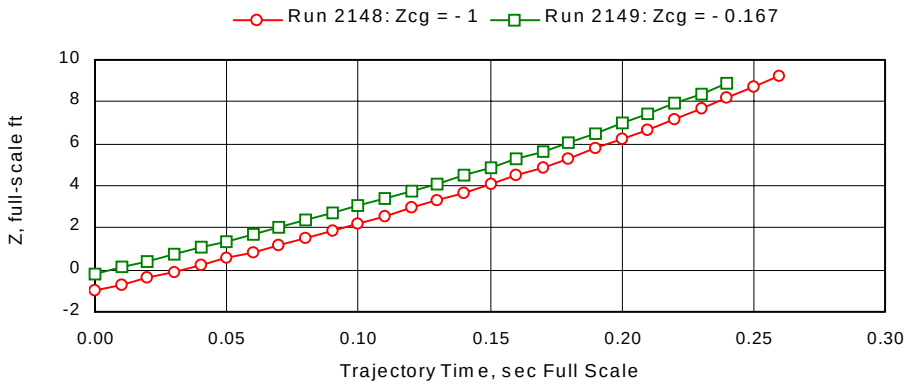

c. Z-direction trajectory parameters
Figure 35. Continued.

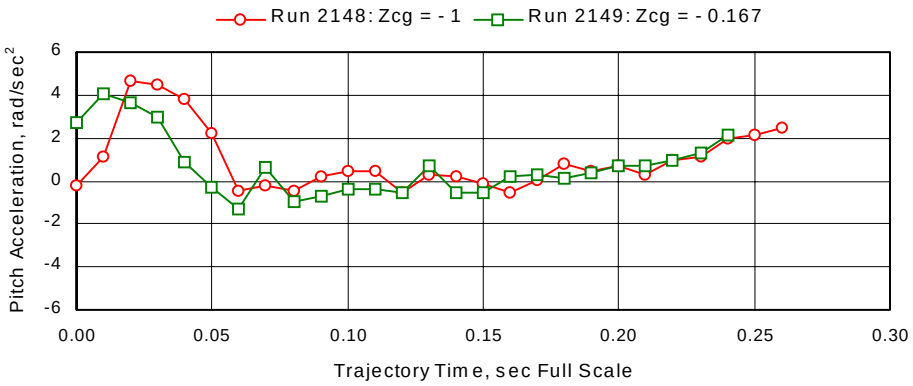

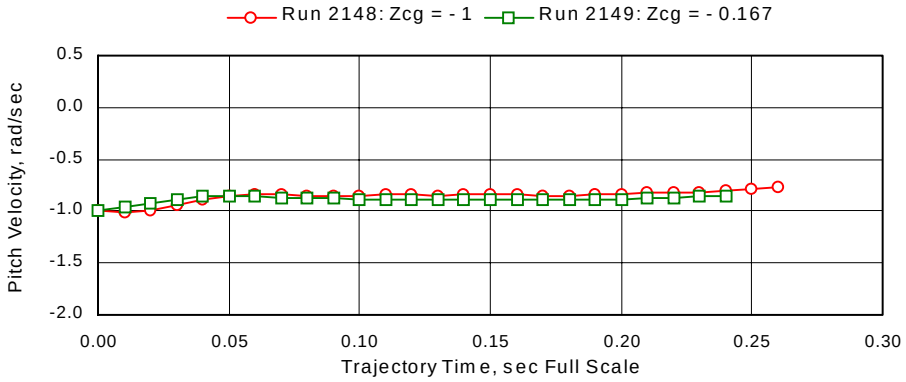

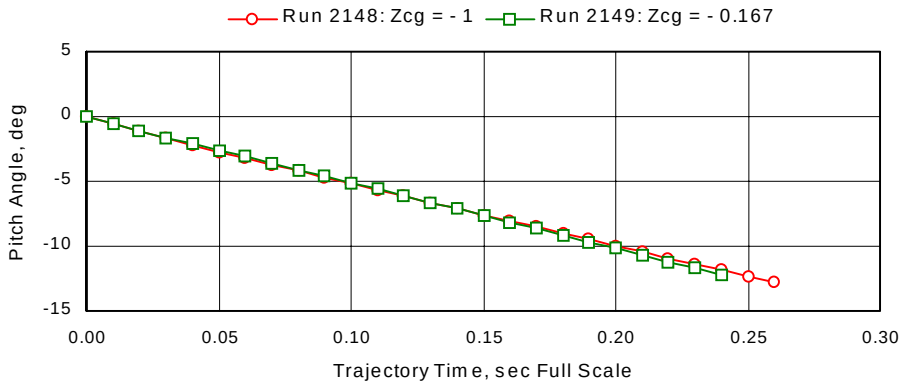

d. Pitching-motion trajectory parameters
Figure 35. Continued.

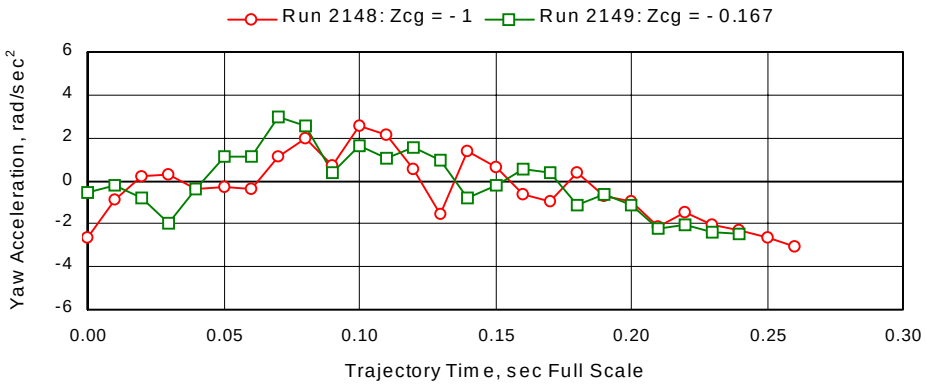

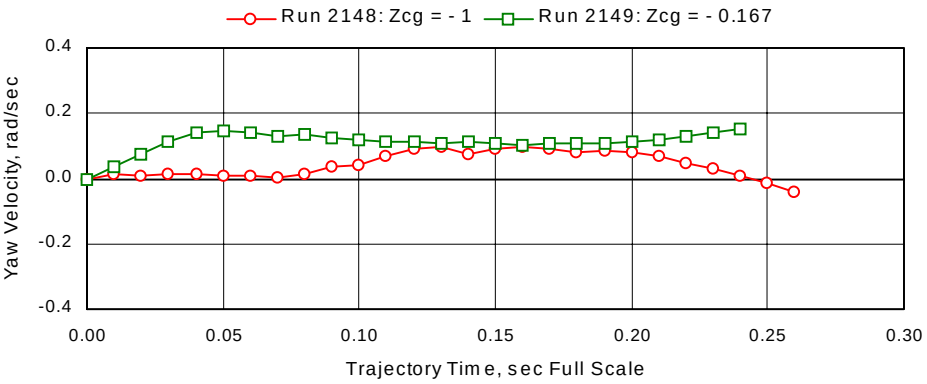

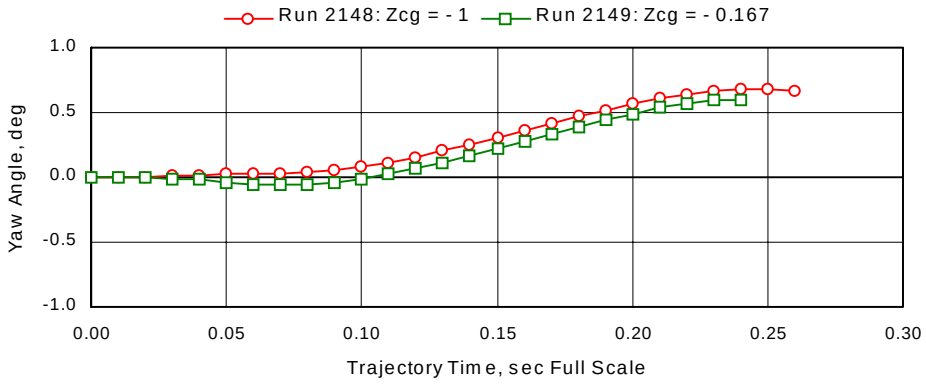

e. Yawing-motion trajectory parameters
Figure 35. Concluded.

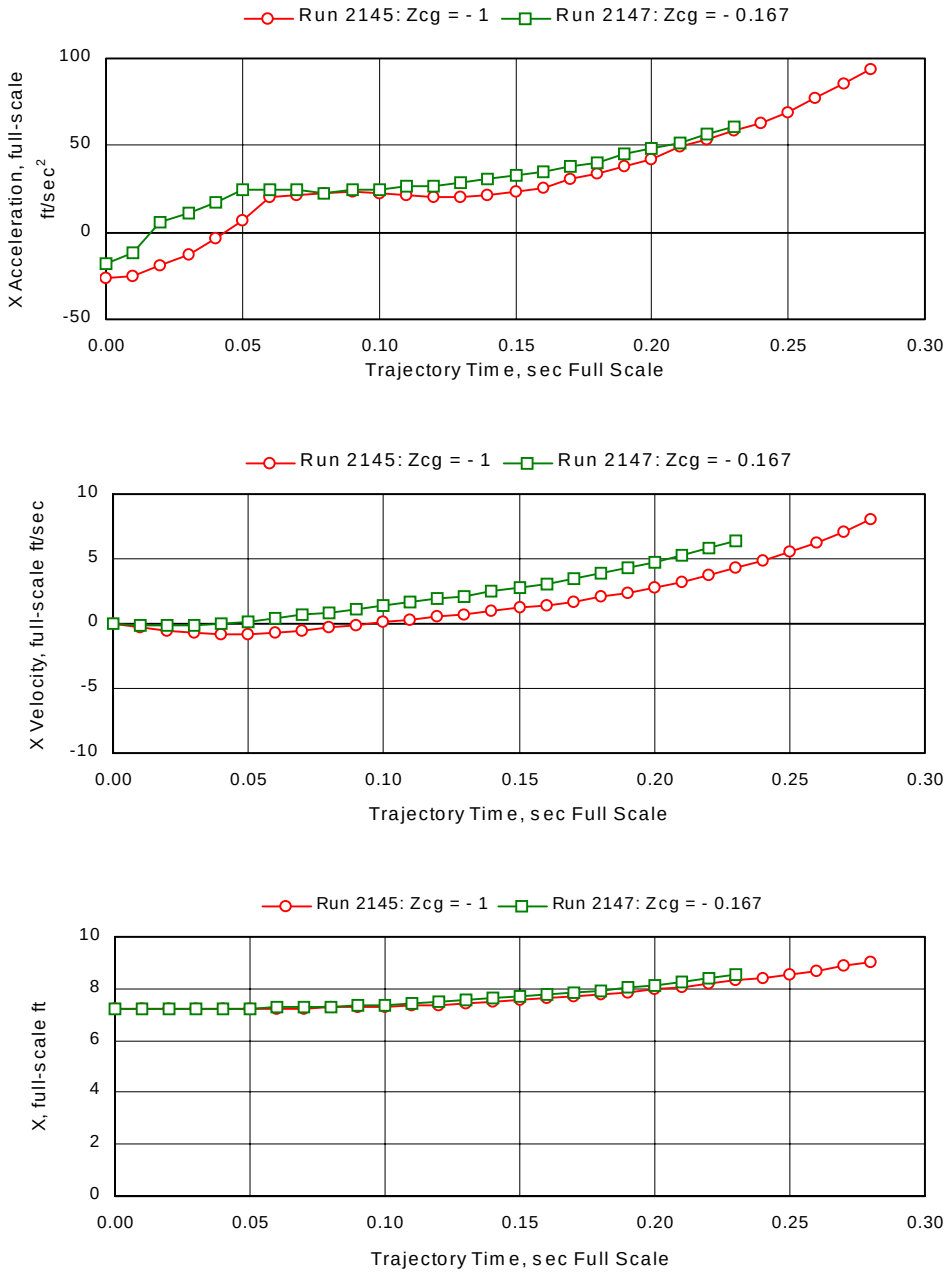

a. X-direction trajectory parameters

Figure 36. Separation trajectories of a store jettisoned from an L/D = 4.5 cavity at two difference release points, M_∞ = 1.20.

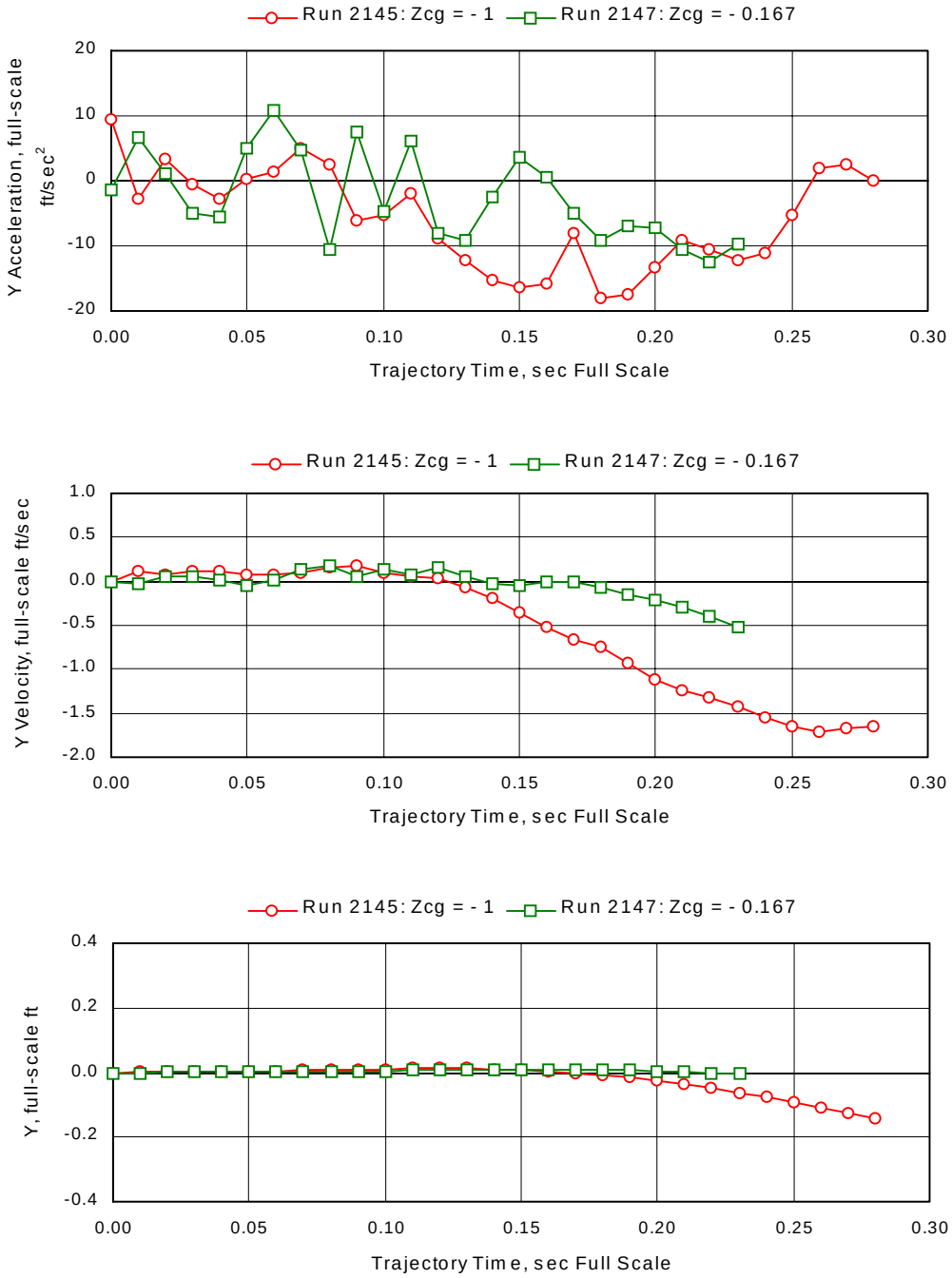

b. Y-direction trajectory parameters
Figure 36. Continued.

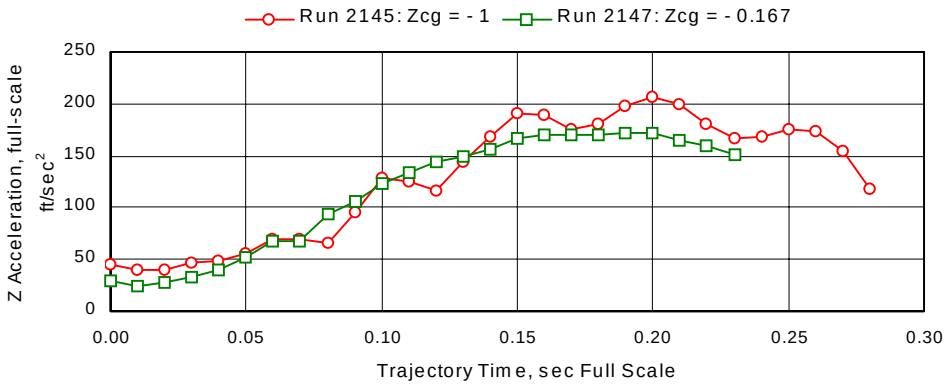

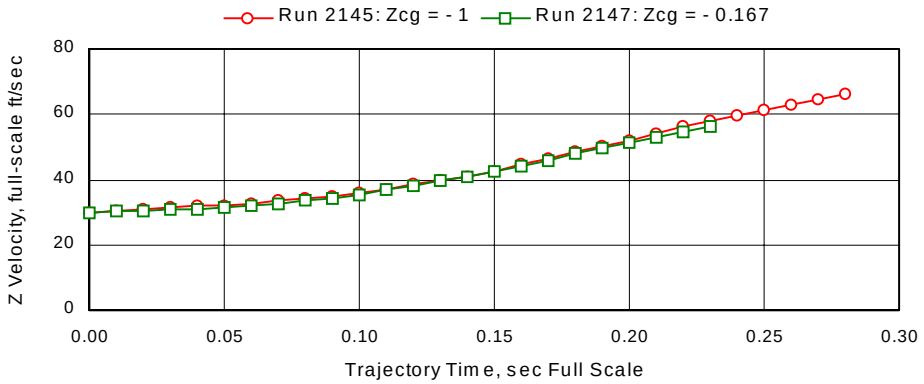

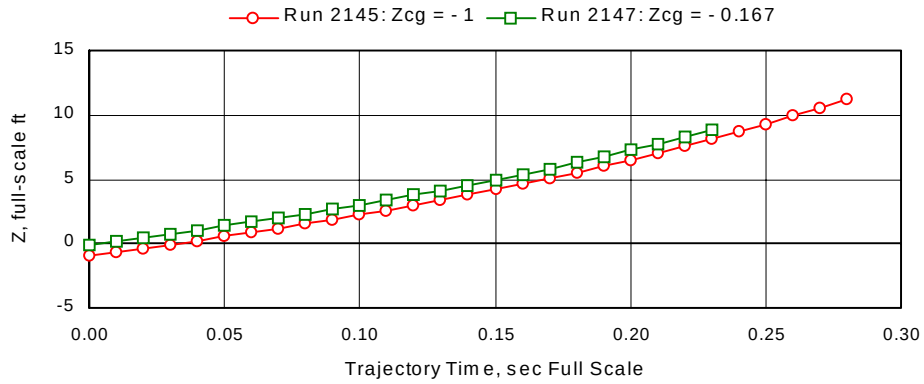

c. Z-direction trajectory parameters
Figure 36. Continued.

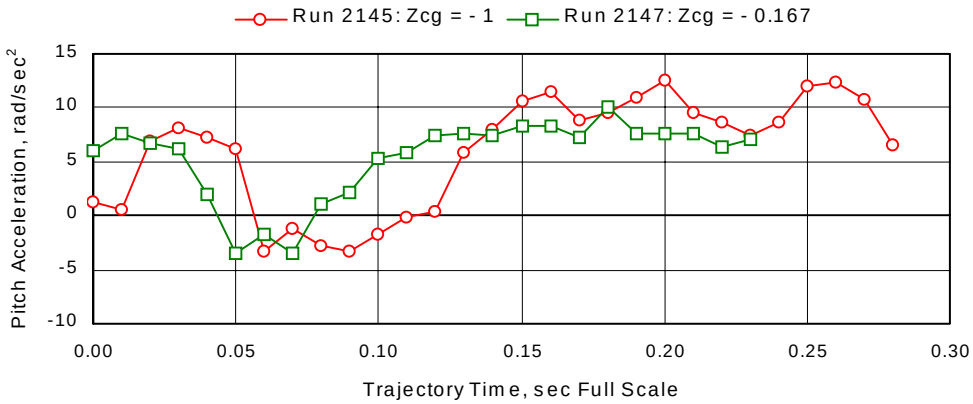

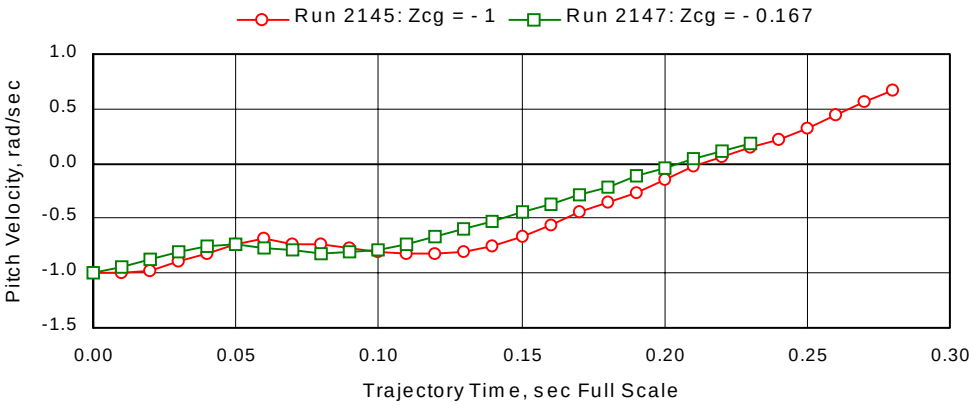

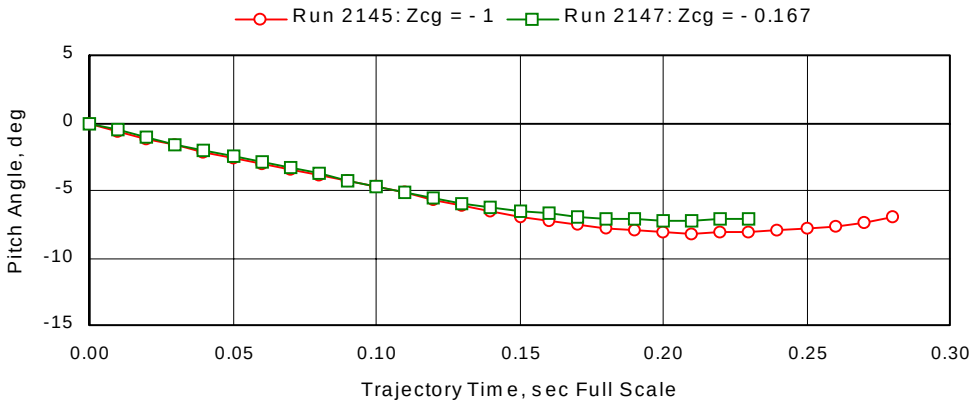

d. Pitching-motion trajectory parameters
Figure 36. Continued.

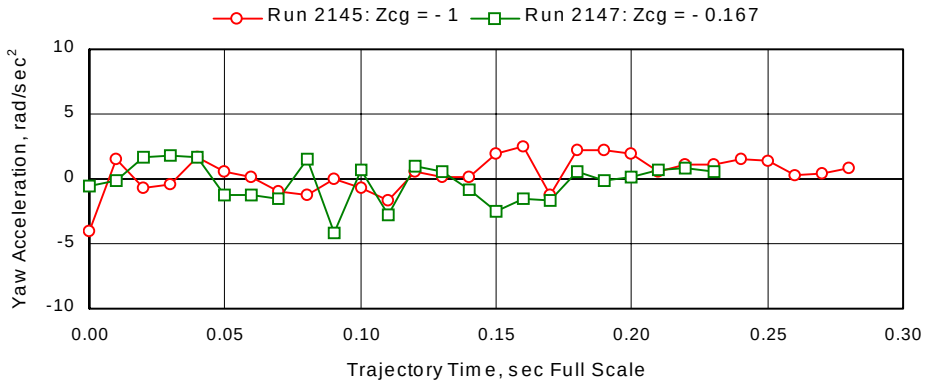

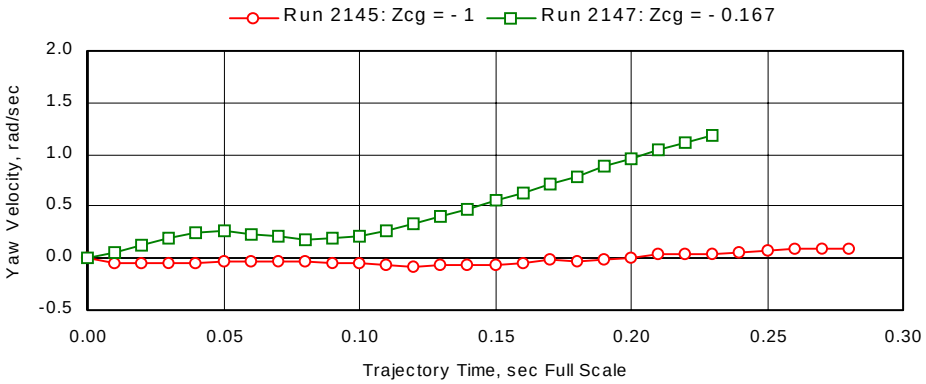

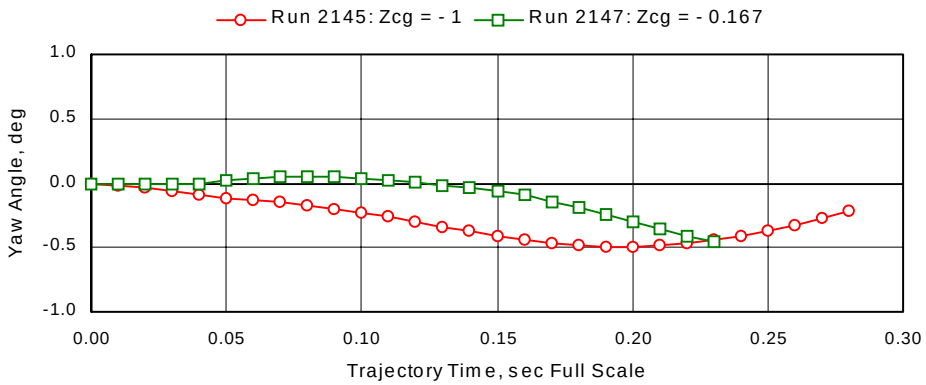

e. Yawing-motion trajectory parameters
Figure 36. Concluded.

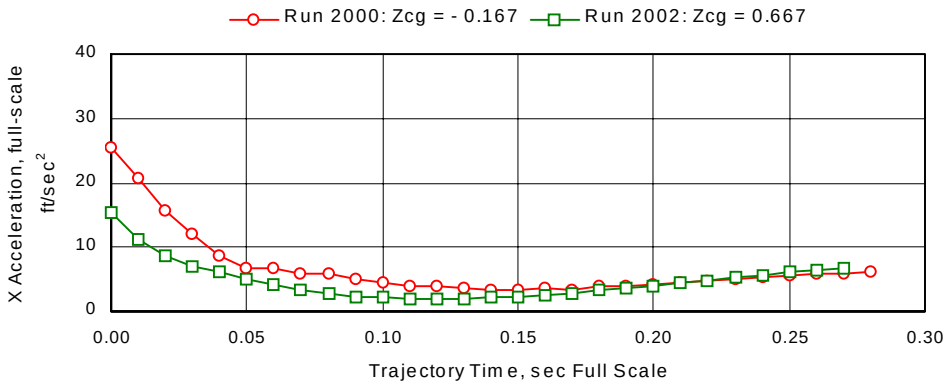

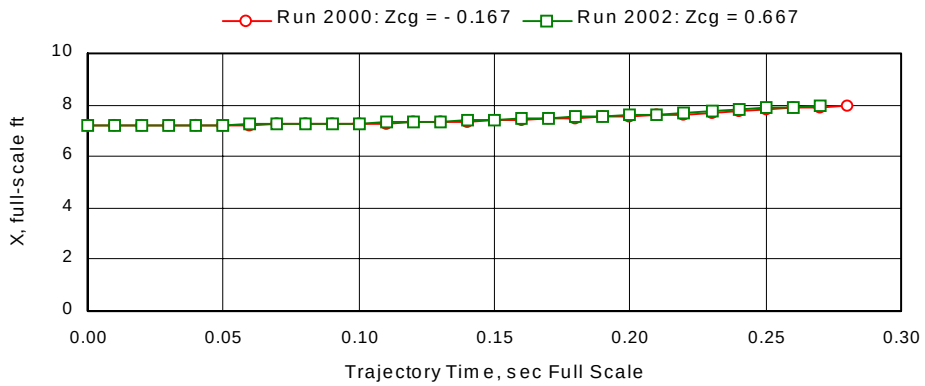

a. X-direction trajectory parameters

Figure 37. Separation trajectories of a store jettisoned from an L/D = 9.0 cavity at two difference release points, M_∞ = 0.95.

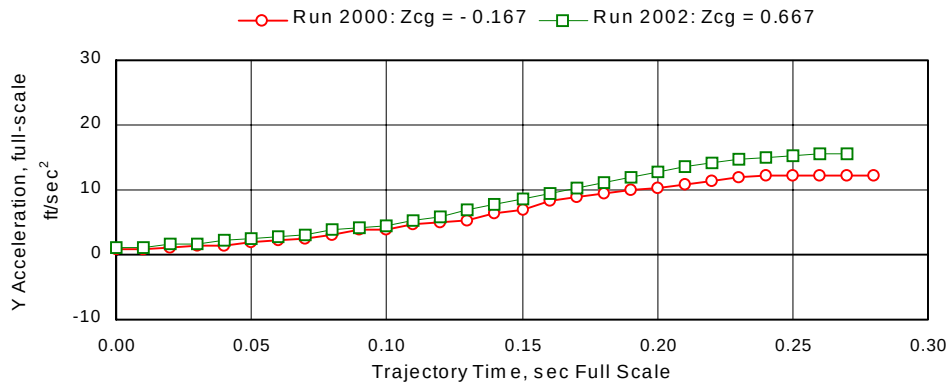

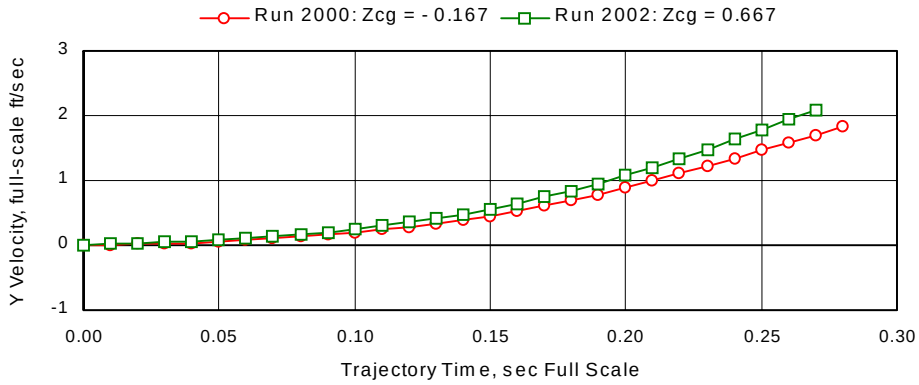

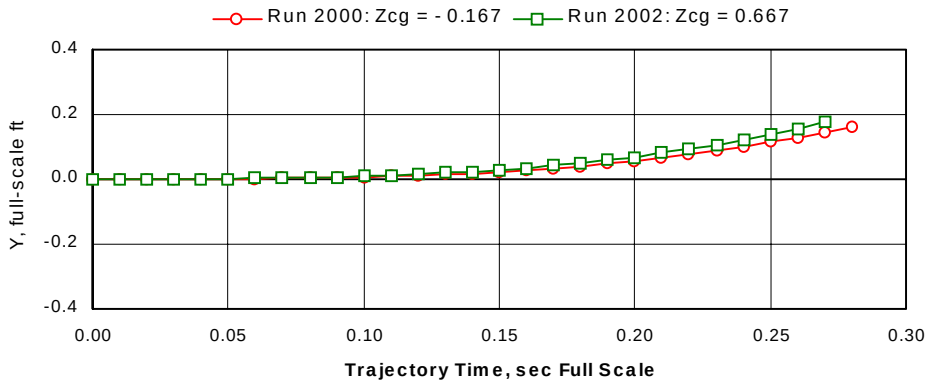

b. Y-direction trajectory parameters
Figure 37. Continued.

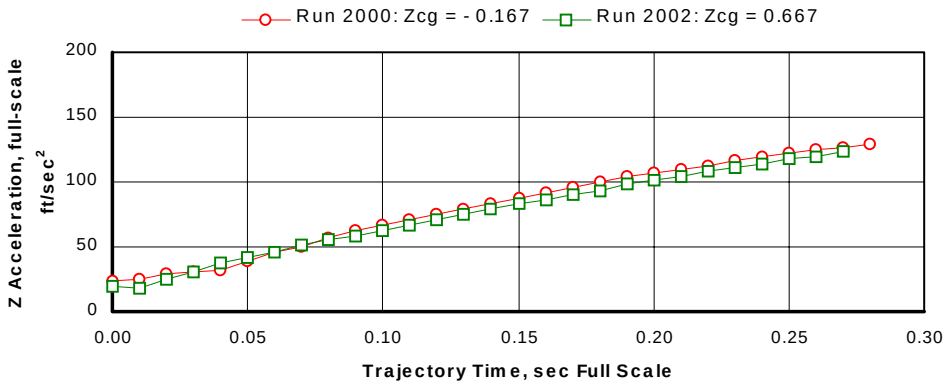

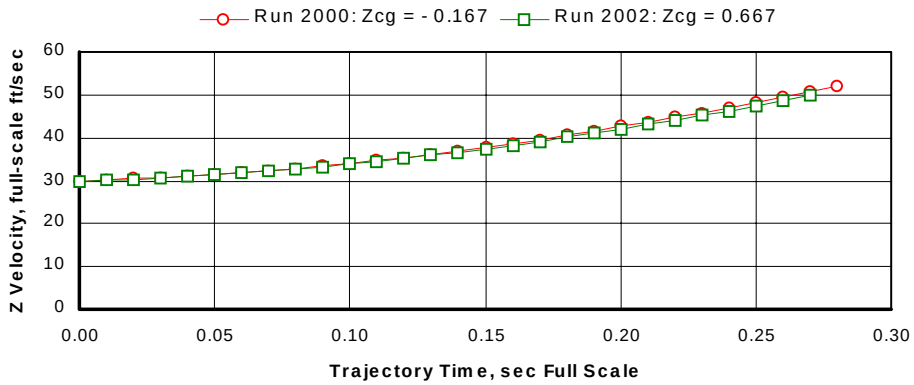

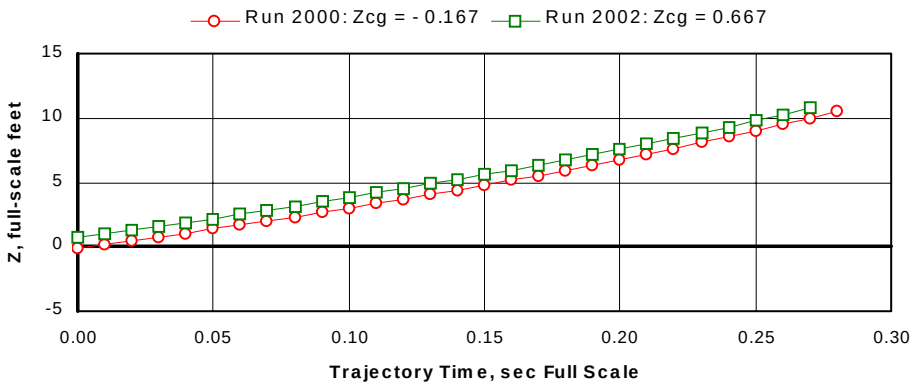

c. Z-direction trajectory parameters
Figure 37. Continued.

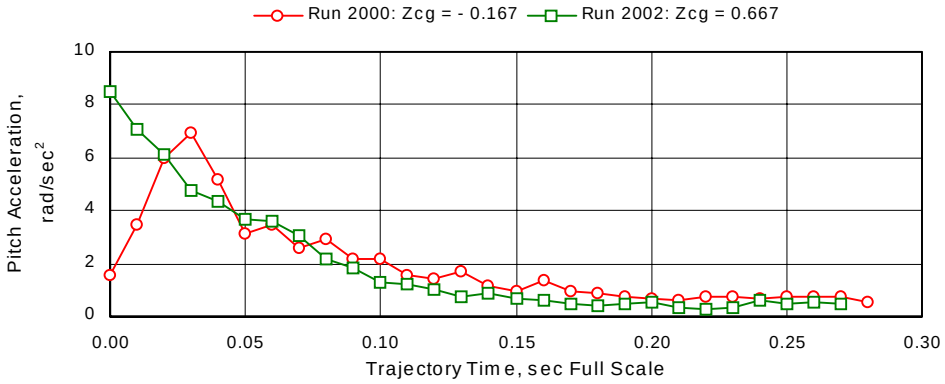

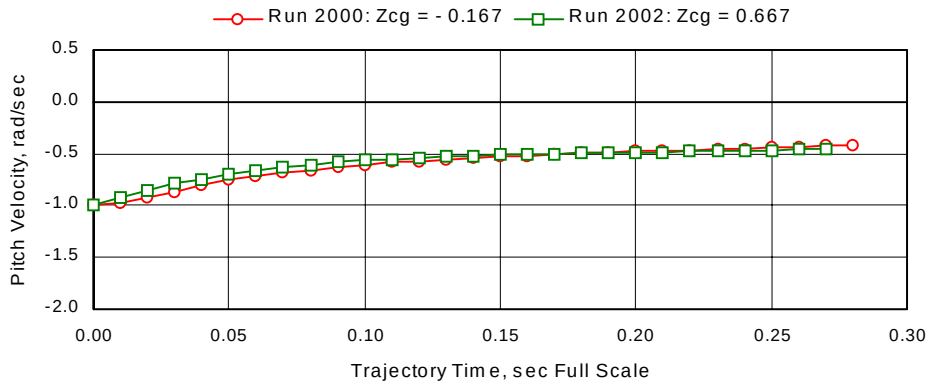

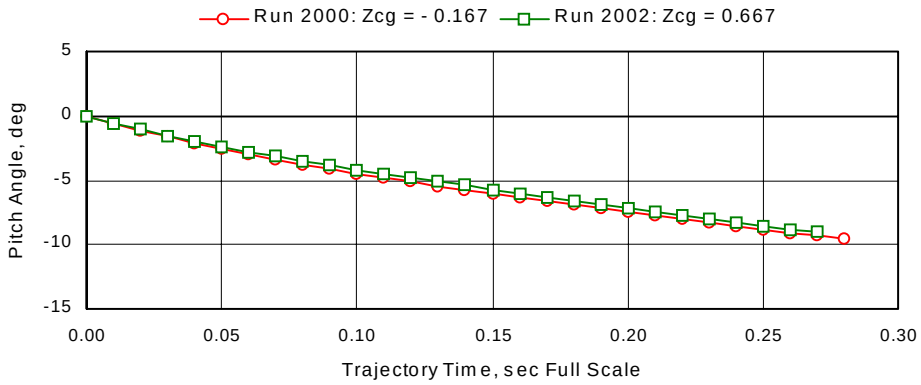

d. Pitching-motion trajectory parameters
Figure 37. Continued.

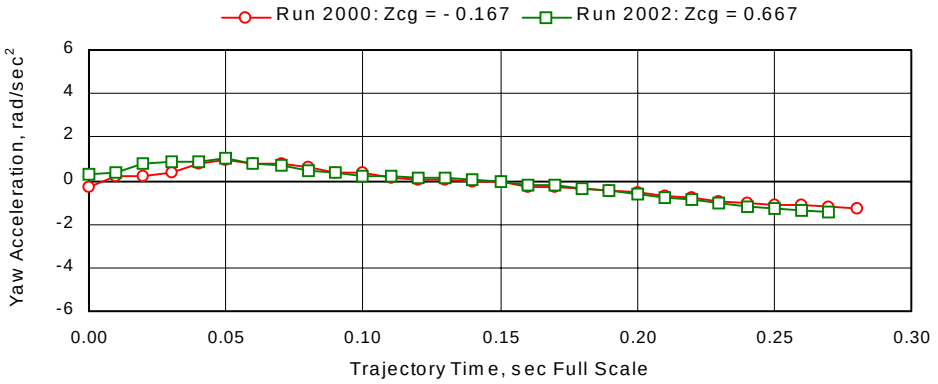

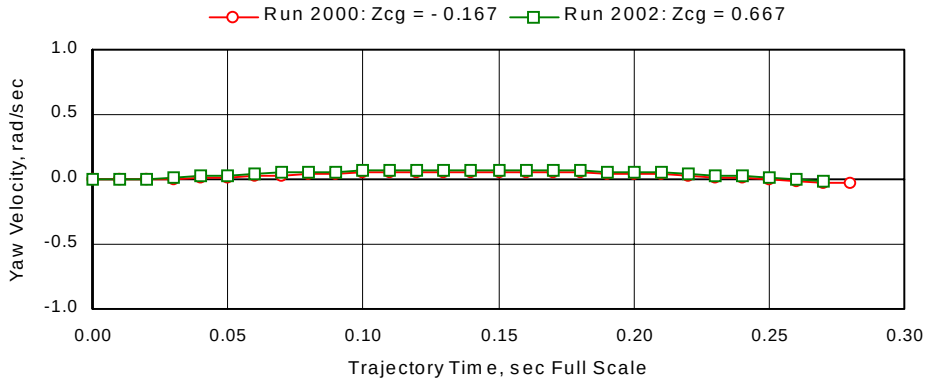

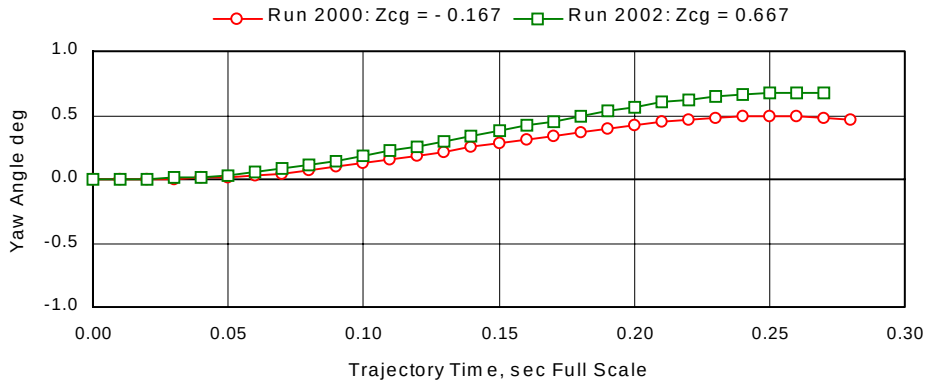

e. Pitching-motion trajectory parameters
Figure 37. Concluded.

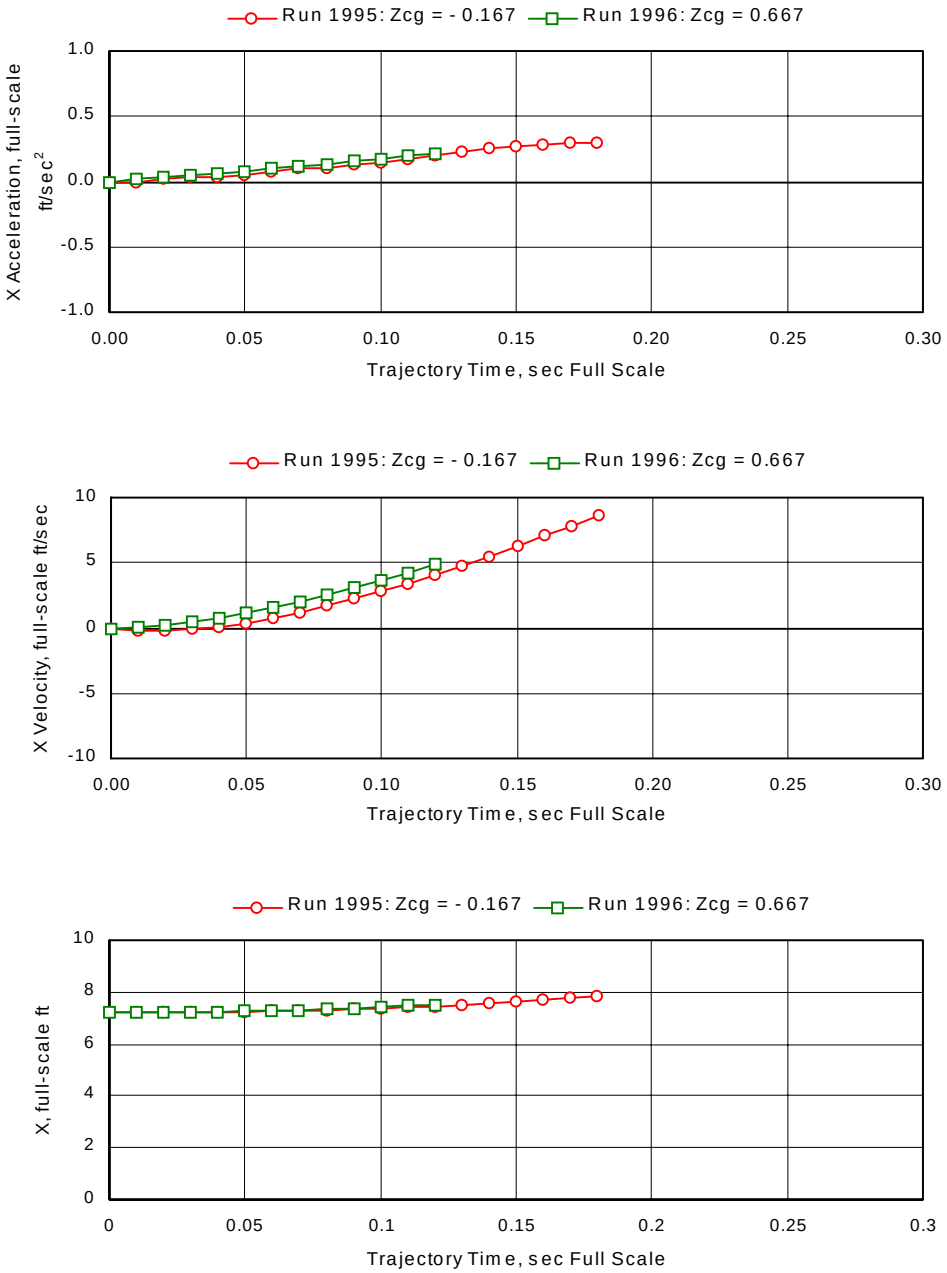

a. X-direction trajectory parameters

Figure 38. Separation trajectories of a store jettisoned from an L/D = 9.0 cavity at two difference release points, M_∞ = 1.20.

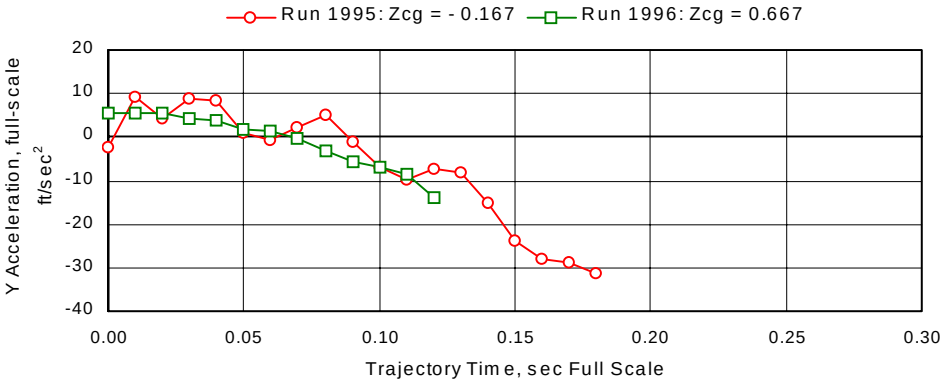

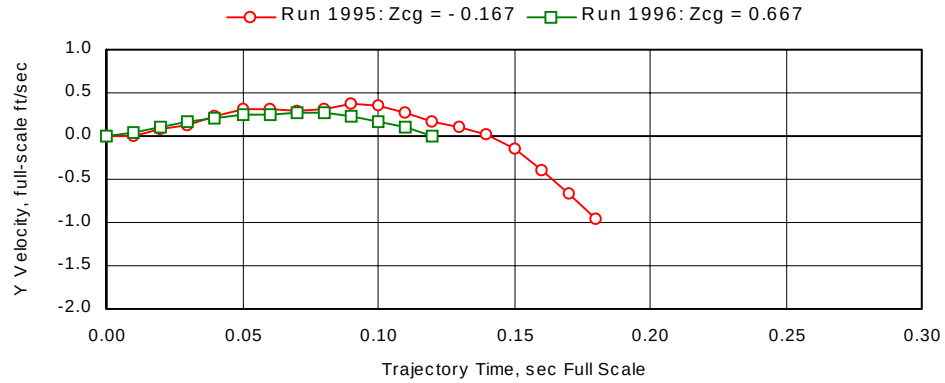

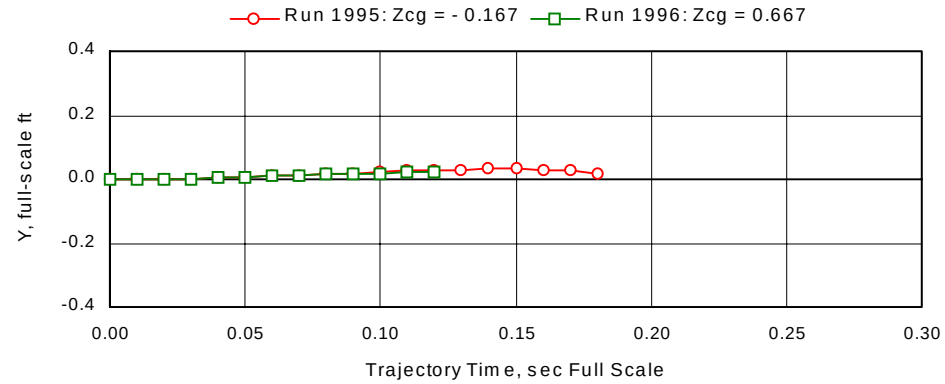

b. Y-direction trajectory parameters
Figure 38. Continued.

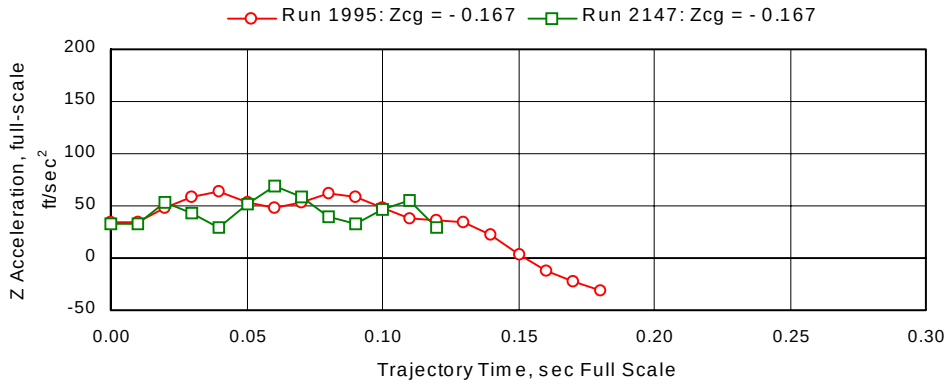

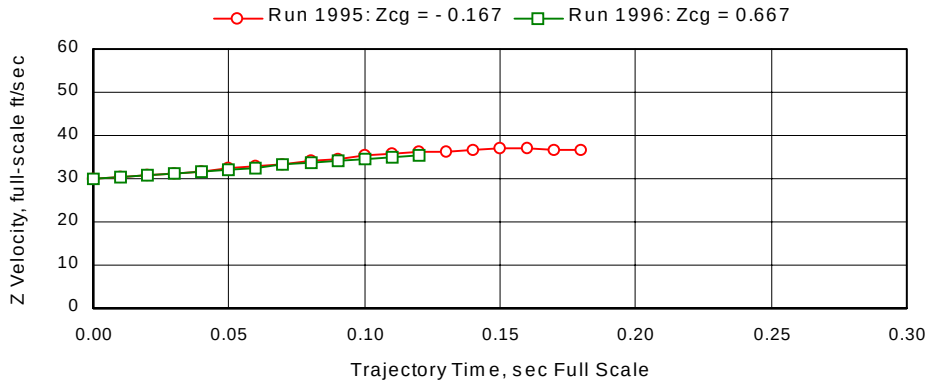

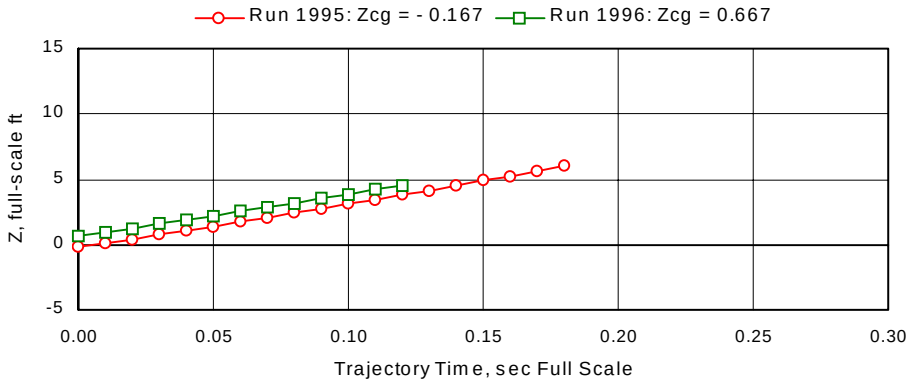

c. Z-direction trajectory parameters
Figure 38. Continued.

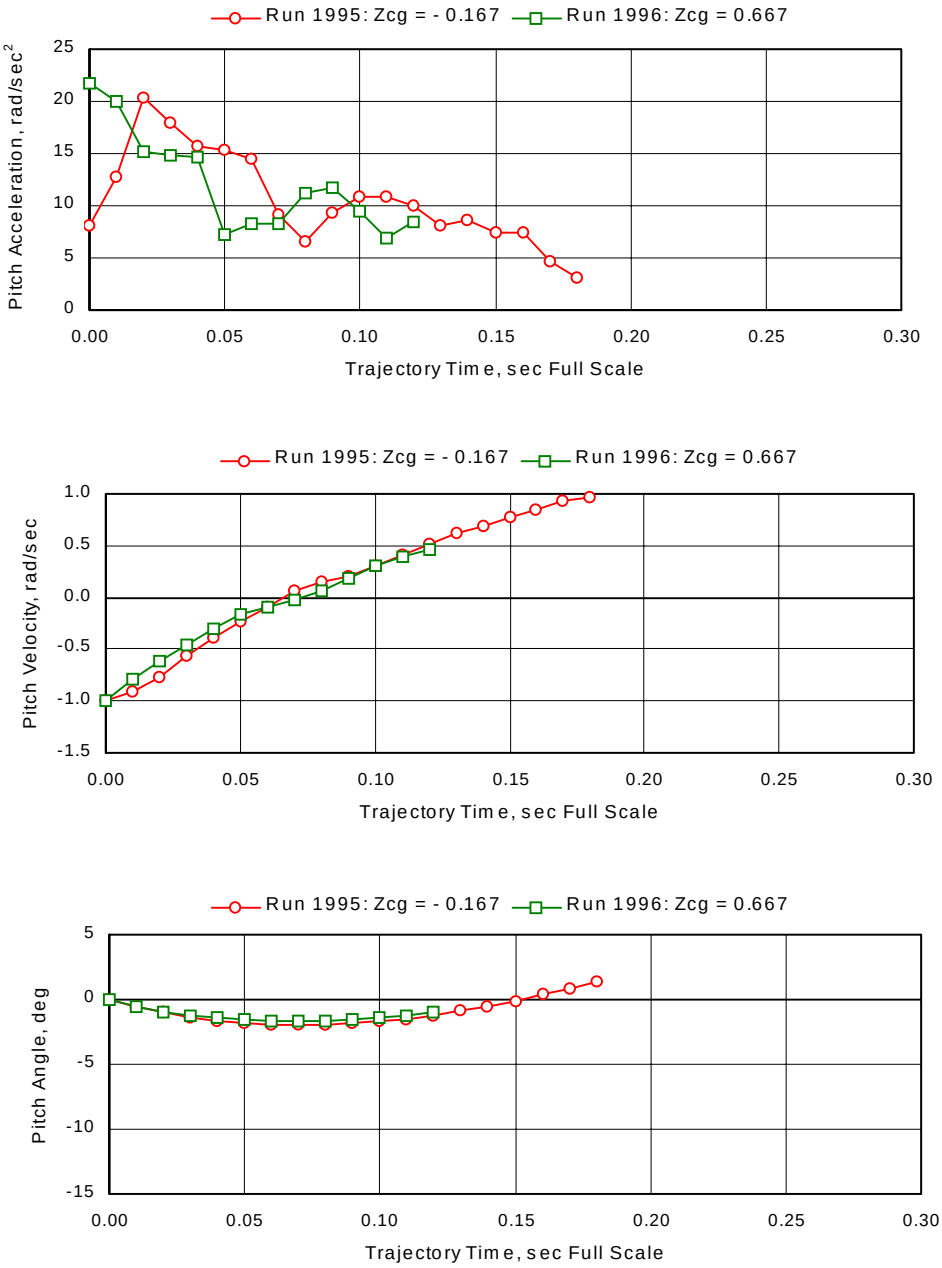

d. Pitching-motion trajectory parameters
Figure 38. Continued.

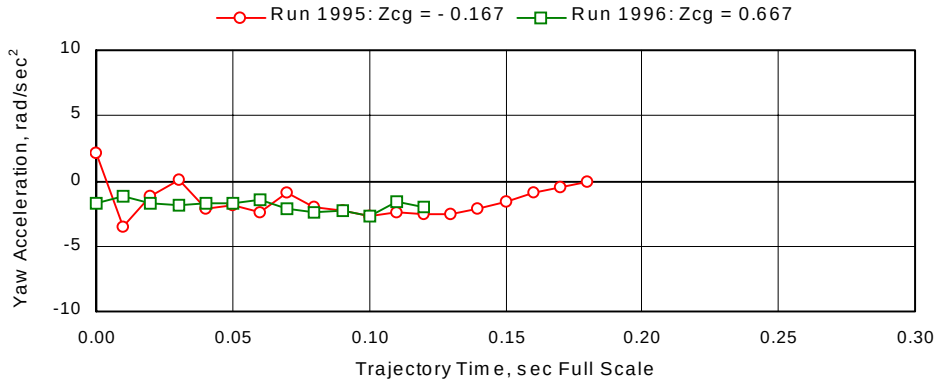

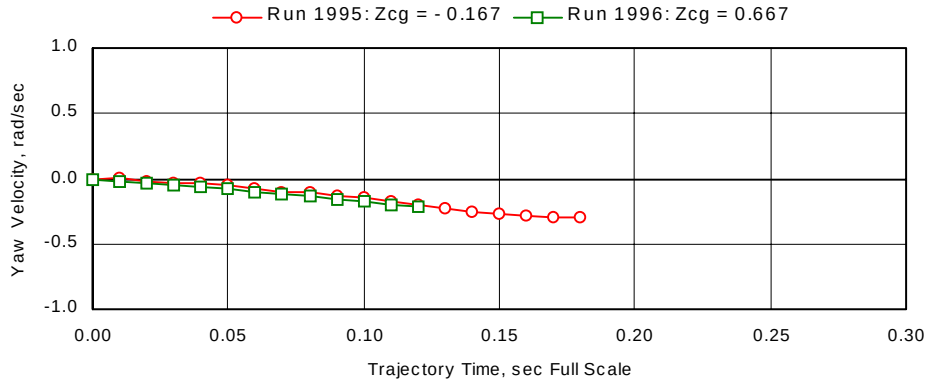

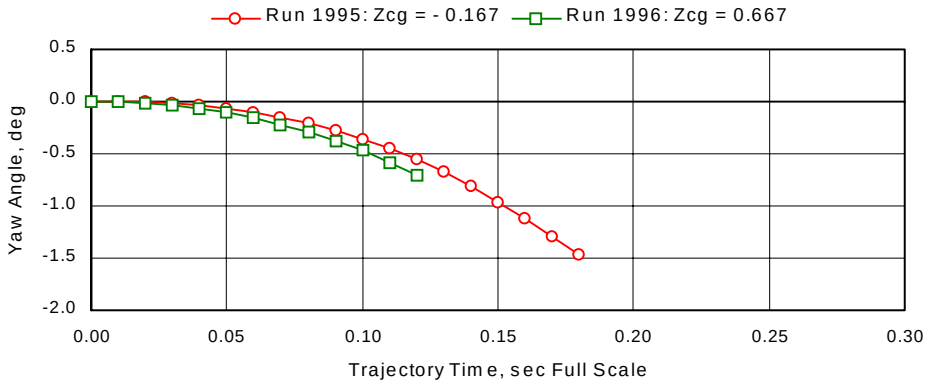

e. Yawing-motion trajectory parameters
Figure 38. Concluded.

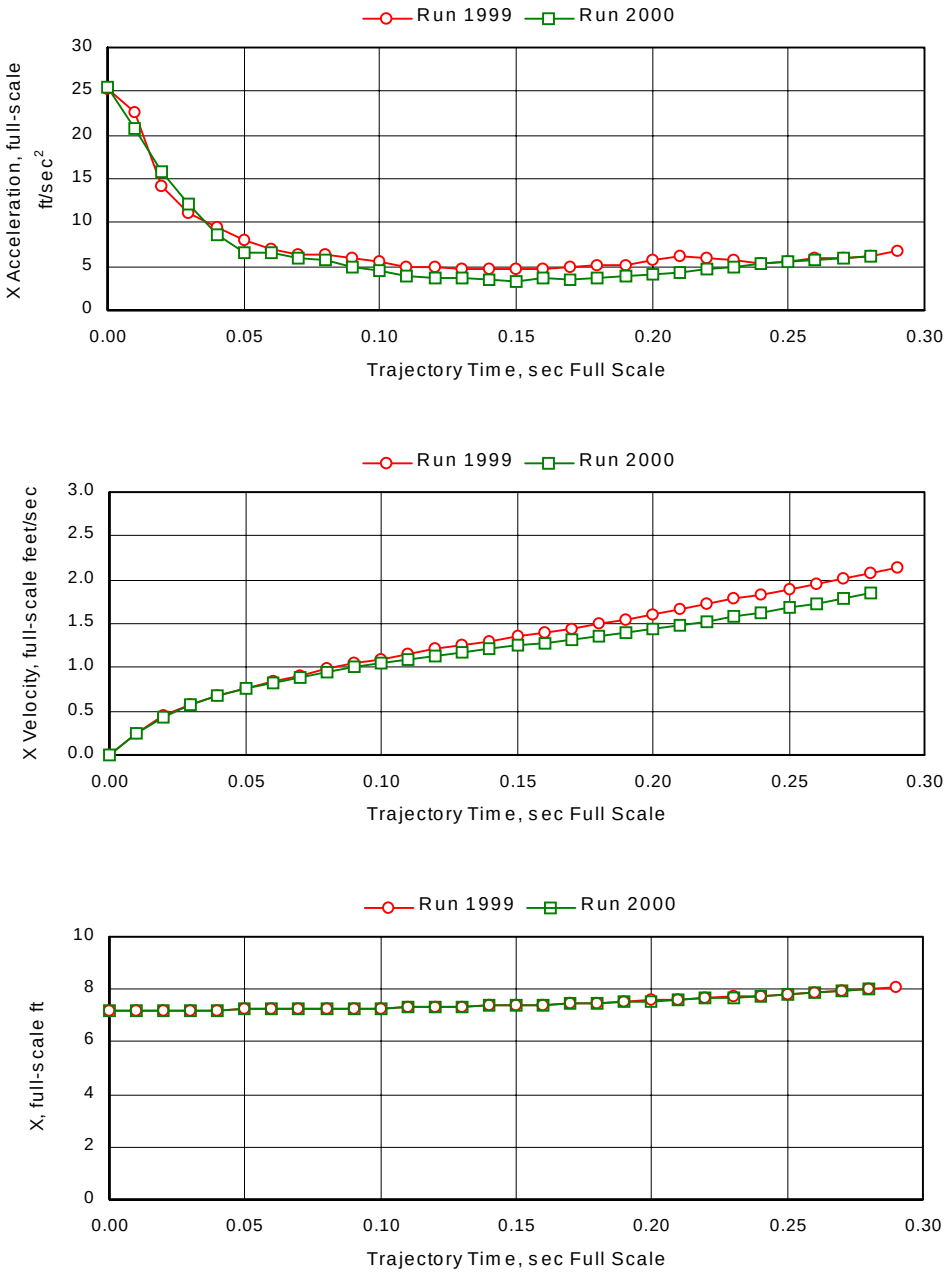

a. X-direction trajectory parameters

Figure 39. Repeatability of a separation trajectory of a store jettisoned from an L/D = 9.0 cavity, M_∞ = 0.95.

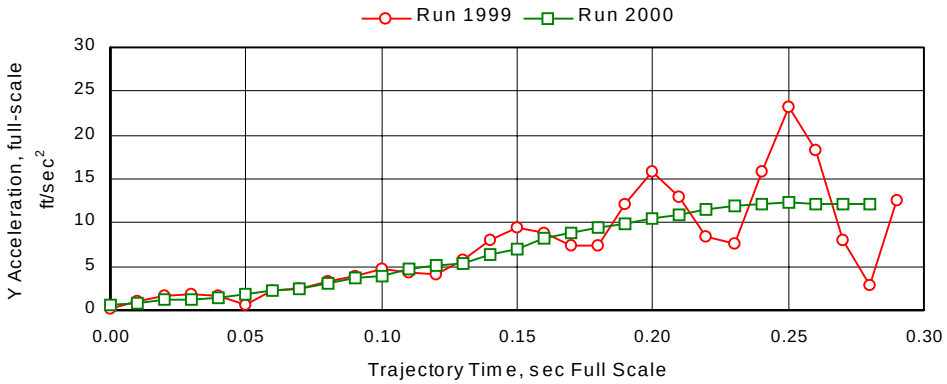

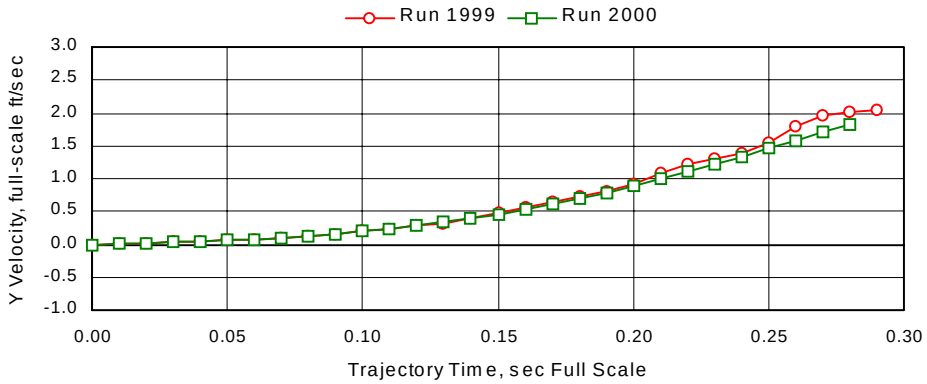

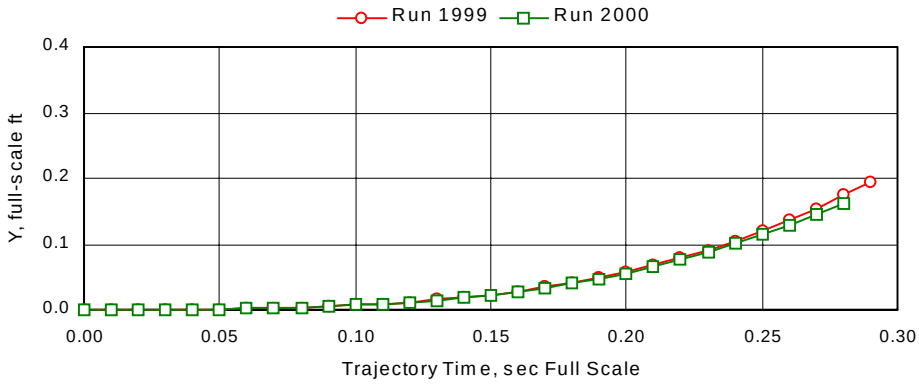

b. Y-direction trajectory parameters
Figure 39. Continued.

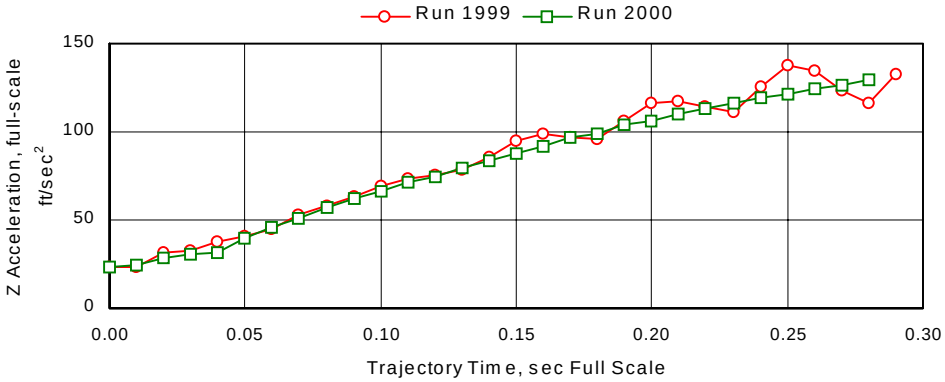

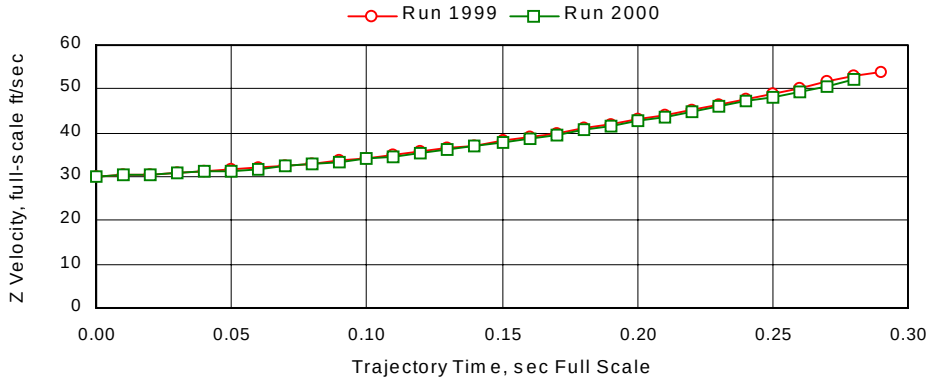

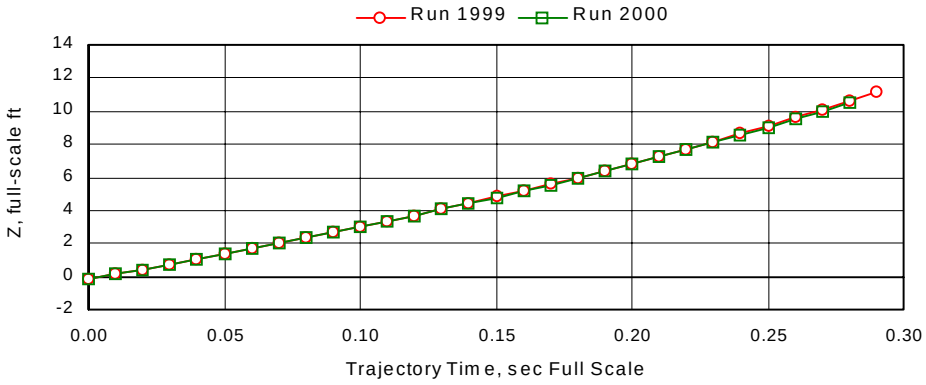

c. Z-direction trajectory parameters
Figure 39. Continued.

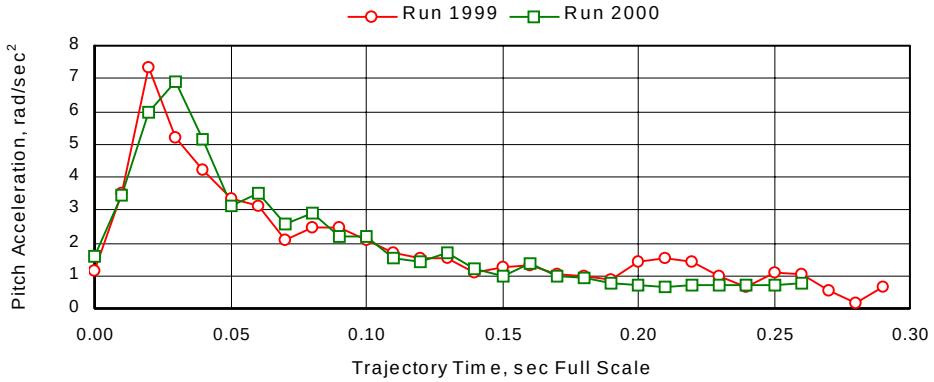

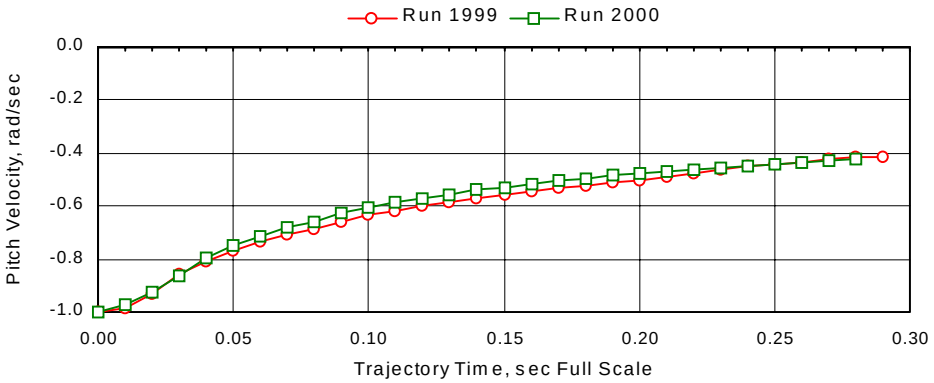

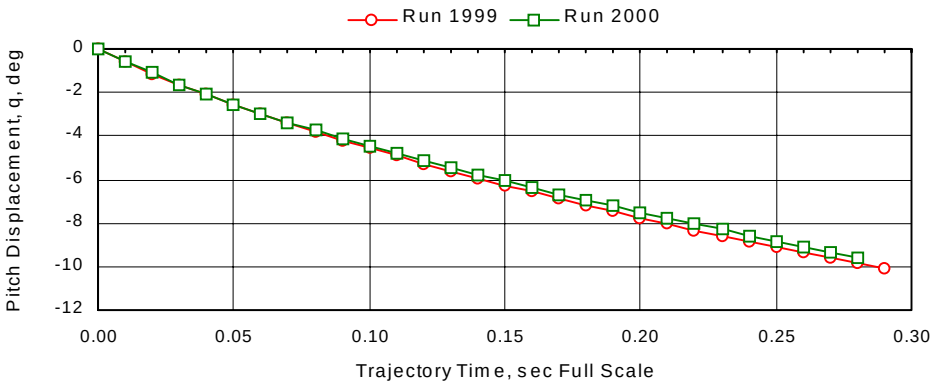

d. Pitching-motion trajectory parameters
Figure 39. Continued.

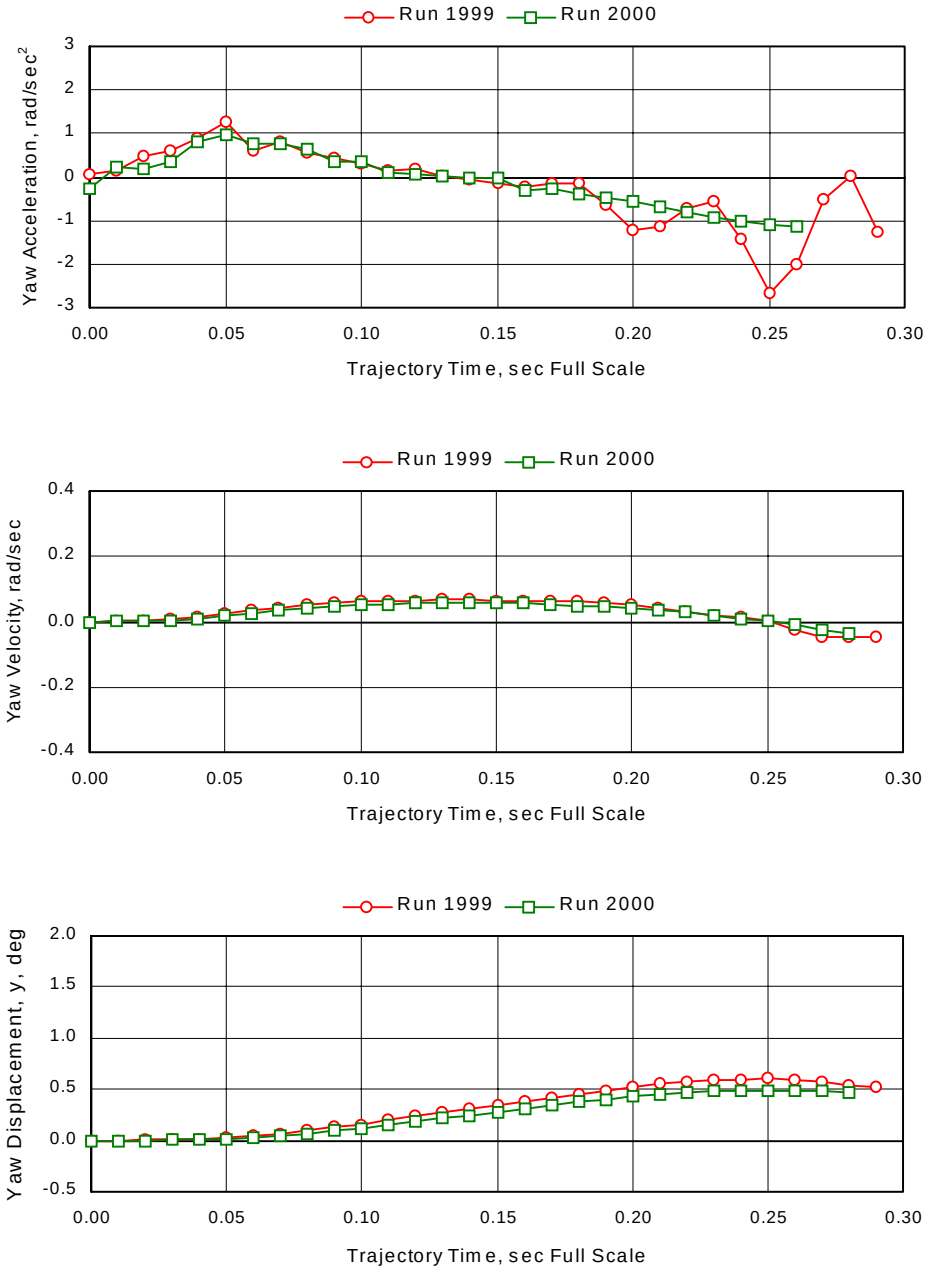

e. Yawing-motion trajectory parameters
Figure 39. Concluded.

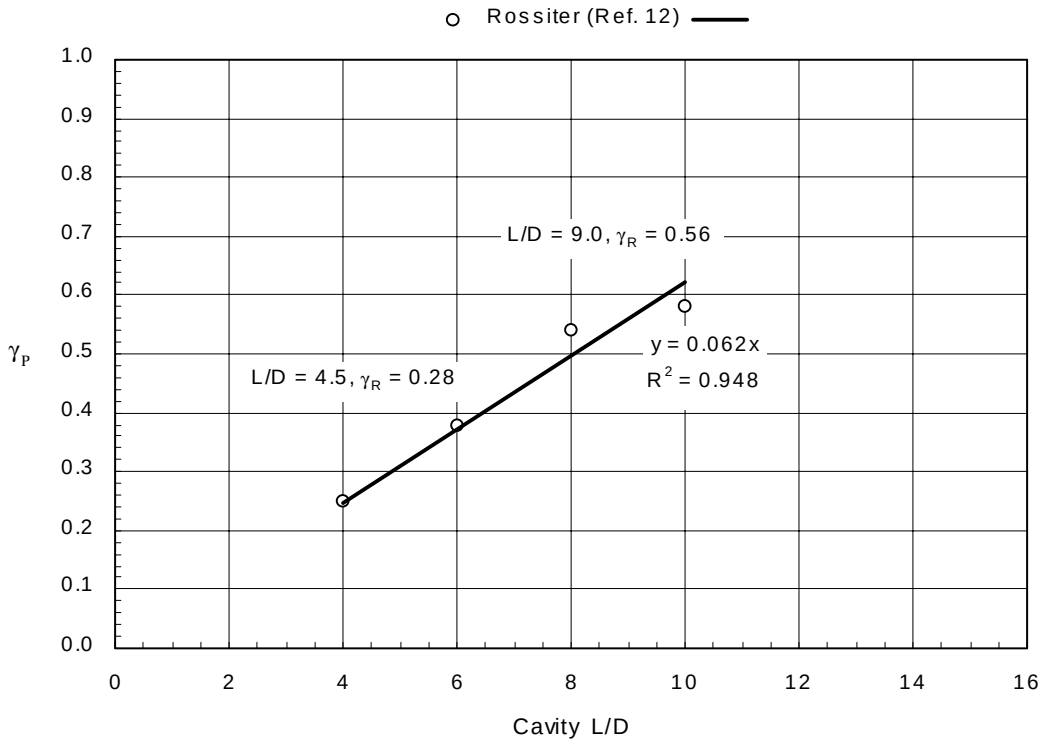

Figure 40. Relationship between Rossiter's vortex phase constant, γ_B, and cavity L/D.

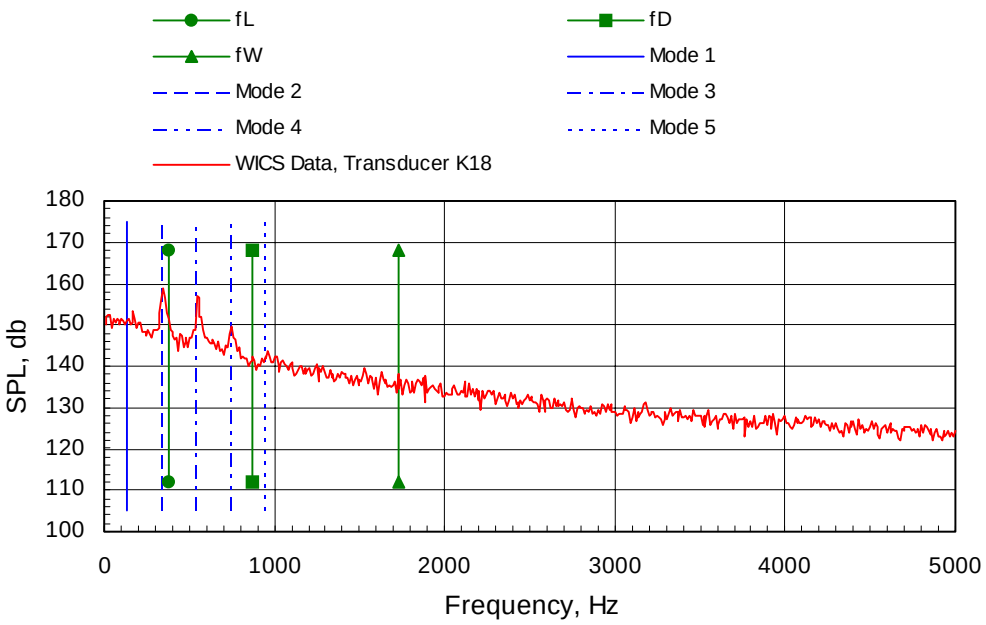

a. M_∞ = 0.60

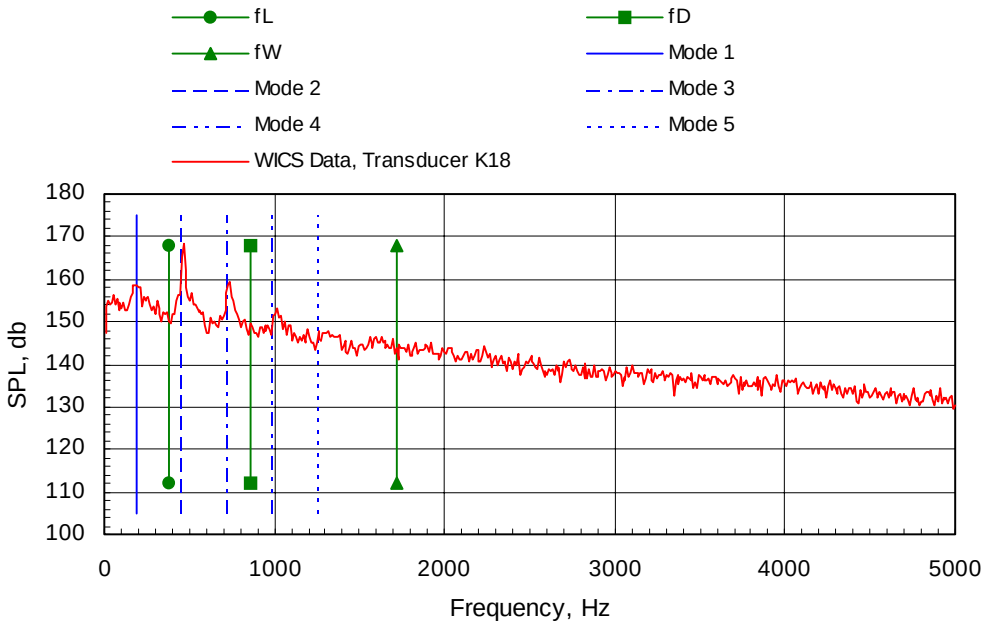

b. M_∞ = 0.95

Figure 41. Typical spectra and Rossiter's predicted edgetones for an L/D = 4.5 cavity.

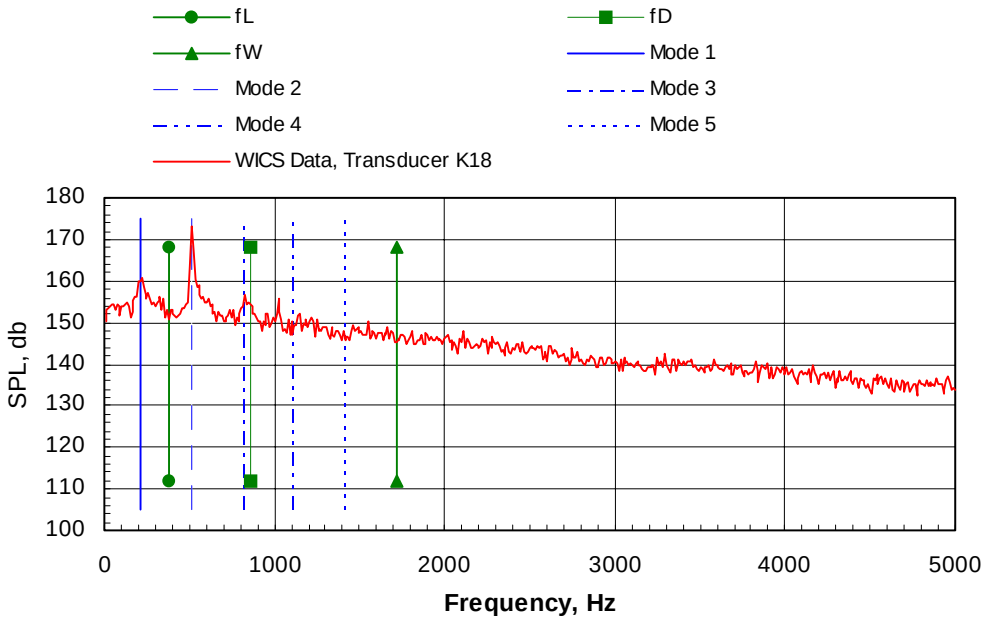

c. M_∞ = 1.20

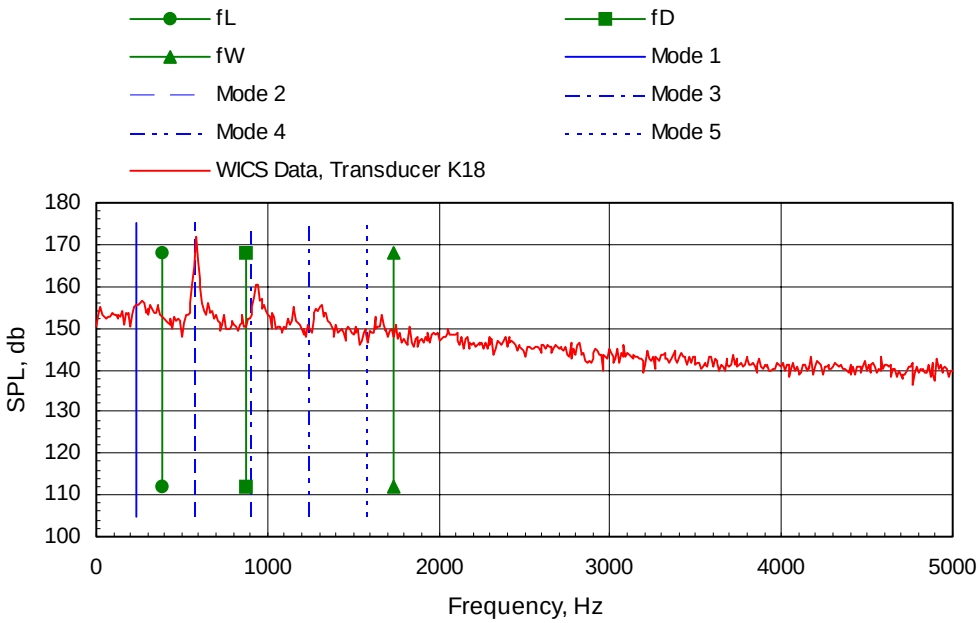

d. M_∞ = 1.50

Figure 41. Continued.

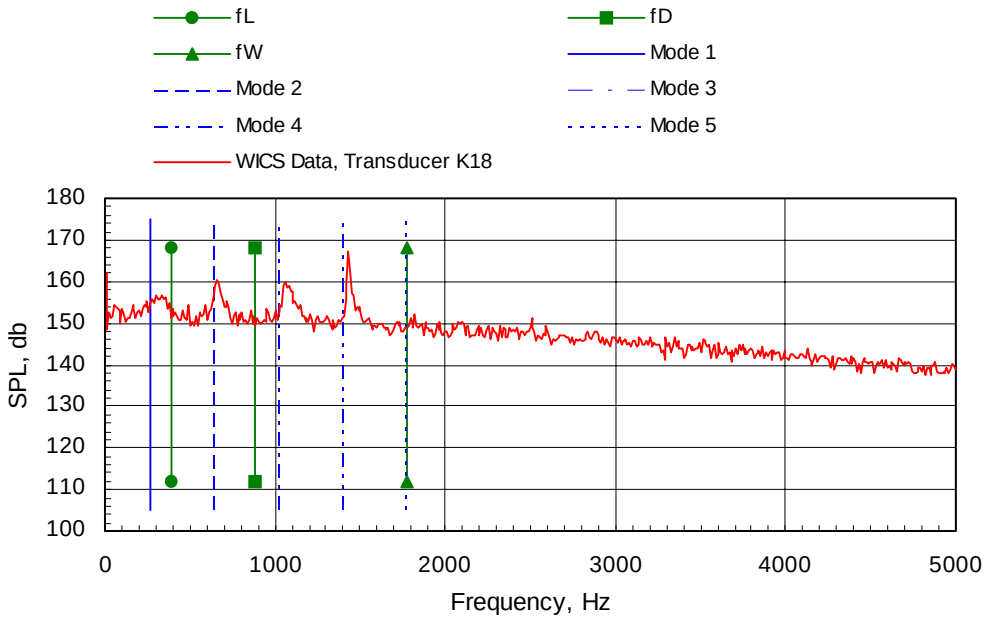

e. M_∞ = 2.00

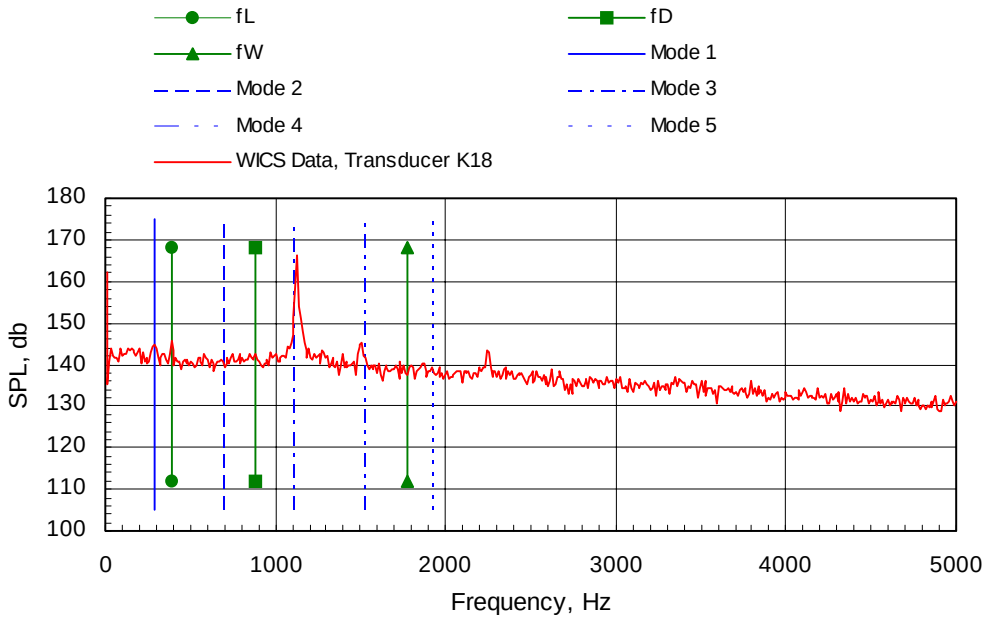

f. M_∞ = 2.75

Figure 41. Continued.

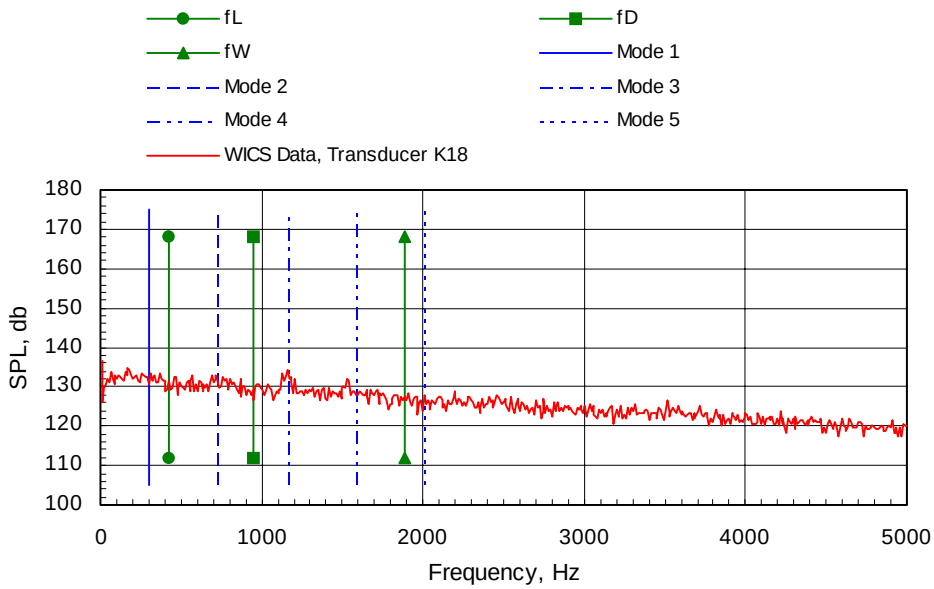

g. M_∞ = 3.51

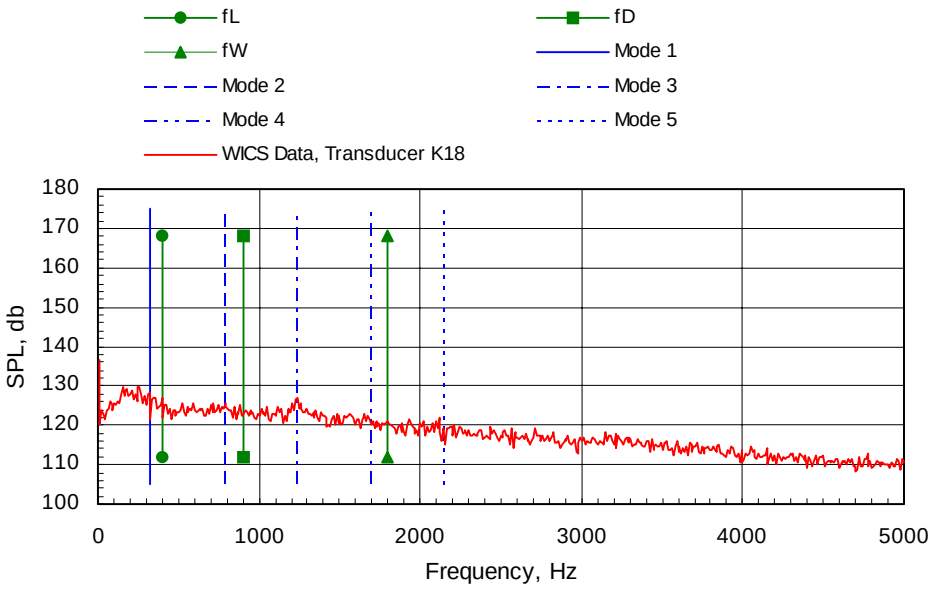

h. M_∞ = 5.04

Figure 41. Concluded.

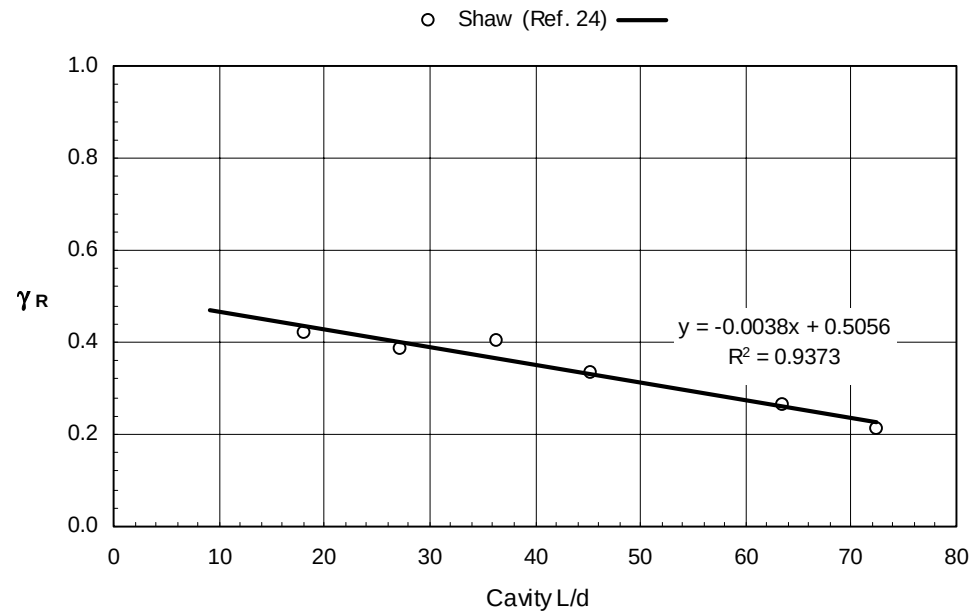

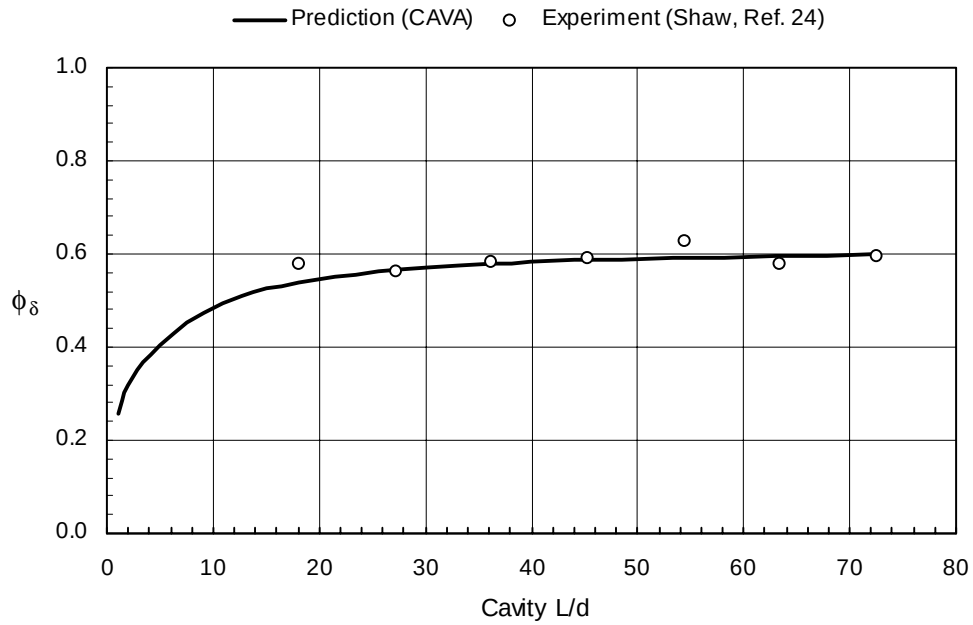

Figure 42. Experimental values of γ_R and theoretical and experimental values of ϕ_D for a cavity of L/D = 4.5 with $M_\infty = 0.6$ and $Re = 3 \times 10^6$.

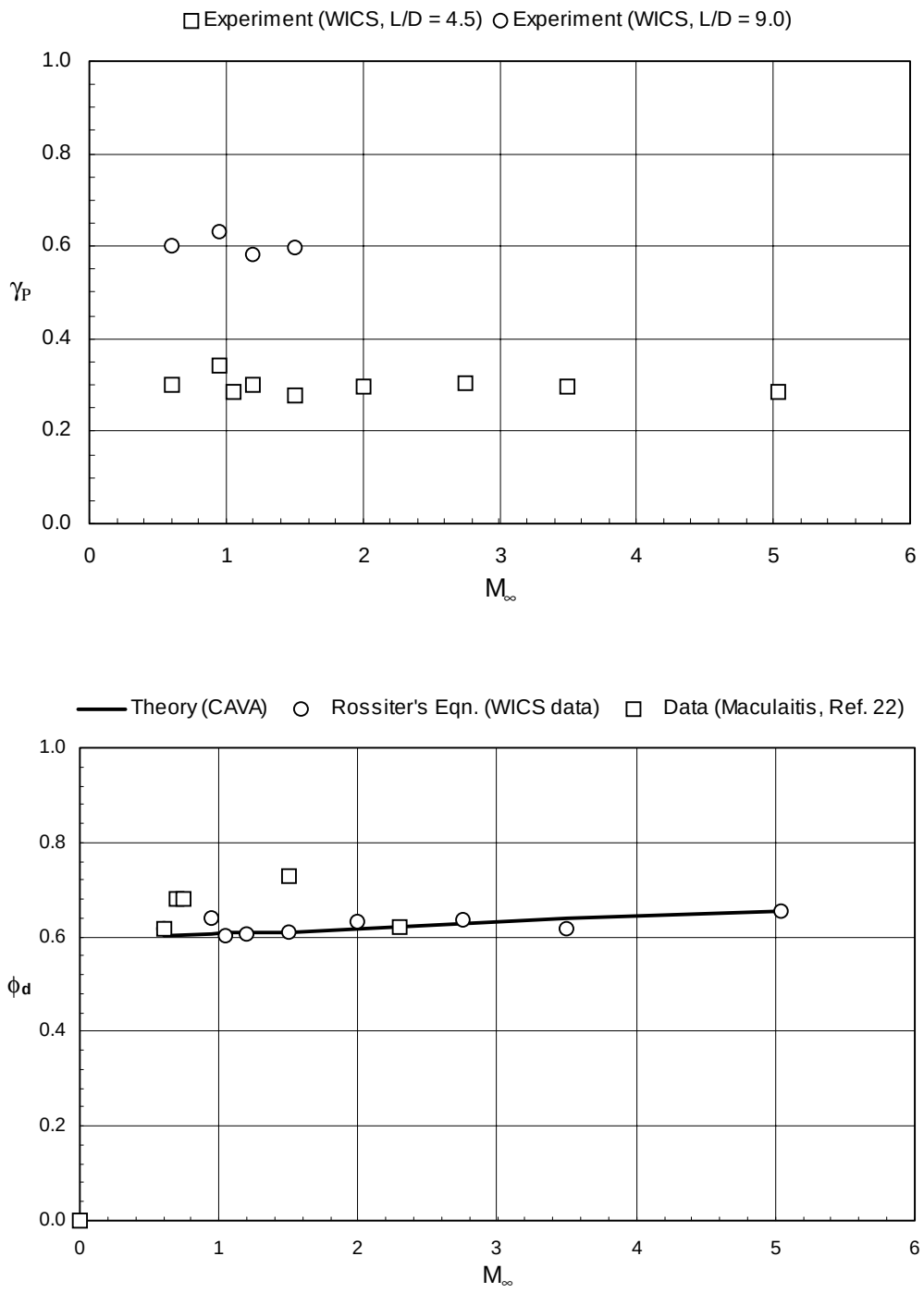

Figure 43. Variation of γ_R and ϕ_D with free-stream Mach number, from data and CAVA.

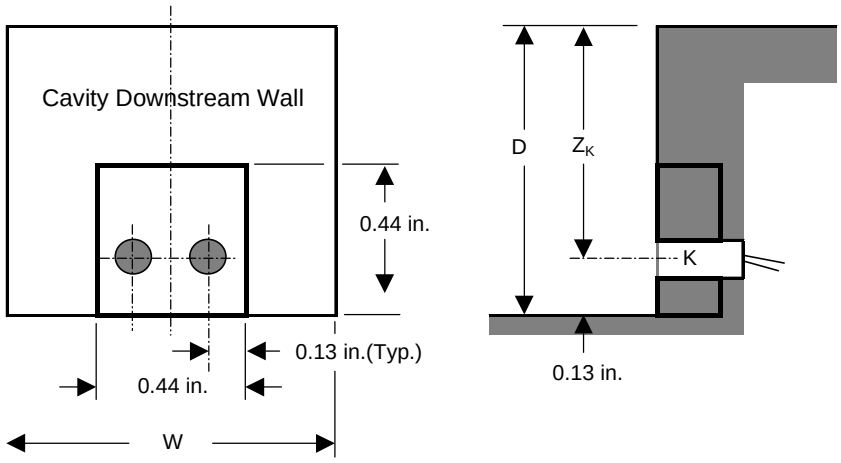

Insert No.	D, in.	Z^k, in.	$(Z/D)_k$	W, in.	Y_K, in.	$2Y_K/W$
1	3.69	–3.56	–0.96	3.69	0.09	0.05
2	3.44	–3.31	–0.96	3.44	0.09	0.05
3	3.19	–3.06	–0.96	3.19	0.09	0.06
4	2.94	–2.81	–0.96	2.94	0.09	0.06
5	2.69	–2.56	–0.95	2.69	0.09	0.07
6	2.44	–2.31	–0.95	2.44	0.09	0.07
7	2.19	–2.06	–0.94	2.19	0.09	0.08
8	1.94	–1.81	–0.93	1.94	0.09	0.09
9	1.69	–1.56	–0.92	1.69	0.09	0.11
10	1.44	–1.31	–0.91	1.44	0.09	0.13
11	1.19	–1.06	–0.89	1.19	0.09	0.15
12	0.94	–0.81	–0.86	0.94	0.09	0.19
13	0.69	–0.56	–0.81	0.69	0.09	0.26
14	0.44	–0.31	–0.70	0.44	0.09	0.41

Figure 44. Location of the transducer mounting block in the cavity scale experiments (Shaw, Ref. 24).

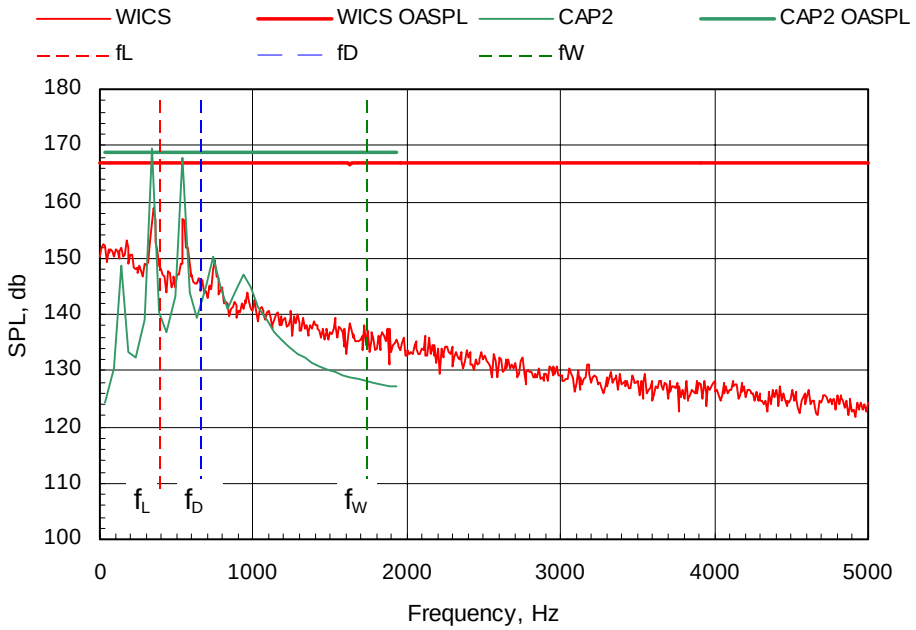

a. $M_\infty = 0.60$

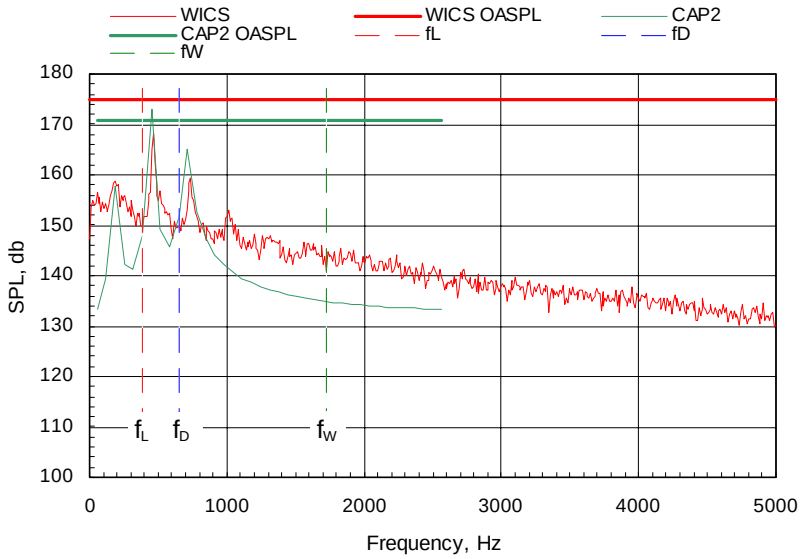

b. $M_\infty = 0.95$

Figure 45. Comparison of measured and predicted spectra for an L/D = 4.5 cavity, including values of the OASPL and the acoustic natural frequencies, Re = 3×10^6.

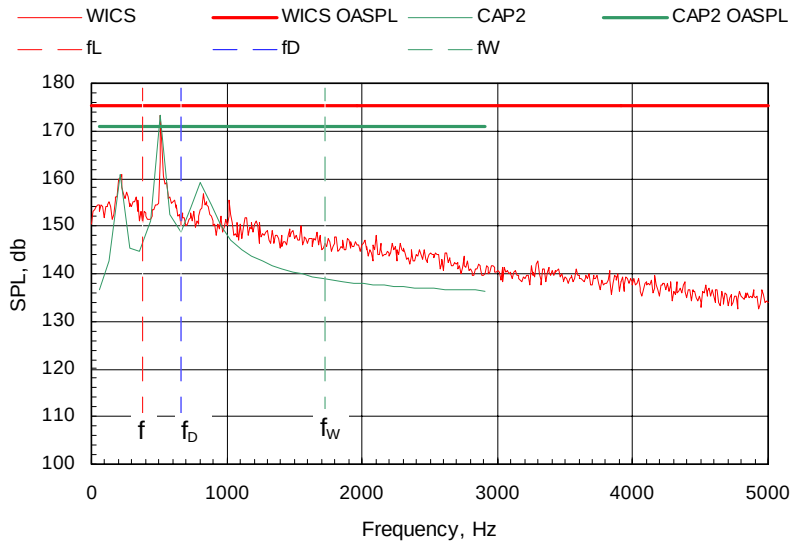

c. M_∞ = 1.20

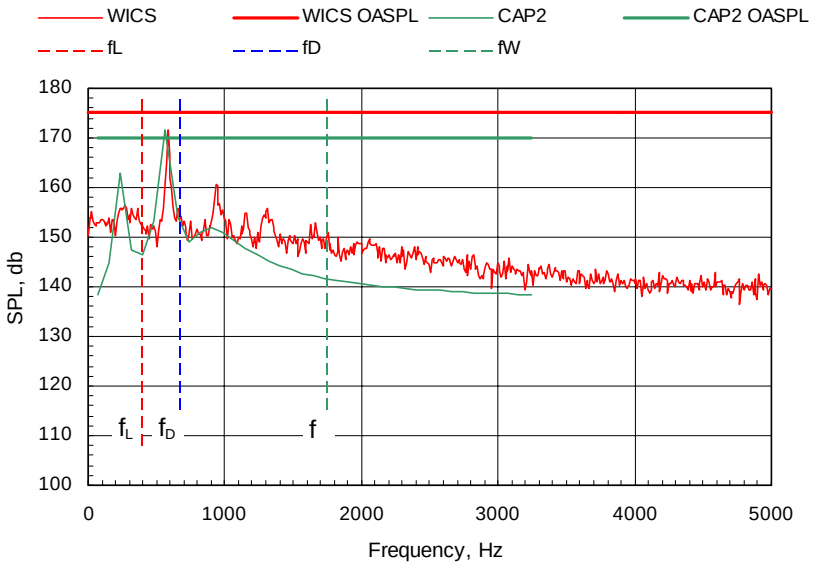

d. M_∞ = 1.50

Figure 45. Continued.

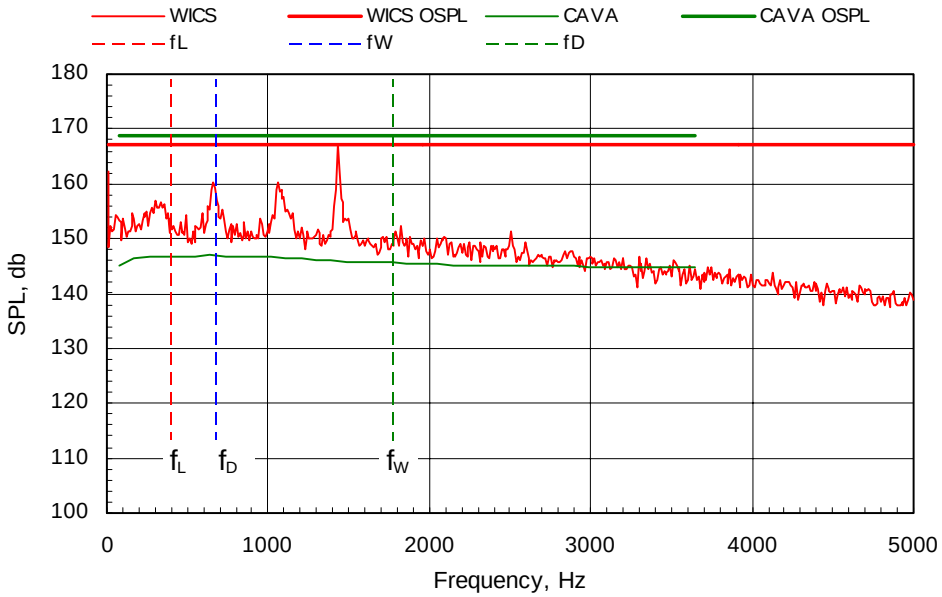

e. M_∞ = 2.00

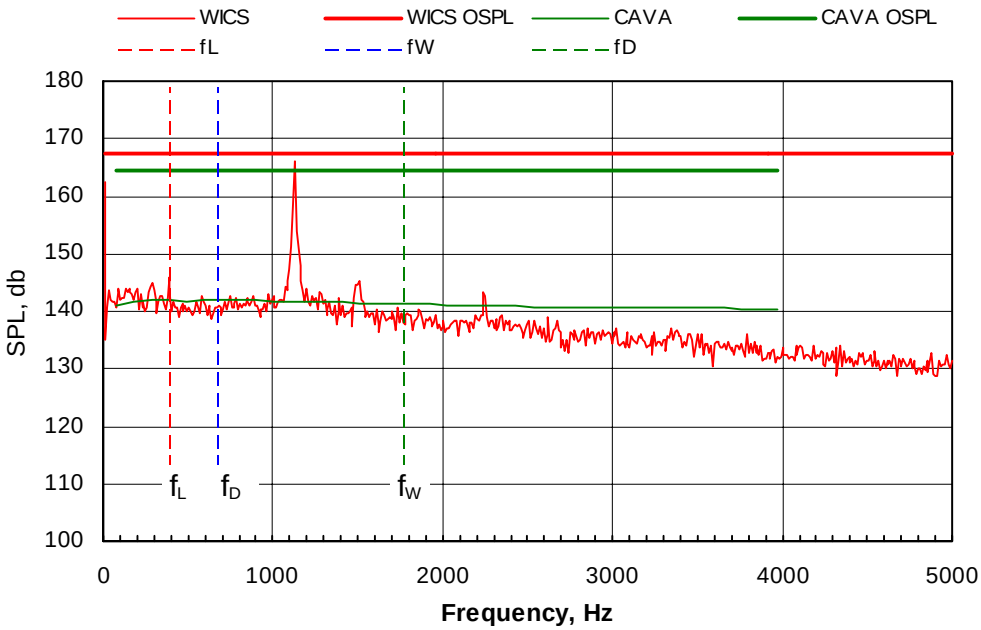

f. M_∞ = 2.75

Figure 45. Continued.

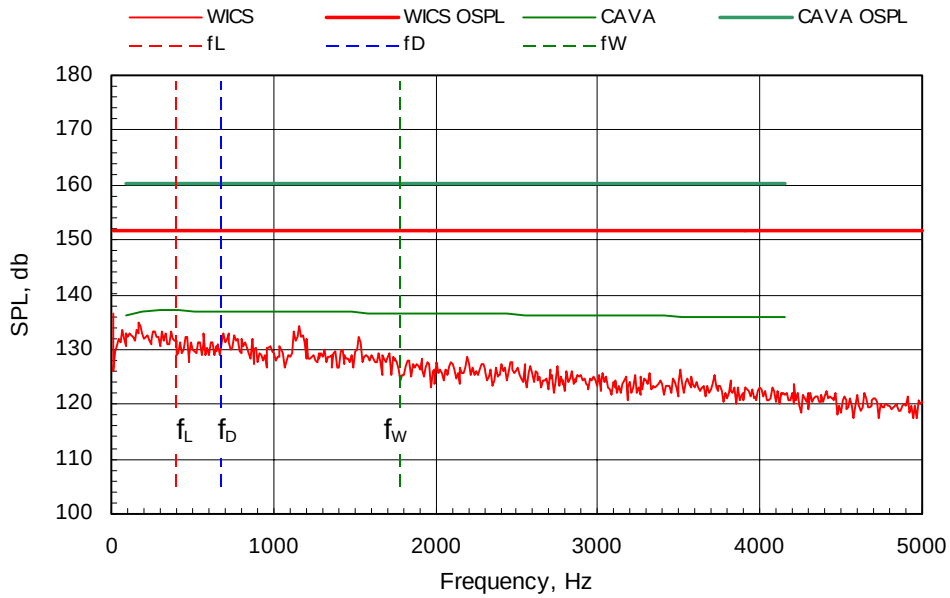

g. M_∞ = 3.51

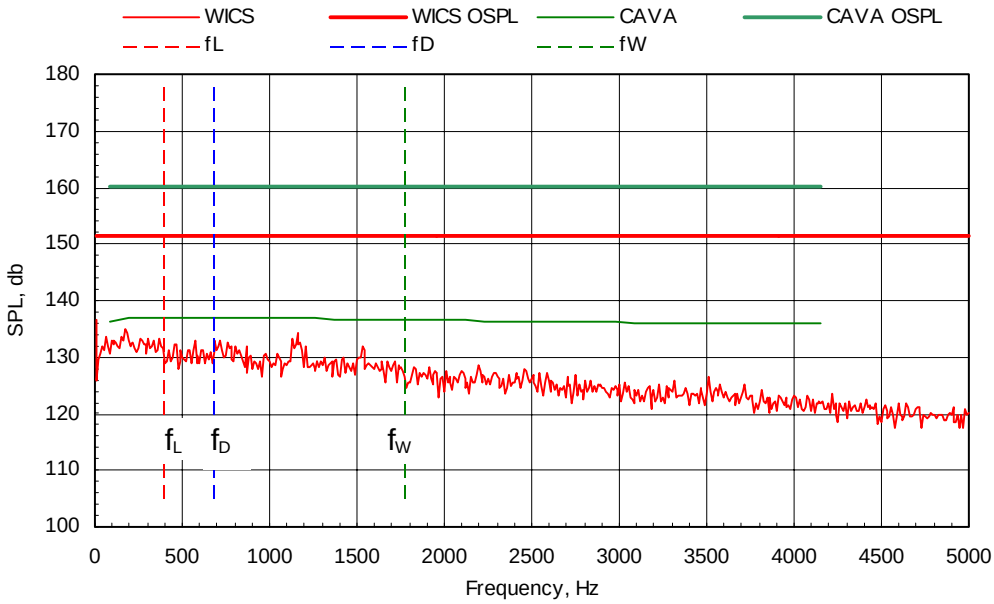

h. M_∞ = 5.04

Figure 45. Concluded.

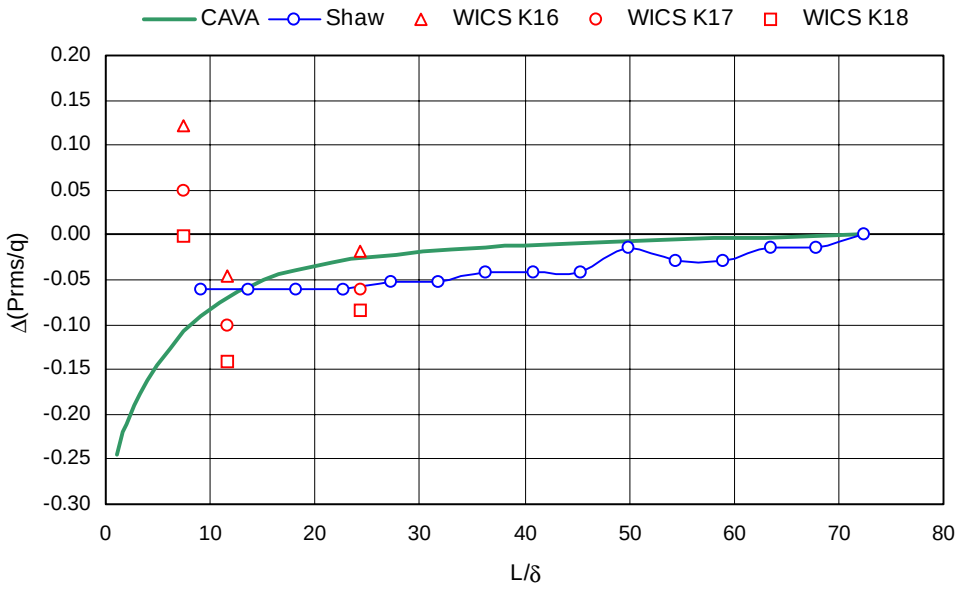

a. Sawtooth spoiler mounted at leading edge of cavity

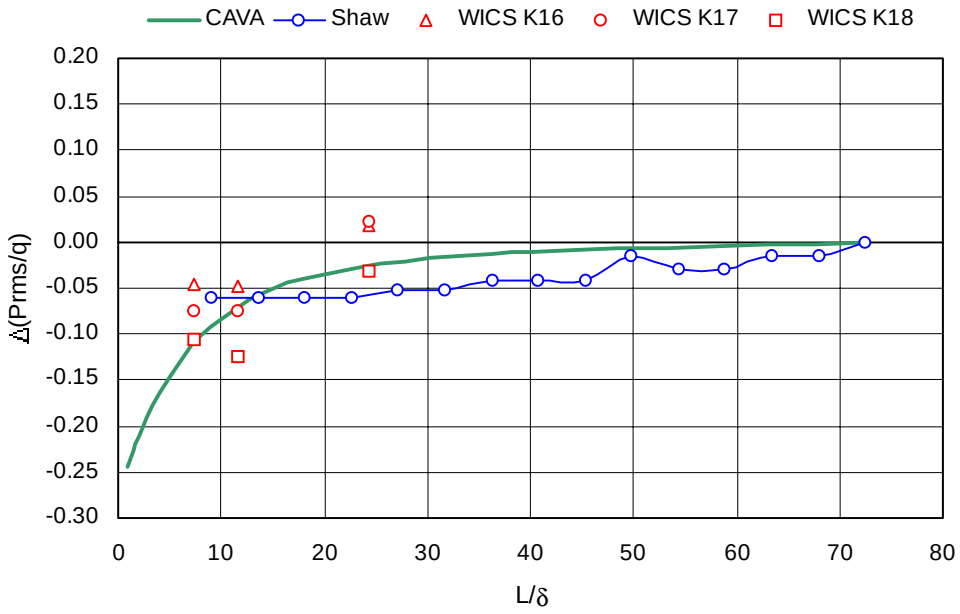

b. Sawtooth spoiler mounted at X/L = -0.20

Figure 46. Comparison of predicted and experimental values of the effectiveness of a spoiler installed near a cavity as a function of the scaling parameter, L/δ; cavity L/D = 4.5 and M_∞ = 0.60.

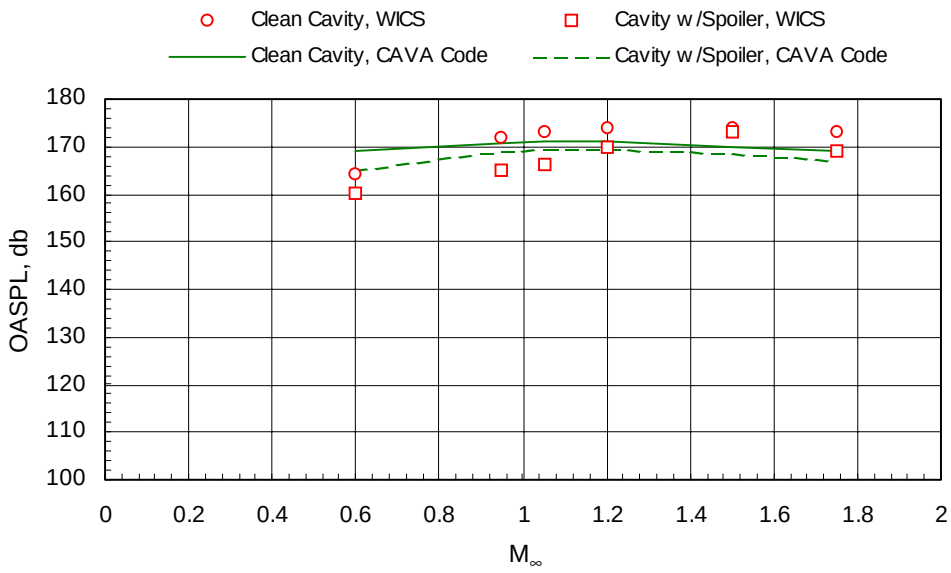

a. Overall sound pressure level

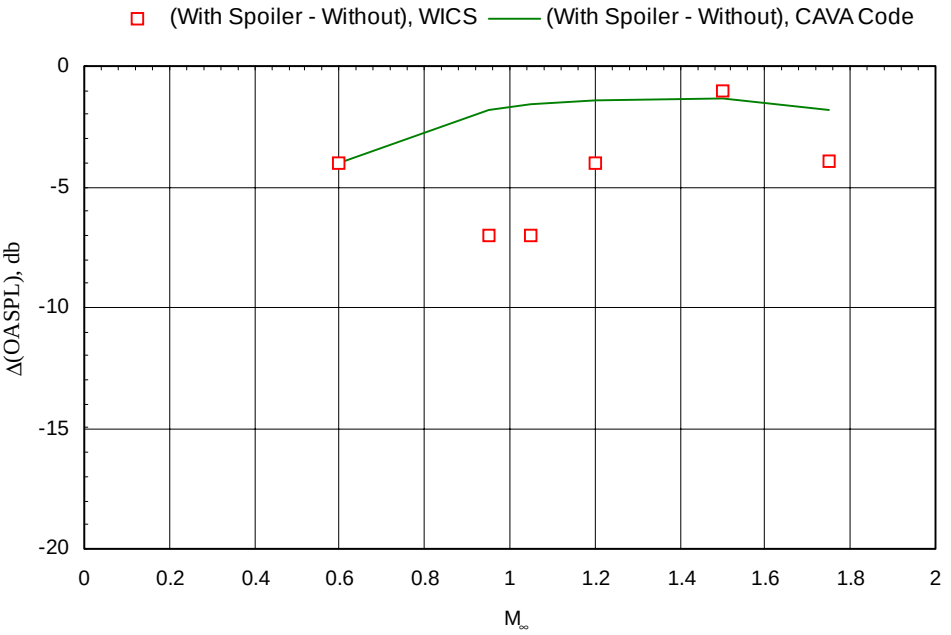

b. Difference in overall sound pressure level attributable to spoiler

Figure 47. Comparison of experimental and predicted OASPL in the presence of a 0.45-in. sawtooth spoiler, L/D = 4.5.

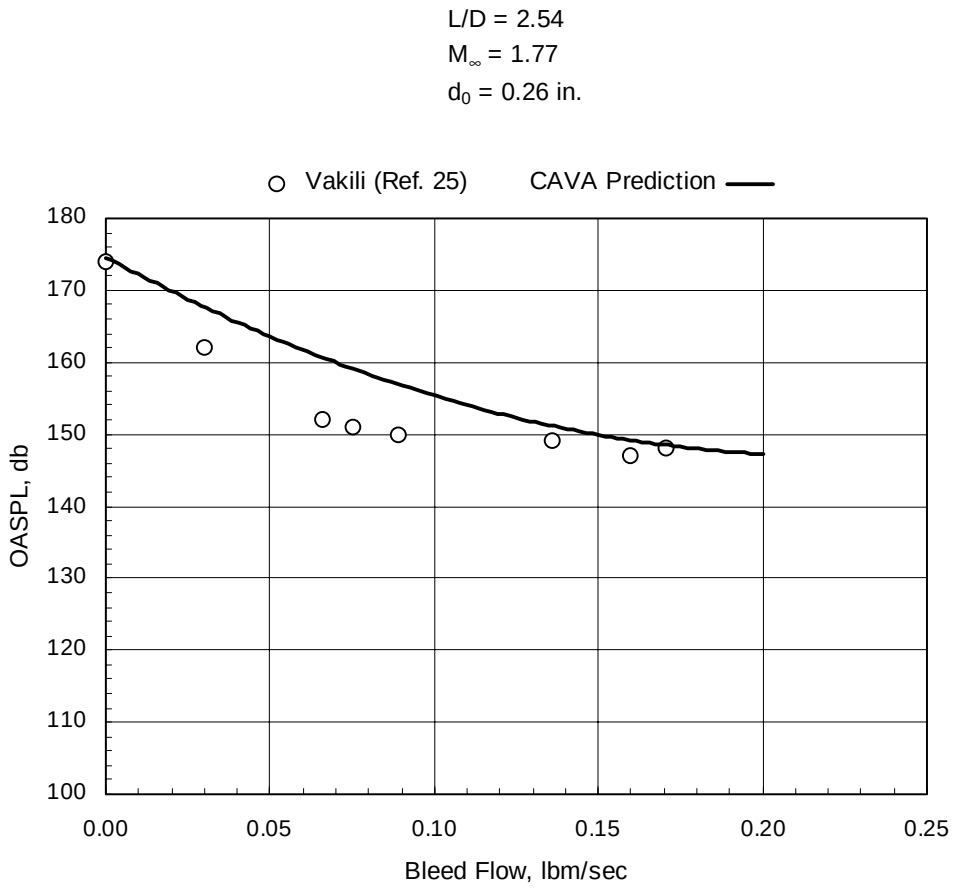

Figure 48. Comparison of experimental and predicted overall acoustic levels in a cavity in the presence of a boundary-layer in-bleed flow upstream of the cavity.

Table 1. Full-Scale Store Characteristics

a. Geometric Dimensions

Store	A, sq ft	L_1, L_2, L_3, ft	L_s, ft	WT, lb	X_{cg}, ft	Y_{cg}, Z_{cg} ft
AIM-9L	0.1360	0.417	9.418	195	5.022	0
GMPM, GMPM-F	1.0000	1.000	11.989	-	6.373	0

b. Inertias

Store	I_{XX}, slug-ft^2	I_{XY}, slug-ft^2	I_{XZ}, slug-ft^2	I_{YY}, slug-ft^2	I_{YZ}, slug-ft^2	I_{ZZ}, slug-ft^2
AIM-9L	**0.50**	**0**	**0**	**45.56**	**0**	**45.56**

c. Installed Incidence with Respect to Pylon; Ejection Parameters

Store	I_P, deg	I_Y, deg	I_R, deg	W_0, ft/sec	q_0, rad/sec
All Stores	0	0	0	30	−1.0

d. Dynamic Derivatives

Store	M_∞	C_{lp}	C_{mq}	$C_{nr}C_{lp}$
AIM-9L	0.95	−54	−6549	−6549

Table 2. Nominal Flow Conditions for the Tests

Tunnel	M_∞	P_t, psf	T_t, °R	V_∞, ft/sec	q_∞, psf	Re, 1/ft
4T	0.60	615	545	663	121	1.0×10^6
4T	0.60	1200	550	670	238	1.9×10^6
4T	0.60	1235	550	666	244	2.0×10^6
4T	0.60	1900	555	670	375	3.0×10^6
4T	0.75	1208	547	818	328	2.2×10^6
4T	0.80	1200	556	871	352	2.3×10^6
4T	0.85	1200	547	911	376	2.3×10^6
4T	0.90	1200	547	957	403	2.4×10^6
4T	0.95	478	542	998	169	1.0×10^6
4T	0.95	980	545	1000	343	2.0×10^6
4T	0.95	1200	550	1008	424	2.5×10^6
4T	0.95	1480	551	1008	525	3.0×10^6
4T	1.00	1188	548	1028	430	2.5×10^6
4T	1.05	468	545	1089	180	1.0×10^6
4T	1.05	948	548	1091	366	2.0×10^6
4T	1.05	1200	550	1095	463	2.5×10^6
4T	1.05	1447	554	1099	557	3.0×10^6
4T	1.10	1200	549	1135	476	2.5×10^6
4T	1.15	1200	551	1178	490	2.6×10^6
4T	1.20	455	544	1208	189	1.0×10^6
4T	1.20	930	547	1212	386	2.0×10^6
4T	1.20	1200	552	1220	499	2.6×10^6
4T	1.20	1411	552	1219	586	3.0×10^6
4T	1.30	1197	555	1297	511	2.5×10^6
4T	1.40	1208	558	1374	520	2.5×10^6
4T	1.50	510	558	1448	219	1.0×10^6
4T	1.50	987	557	1441	424	2.0×10^6
4T	1.50	1200	557	1442	515	2.4×10^6
4T	1.50	1398	562	1447	600	2.8×10^6
4T	1.60	1202	557	1506	506	2.4×10^6
4T	1.75	1200	556	1593	483	2.3×10^6
4T	1.90	1207	566	1674	455	2.2×10^6
4T	2.00	1200	560	1728	430	2.0×10^6
4T	2.00	1400	562	1734	501	2.4×10^6

Table 3. Statistical Confidence Intervals for the Test Data

a. Aerodynamic Force and Moment Coefficient Uncertainties

Store	M_∞	P_t, psf	$\varepsilon(C_N)$	$\varepsilon(C_Y)$	$\varepsilon(C_{AT})$	$\varepsilon(C_l)$	$\varepsilon(C_m)$	$\varepsilon(C_n)$
AIM-9L	0.60	1200	±0.057	±0.109	±0.056	±0.090	±0.037	±0.042
	0.80	1200	±0.042	±0.078	±0.042	±0.067	±0.028	±0.031
	0.95	1200	±0.031	±0.055	±0.031	±0.050	±0.021	±0.023
	1.05	1200	±0.028	±0.049	±0.029	±0.045	±0.019	±0.021
	1.20	1200	±0.026	±0.043	±0.027	±0.042	±0.018	±0.019
	2.00	1858	±0.050	±0.035	±0.044	±0.037	±0.320	±0.272
	2.75	1200	±0.063	±0.046	±0.050	±0.046	±0.498	±0.363

b. Model Position and Attitude Uncertainties

Model	Item	Uncertainty
Flat plate/cavity	Pitch attitude	±0.10 deg
Store models (all)	Pitch attitude	±0.15 deg
	Yaw attitude	±0.15 deg
	Roll attitude	±2.00 deg
	X , Y , Z position	±0.05 in. (±0.042 ft full scale)

c. Full-scale Store Trajectory Uncertainties

Store	M_∞	Elapsed Time, sec	$\varepsilon(X_p)$, ft	$\varepsilon(Y_p)$, ft	$\varepsilon(Z_p)$, ft	$\varepsilon(\theta)$, deg	$\varepsilon(y)$, deg	$\varepsilon(f)$, deg
AIM-9L	0.95	0.30	±0.04	±0.05	±0.06	±0.03	±0.02	---

APPENDIX A
DEVELOPMENT OF THE CAVITY ACOUSTICS SPECTRAL PREDICTION CODE (CAP2 CODE)

A.1 DEVELOPMENT OF THE PHENOMENOLOGICAL MODEL

A.1.1 Freestream Flow Conditions

Assuming air as the gas flowing tangent to the cavity opening, the required flow conditions are the Mach number, total pressure, and total temperature. In addition, the boundary-layer thickness must be known, although a value of zero is allowed. If the shape of the boundary-layer velocity profile can be represented by a power law involving the exponent 1/N, then the value of N is determined from the following empirical equation from Ref. 10:

$$N = 0.89 \times \ln(Re_{N\theta}) - 1.65 \tag{A-1}$$

If a flat-plate spoiler is present, then the boundary-layer thickness and shape downstream of the spoiler are estimated from a momentum analysis based on the known height and assumed drag coefficient of the spoiler. The equation is:

$$\frac{\delta_s}{\delta} = \frac{\left(\frac{\theta}{\delta}\right) + C_{D_s} h_s \left(\frac{\bar{q}}{q_\infty}\right)}{\frac{\theta_s}{\delta_s}} \tag{A-2}$$

If the spoiler is a porous flat plate with or without flow under it, the flow conditions downstream of the spoiler must be specified. If bleed flow is used as a spoiler, then the change in the boundary layer attributable to the bleed flow is estimated from a momentum analysis, which produces the result:

$$\frac{\delta_B}{\delta} = \frac{\left(\frac{\theta}{\delta}\right) + \left(\frac{m_B}{W\delta\rho_\infty u_\infty}\right)}{\left(\frac{\theta_B}{\delta_B}\right)} \tag{A-3}$$

Once the initial boundary layer is known, then the displacement and momentum thicknesses are determined from the following standard equations:

$$\frac{\delta^*}{\delta} = 1 - \left(1 - C_\infty^2\right) I_2 \tag{A-4}$$

$$\frac{\theta}{\delta} = 1\frac{\delta^*}{\delta} - \left(1 - C_\infty^2\right) I_2 \tag{A-5}$$

A.1.2 Cavity Geometry and Acoustic Response

Extending the applicability of a given database to other cavities depends on the development of an appropriate mathematical model to describe the phenomena involved. Of course, the two fundamental components of the cavity's acoustic response that must be defined are the frequencies and the amplitudes. In searching for a suitable theoretical model for the cavity, one might consider the closed organ pipe, which, by definition, is physically closed on just one end, which would then represent a displacement node. But the application to a cavity is invalid, since the cavity is closed on both ends in the length and width directions. Instead, it is asserted that the best analogy is that of the open organ pipe, for which each end is a pressure node, i.e., the pressure amplitude at each end is a maximum. Then, proceeding from the fundamental relationship for wave motion,

$$f = \frac{\alpha}{\lambda_\alpha} \tag{A-6}$$

and assuming the cavity responds like an open organ pipe, the frequencies of the fundamental acoustic modes for the length (L), width (W), and depth (D), are:

$$f_L = \frac{a_t}{2L} \tag{A-7}$$

$$f_W = \frac{a_t}{2W} \tag{A-8}$$

$$f_D = \frac{a_t}{4D} \tag{A-9}$$

where a_t represents the speed of sound at the total temperature of the flow. The frequencies of the natural, or fundamental, acoustic modes for the cavity calculated in this manner are identified in Fig. 41 along with the typical SPL spectra for the deepest of the WICS cavities. (The output of transducer K18 – located as illustrated in Fig. 11 – is used throughout the following analysis as a criterion, since that location is in the region of highest acoustic levels in the cavity, and was never covered by the adjustable floor.) Note that the frequencies of the tones that are detected do not match the natural acoustic frequencies. Therefore, if the open organ pipe analogy is not appropriate for the cavity of interest, then the acoustic natural frequencies that are used as inputs for the CAP2 Code must be determined from either an acoustic analysis or experiment.

A.1.3 Turbulent Mixing Analysis

The Chapman-Korst mixing analysis (Ref. 17) is used to determine the velocity ratio on the dividing streamline and the Reynolds shear stress. The mixing analysis consists of two parts: the first determines the velocity profile including the effect of an initial boundary layer, and the second determines the locations in the mixing zone of the dividing streamline and the inviscid jet boundary, as illustrated here:

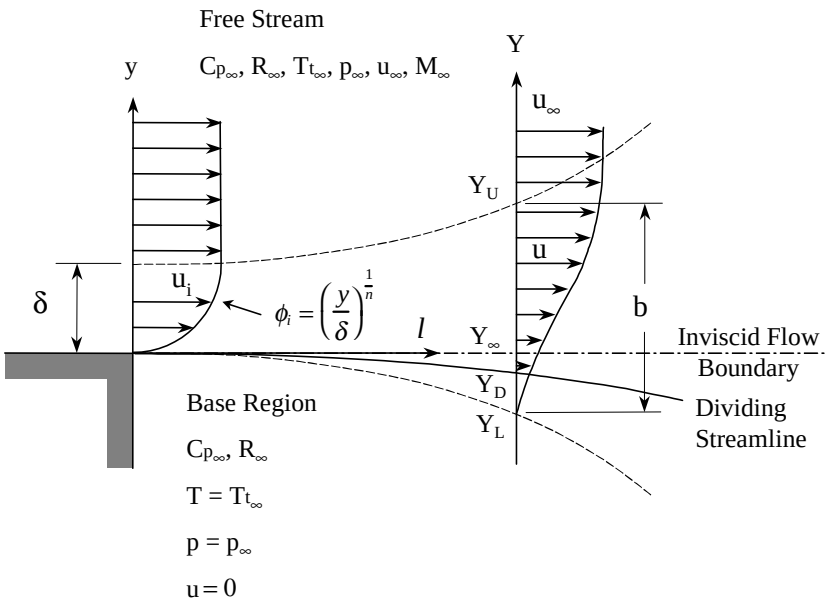

The velocity profile is obtained by solving a simplified equation of motion of the heat conduction form:

$$\phi = \frac{1}{2}[1 + erf(\eta - \eta_P)] + \frac{\eta_P}{\sqrt{\pi}}\int_0^{1.0} \phi_i e^{-\left[\eta - \eta_P\left(\frac{y}{\delta}\right)\right]^2} d\left(\frac{y}{\delta}\right) \qquad \text{(A-10)}$$

where $\eta = \sigma y/x$. . Equation (A-10) defines a parametric family of velocity profiles in terms of η_p ranging from the initial boundary-layer profile for $\eta_p = \infty$, to the fully developed mixing profile for $\eta_p = 0$. Experiment has shown that the value of η_p at any mixing distance, X, can be estimated by the following equation from Ref. 20:

$$\eta_P = \frac{\sigma\delta}{X} \qquad \text{(A-11)}$$

This equation can also be theoretically derived by assuming the turbulent, apparent kinematic viscosity is a linear function of the mixing distance (Ref. 17). The similarity parameter, σ, accounts for the effect of Mach number on the thickness of the mixing zone, and is assumed to be constant for all mixing distances. The theoretical relation between σ and Mach number is a function of the assumed model for the Reynolds stress, as shown in Refs. 18 and 19. In this analysis, experimental values of σ for single-stream free mixing are empirically fit by the following equations:

For $M_\infty \le 1.0$: $$\sigma = 3M_\infty + 12 \qquad \text{(A-12)}$$

For $M_\infty > 1.0$: $$\sigma = 8M_\infty + 7 \qquad \text{(A-13)}$$

The location of the dividing streamline, η_d, and the inviscid jet boundary, η_∞, are determined by the conservation equations for momentum and mass flow:

$$(I_1)_{\eta D} = (I_1)_{\eta U} - (I_2)_{\eta U} - \frac{\eta_P}{(1 - C_\infty^2)}\left(\frac{\theta}{\delta}\right) \tag{A-14}$$

$$\eta_\infty = \eta_U + -\eta_P\left[\frac{\delta^*}{\delta} + \frac{\theta}{\delta}\right] - (1 - C_\infty^2)(I_2)_{\eta U} \tag{A-15}$$

The I_1 integral is the nondimensional integral of mass flow, ρu, while the I_2 integral is the nondimensional integral of momentum, ρu^2. The momentum equation is based on the assumption that the static pressure is constant and equal to the free-stream value, both across the mixing zone and in the downstream direction. The velocity ratio on the dividing streamline, ϕ_D, is then obtained by evaluating the velocity profile equation [Eq. (A-10)] at $\eta = \eta_d$.

The Reynolds shear stress on the dividing streamline at any mixing distance is obtained by applying the basic principle that the momentum, or stream force, of the entrained mass flow must equal the total shear force acting on the dividing streamline, which is to say:

$$\int_0^x \tau_D dx = \int_{Y_L}^{Y_D} \rho u^2 dY \tag{A-16}$$

The local Reynolds shear stress on the dividing stream line at any mixing distance, X, is obtained by differentiating Eq. (A-14) with respect to X, which yields:

$$C_{f_D} = 2\left(\frac{1 - C_\infty^2}{\sigma}\right)(I_2)_{\eta D} + \left(1 - C_\infty^2\right)\frac{d(I_2)_{\eta D}}{d\eta_P} \tag{A-17}$$

This equation is numerically evaluated to obtain the local coefficient of friction on the dividing streamline.

A.1.4 Turbulent Kinetic Energy

Experiments have shown that for both turbulent boundary layers and free-jet mixing zones, a linear relation exists between the Reynolds shear stress parallel to the mean flow and the turbulent kinetic energy. Therefore, it is assumed that

$$\tau_D = a_i \rho_D \tau_{KE} \tag{A-18}$$

where

$$\tau_{KE} = \frac{u_{rms}^2}{2} \tag{A-19}$$

An application of this equation to various free-jet mixing processes is presented by Harsha and Lee in Ref. 20, including a large number of experimental results that show the constant a_1 has a value of 0.3. With this equation, it is possible to determine the local turbulent kinetic energy on the dividing streamline.

A.1.5 Euler's Equation

The relation between the overall rms pressure and the turbulent kinetic energy is obtained by a unique interpretation of the basic Euler equation. The basic Euler equation is sometimes referred to as the strong form of Bernoulli equation, or:

$$dp = -(\rho)(u)(du) \tag{A-20}$$

In this equation, the velocity is the total velocity, and the differentials can be interpreted as perturbations in the static pressure and total velocity attributable to turbulence. The resulting equation is:

$$p_{rms} = (\bar{\rho})(\bar{u})(u_{rms}) \tag{A-21}$$

Since the turbulent kinetic energy is defined by Eq. (A-19), the final equation for the ratio of the overall rms pressure to the freestream dynamic pressure is

$$\frac{p_{rms}}{q_\infty} = 2\phi_D \sqrt{\frac{(1 - C_\infty^2)C_{f_D}}{a_1(1 - C_\infty^2\ \phi_D^2)}} \tag{A-22}$$

This overall rms pressure is assumed to be the same as that acting on the downstream wall of the cavity.

A.1.6 Frequency Response Function

The fluctuating pressure on the dividing streamline is assumed to be the same as that acting on the downstream cavity wall, and is modeled as the sum of 512 sine waves of frequencies equal to the first 512 edgetones, or:

$$p_D = \sum_{m=1}^{512} a_m \sin(2\pi f e_m t) \tag{A-23}$$

Note that Eq. (A-14) is not exactly a Fourier series since the difference in consecutive frequencies is not equal to the fundamental first mode edgetone because of the phase parameter, γ_R, in Rossiter's equation. The equation for the overall rms pressure is:

$$p_{D_{rms}} = \sqrt{\sum_{m=1}^{512} \frac{a_m^2}{2}} \tag{A-24}$$

The amplitudes in Eq. (A-15) are determined by a unique response function that is derived in Ref. 21 for unsteady flow in a tube. The equation is:

$$\frac{a_m}{P_{ref}} = \left[\frac{\left[1 + \left(\frac{f}{f_{e_m}}\right)^2\right]^2 + 4d^2\left(\frac{f}{f_{e_m}}\right)^2}{\left[1 - \left(\frac{f}{f_{e_m}}\right)^2\right]^2 + 4d^2\left(\frac{f}{f_{e_m}}\right)^2} \right]^{\frac{1}{2}} \tag{A-25}$$

Equation (A-25) was selected because the amplitudes at the higher frequencies are not damped, which is consistent with the experimental results previously presented for cavities. In this equation, the damping ratio is determined by the energy loss in the unsteady flow process. Since a practical cavity can be seen as a very short tube, the damping attributable to the viscous effects on the walls can be neglected. Another type of damping is also postulated, viz., "wave damping." Wave damping is attributable to the mutual interaction of the various acoustic waves with an ultimate loss of energy out the opening of the cavity, and probably can only be calculated by solving the Navier-Stokes equation. In the present analysis, empirical equations for the damping ratio were developed for each edgetone frequency, relying on the WICS data for Mach numbers 0.6 and 0.95 for the L/D = 4.5 cavity. The equations are the following:

$$d_w = \left(1 - \frac{f_{e_m}}{f_L}\right)^2 + \left(1 - \frac{f_{e_m}}{f_W}\right)^2 + \left(1 - \frac{f_{e_m}}{f_D}\right)^2$$

$$m = 1,\ d = d_w e^{d_w}(0.006617M_\infty + 0.0003734)$$

$$m = 2,\ d = d_w e^{d_w}(0.01284M_\infty - 0.005529)$$

$$m = 3,\ d = d_w e^{d_w}(0.006617M_\infty + 0.0003734) \tag{A-26}$$

$$m = 4,\ d = d_w e^{d_w}(2.837M_\infty - 1.691)$$

$$m = 5,\ d = d_w e^{d_w}(2.845M_\infty - 1.7047)$$

$$m = 6,\ d = d_w e^{d_w}(0.996M_\infty - 0.5954)$$

These equations are formulated so that minimum damping occurs when an edgetone frequency equals one of the three natural acoustic frequencies. Hence, the largest peaks in the spectrum occur for those edgetone frequencies that coincide with the natural acoustic frequencies of the cavity.

A.1.7 Pressure Spectrum

In the previous section, the pressure spectrum was determined relative to an unknown reference pressure. Since the overall rms pressure is known from the mixing analysis, then the reference pressure is determined by the following:

$$p_{ref} = \frac{p_{rms}}{\sqrt{\sum_{m=1}^{512} \frac{1}{2} \left(\frac{a_m}{p_{ref}} \right)^2}} \tag{A-27}$$

The exact reference pressure is unknown; however, comparison with experiment indicates it is the rms pressure of the background noise.

NOMENCLATURE

A	Accelerometer
a	Speed of sound, ft/sec
C_{DS}	Drag coefficient of a solid blade spoiler
C_{f_D}	Coefficient of friction on the dividing streamline, = τ_D/q_∞
CG, cg	Center of gravity
C_{f_p}	Roll-damping coefficient, rate of change of rolling-moment coefficient with respect to rolling velocity, $\partial C_l/\partial(pD/2V_\infty)$, 1/rad
C_{m_q}	Pitch-damping derivative, rate of change of pitching coefficient with respect to pitching velocity, $\partial C_m/\partial(qD/2V_\infty)$, 1/rad
C_{n_r}	Yaw-damping derivative, rate of change of yawing moment with respect to yawing velocity, $\partial C_n/\partial(rD/2V_\infty)$, 1/rad
C_p	Specific heat at constant pressure in the freestream
C_∞	Freestream Crocco number, $\mu_\infty / \sqrt{2C_p T_{t_\infty}}$
D	Maximum depth of a cavity, in.
erf(η-η_p)	Error function of the expression $(2/\sqrt{\pi}) \int_0^{(\eta-\eta_p)} \exp^{(\eta-\eta_p)^2} d\eta$
f	Frequency, Hz
f_m	Modal frequency, Hz
HFG	Hot-film gage
h_s	Height of a solid blade spoiler, in.
$(I_1)_i$	the integral $\int_0^1 (\phi_i / 1 - C_\infty^2 \phi_i^2)\ d\ (y/\delta)$
$(I_2)_i$	the integral $\int_0^1 (\phi_i^2 / 1 - C_\infty^2 \phi_i^2)\ d\ (y/\delta)$

$(I_1)_\eta$ the integral $\int_{-3}^{\eta} (\phi_i / 1 - C_\infty^2 \phi_i^2)\ d(\eta)$

$(I_2)_\eta$ the integral $\int_{-3}^{\eta} (\phi_i^2 / 1 - C_\infty^2 \phi_i^2)\ d(\eta)$

I_P Angle of incidence in pitch between the longitudinal axis of the store and the longitudinal axis of the generic plate/cavity, deg

I_R Angle of incidence in roll between the store model and the generic plate/cavity, deg

I_Y Angle of incidence in yaw between the longitudinal axis of the store model and the XZ plane of the generic plate/cavity, deg

I_{XX} Moment of inertia of a full-scale store about the XB axis, slug-ft^2

I_{XY} Product of inertia of a full-scale store about the XBYB plane, slug-ft^2

I_{XZ} Product of inertia of a full-scale store about the XBZB plane, slug-ft^2

I_{YY} Moment of inertia of a full-scale store about the YB axis, slug-ft^2

I_{YZ} Product of inertia of a full-scale store about the Y_BZ_B plane, slug-ft^2

I_{ZZ} Moment of inertia of a full-scale store about the Z_B axis, slug-ft^2

K Kulite® pressure transducer (accompanying digits identify a specific transducer)

L Length of the cavity, in.

L_s Length of a store, ft full scale

L/D Ratio of cavity length to cavity depth

L_1,L_2,L_3 Reference length for calculation of force and moment coefficients (the maximum diameter of a store), ft full scale

M_∞ Mach number in the freestream

m Mode number for acoustic disturbance resonance

m_s Total mass flow rate of a bleed flow acting as a spoiler, lbm/sec

N Exponent for the initial boundary-layer profile

P	Static pressure, psfa
P_t	Total, or stagnation pressure, psfa
PHI S	Roll angle of a store model about the X_B axis, deg
P_{ref}	International threshhold of audibility, 2 Pa (= 2.9×10^{-9} psi)
P_{rms}	Root-mean-square of fluctuating pressure values, psf
PSI S	Yaw angle of a store model about the ZB axis, deg
p	Rolling velocity of a store model, rad/sec
q	Pitching velocity of a store model, rad/sec
$\bar{q}$	Mean dynamic pressure over the front of a solid blade spoiler, psf
q_o	Pitch rate of the store model at the end of the ejector stroke, rad/sec
q_∞	Dynamic pressure in the freestream of the wing tunnel, psf
Re	Unit Reynolds number, per foot
Re_{N_θ}	Reynolds number based on freestream conditions and the initial boundary-layer momentum thickness
RMSKxx	Overall level recorded at a Kulite® transducer for the frequency range 0-5000 Hz, either SPL (db), or P_{rms}(psf)
r	Yawing velocity of a store model, rad/sec
rms	Root mean square
S	Area of maximum cross section of a store model, ft^2, full scale
SPL	Sound pressure level, db (referenced to 2.9×10^{-9} psi)
St	Strouhal number, fL/V_∞
Tn	Thermocouple (accompanying digit identifies a specific thermocouple)
THETA S	Pitch angle of the store model about the Y_B axis, deg
TS	Tunnel station, in. full scale

T_∞	Static temperature in the freestream of the wind tunnel, °R
t	Time, sec
V_∞	Freestream velocity in the wind tunnel, ft/sec
W	Width of the generic cavity, ft full scale
WT	Full-scale weight of a store, lb
W_O	Velocity of a store in the Z_B direction at the end of the ejector stroke, ft/sec full scale
X	Distance from the leading edge of the cavity opening in the flat plate, measured in the X direction, positive downstream, ft full scale
Xcg	Axial distance in the XB direction from the nose of a store to the store cg, ft full scale
Xp	Displacement in the Xp direction from the location of the cg of a store at the end of the ejector stroke to the cg location at a point in the separation trajectory, ft full scale
XPITC	Axial distance from the CTS pitch center to the face of a balance, in.
y	Initial boundary-layer coordinate, measured from the upstream surface
Y	Distance from the longitudinal centerline of the cavity opening in the flat plate, measured in the Y direction, ft full scale; also the axis system ordinate in the mixing region
Y_{cg}	Lateral distance in the Y_B direction from the longitudinal axis of a store to the store cg, ft full scale
Y_D	Ordinate of the dividing streamline
Y_L	Ordinate of the low-speed edge of the mixing zone
Y_p	Displacement in the Y_p direction from the location of the cg of a store at the end of the ejector stroke to the cg location at a point in the separation trajectory, ft full scale
Y_U	Ordinate of the freestream edge of the mixing zone
Z	Displacement from the plane of the surface of the flat plate, measured in the Z direction, ft full scale
ZPITC	Vertical distance between the CTS pitch center and the face of a balance, in.

Z_{cg}	Vertical distance in the Z_B direction from the longitudinal axis of a store to the store cg, ft full scale
Z_p	Displacement in the Z_p direction from the location of the cg of a store at the end of the ejector stroke to the cg location at a point in the separation trajectory, ft full scale
α_C	Angle of attack of the plate/cavity model, deg
δ	Turbulent boundary-layer thickness; also the initial boundary-layer thickness upstream of a spoiler, in.
δ_B	Initial boundary-layer thickness downstream of a bleed flow spoiler, in.
δ_S	Initial boundary-layer thickness downstream of a solid blade spoiler, in.
δ^*	Initial boundary-layer displacement thickness, in.
$\varepsilon(\ )$	Half-width of a two-standard deviation (2σ) bandwidth of values of the independent variable that is calculated to include approximately 95 percent of the measurements of the independent variable
γ	Phase constant in Rossiter's equation (Section 5.1.1)
λ	Model scale factor, model dimension/full-scale dimension
λ_a	Acoustic wave length
$\bar{u}$	Mean velocity of the flow, ft/sec
ϕ	Velocity ratio, u/u_∞; also roll angle of a store model, deg
ϕ_i	Initial boundary-layer velocity ratio, Vu/u_∞
ψ	Yaw angle of a store model, deg
θ	Boundary-layer momentum thickness, in.
θ_B	Initial boundary-layer momentum thickness downstream of a bleed flow, in.
θ_s	Initial boundary-layer momentum thickness downstream of a solid blade spoiler, in.; also the pre-bend angle of a CTS support sting in the pitch plane, deg
ρ	Density of the flow at any point in the mixing zone, slugs
$\bar{\rho}$	Mean density of the flow at any point in the mixing zone, slugs

σ Turbulent mixing similarity parameter for the effect of Mach number on the growth of the mixing zone

τ_D Shear stress on the dividing streamline

τ_{KE} Turbulent kinetic energy

μ_{rms} Root-mean-square value of the total turbulent velocity fluctuations

SUBSCRIPTS

C, cav Cavity

S Store

t Total, or stagnation conditions in the freestream

v Vortex, propagation velocity across cavity, ft/sec

∞ Freestream conditions

CAVITY AXIS SYSTEM

Origin: At a point on the cavity opening leading edge (defined by the intersection of two planes: the surface of the flat plate and the forward wall of the cavity), and midway between the sides of the cavity opening. The cavity axes did not vary in location or orientation throughout the test.

Directions of the Axes:

X Parallel to the longitudinal axis of symmetry of the generic flat plate/cavity model, and in the plane of the opening of the cavity, positive downstream.

Y Perpendicular to the X axis and in the plane of the opening of the cavity. If the flat plate/cavity were considered to be on the underside of an aircraft, the positive direction was out the right wing.

Z Perpendicular to the X and Y axes. The positive direction was away from the cavity, downward as sensed by a pilot of the imaginary aircraft in an upright level attitude.

REFERENCE AXIS SYSTEM

Origin: Selected arbitrarily as the initial point for movement of the store model through the specified matrix of spatial locations (grid). Here, the origin was defined as:

X_{REF} = 0 at a location 7.216 ft full scale downstream of the leading edge of the cavity opening along the X axis

Y_{REF} = 0 at the longitudinal centerline of the cavity

Z_{REF} = 0 in the plane of the surface of the flat plate

Directions of the Axes:

X_{REF} Parallel to the X direction, positive upstream.

Y_{REF} Perpendicular to the X_{REF} direction, and parallel to the Y axis. If the flat plate/cavity were considered to be on the undeside of an aircraft, the positive direction was out the right wing.

Z_{REF} Perpendicular to the X_{REF} and Y_{REF} axes. The positive direction was away form the cavity, downward as sensed by a pilot of the imaginary aircraft in an upright level attitude.

The axes were attached to the flat plate/cavity throughout the test, and did not rotate.

PYLON AXIS SYSTEM

Origin: Coincident with the projection of the store cg onto the longitudinal plane of symmetry of the cavity when the store was in the captive position. The pylon axes remained with the flat plate/cavity and translated along the flight path at the freestream velocity. The axes rotated to maintain constant angular orientation with respect to the flight path direction.

Direction of the Axes:

Xp Parallel to the longitudinal axis of the store at release, and at a constant angular orientation with respect to the current flight path direciton, positive upstream.

Yp Perpendicular to the Xp direciton and parallel to the XFYF flight plane. If the flat/plate cavity were considered to be on the underside of an aircraft, the positive direction was out the right wing.

Zp Perpendicular to the Xp and Yp directions. The positive direction was away from the cavity, downward as sensed by a pilot of the imaginary aircraft in an upright level attitude.

STORE BODY AXIS SYSTEM

Origin: Coincident with the cg of the store at all times. Since the axes rotated with the store in pitch, yaw, and roll, the mass moments of inertia and products of inertia of the store were constant.

Direction of the Axes:

X_B Parallel to the longitudinal axis of the store, positive upstream at release of the store.

YB Perpendicular to the XB and ZB directions, positive to the right when looking upstream with the store at zero yaw and zero roll angles.

ZB Perpendicular to the XB direction and parallel to the plane of symmetry of the flat plate/cavity model when the store and cavity models were at zero yaw and zero roll angles. The positive direction was downward as sensed by the pilot of the imaginary aircraft when the store was at zero pitch and zero roll angles.

FLIGHT AXIS SYSTEM

Origin: Coincident with the origin of the Reference Axis System.

Direction of the Axes:

XF Parallel to the direction of the flight path of the imaginary aircraft, positive downstream.

YF Perpendicular to the XF and ZF directions. If the flat plate/cavity were considered to be on the underside of an aircraft, the positive direction was out the right wing.

Z_F Parallel to the flat plate/cavity longitudinal plane of symmetry, and perpendicular to the aircraft flight path. The positive direction was away from the cavity, downward as sensed by a pilot of the imaginary aircraft in an upright level attitude.